The University Of Sheffield.

Polymer/Graphene Oxide Nanocomposites: Surface Adsorption and Interfaces

By

Ehssan Dhiaa Jawad Al-Bermany

Thesis submitted in partial fulfilment of the requirements for the degree of Doctor of Philosophy

The University of Sheffield

Faculty of Engineering

Department of Materials Science and Engineering

September 2017

Declaration

I hereby declare that this report is my own work and effort. Where other sources of information have been used, they have been acknowledged.

Signed: _____

By Ehssan Al-Bermany

Abstract

Polymer/graphene oxide (GO) nanocomposites are attracting growing attention of scientists and engineers in widely spread important applications. This work aims to study the structure-property relationships in polymer/GO nanocomposites and understand the adsorption behaviour of polymer on GO nanosheets. A series of parameters were used to achieve optimum adsorption and investigate the effect of each parameter on the structure and properties of the polymer adsorbed on GO nanosheets. Various characterization techniques were utilized to characterize the polymer/GO nanomaterials.

In the first chapter, semicrystalline poly(ethylene glycol)s (PEGs) with different molecular weights were used as model polymers to prepare a series of PEG/GO hybrid nanomaterials. The effect of mixing time, mixing ratio, polymer molecular weight and washing procedure on surface adsorption behaviour of PEG on GO nanosheets were investigated. The characterization results confirmed the adsorption of PEG on GO nanosheets. The adsorption amount of PEG was increased by 46% after reducing the mixing time from 192 h to 72 h. It was increased significantly by 1700% by increasing the molecular weight from 1k to 100k, by 13% by doubling the mixing ratio of the PEG and by 73% by applying these two changes simultaneously. The incorporation of GO reduced the crystallinity of the PEGs as confirmed by differential scanning calorimetry (DSC). Scanning electron microscopy (SEM) and atomic force microscopy (AFM) images illustrated the varied roughness of the polymer on the surface of the GO nanosheets. The additional washing procedure reduced the adsorption amount of polymer to less than 2 wt.%.

In the second chapter, the investigation focuses on the influence of polymer functional group on the adsorption behaviour of polymers onto GO nanosheets. Poly(methyl methacrylate) (PMMA), poly(methyl methacrylate-co-methacrylic acid) (PMMA-co-MAA) and

poly(methacrylic acid) (PMAA), with a similar backbone but different functional groups, were used as polymer models. The presence of acid groups in MAA enhanced the adsorption amount by 27% and 82% for PMMA-co-MAA and PMAA, respectively, compared to that of PMMA. The water contact angles (CA) were increased by 0.5^{o} and 9.4^{o}, accordingly. PMAA demonstrated the best adsorption capability on GO nanosheets. Also, the adsorption amounts were reduced to less than 10 wt.% by the use of washed compared to not washed samples.

GOs with narrow size distributions were produced through separating the GO particles using centrifugal and sonication methods. This green approach relied on three different parameters: sonication duration, centrifugal force and centrifugal duration. Two graphite flakes with different particle sizes (≤20 and ≤149 μm) were used to prepare the GOs. Dynamic Light Scattering (DLS) and AFM were used to characterize the sizes of the separated GOs. GOs with various average sizes, such as ~200, 600, 800, 1000, 1200, 1450, 1600, 1800 and 2000 nm were successfully obtained. The combination of low-power sonication, high centrifugal speed and short centrifugal duration (e.g., 10 seconds) was preferred for the separation of large size GO particles. A longer sonication time reduced the GO size. This method facilitated the production of narrow size-distribution of GO particles for a range of applications.

The effects of the GO size on polymer adsorption behaviour and the mechanical properties were investigated with poly(ethylene oxide) (PEO) as the model polymer. A broad and narrow size distribution and three GOs with different particle sizes, namely 1894 nm (large), medium 1086 nm (medium), and small 360 nm (small) were used. The GO with the narrow size distribution and largest size showed the best PEO adsorption capability where the PEO adsorption amount increased up to 15% and 42%, respectively. PEO/GO nanocomposites were reinforced by these three GOs, a broad and narrow size distribution at 0.2 wt.% loading that were also prepared by a solution blending method. Owing to the contribution of GO,

especially large GO particles, the melting temperature of PEO was increased from 68.6 ^{o}C up to 70.6 ^{o}C. Tensile Young's modulus of the PEO/GO nanocomposites were significantly improved by 179% for the narrow size distribution compared to the value for the broad size distribution, whereas it improved up to 297%, 200% and 125% by the incorporation GOs of large, medium and small particle sizes, respectively. The elastic modulus determined by nanoindentation increased by 154%, 21% and 14% for the three different sizes of GOs. SEM images showed a smooth morphology for the samples containing the large GO particles which overcame the issue of cracks or cavities, compared to other samples. Crystallinity was reduced by 17%. The narrow size distribution and large size of GO demonstrated the strongest reinforcement effect in the PEO matrix and greatly improved the mechanical properties compared to a broad size distribution and smaller size of GO particles.

Manipulating the methods and using different parameters showed a strong influence on the interfacial interaction between the polymer and GO and hence the properties of the bulk polymer/GO nanocomposites. This provided a better understanding of the behaviour of an adsorption polymer on GO nanosheets and the structure-property relations of polymer/GO nanocomposites.

Dedication

To my home land Iraq

My lovely famous city Babylon

To my father how died before I started this project, mum,

To My wife to support and stand with me during my hall life,

My uncle Zaki Al-Rashid, his family, my brothers, Laith, Hasnaa and Ahmed

My family and friends, I lovely you all.

Acknowledgements

This research project would not have been possible without the support of many people. Firstly, I wish to express my gratitude to my supervisor, Professor Dr. Biqiong Chen for her support throughout the project, for the great amount of time and effort she spent to help me to finish my project. She has always believed in my abilities, provided whatever advice and resources necessary for me to accomplish my goals. Deepest gratitude is also to my second supervisor Prof. Goran Ungar for his support during the first year. Deepest gratitude is also to my examiners in the first and second years Dr X Zeng and Dr S A Hayes for their many invaluable inputs, suggestions and comments to the project. Special thanks to Dr Tongfei Wu, Dr Oday Hussein and Dr Lynne Newcombe for their assistant.

Also, I would like to convey thanks to the Iraqi ministry of high education and scientific research, Iraqi cultural attaché and the University of Babylon, the faculty of pure since, physics department for providing the support means and funded my PhD scholarship.

I would like to thank the technical, administrative staff and my group research at the Department of Materials Science and Engineering, Engineering Faculty for providing laboratory facilities, in particular, Ben Palmer, Dawn Bussey and Ann Newbould. Great appreciation is for staff in chemistry department Heather Grievson for here support. My group works specific Zaid Jerjees and Ahmed Alzahrany. Thank you for who have given me wonderful advice, inspiration and friendship over the years.

Finally, I wish to express my love and gratitude to my beloved family; for their understanding & endless love, who have always given me their support through the duration of my studies. My wife, Dr. Sura Al-Rashid, my children Mustafa, Orjuwan and Murtadha, and my friends, Murtakab Al-Hejjaj, Adnan Al-Mousawi, Salah Al-obaidi and Naer Al-Kaabawi, I love you all.

Table of Contents

List of Abbreviations

AFM	Atomic Force Microscopy
CA	Contact angle measurement
DSC	Differential scanning calorimetry
DLS	Dynamic light scattering
DMF	N,N-dimethylformamide
d_h	Hydrodynamic diameter particle size
d	Interlayer spacing
EG	Ethylene glycol
FT-IR	Fourier transform infrared spectroscopy
GO	Graphene oxide
GPa	Gaga Pascal
g-force	Centrifuge force
HCl	Hydrochloric acid
h	Hour
Mw	Molecular weight
MPa	Megapascal
mm	Millimetre
µm	Micrometre
nm	Nanometre
OLM	Optical light microscopy
PEG	Poly(ethylene glycol)
PEO	Poly(ethylene oxide)
PMMA	Poly(methyl methacrylate)
PMMA-co-MAA	Poly(methyl methacrylate-co-methacrylic acid)
PMAA	Poly (methacrylic acid)
pR-GO	Partially reduced GO
QCM	Quartz crystal microbalance
RGO	Reduce Graphene oxide
rpm	Revolutions per minute
SEM	Scanning electron microscopy
TGA	Thermogravimetric analysis
TEM	Transmission electron microscopy
T_c	Crystalline temperature
T_d	Degradation temperature
T_g	Glass temperature
T_m	Melting temperature
X_c	Crystallinity
XRD	X-ray diffraction
wt.%	Weight fraction percent
ΔH_m	Enthalpy peak change of melting point
ΔH_c	Enthalpy peak change of crystalline point
Ω	Ohm, resistance unit

List of Figures

List of Tables

Chapter 1: Introduction

1.1 Introduction

Polymers are macromolecules consisting of many repeated units. They play an essential and ubiquitous role in everyday life [1,2]. They have excellent and amazing properties, such as light-weight, high toughness, good elongation, easy processing and low cost [3]. Comparing to metals and ceramics, polymers have a low strength and stiffness, which are important in some applications and could be enhanced by adding fillers to the polymer matrix for other applications [4].

Various studies have been carried out in this field using different types of filler to produce and enhance the properties of polymer composites that may be different from the properties of their constituent components. These polymer composites have shown important improvements in terms of their mechanical, electrical and thermal properties [5], in addition to various properties intrinsic of polymers, giving them a wide range of applications [6,7]. Nanoscale fillers such as clay, carbon nanotube and recently graphene have increasingly attracted research interests [8]. A polymer nanocomposite is defined as a composite with two or more phases that has reinforcement filler on a nanometre scale in at least one dimension. Mixing these nanofillers with a polymer matrix produced a notable enhancement in the polymer nanocomposite properties compared to their conventional composite counterparts and the polymer composites [9], where nanofillers give possible benefits and achieve the required properties of nanocomposite materials. These include lower loading and component weight reductions in impact resistance or toughness, which reduces the input energy during the processing [10] and makes important improvements in the properties of polymer nanocomposites, even at a low concentration of nanofillers [6,7,11,12].

The fine dispersion and interfacial interaction of the nanofillers with the polymer matrix are considered the keys to improving the properties of polymer nanocomposites, where

it is responsible for transferring the stress between the nanofiller and polymer matrix [13]. Transferring of the stress between the nanofiller and the polymer matrix at the interface is an important issue, and depends on their compatibility. In addition, understanding the processing method and the relationships between the structures and properties of the nanocomposites has led to an enhancement in the properties and in the ability to prepare specific nanocomposites for various applications [14].

In the last three decades, polymer nanocomposites have attracted the attention of the scientific and technological disciplines [8,15,16]. Most of the early and some of the recent efforts have focused on the understanding of the synthesis and properties of nanocomposites, such as the physical aspects of colloidal particles [8], and their physical, mechanical and thermal properties [9,15]. The properties of a polymer nanocomposite not only depend on the structure and properties of its constituents, but also on their interfacial characteristics between the nanofiller and the polymer matrix [15,17].

In the 1980s, polymer nanocomposites research began by exfoliating the layered silicates, which are referred to as nanoclays. This showed substantial enhancement in the mechanical properties of thermoplastic polymers [18]. Significant attention was given to carbon nanotubes as fillers in a polymer matrix, in the following years [8,12]. Recently, significant attention has been paid to other carbon-based nanomaterials, in particular, graphene nanosheets as reinforcing fillers for polymers [8]. Graphene and graphene oxide have been investigated for use in a wide range of applications, including nanocomposites, healthcare, biosensing and semiconductors [19,20]. The unique shape and high surface area to volume ratios of these nanofillers and exceptional physical properties are the main reasons for the performance advantage of these nanomaterials [12,21,22].

Figure 1-1 summarizes the increasing popularity of graphene and carbon nanotube polymer composites, where topical research on nanoclay and silicate polymer composites has fallen recently in the Web of Science, as of December 2016. Meanwhile, research interest in

the former topics has rapidly grown in the nanomaterials. Recently, interest in the carbon family has increased because it has opened new and wide-ranging ways to create new products, properties and nanomaterials [23,24].

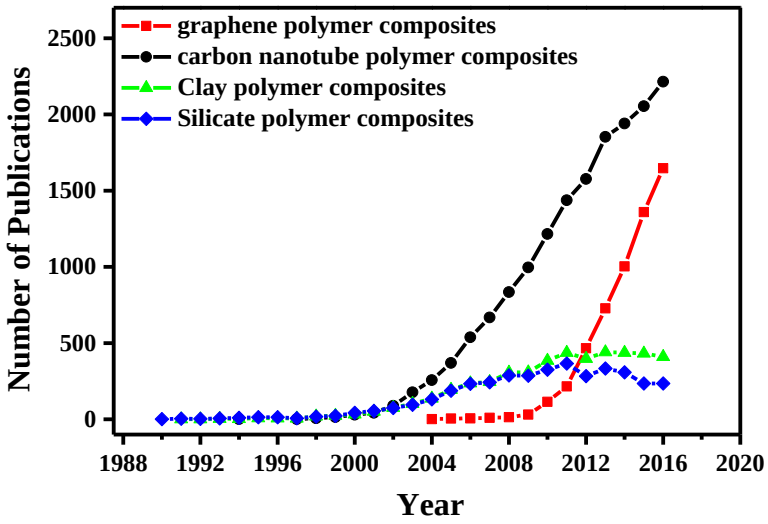

Figure 1-1: The number of publications returned by a Web of Science search using graphene, carbon nanotube, nanoclay and silicate composites as topics.

In spite of previous publications of polymer nanocomposites, many challenges remain in the polymer/graphene nanocomposites field. The main aspects of the structure-property-processing relationship of these materials and some details are missing, and those required for a full understanding of this area, a problem that needs to be addressed [6].

1.1 Project aims and objectives

Polymer nanocomposites are promising materials for a wide variety of industrial sectors, including aerospace, automotive, packaging, healthcare and energy, because the addition of a small ratio of nanoparticles may provide substantial enhancements to the mechanical, thermal and barrier properties of the polymer matrix. One of the main challenges facing the design, processing and application of polymer nanocomposites is to understand the interactions between the filler and the polymer matrix. Achieving this understanding will lead to the control of the structure and enable one to reach the required properties of nanocomposites. Therefore, this project aims to investigate the structure and property relationship of polymer

graphene nanocomposites, in particular in relation to the interfacial regions. A number of selected polymers and graphene oxide (GO) based nanoparticles were used for processing nanocomposites.

GO was prepared using a modified Hummer's method [25] to investigate the effect of GO on the surface adsorption behaviour of a semicrystalline polymer and its mechanical properties of polymer/GO nanocomposites. Semicrystalline poly(ethylene glycol) (PEG) was selected as a polymer model for initial studies using several parameters and methods. Polymers' functional groups were then selected to study the effect of functional group on their adsorption behaviour onto GO nanosheets. Sonication-centrifugal-based methods were applied to separate one uniform size of the GO particle and the effect of particle size of GO on the adsorption behaviour and mechanical properties of high molecular weight poly(ethylene oxide) (PEO) were investigated. The principal objectives of this study are outlined below.

- Prepare GO and poly(ethylene glycol)/GO hybrid nanomaterials and investigate the effect of mixing time, mixing ratio, washing procedure and the polymer molecular weight on the surface adsorption behaviour of PEG on GO nanosheets.
- Investigate the effect of functional groups of three polymers that have the similar backbone but structures with different functional groups on the adsorption behaviour of polymer on GO nanosheets.
- Develop methods that separate GOs into nanosheets of relative particle size using centrifugal and sonication-based green methods.
- Investigate the effect of particle size and size distribution of GO on the polymer adsorption behaviour onto GO nanosheets, structure and mechanical properties of poly(ethylene oxide) at the macroscopic scale.

This project will help advance the understanding of the structure-property relationships of polymer/graphene nanocomposites, which may lead to better control in these materials.

Chapter 2: Literature Review

2.1 Introduction of composites materials

Since the early 1940s, composites have rapidly developed and widened into areas, such as understanding the principles of related filler interactions with the polymer matrix. A composite consists of two or more components [1]. Polymer composites improve some of the properties of the polymer matrix, such as an increase in stiffness, electrical output and the temperature of deformation, as well as reducing the cost. These advantages of composites mean that they have properties that offer a wider range of applications, for medical, solar cells and transistors etc. [26].

Malkin and others [27] reported an improvement in the properties of polyamide 6.6 composites simply by melting them with carbon and glass fabrics, and this improvement depends on the nature of the polymer and the type of material added to the polymer, among others. Adding components to the polymer has illustrated some of the difficulties and problems involved in industrialization, e.g. the non-uniform dispersion of the constituents and an adversely change the physical properties of the polymer [26,28]. Therefore, the characteristics of the continents, the nature of the interaction between the polymer and the filler determine the characteristics of composites [1,27].

On the other hand, filler materials interact with the polymeric matrix, which may improve properties, such as strength and durability. Many types of fillers are used in accordance with the desired goal, such as carbon black and graphite. Figure 2-1 shows the summary of composite component [1].

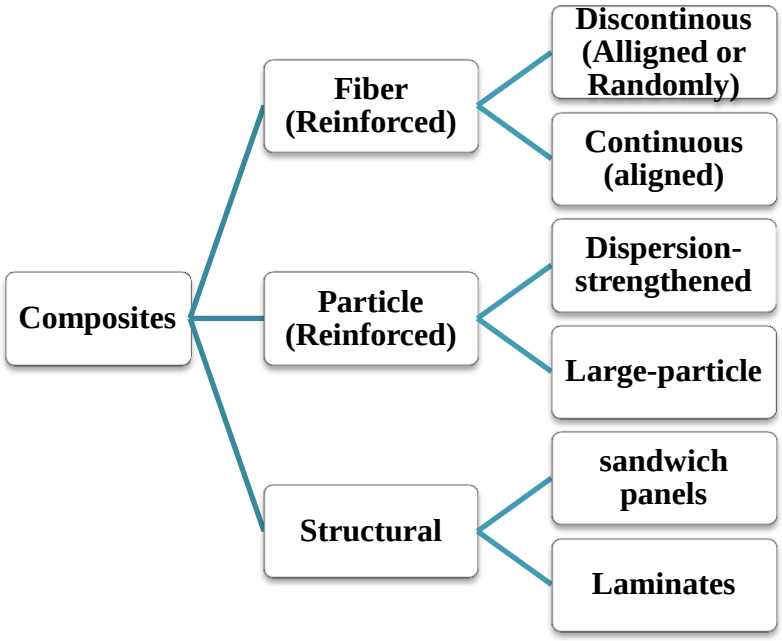

Figure 2-1: The classification of composites.

Currently, one of the most popular areas of scientific research is nanotechnology. Many technical disciplines have been developed in nanometre scale structures [7], bringing a revolution in many fields in terms of design and performance. It shows distinctive properties in the same materials at this nanosize scale, with a high surface to volume and aspect ratio, which makes nanofillers preferable to be used in polymeric materials compared to the microscale filler size [11]. This filler, which is organic or inorganic, can be amorphous, semicrystalline or crystalline [29]. The properties of nanocomposites depend on the interfacial characteristics, morphologies and properties of the components.

Polymer nanocomposites have triggered an increased interest among scientists and engineers over the last two decades [6,8]. It contains nanofillers that exhibit unique advantages. The larger surface-to-volume ratio is one of the main benefits for nanometer-sized nanoparticles, as compared to microparticles [6]. The volume of the interphase of polymer nanocomposites is increased dramatically due to the larger surface-to-volume ratio of the nanofillers [30].

The properties of nanocomposites cannot be achieved by the microcomposite counterparts, and offer new opportunities for a variety of applications [31]. Therefore, understanding the processing method, the properties of continents, the structures and the interfacial interactions are important in preparing and developing polymer nanocomposites.

In the early 1990s, the first studies of polymer nanocomposites were reported in the literature [29,32–34]. Komarneni et al. [29] reported the first nanocomposites, where rubber was reinforced with carbon nanoparticles. In recent years, many studies have investigated the effect of loading different types of fillers onto the polymer matrix to prepare and enhance the properties of polymer nanocomposites. At low concentrations, nanofillers offer a notable improvement in the properties of the polymer for a wide range of applications [35]. During the last decade, nanocomposites have used clays and carbon nanotubes, most recently a popular nanofillers has been graphene [8].

2.2 Carbon nanofillers

Low-dimensional carbonaceous nanofillers present unique and tailorable mechanical, electrical, thermal and optical properties. In addition, they have unique structures, which are (0D) nano-diamonds, (1D) carbon nanotubes and graphene (2D). These have attracted more attention recently regarding the use of carbon nanomaterials as nanofillers [6,7,36], as shown in Figure 2-2.

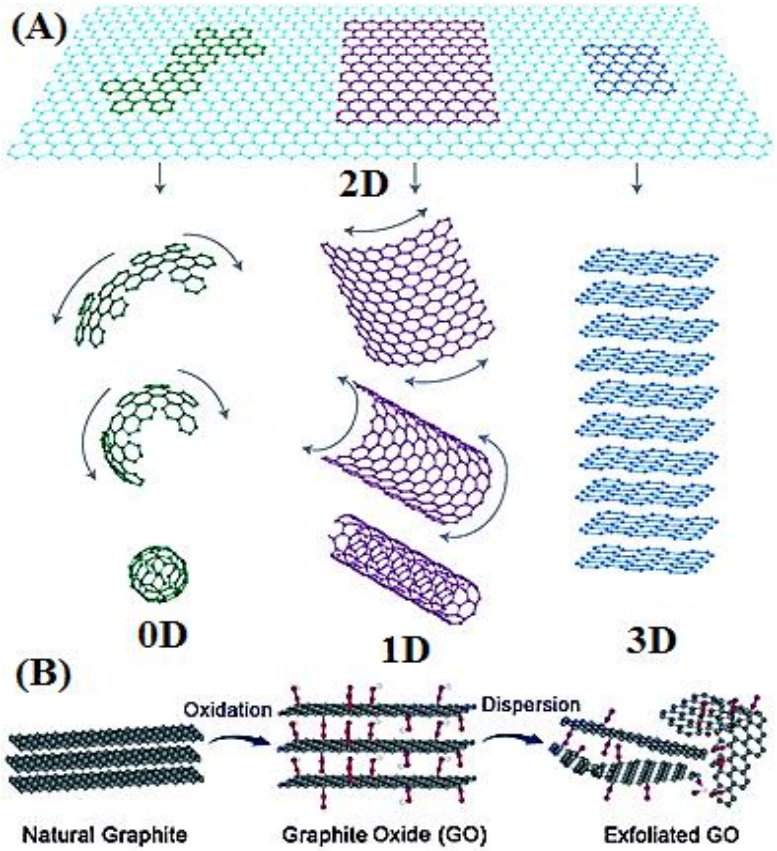

Figure 2-2: The structures of carbonaceous nanofillers of (A) graphene, buckyballs and carbon nanotubes that are derivatives from 3D graphite; (B) the synthesis of graphene oxide. (Adapted with permission from ref. [37] and [38]. Copyright 2007 and 2012, Nature and The Royal Society of Chemistry publications, respectively).

2.3 Graphene and graphene oxide-based carbon nanofillers

2.3.1 Introduction to graphene

Graphene consists of two dimensions of carbon sheets with one atom thickness. In it carbon atoms with sp^2 orbital are bonded and arranged in a honeycomb lattice, as shown in the transmission electron microscopy (TEM) image in Figure 2-3. It is derived from graphite, an inexpensive source. Graphene has an unusual structure with unique mechanical, electrical, physical and chemical properties [39], with a high electrical conductivity at room temperature 10^6 S cm^{-1}[40,41], a high thermal conductivity ~ 5000 W m^{-1} K^{-1} [42], a large theoretical specific of surface area 2630 m^2 g^{-1}, a high electron mobility 200 000 cm^2 v^{-1} s^{-1} [74, 75], an

ultimate tensile strength of 130 GPa, a high Young's modulus ~ 1 TPa [43] and ~ 97.7% optical transmittance [40]. It absorbs only 2.3% of the light for each graphene layer over a broad wavelength range, which makes it suitable for specific optoelectronic applications [41]. Graphene is considered a strong, flexible membrane and able to modify in the carbon backbone, such as functionalization the graphene.

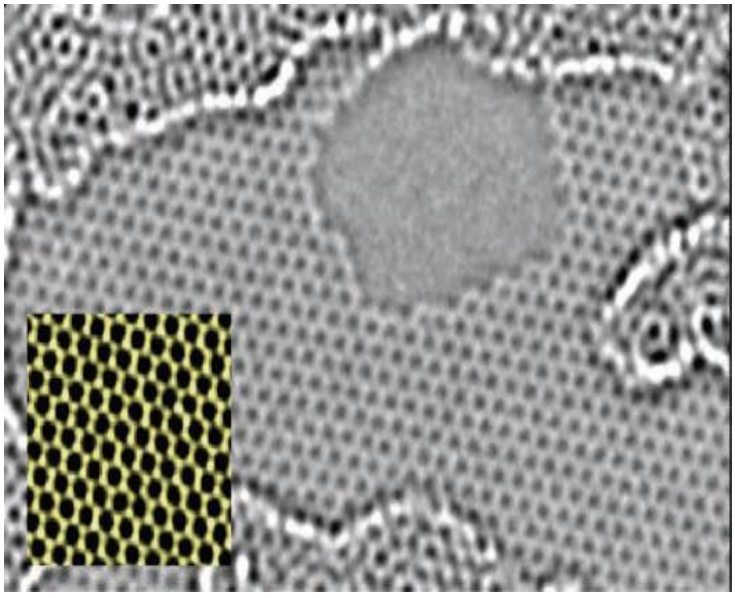

Figure 2-3: The TEM image of a single layer of graphene. (Adapted with permission from ref. [44]. Copyright 2009, Science publications).

These features of graphene have brought specific attention from scientific and industrial communities [19,39,41,45] aiming to produce newly emerging and novel nanomaterials. The excellent properties and unique structure of graphene have led to a wide variety of applications, in areas such as Li-ion batteries [46,47], electronic components [48], chemical sensors [49], storage and conversion energy [50] and catalyst support [51].

2.3.2 Introduction to graphene oxide

Nowadays, oxidizing the graphite oxide (GO) is the most common method used to produce graphene in large quantities from inexpensive graphite [52]. Over 60 years ago, the first preparation of graphite oxide was made by Hummers et al. [25]. This method depends on strong oxidation of graphite used potassium permanganate ($KMnO_4$), potassium chlorate ($KClO_3$) and sodium nitrite ($NaNO_3$) in the presence of sulfuric acid or concentrates with nitric acid, as shown in Figure 2-2. Graphite consists of stacks of graphene sheets, whereas graphite oxide consists of graphene oxide sheets stacked. The latter is a graphene sheet with oxygen functional groups. These groups lead to an increase in the interlayer spacing of GO nanosheets between 0.6 and 1.0 nm. This distance depends on the content of functional groups in the GO nanosheets [53].

Figure 2-4 (a) shows the structure of graphene oxide. Graphene oxide is described as built of pristine aromatic “islands”. These are separated from each other by aliphatic regions, which contain epoxide, hydroxyl groups and double bonds. This is a theoretical description [54,55]. The Lerf-Klinowski model [56,57] is the most likely GO structure description. Figure 2-4 (B) illustrates the ketones, 6-membered lactol rings and tertiary alcohol in GO nanosheets with epoxide and hydroxyl groups [58–60].The ratio of C, O and H in the GO nanosheets are 2, 1 and 0.8, respectively [59,61].

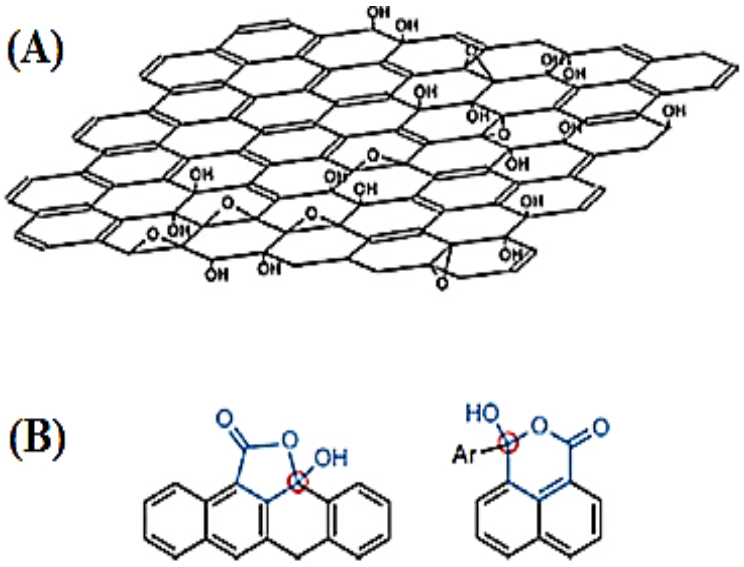

Figure 2-4: The structure of GO (A) consisting of aromatic islands separated by aliphatic regions containing oxygen bonded carbons as described by the Lerf-Klinowski model. (Adapted with permission from ref. [57]. Copyright 1998, Science Directs publications). (B) ketone groups in 6- and 5-membered ring. (Adapted with permission from ref. [60]. Copyright 2009, Nature publications).

The elastic modulus (E) of GO is in a range between 207 to 470 GPa, whereas it is between 290 to 430 GPa of amorphous GO in the literature, which is the functional groups are attached amorphously on the GO sheets, whereas the mechanical parameters (Young's modulus and intrinsic strength) decrease moderately with increasing the coverage due to the disturbance by sp^3 carbons. Therefore, mechanical properties of GOs depend mainly on the surface coverage and arrangement (ordered or amorphous) [62,63]. The E value of graphene is higher than GO due to the limitation of the sp^2 carbon structure of GO [63]. Increasing the functional groups in the GO structure leads to an increase in the ratio of sp^3 to sp^2 carbon [64]. This limitation of sp^2 and the defects in the GO structure turn it into an electrical insulator [65,66]. The conductivity value of GO is 1-5 * 10^{-3} S cm^{-1} [67], whereas the value of resistance is ~1*10^{12} Ω [68].

GO is considered to be a highly hydrophilic material due to the high ratio of oxygen in the inter-lamellar regions and edge. Therefore, GO has an excellent dispersibility within many solvents, such as water, methanol and benzene. These solvents can be compatibly accommodated between GO layers with a high degree long-range order [69,70]. Additionally, alkylamines [71], alkylchlorosilanes [72], cationic surfactants [73] and macromolecular systems, as well as the high-molecular-weight polymers are able to compatibly accommodate themselves in GO [74]. Controlling the degree of oxidation and exfoliation of GO presents advantages to using it as a host material [74,75]. Graphene oxide is unstable thermally and insulating electrically. The electrical conductivity of graphene oxide can be restored with a partial reduction for some applications [58].

2.3.3 Preparation of graphene

In 2004, Graphene was separated by Novoselov et al. [76] using micromechanical cleavage. It was the first free-standing single-layer graphene from graphite. Today, there are several methods for generating graphene from graphite, as follows [58].

2.3.3.1 Direct exfoliation of graphite methods

There are four methods, as follows.

a) The micromechanical cleavage method is the first method which isolated graphene. It is suitable for fundamental studies, electronic applications and the production of graphene with high-quality sheets and a large size, with limitation in the quantities [76].

b) The exfoliation and dissolution methods refer to the separation of graphene sheets due to exfoliating graphite to produce a large-scale production from the dissolution of graphite in chlorosulfonic acid, It is naturally hazardous due to the hydrosulfonic acid and has a high cost [77].

c) The direct sonication method produces single and multiple layers of graphene by sonication in combine with N-methylpyrrolidone [78] or polyvinylpyrrolidone, as a solvent [79].

d) The electrochemical exfoliation method is a functionalization of graphite with imidazolium groups as the ionic liquid [80] or through dissolution in superacids [77] using electrochemical functionalization, which assists the dispersion in aprotic solvents [80].

2.3.3.2 Exfoliation of graphene oxide

a) Chemical reduction of graphene oxide

The chemical reduction of graphene oxide sheets produces a stable colloidal dispersion of GO. A sonication or long stirring methods are applied after dispersing the graphene oxide in the solvent, such as alcohol, water and other solvents. Additionally, GO can exfoliate in the polar aprotic solvents then react with isocyanate [81] and octadecylamine [82], which is an organic compound or surfactant [81–83]. Appling this method presented poor thermal stability and low electrical conductivity of GO/polymer nanocomposites, whereas the chemical reduction of GO led to the restoration of electrical conductivity. This method also shows a limitation in the applications, due to the hazard of chemical reductions and material costs [81,82,84].

b) Thermal exfoliation and reduction of graphene oxide

Dry graphene oxide was heated under inert gas at a high temperature to produce a thermal reduction of graphene oxide (TRGO). TRGO is produced by heating GO up to 1000 ^{o}C for 30 seconds [85–88]. This reduction degrades the epoxy and hydroxyl located in the GO structure and holds the nanosheets of GO together via van der Waals forces. This degradation reduced the GO mass by about 30%, due to degraded oxygen groups [114], whereas the volume expanded by between 100 to 300 times, due to exfoliation. This produces a very low-bulk

density of thermal reduction of the GO nanosheets, due to the weight loss in form of CO_2 [85,86]. The electrical conductivity is restored by the thermal reduction, which settles at between 10 to 20 S cm^{-1} of film and a density of 0.3 g cm^{-3} [85].

An alternative green-reduction method of GO reported by Zhou et al. [89], used a "water-only" method of dehydrating the hydroxyl groups on graphene oxide by controlling the hydrothermal temperatures. They reported combined advantages, including repair of the aromatic structures and removal of oxygen functional groups from GO.

These methods present a large number of different scales and quantities of single or multiple layers of graphene. These methods offer a wide range of important nanocomposite applications. Figure 2-5 summarises the preparation methods of graphene and graphene oxide.

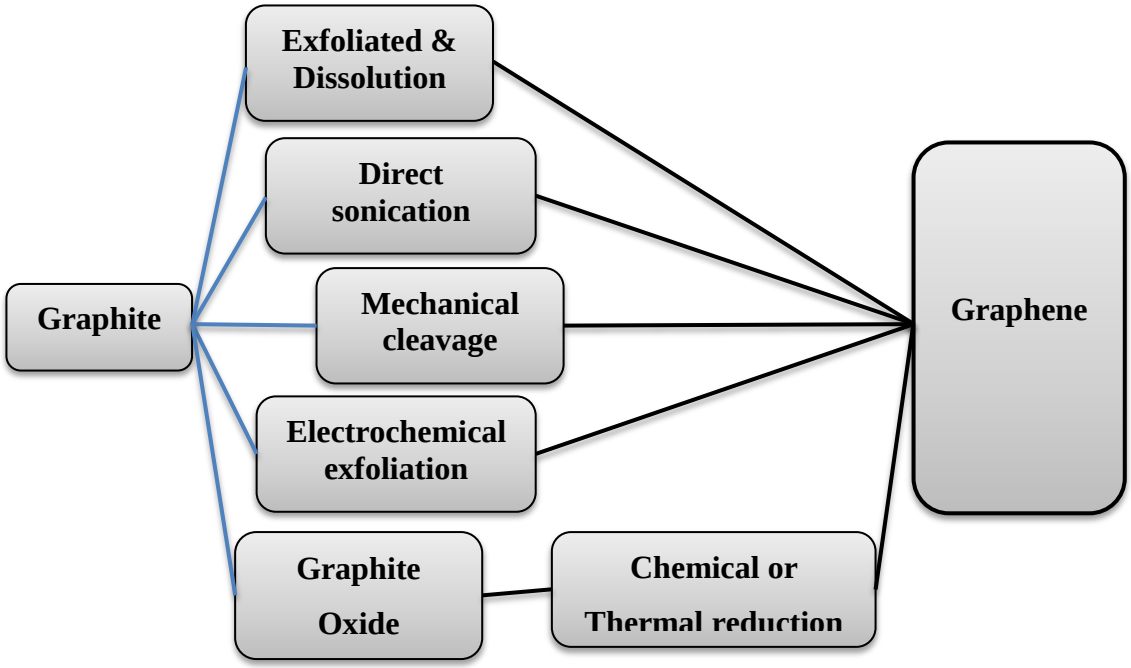

Figure 2-5: The methods of produce graphene and modified graphene starting from graphite and graphite oxide (GO).

2.3.3.3 Functionalisation of graphene

Many materials can be used to functionalize graphene; the three main methods are as follows:

a) Functionalization with small molecules

Small molecules, such as surfactants, deoxyribonucleic acid (DNA), proteins, pyridine, complex compounds and anticancer drugs are the most popular molecules for functionalizing graphene. This method leads to the enhancement of various electronic, optical, and bio-related properties or solution-processing capabilities, and an important purpose of this method is to improve solubility in various solvents [80,90].

b) Functionalization with nanoscale objects

Nanoobjects, such as nanosheets, nano-wires, nano-rods and nanoparticles, are used to functionalize graphene, which depends on the materials' intrinsic characteristics. This method offers potential applications of graphene in electronic and optoelectronic applications [91].

c) Functionalization with polymers

Functionalizing graphene with a polymer as the functionalizing molecule improves graphene dispersion in various organic and inorganic solvents, where [92] reported a new design and synthesis of the graphene composite using a coil-rod-coil conjugated triblock copolymer (PEG-OPE), as a binding stabilizer, in order to modify the reduced graphene oxide (RGO), where a notable enhancement in the dispersion of graphene appears in the organic solvents and water using the amine-terminated polystyrene [93].

2.3.4 Applications of graphene-based materials

Graphene is a fast developing field with different applications due to its unique structure and properties. In spite of the characteristics of graphene, it is still limited in many applications, as graphene faces the challenge of inducing and controlling the functionalizing of graphene sheets. For example, it is weak in absorbing light and this makes graphene unsuitable for collecting solar light efficiently. Recently, researchers have focused on using graphene as a

general platform for nanocomposites, which offers many possibilities for energy and environmental applications [12,94].

2.3.4.1 Functionalized graphene for energy applications

Functionalized nanocomposites have been investigated for many energy-related applications, such as:

a) Solar energy conversion: Photovoltaic and photo-electrochemical devices

The first exploration with pure graphene was in transparent electrode solar cells [95,96], then in photovoltaic and photoelectrochemical devices, and as competitive transparent electrodes [97–99]. Furthermore, graphene can be not only a conductive platform but also an active element, such as an electron acceptor in photoelectrochemical and photovoltaic devices [94].

b) Artificial photosynthesis

Graphene has been used in inorganic semiconductor-based photochemical water splitting applications because it can replace the noble metal cocatalysts, such as platinum nanoparticles [41]. It can also be used as conductive channels. Zhang et al. [100] reported preparing pure titanium oxide (TiO_2)/graphene nanocomposites through facile-gel processing, as photo-catalysts for generating H_2. Their results showed 1.9 times higher hydrogen evolution than TiO_2.

c) Electrochemical energy devices: Lithium and lithium-ion batteries

Rechargeable lithium ion batteries (RLBs) and electrochemical double layer capacitors are considered to be clean energy devices, being made from graphene-based electrodes, as reported in several publications [101,102].

d) Supercapacitors

Graphene, with its excellent electronic properties, improves the capacitance and the stability of electrochemical in the supercapacitor electrodes. For instance, graphene is used as a negative electrode in an asymmetric supercapacitor to manganese dioxide (MnO_2)

nanowire/graphene composite as a positive electrode. This provides an energy density of 30.4 Wh kg^{-1} and high power density at 7.0 Wh kg^{-1}, as shown Figure 2-6 [103].

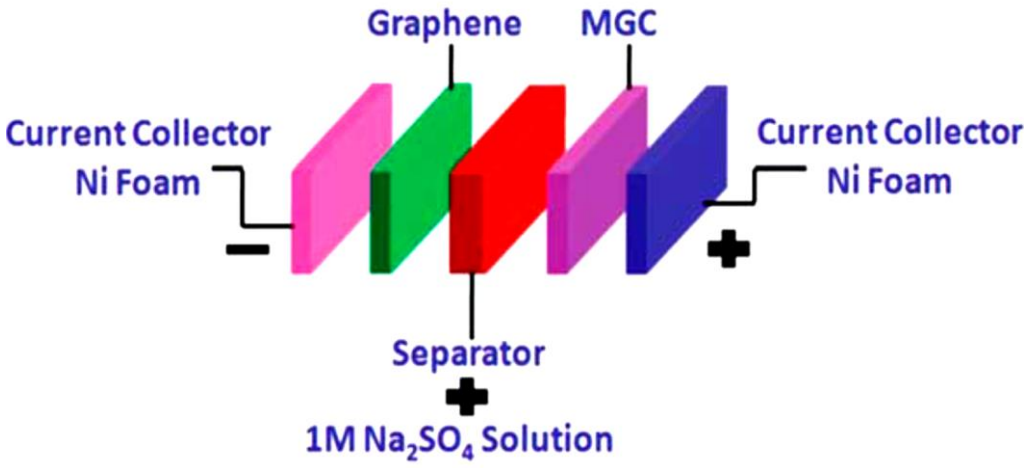

Figure 2-6: The asymmetric supercapacitors using graphene as the negative electrode and a MnO_2 nanowire–graphene composite as the positive electrode. (Adapted with permission from ref. [103]. Copyright 2010, American Chemical Society publications).

e) Fuel cells

Graphene nanocomposites have produced new alternative metal electrocatalysts that have been widely applied as electrocatalysts in fuel cells for hydrogen evolution reaction, methanol oxidization and oxygen evolution reaction. Guo et al. [104] fabricated the seven-nanometer iron–platinum nanoparticle (FePt NP)/graphene nanocomposites using a solution-phase self-assembly method, where graphene helps to improve nanoparticle activity and durability.

2.3.4.2 Functionalized graphene nanocomposites for environmental applications

Environmental sensing and monitoring of remediation are promising applications of functionalized graphene nanocomposites. This is considered as a platform for preparing the removal of hazardous species in the environment, as well as an organism's biomolecules and sensing inorganic ions. Moreover, graphene and graphene nanocomposites can be used to

bring about organic species degradation, to act as environmental gas sensors for bacterial detection and to detect and remove heavy metal ions [94].

a) Heavy metal ion detection and removal

Wen, et al. [105] developed graphene nanohybrids/silver-specific cytosine-rich oligonucleotide (SSO) nanocomposite detection, where it is a fluorescence sensor and is very sensitive to silver ions (Ag+) with a detection limit of 5 nM, as illustrated in Figure 2-7.

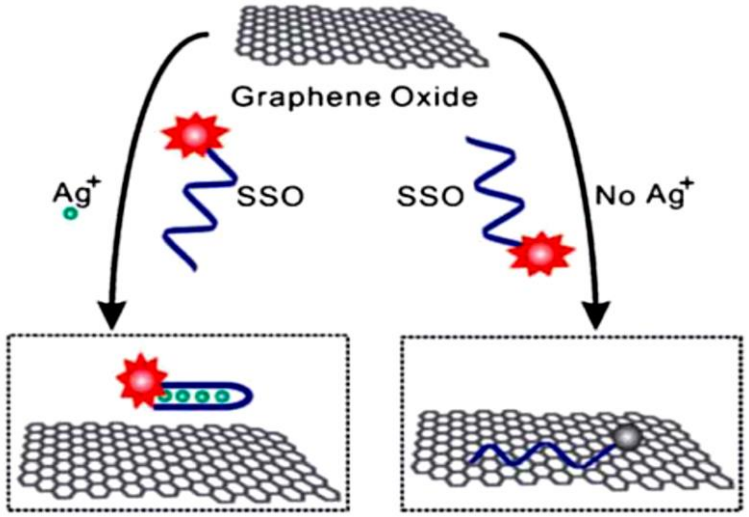

Figure 2-7: The fluorescence sensor for Ag+ ion detection. (Adapted with permission from ref. [105]. Copyright 2010, The Royal Society of Chemistry Publications).

b) Degradation and removal of organic species

Graphene nanocomposites are used to reduce or direct removal of organic species. These are considered to be the most serious environmental pollutants. A TiO_2/graphene nanocomposite photocatalyst was prepared by Zhang et al. [106] for the photo-degradation of organic dyes in both visible light and UV: for instance, methyl blue (MB).

c) Environmental gas sensors for inorganic and organic vapour

Applying graphene to a vapour pollution is a good detection method for various gases, such as nitrogen dioxide (NO_2), nitric oxide (NO), carbon monoxide (CO), carbon dioxide (CO_2) and hydrogen (H_2), in addition to acetone, benzene and toluene [107–111]. Many studies have improved these sensors. One of the most important studies was by Ji et al. [109], who prepared the toxic organic hydrocarbon vapour detection after the reduction of graphene oxide. Layer-by-layer assembly methods were used to prepare graphene/ionic liquid (G–IL) films, as shown in Figure 2-8. The increase in graphene layer spacing enhances the adsorption of aromatic gas [109].

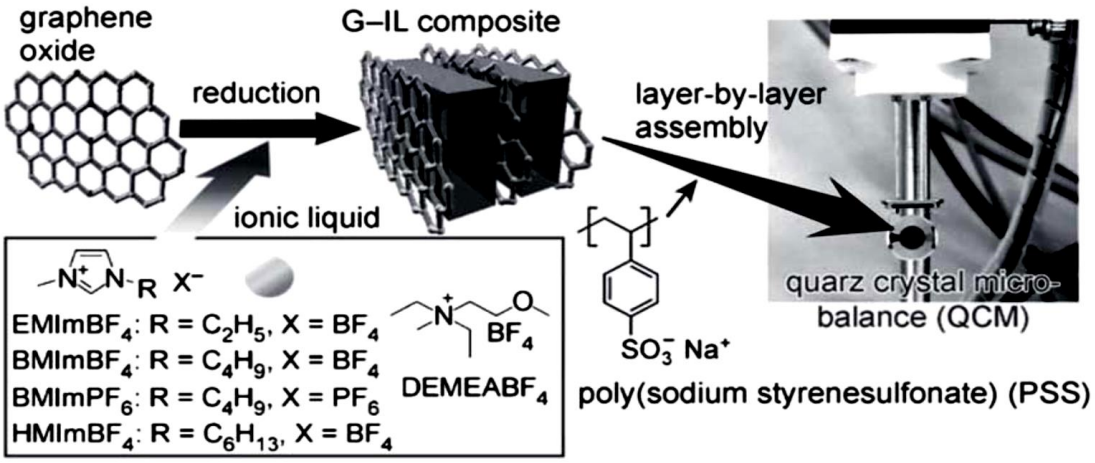

Figure 2-8: The graphene-ionic liquid assembly for organic vapour detection using a quartz crystal microbalance. (Adapted with permission from ref. [109]. Copyright 2010, Wiley publications).

d) Bacterial detection and removal

There are interesting interactions between graphene-based composite materials and bacteria. This is associated with investigations into bacteria detection and removal [112,113]. Figure 2-9 demonstrates the bioselectively detected bacteria at the single-cell level by

antimicrobial peptide/graphene hybrids. The amazing thing is that the graphene nanohybrid-based biointerfaces are capable of working as sensors for remote pathogenic bacteria monitoring without batteries, which is promising for future applications [114].

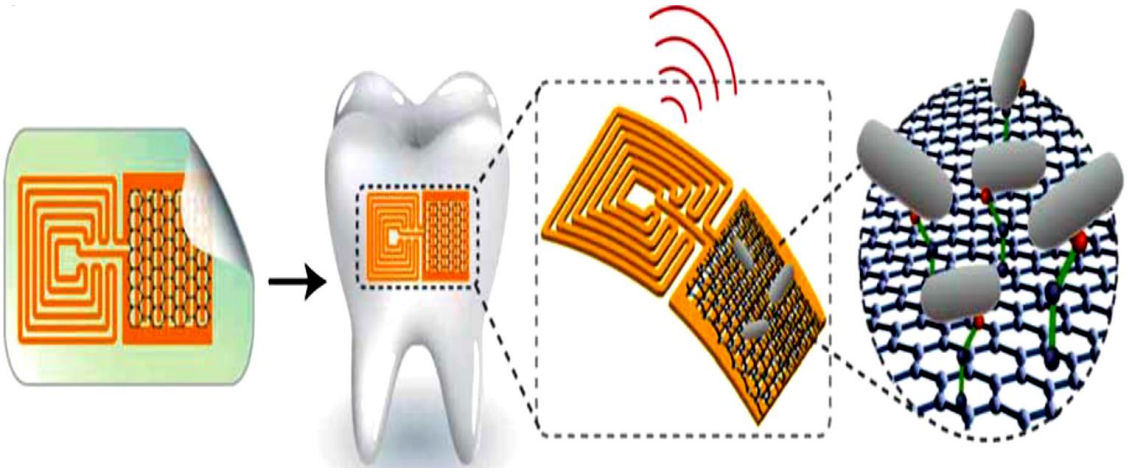

Figure 2-9: The graphene oxide-based hybrids with a silver enhancement for detecting sulfate-reducing bacteria (SRB). (Adapted with permission from ref. [114]. Copyright 2012, Nature publications).

e) Field effect transistors

The graphene carriers are bipolar and the unique band structure, which was used as a gate to control the electrical and field [76]. Many researchers have investigated the field-effect mobility of graphene (FET) devices [76,115,116], which are valued more highly than silica devices. This achieves large-scale transistor arrays with uniform electrical properties [117], whereas the operation of the frequency of graphene FET reaches a high of up to 26 GHz by top gate geometry [118]. One of the most important applications of graphene is that it can be used as a single electron transistor (SET) [119].

f) Transparent conductive films

Graphene promises to prepare transparent conductive films (TCFs) because it has a high optical transmittance in a spectrum visible range, high conductivity of electricity and high

carrier mobility [120]. Composing anodes with reduced graphene oxide nanosheets exhibits a specific capacity of up to 540 mA h g^{-1}. An increase in the storage capacity is related to increases the interlayer spacing distance between the graphene sheets [42].

2.4 Polymer/graphene nanocomposites

Recently, the family of carbon has attracted significant attention as a base nanofiller for materials due to the unique properties and various derivatives of graphite, such as carbon nanotubes and graphene nanosheets [8]. Graphene is not just a traditional nanofiller with high mechanical properties but also has derivative materials with impressive functional properties, such as fluorescence quenching, electrical (semi-) conductivity, anisotropic transport, low permeability, and unique optical transportation [121,122], whereas these functional groups and a significant amount of the sp^2-hybridized carbon backbone structure render the graphene oxide nanosheets with a high degree of planarity [123] and a large surface area to volume ratio [124]. Polymer graphene nanocomposites demonstrate the tremendous potential enhancement in chemical, electrical, mechanical performance and thermal properties, even with a small fraction of graphene, which was used in this case to reinforce the polymeric matrixes [121,125]. Graphene and graphene oxide show a wide range of emerging applications, such as nanocomposites, healthcare, biosensing and semiconductors [19,20].

2.4.1 Preparation of polymer/graphene nanocomposites

The morphology of the nanocomposite is the key to improving the properties of nanocomposites. This depends on the nanocomposite processing approach and graphene preparation method. Graphite particles are difficult to disperse using a conventional processing technique due to the high aspect ratio of graphene [12]. Graphene needs to be produced by specific methods that can achieve effective dispersion in the polymer matrix. The methods of preparing graphene nanocomposites have been developed, each of which with its advantages and shortcomings. Specific nanocomposites capable of improving the properties

of nanocomposites have been fabricated by adopting suitable preparation methods, where solvent, melt and in-situ polymerization processing methods are the three main ways of preparing polymer nanocomposites.

In the solution-based methods, the suspensions of GO/graphene are mixed by stirring or shear mixing with the desired polymer. In this method, the polymer could either be added to the GO/graphene suspension or after dissolving it [126]. In the melting methods, the polymer and filler are melted in a dried powder form during mixing under high shear conditions. The melting methods are compatible with many current industrial practices. Consequently, they are often considered to be more economical than previous approaches [6], but only a limited number of studies have used these methods, due to the thermal instability of the modified graphene [12].

The in situ polymerization method can produce neat, multiple or solutions of monomer and a dispersed filler to prepare the polymer composites [126]. Many studies have reported using in situ polymerization methods of a variety of polymers, such as polyethylene [127], poly(methyl methacrylate) [128] and polypyrrole [129]. This produces a covalent linkage between the filler and matrix as composites. Graphene/graphene oxide can be covalently bonded, not only with particles such as amide bonding and atom transfer radical polymerization diazonium salt [83] but also with other materials, such as ionic liquids [130], per-luorophenylazide (PFPA) [91] and porphyrin [131].

Solution mixing and in situ polymerization methods offer the same level of dispersion of the filler, which is better dispersion than the melting method [132]. Many molecules can be non-covalent when attached to modified graphene: for instance, 1-pyrenecarboxylic acid [90], dendronized perylenebisimides [133] and 1-pyrenebutyrate [134]. Stankovich et al. [135] investigated using organic isocyanate to treat the graphene oxide by carbamate esters or amides formation, which is commonly used to functionalize the graphene sheets covalently. Using the carbamate esters lead to a derivative of the surface with hydroxyl functional groups

[136], whereas amide formation produces hydroxyl groups [137] on the surfaces treated with graphene oxide. Figure 2-10 shows the covalent functionalization of graphene oxide with an amine-functionalized porphyrin [131] and graphene sheets with perfluorophenylazide (PFPA) by photochemical or thermal activation [91], respectively. The choice of method depends on the type of interaction, properties and application required. Therefore, graphene can offer many potential applications with these methods.

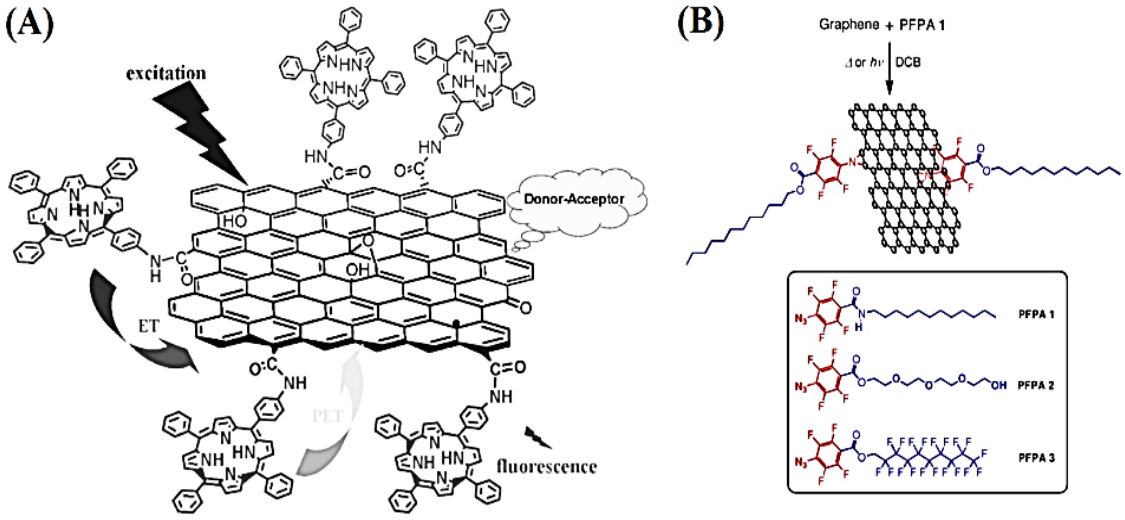

Figure 2-10: (A) Graphene–porphyrin hybrids produced by amine covalent bonding, Adv. Mater. (Adapted with permission from ref. [131]. Copyright 2009, Wiley publications) and (B) functionalization of pristine graphene with PFPA. (Adapted with permission from ref. [91]. Copyright 2010, American Chemical Society publications).

2.4.2 Interfacial interaction

The strong interfacial bonding is very necessary for enhancing the properties of the nanocomposites, such as the mechanical properties. This requires a strong interfacial interaction between the reinforcement fillers and the polymer matrix. The most effective factor in this strong interfacial interaction is the effective dispersal of the filler with the matrix. However, the matrix will yield, if the interfacial interaction is stronger than the

matrix, whereas de-bonding may be initiated between the polymer and filler along the interface due to the weak interfacial interaction. This leads to aggregated nanofillers in solvents due to strong electrostatic interactions and van der Waals forces between the nanofiller layers and matrix. This aggregation leads to a reduction in the mechanical properties of the polymer matrix. Van der Waals forces is considered very important at the nanoscale, even though it is a weak force because of the large surface area per unit mass of the nanomaterials [4]. The reduction in the aspect ratio of the nanofiller or small size of fillers presents another important reason for reducing the reinforcement of the [4,138].

On the other hand, a hydrophobic, van der Waals force and π-π stacking are weak physical bonds that act on a polymer with non-functionalized graphene [139]. Therefore, graphene disperses with different types of solvents. This depends on the exfoliation procedure with the aid of a surfactant: for instance, water with sodium dodecylbenzene sulfonate (SDBS), surfactants as dimethylformamide (DMF), cyclohexanone as organic solvents, chloroform, acetone and isopropanol as low boiling solvents [140]. For better dispersion, the concentrations of surfactants must be below the critical micelle concentration in case of graphene and carbon nanotubes [141], where the low concentration of surfactant leads to an enhancement of the dispersion quality [142,143].

The graphene sheets stack together several hundreds of nanometres thick by van der Waals forces in graphite. These forces prevent the stack of graphene sheets interacting with the polymer leading to limited performance, which is a similar phenomenon as of the clay. The dispersion of nanoparticles in the solvent could be improved using an acoustic solution or functionalization, whereas the latter could affect the properties of some nanoparticles, such as carbon nanotubes [144]. The use of strong acids or ultrasonication may shorten the length or unzip the particles [145]. The significant reduction of the transfer of loads between the shorter carbon nanotubes and polymer can result from present a reduction in the aspect ratio of the nanofillers [4]. The amount of GO dispersion in polymers governs the interfacial interaction

[146], due to hydrogen bonding, van der Waals attractions and/or non-covalent electrostatic interactions between the polymer and filler in the nanocomposites, where the properties of the polymer nanocomposites depend on the structure, properties and interfacial characteristics of its constituents [147]. The interfacial adhesion between the nanoparticle and the polymer matrix determines the stress transfer, which can reduce the cooperating segment mobility of the adsorbed polymer onto the nanoparticle [148]. Many types of methods have been used to bring about reactions of polymers with nanofillers.

2.4.3 Properties of polymer/graphene nanocomposites

The types of nanofillers or components used have an important effect, improving the strength of interfacial interaction and composite homogeneity. These lead to improvements in the properties of the polymer nanocomposites [149]. Significant attention has been given to polymer/graphene nanocomposites [12]. A considerable amount of literature has been published on polymer/graphene nanocomposites.

The first preparation and analysis of polymer/graphene nanocomposites emerged during 2006, when Stankovich, with co-workers [150] applied different methods, such as via molecular-level dispersion of individual items, complete exfoliation of graphite and chemically modified graphene sheets with the polymer, which led to a reduction in the graphene with polystyrene, They succeeded in enhancing the electrical properties of the polymer using graphene. The electrical conductivity of this composite gradually improved from ~0.1 S m^{-1} at 1 vol.% to ~1 S m^{-1} at 2.5 vol.% within an increase in graphene sheet loading to above 0.5 vol.%, as shown in Figure 2-11. The exceptional physical and potential properties of graphene, which is used as nanofillers, showed great promise for becoming an inexpensive product available on a large-scale [150].

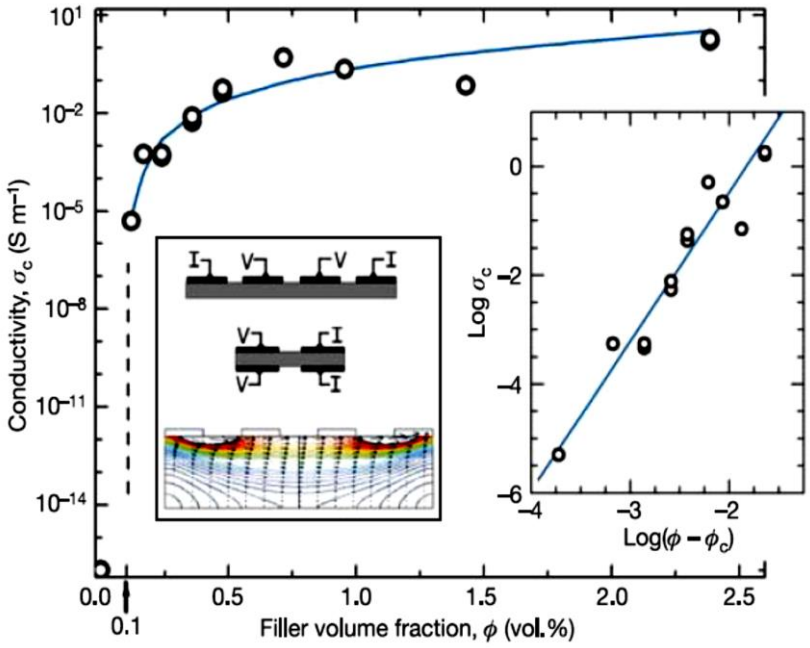

Figure 2-11: The electrical conductivity of the polystyrene-graphene composites as a function of the filler volume fraction. (Adapted with permission from ref. [150]. Copyright 2006, Nature publications).

In 2008, Ramanathan et al. [94] reported an improvement in glass transition temperatures and the thermo-mechanical properties of functionalized graphene/polymer nanocomposites, where the glass transition temperature was increased by 40 ^{o}C of poly(acrylonitrile) with a 1.0 wt.% loading ratio of functionalized graphene, whereas only a 0.05 wt.% ratio of functionalizing graphene increases the glass transition temperature to 30 ^{o}C of poly(methyl methacrylate). Functionalized graphene/poly(methyl methacrylate) (FGS–PMMA) provides an improvement of 1 wt.% and 33% for 0.01 wt.% of the thermos-mechanical property and the elastic modulus, respectively, compared to single-walled carbon nanotubes/poly(methyl methacrylate) (SWNT–PMMA) and expanded graphite/poly(methyl methacrylate) (EG–PMMA) composites. Functionalizing graphene sheets with various polymers provided good interactions between the polymer and graphene sheets. The high surface area and the oxygen functionalities of graphene allow for very good dispersion with better, more intimate interaction with polar polymers, such as PMMA.

This leads to the creation of a percolated domain of strong interphase interaction between the graphene and polymer that introduces in the dramatic improving in the thermal and mechanical properties even at low loadings, such as 0.05 wt.% as shown in Figure **2-12**. Additionally, other composites illustrated an extraordinary difference in the interfacial interaction between the nanofiller and the polymer matrix. Figure **2-12** summarizes the enhancement in the Young modulus, glass transition, ultimate strength and thermal degradation of (FGS–PMMA) instead of (SWNT–PMMA) composites and (EG–PMMA) [94].

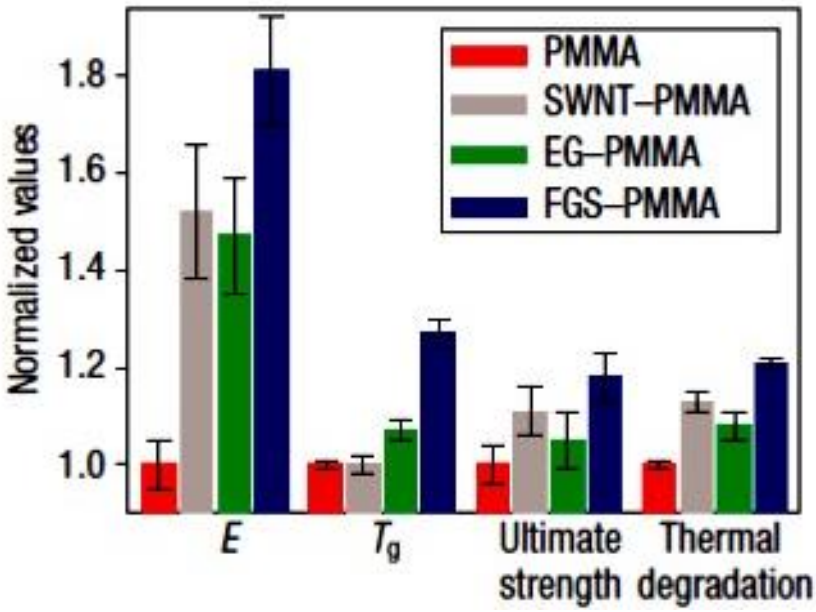

Figure 2-12: The property improvements glass transition temperature and Thermomechanical properties. (Adapted with permission from ref. [94]. Copyright 2006, Nature publications).

In 2010, Huating and co-authors [151] reported an environmentally-friendly technique to functionalize the graphene sheets and prepared polystyrene/absorbed graphene nanocomposites. Graphene improves the thermal stability of polystyrene, which starts to degrade from between 270 and 420 ^{o}C to a higher temperature range, from 350 to 450 ^{o}C. Also, the glass transition temperature of polystyrene increased from 101^{o}C to 109 ^{o}C after the

incorporation of the graphene. The reason is that graphene can impose a strong interfacial interaction with a polymer that leads to restrictions on mobilizing of the macromolecules of polystyrene with homogeneous heating, as shown in Figure 2-13, respectively.

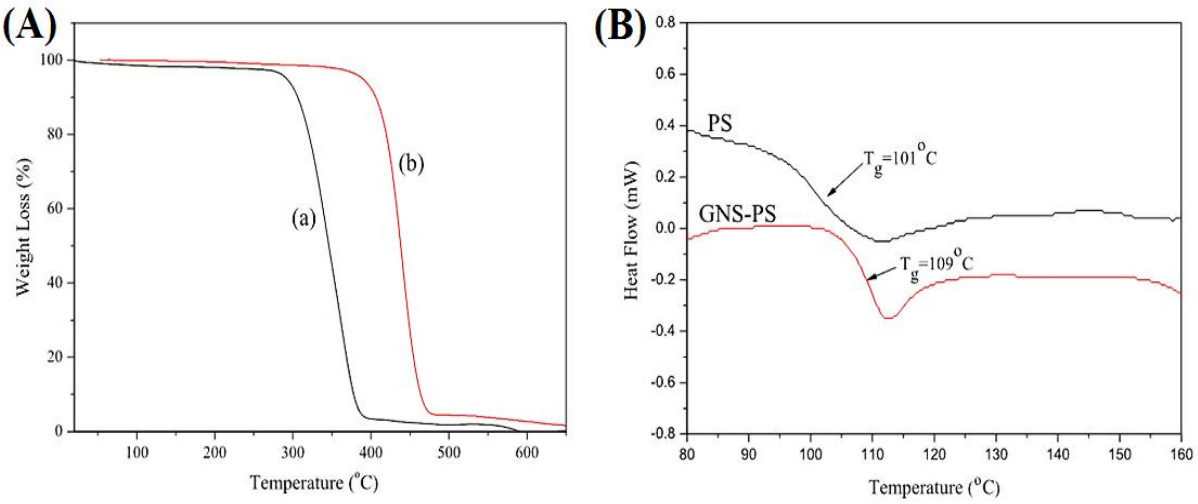

Figure 2-13: (A) TGA and (B) DSC curves of (a) PS and (b) PS/graphene nanocomposites sand. (Adapted with permission from ref. [151]. Copyright 2010, American Chemical Society Publications).

Zhao et al. [149] reported the effect of the loading ratios of graphene on the tensile strength of the polymer nanocomposites. The tensile strength was enhanced by 150%, 42 MPa with a 1.8 vol. % loading ratio of graphene in the nanocomposites, whereas adding a lower loading of 0.6 vol. % graphene led to an enhancement in the modulus up to 73%. The strong interfacial interaction between graphene with the polymer matrix and good homogeneity of the composites improved the mechanical properties of the poly(vinyl alcohol) matrix with the lower loading of graphene, whereas increasing the loading ratio of graphene also decreased the value of the elongation at break from 220% to 98%, accordingly. This could be attributed to restricting the movement of the polymer chains by the large aspect ratio of graphene, and interaction with the polymer matrix. Therefore, adding further graphene to the matrix is

assumed to re-stack the graphene sheets, via van der Waals forces. This could reduce the effective enhancement of the mechanical properties during the tensile testing by the slippage of stacked graphene sheets, as shown in Figure 2-14.

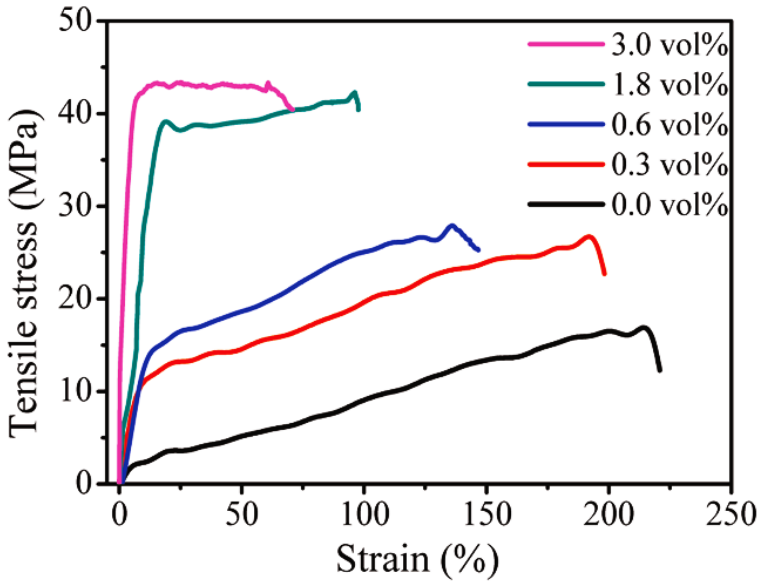

Figure 2-14: The typical stress-strain plots of the nanocomposites with various graphene loadings. (Adapted with permission from ref. [149]. Copyright 2010, American Chemical Society Publications).

In 2012, Potts [12] developed processes to investigate the structure and property relationships of graphene/polymer nanocomposites. Different reduction degrees of graphene were prepared from graphite oxide. Graphene was dispersed into various elastomers and thermoplastic polymers using a developed solution and melting dispersion methods. Higher electrical and thermal conductivity were revealed for the solution treated samples compared to the milled samples. This resulted from the difference in morphology due to the different preparation procedures. The incorporation of reduced graphene oxide (RGO) significantly increased electrical conductivity, where more pathways for conduction, provided by the segregated filler networks in the solution treated samples, compared to the milled samples. In

a solution method, graphene also exhibited a better enhancement in electrical and thermal conductivity of natural rubber (NR) as shown in Figure 2-15 (A), in addition to the mechanical properties, as shown in Figure 2-15 (B).

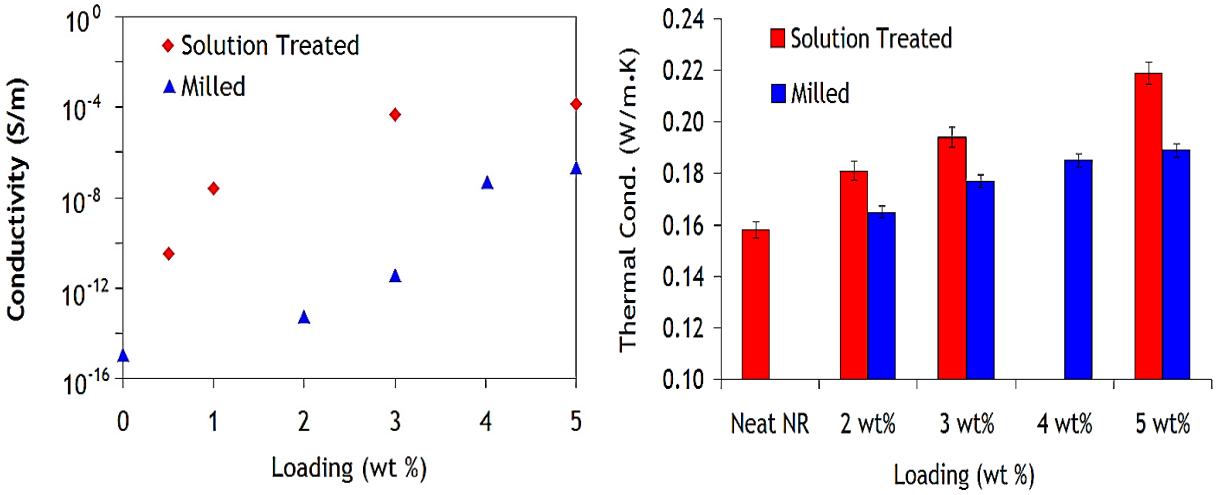

Figure 2-15: (A) The electrical conductivity and (B) thermal conductivities of solution treated and milled RGO/NR nanocomposites as a function of RGO loading. (Adapted with permission from ref. [12]. Copyright 2012, The University of Texas at Austin).

Several reports reveal that polymer/graphene nanocomposites improve matrix properties such as strength, stiffness**,** and electrical and thermal conductivity at a relatively low ratio of graphene loading [152]. These characteristics make graphene very promising for potential applications over a wide range of areas, such as solar cells [153], transistors [154], memory devices [155], batteries [156], the environment [157], supercapacitors [158], catalysts [159], medicine [160] and transparent conducting electrodes [161]. Synthesis methods, important features and some applications of graphene are demonstrated in Figure 2-16[145].

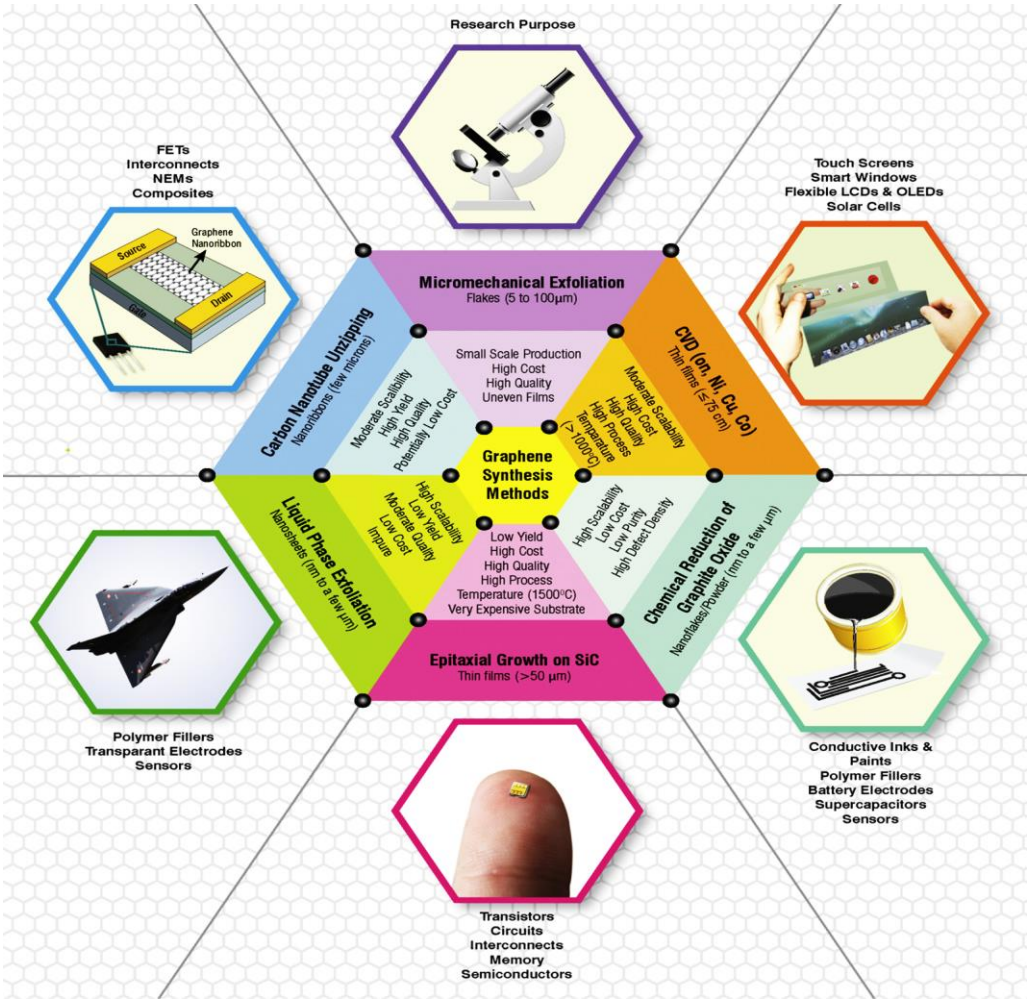

Figure 2-16: Scheme illustrating various conventional preparation methods of graphene sheets, important features, and current and prospective applications of graphene. (Adapted with permission from ref. [145]. Copyright 2012, Elsevier publications).

2.5 Adsorption of polymers onto nanoparticle surfaces

The surface energy of a solid material usually appears as heterogeneous distribution. Therefore, if the gas, vapour or liquid molecules are near enough to the surface they may interact and become bonded. Physical adsorption involves relatively weak forces, such as van der Waal's forces, which result from the weak solid-gas interaction. Therefore, the adsorbed molecules are not bounded to a specific location on the surface but may diffuse along the surface of the adsorbent material. Physical adsorption is easily reversed, due to weak binding, whereas chemical adsorption is difficult to reverse, as it produces a chemical bond between

the adsorbent and the adsorptive, which includes the share of electrons between it, and it may be regarded as the formation of a surface compound [162].

The interactions between the surfactant and the solid surface as the adsorption of a surfactant has been extensively studied in simulations and theoretical, in addition to several experimental investigations, such as atomic force microscopy (AFM) [163,164], ellipsometry [165], neutron reflection [166] and quartz crystal microbalance (QCM) [167], as well as adsorbed aggregate thickness on different substrates. The adsorption energy of homogeneous surfaces depends on the availability of different adsorption sites because it is a function of the spatial location [168]. Moreover, the density and proximity of adsorbed species are considered important to the intermolecular interactions [169].

Understanding the structure and surface chemistry of the material is important for good design and efficient utilization of the properties of polymer nanocomposites. Several factors, such as surface chemistry, ionic strength and solution pH influence the process of surfactant adsorption onto the solid/liquid interface and the morphology of the aggregates on the substrate surfaces. These factors influence adsorption processing on the nanofillers surfaces [170]. The properties of the adsorbed layer are determined by intermolecular surfactant-surfactant interactions, as well as electrostatic hydrophobic aspects, the surfactant, the solvent and van der Waals interactions between the materials [171]. Therefore, exploiting the properties are important issues [146,147].

2.6 Adsorption of polymer onto graphene oxide nanosheets

2.6.1 Poly(ethylene glycol) and poly(ethylene oxide)

The general formula of poly(ethylene glycols) (PEG) is H-(O-CH_2-CH_2)$_n$-OH, where n is the number of repeat units. It is a solid or liquid polymer, being semicrystalline, polar, and highly hydrophilic nature, with water retention and lubrication properties. The molecular weights for

PEG above 20000 g $mol^{-1}$are called poly(ethylene oxide) (PEO) [172]. Their chemical properties are nearly the same, but due to the chain length effect show different physical properties (e.g. viscosity).

PEG has good solubility in both organic and aqueous media, which involves high flexibility and hydration. Furthermore, it appears to have no immunogenicity, toxicity, or antigenicity. These properties make PEG an important polymer of various applications, such as pharmaceutical, biomedical [173] and polymer electrolyte [174]. Moreover, PEG is considered to be a commercial polymer in some applications, such as polymer-drug conjugates [175–179], batteries, supercapacitor, and fuel cell applications [180,181]. Each molecular weight of PEG has a different application [182]. The low ionic conductivity of the conventional PEO solid polymer electrolytes is the main problem for PEO. This is related to the relatively weak interfacial interaction as also presented a weak mechanical properties.

2.6.2 Effect of graphene oxide on adsorption behaviour of poly(ethylene glycol)

The incorporation of a nanoscale filler may enhance the properties of polymer materials, such as their mechanical, electrical, thermal and/or magnetic properties, without losing optical transparency [183]. The interfacial polymer constitutes a significant volume fraction of the nanocomposites. Therefore, to achieve this goal, understanding the unique structure of nanocomposites and the interfacial interaction between the nanofiller and polymers is considered of paramount importance, as they govern the property of the nanocomposite [183].

The adsorption mechanism of PEG was reported to be a systematic adsorb onto flocculate silica particles by Rubio and Kitchener [184], where the hydrogen bonding mechanism involved ether oxygen and isolated surface hydroxyls, such as silanol groups of the PEO molecule. This is considered to be the mechanism of the principal adsorption sites for PEO [185], whereas the degree of nanofiller dispersion in polymers influences the interfacial interactions [146], including hydrogen bonding, van der Waals attractions and/or

electrostatic interaction between the polymer and filler in the nanocomposites. The interfacial interaction between the polymer and filler further determine the stress transfer [148].

Other factors, such as the surface chemistry of the nanofiller, ionic strength, pH and polymer matrix properties, also affect the interfacial interaction and adsorption process on the nanofillers surfaces [170]. Therefore, exploiting these properties of the polymer chains adsorbed on the nanofiller surface and quantitative evaluation of the interphase zone of nanofiller arise as important issues [146,147]. The unique properties of a GO sheet were used to improve the material properties, such as thermal storage, as a supercapacitor and in adsorption of PEG. In 2014, Qi et al. [186] used GO for the solid/liquid phase change process and enhanced the heat storage density of PEG-based shape-stabilized nanoparticles, as well as their thermal energy storage. Other researchers have used ethylene glycol to reduce the graphene oxide-polypyrrole composite for the supercapacitor application [187].

Barroso-Bujans and co-workers [188] investigated poly(ethylene oxide) (PEO) adsorption onto GO and reduced graphene oxide (RGO) using the calorimetry diffraction scanning (DSC), employing a combination of diffraction and spectroscopic methods. The study observed that the total amount of PEO intercalated between the interlayer space of GO was 20 wt.%, whereas the amount of adsorbed PEO on the surface of GO nanosheets was less than 1 wt.%. This is a consequence of topological constraints and hydrogen bonds that lead to the complete suppression of the crystallization phenomena during the restriction of the mobility movement of the PEO chains. The same group [74] also reported the effect of GO oxidation degree and thermal exfoliation of RGO on the uptake of PEO. The amounts of PEO intercalated in GO was increased from 9 wt. % to 27 wt. % by increasing the GO oxidation degree, which reached 0.38 as a maximum ratio of O/C. A large endotherm presented at 333 K for the neat PEO, with a small feature at 255 K, corresponding to the regions of crystalline melting transition, whereas the glass transition of amorphous PEO was at 218 K. Clear glass transition presented at 209 K and the melting transition showed at 304 K of the PEO. In the

PEO/Graphene nanocomposites, the glass and melting transition temperatures were found to be lower than the values of neat PEO. The shifting of the glass and melting transitions was related to the additional conformational flexibility of the PEO applied by graphene. However, in both these studies [74,188], PEO was unable to either crystallize or display a glass or melting transition with GO and RGO because the PEO chains were intercalated between the nanosheets.

Consequently, the authors [169] investigated using high-resolution inelastic neutron spectroscopy (INS) to provide insights into confined and adsorbed PEO on graphite oxide nanosheets with various degrees of reduction. The amounts of intercalated PEO in the samples were 27, 21, 2, and 28 wt.% of PEO/GO, PEO/partial reduced GO (pR-GO), PEO/RGO, and PEO/graphene (G), respectively. The oxygen/carbon (O/C) ratio was calculated as follows: GO (0.40), pR-GO (0.30), RGO (0.13) and G (0.13) of these samples. In the PEO/G nanocomposites, the PEO exhibits a glass transition and melting peak at 304 K and 209 K, respectively, for these samples only, which gives lower values of the neat PEO, as shown in Figure 2-17.

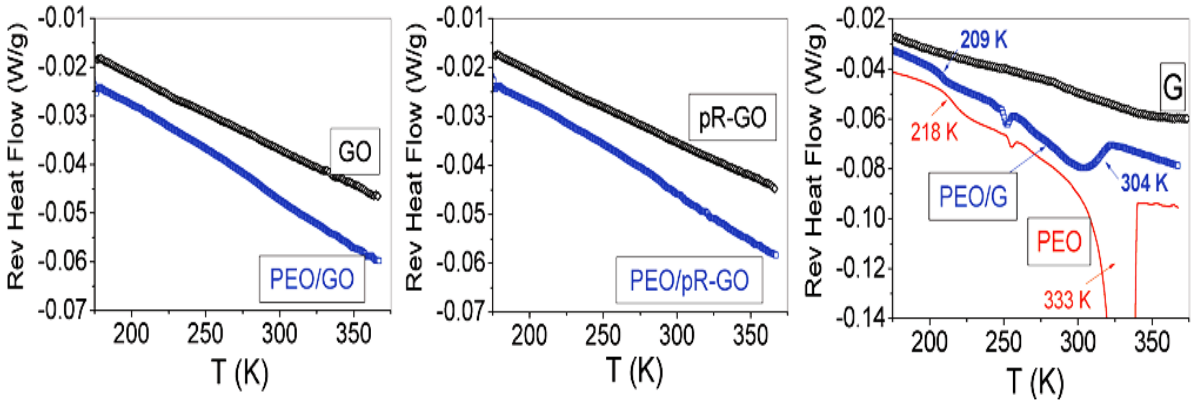

Figure 2-17: Temperature-modulated differential scanning calorimetry (TM-DSC) measurements for PEO/GO, PEO/pR-GO, and PEO/G. (Adapted with permission from ref. [169]. Copyright 2012, American Chemical Society Publications).

The same group [189] went on to investigate the effect of the chain sizes of adsorbed ethylene glycol (EG) onto GO nanosheets using a high-resolution INS technique. The structure and dynamics of confined polymer in GO interlayers were notably changed due to the strong geometric restrictions of EG and PEO by the GO nanosheets. Restricting the polymer led to a significant reduction in the vibrational motions of polymer chains by GO. In all of these investigations by Barroso-Bujans groups [74,169,188,189], clear evidence of the disappearance and complete suppression of the glass and melting transition of the PEO phase on both the GO and RGO nanosheets of PEO/GO, PEO/pR-GO, PEO/RGO, small PEG chain PEG/GO and large PEO chain PEO/GO sizes is seen, despite the use of different preparation methods, mechanisms and technics. All these studies [74,169,188,189] have shown that the PEG and PEO are strongly restricted between the GO or RGO nanosheets but are adsorbed on graphene.

The findings above match the results of other studies that have focused on adsorption of PEO. The PEO can be strongly restricted through hydrogen bonding by the layers of montmorillonite [190], fluoromica-based clay [191], hematite, alumina surface [192] and smectite clay [193]. These materials exhibited no glass or melting transitions in the PEO phase. Yuang and Shen [193] demonstrated that the high molecular weight PEO was adsorbed as monolayer coverage, which was formed as train sediments predominantly on the surface of the smectite clay. However, PEGs are consistently adsorbed onto silica [194] and oxides such as SiO_2, MoO_2 and V_2O_5 because they contain a strong Bronsted acid site on the surface that tends to interact with the ether oxygen of PEO [185], as well as graphene [169].

2.7 Effect of polymer functional groups on adsorption polymer behaviour

2.7.1 Poly(methyl methacrylate)

Poly (methyl methacrylate) (PMMA) has been widely applied in many industrial and important applications, such as dental fillers, tooth structures and bio-applications because it is amorphous, thermoplastic and inexpensive [195,196]. In addition, it has excellent chemical, physical, biological, and mechanical properties. PMMA has drawn considerable interest because of a desire to develop materials for applications in polymer-based memory devices [196]. The high C/O ratio graphene surface is more compatible with the PMMA [197]. Meng et al., 2014 [198] reported a greater improvement in fracture toughness and solvent absorption resistance when investigating the interface effect on structure and properties of PMMA/graphene nanocomposites.

2.7.2 Effect of polymer functional group on adsorption behaviour of polymer on graphene oxide

Stable and fine homogeneous dispersion is the key event needed to produce good interfacial interactions between the polymers and nanofillers to enhance the polymer nanocomposite properties [199]. Therefore, most of the investigation focused on increasing the homogeneity of the nanoparticles by functionalizing them, such as with silica and graphene [200]. This provided a significant improvement in the ability of the nanoparticles compatibility to interact with polymers. This functionalization of nanoparticles could change their properties. This offers a variety of possible ways of applying nanoparticles, such as medical [201], electrical [202], optical [203] and mechanical [204]. For instance, Sui, et al. [200] investigated the modification of hairy silica nanoparticles (HSNs) with different functional groups as additives to polyalphaolefin (PAO), which, when using functionalizing HSNs, can form a stable homogeneous solution and has good anti-wear and friction reduction properties, in order to be dispersed in PAO. Functionalizing HSNs with NH_2 illustrated the best friction-reduction and anti-wear properties, where the non-polar end groups increased the compatibility between the HSNs and PAO.

The single graphene sheets tend to undergo agglomeration due to strong $\pi - \pi$ and Van der Waals interactions because graphene has no functional groups in the structure, which means it has lower compatibility with the polar polymers [205]. This leads to a significant influence on the final nanocomposite properties. To overcome this problem, increasing the compatibility of the graphene with a host polymer is required [206], where the fine homogeneous dispersion between the polymer and graphene may enhance the polymer/Graphene nanocomposite properties. Therefore, different functionalization methods were applied to expand the current use of graphene and offer a new number of potential applications of graphene-based materials [207]. This depends on the methods and materials used, such as noncovalent, covalent, hybridization with nanoparticles and substitutional doping [207].

In the covalent functional modification, significant progress was made when attaching small organic molecules onto a graphene surface. This exhibited better interaction than the non-covalent functionalize group, which involves weaker and lower force interaction between the graphene surface and molecules [199]. Bai et al [208] reported functionalizing the graphene sheets with non-covalent functionalization to prepare sulfonated polyaniline-functionalized graphene composites. This composite presented a stable, good electrocatalytic activity and high conductivity. Jiang and co-authors [204] investigated functionalizing silica nanoparticles with 3-aminopropyltriethoxysilane to prepare silica-functionalized GO, then mixed this with epoxy to prepare the composites using a solution method. They reported a good interfacial interaction between the fillers and the matrix, such as the interaction between hydroxyl and amino groups. This interaction enhanced the mechanical properties due to the good dispersion of silica-functionalized GO into the epoxy, where the tensile strength and modulus improved to 29.2% and 22.0%, respectively, compared to pure epoxy [209].

2.8 Effect of the size of graphene particles

A good compatibility and the homogeneous dispersion of nanofiller with the polymer matrix have been reported as important factors in achieving efficient reinforcement in the final polymer nanocomposites [126,210]. The incorporation of graphene can offer a significant enhancement of nanocomposite properties from the bulk, even at a low loading ratio [183]. The effective length scale of the nanoparticles like GO nanosheets can vary from several hundred nanometers [146] to several microns [211] in the polymer/graphene-based nanomaterials. This plays an important role in the interfacial adhesion and transference of the load stress from the polymer matrix to the nanoparticles. Poor stress transfer was related to the not particularly strong interface interaction between the fillers and the polymer matrix [146,152,212].

Despite the lower Young's modulus of GO, it may provide some advantage for a stronger interface with the matrix due to the presence of the functional groups compared to the present of graphene or graphite particles [213]. Furthermore, both experiment [214] and theory [152,212,215,216] demonstrate the interface (the "interphase") interaction as an important interaction between the filler and polymer matrix when considering the reinforcement mechanisms of the nanocomposites. Thus, details are missing and required for understanding the effect of atomic-scale mechanisms on stress transfer by the interfacial interaction at polymer/graphene nanocomposites [152]. Therefore, the aspect ratio of the nanofiller is considered to be another important factor that strongly influences the reinforcement of the mechanical properties of polymer nanocomposites [4,138]. However, controlling the filler size is required to achieve high-performance interface interaction and better transfer of the stress between the filler and polymer matrix of the polymer nanocomposite [152,211,212,214–216].

Recently, both theoretical [152,212] and experimental studies [211,217] have examined this important issue in the understanding of how the filler size controls the

mechanical response. For example, the interfacial stress transfer of high-density polyethylene-graphene nanocomposites was theoretically investigated by Weerasinghe et al. [152] using a multiscale atomistic-to-continuum approach. They developed a modified shear-lag model of short nanofillers and illustrated the stress concentration at the ends of fillers, providing a dependence on filler size. This was obviously determined from atomistic simulations in the correct accounting of stress without any ad hoc modelling assumptions. They quantified the atomic-level stress profiles in graphene fillers using two parameters to quantify the end stress concentration and one for the shear-lag parameter, which is reliable for fillers with ~10 nm dimensions. Their model developed a shear-lag model of hierarchical multiscale models of short filler 2D filler-based nanocomposites for solution-processed 2D materials. Additionally, the elastic moduli increased with an increase in the radius of graphene particles in the composites, as shown in Figure 2-18.

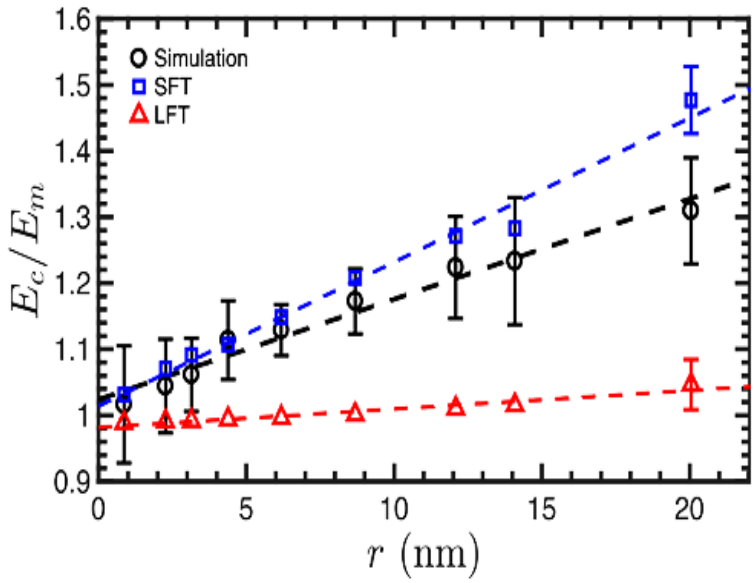

Figure 2-18: Elastic moduli of high-density poly(ethylene oxide)-graphene nanocomposites computed from molecular statics and molecular dynamics (MD) simulations of tensile straining tests as a function of filler radius (r) calculated according to short-filler theory. (Adapted with permission from ref. [152]. Copyright 2017, American Chemical Society publications).

The same model of nanocomposites was investigated by the same group [212], using molecular-dynamics simulations. They reinforced the high-density polyethylene by using different nanocarbon fillers, such as fullerenes and graphene. This composite introduced a clear stiffness with reinforcement by systematically varying the morphology, size and concentration of the fillers. A strongly size-dependent responsibility was induced from the two-dimensional graphene flakes, in contrast with the filler, where the flake, with a radius range of 2-4 nm (thus approaching typical experimental flake sizes between ~0.1–1 μm), provided significant enhancement in stiffness. Increasing the flake sizes of graphene displays strong filler-size dependence for stiffness enhancement in nanocomposites, where they find substantial enhancement in the modulus of the composites, with a typical flake size in the range of 1-10 μm for optimal reinforcement of mechanical properties of nanocomposites. This improvement could be extended with strong covalent bonding, such as hydrogen bonding, between filler and matrix, which could be provided by functional groups of GO to create a stronger bonding of the composite's constituents, leading to an improvement in its mechanical properties. They induced further control at the atomic-scale, providing insights into avenues for the improvement of the mechanical properties of polymer/Graphene-based nanocomposites.

Anagnostopoulos et al. [211] observed the means of measurement of stress transfer mechanism at the submicron level from a polymer substrate to a nano-inclusion affected by different phenomena appearing in the vicinity of flake edges. An epoxy-based photoresist/poly(methyl methacrylate) with a monolayer graphene flake was measured through detailed Raman line mapping near the edges, at steps as small as 100 nm. The procedures for preparing the samples caused exfoliation and the presence of compression, which led to interaction between the flake and matrix. Interaction affects the stress transfer mechanism and can reach a distance of 2 μm away from the edges of the flake. This resulted in the expected classical shear-lag prediction of both the interfacial shear-stress distributions

along the flake and the corresponding axial stress (strain). The transfer length of graphene flake for the stress transfer from each side of edge consists of two regions: the shear elastic due to shear-lag type, and doping effects. The latter provides a poor stress transfer. The estimated length for the effective load transfer from each end of the graphene flake is ~4 μm. Additionally, they reported the measurement of a 0.4 MPa maximum value of interfacial shear stress of the large flakes, due to flake slippage.

May et al. studied the effect of graphene size on the reinforcement effect in graphene/PVA systems [217]. Two graphenes with different average sizes (633 nm and 2 μm) were separated from an aqueous graphite flake suspension, using sonication and centrifugal with polyvinyl alcohol (PVA) as a dispersion stabilizer. Graphite was dispersed in polyvinyl alcohol (PVA)/H_2O and centrifuged for 45 min at 1000 rpm and sonicated for 100 h; it was then filtered through a 0.45 mm pore size to remove any aggregates. Afterwards, it was sonicated for 4 h in the bath after re-dispersal in PVA/H_2O. The sediment of graphene was sonicated for an hour and then centrifuged at 500 rpm for 45 minutes after re-dispersal with the fresh PVA/H_2O, to separate the larger-sized flakes. The separate graphene was mixed with the polymer to prepare the samples, which is also a centrifuge at 1000 rpm for 45 min. The dimensions of the separated flakes were of length 1.1 μm, width 0.56 μm and thickness 1.0 nm, as determined by TEM. The obtained graphene presented edge defects determined by TEM during the separation. The results showed that microsize graphene (2 μm) had a strong reinforcement effect, raising the modulus and strength of samples by one time, whereas nanosize graphene (633 nm) demonstrated a very low reinforcement effect.

Khan et al. [218] reported the exfoliation of graphite in the solvent of N-methyl-pyrrolidone (NMP) using 500 and 4000 rpm, centrifuging speed with low and mild power, and sonication for long periods of up to 460 h. The concentration of graphene could reach up to 1.2 mg mL^{-1}. Increasing the sonication duration reduced the graphene size. Long sonication duration (up to 460 h) was employed and the graphene presented topological defects in the

sheet and at edges. In addition, the defects mostly presented at edges rather than on the basal planes, as the power of the sonication was gradually increased. TEM was used to examine dimensions of the exfoliated graphene sheets. Meanwhile, after sonicating for 100 h almost all graphene sheets contained in the dispersions had a layer number <10, while for over 90% of the graphene sheets, the layer number was less than 5. This graphene dispersion can be reasonably employed for the preparation of graphene nanocomposite films with high-profile electrical and mechanical properties [218].

Yue et al. [219] prepared GO and separated them into two different average sizes with a centrifuge, and investigated the effect of GO size on the regulation of cellular responses to six cell types (e. g. Mouse BALB/c monocyte-macrophage). Atomic force microscopy (AFM) was used to characterize the size of the separated GOs. The average size of the resultant GOs was generally in the range of 350 nm to 2 μm in the lateral dimension, whereas the average heights were between 3.9 and 4.05 nm. It was found that the microsize GO exhibited a stronger response from the cells in comparison to the nanosized GO.

All these studies showed a strong interfacial adhesion between the large graphene flakes with the matrix, providing the best nanocomposite properties due to reinforcement.

2.9 Summary of literature review

Graphene-based nanocomposites are one of most interesting materials today. Many researchers have been investigating the use of graphene as the filler in based nanocomposite materials for different applications. It has been found that graphene improves the properties of the polymer matrix, depending on the application that is required. To achieve this, it is very necessary to understand the interaction between the graphene and the polymer. In addition to investigating the influence of this interaction on the structure of the nanomaterials, this, in turn, affects the required properties. In spite of various theoretical and experimental studies in

the literature, the interfacial interactions between the filler and polymer matrix are yet to be well understood. Understanding the effects of GO on the structure and adsorption behaviour of polymer in polymer/Graphene nanocomposites and reaching a consensus has been difficult [74,169,188,189,193] because various factors can critically affect the structure and properties of the polymers adsorbed onto the GO nanosheets. Different approaches have been used in various studies in an attempt to understand the structure and property relationships of polymer graphene nanocomposites, which could lead to the control of the structure and enable one to reach the required properties of nanocomposites.

According to previous studies [74,169,188,189] discussed in Section 2.6.2, the PEG and PEO are strongly restricted between the GO or RGO nanosheets but are adsorbed onto the graphene. The finding matches the results of other studies that focus on the adsorption of PEO on to other nanoparticles. The PEO can be strongly restricted through hydrogen bonding by layers of montmorillonite [190], fluoromica-based clay [191], smectite clay [193], or a hematite and alumina surface [192]. To understand the adsorption behaviour of PEG in terms of interfacial interaction with graphene derivatives, developed protocols with different parameters are needed, such as different mixing times, washing procedures, mixing ratios of materials and the molecular weight of PEG, in order to improve the adsorption behaviour of polymers onto GO nanosheets. These significant factors have not been systematically addressed before but could offer an improved understanding of the polymer adsorption behaviour and reduce this knowledge gap. A number of selected parameters, methods, polymers and prepared graphene oxide (GO) based nanoparticles were used for processing nanocomposites, where poly(ethylene glycol) (PEG), which is a semicrystalline polymer with different molecular weights, was selected as a polymer model for initial studies to prepare PEG/GO hybrid nanomaterials and investigate the influence of these parameters on the surface adsorption behaviour of PEG on GO nanosheets, as explained in detail in Chapter 3.

Another important factor that could affect the interfacial interactions between polymer and filler is the functional groups, which are responsible for more homogenous dispersion and strong interaction between the filler and polymer matrix, which is dependent on this compatibility [199]. According to the review in Section 2.7.2, most of the investigations have focused on functionalizing the graphene nanofillers to improve the homogeneity of the filler dispersion [200]. Therefore, polymers functional groups were selected to study the effect of functional group on their adsorption behaviour onto GO nanosheets that have been not addressed before. The effect of functional groups of three polymers that have a similar backbone but structures with different functional groups were selected as polymer models to investigate the influence of this factor on the adsorption behaviour of polymer on GO nanosheets, as clarified in details in Chapter 4.

Most of the previous studies [220–224], as reviewed in Section 2.8, have focused on the dispersion of GOs and the interfacial interaction between GOs and the polymer matrix. These studies did not consider other parameters that could strongly affect the properties of nanocomposites. In fact, the narrow and wide distribution of filler size, particle size and the effective length scale of the fillers can play an important role, strongly influencing the reinforcement of the mechanical properties of polymer nanocomposites. Recently, this significant subject has attracted theoretical investigation [152,212], whereas only one important experimental investigation has focused on the effective length scale of graphene particles, while another [217] has investigated the effect of two particle sizes of GO on mechanical properties. Hence, the size of graphene particle should be considered, as a way of achieving a high-profile interface interaction and effective stress transfer [152,212,214–216], as reviewed in Section 2.8. The influence of graphene/GO particle size on polymer adsorption behaviour and the mechanical properties of polymer/GO nanocomposites have not yet been fully understood. The formation of a strong interfacial interaction between GOs and the polymer matrix still needs to be investigated as an urgent issue for a full understanding of the

particle size effect on the interfacial interaction between filler and polymer matrix, and how this affects the properties of the polymer/GO nanocomposites [225].

Therefore, Sonication-centrifugal based methods were applied to separate one uniform size of the GO particle and the effect of particle size of GO on the adsorption behaviour and mechanical properties of high molecular weight poly(ethylene oxide) (PEO) were investigated. The principal objectives of this study are outlined below. The objectives of this study are to investigate the influence of the particle size and particle size dispersion of GO on the adsorption behaviour and the mechanical properties of PEO/GO nanocomposites, as presented in Chapters 5 and 6.

Graphene oxide nanosheets still offer a significant opportunity to investigate the structure and properties of the intercalated polymer. There are different and important factors, that have not been addressed before, which could have a direct effect on the interfacial interactions, structure and properties of polymer/Graphene nanocomposites, and thus offer an understanding of the polymer adsorption behaviour and enhance other properties, such as mechanical ones. Therefore, protocols with different parameters are still needed to help us to understand this relationship and to control the structure, in order to attain better properties in polymer/Graphene nanocomposites.

Chapter 3: Preparation and characterization of poly(ethylene glycol)-adsorbed graphene oxide nanosheets

3.1 Introduction

This section introduces the issues of understanding the unique structure of polymer nanocomposites, in terms of the adsorption and interfacial interaction between the nanofiller and the polymers matrix and how they effect on the adsorption behaviour of a polymer on GO nanosheets. These relationships are affected by several factors, such as the degree of nanofiller dispersion in polymers [146], hydrogen bonding, the nature of the polymer matrix and the surface chemistry of the nanofiller. All these and a number of other factors could influence the interfacial interactions and the adsorption process on nanofiller surfaces [170]. Therefore, exploring the properties of the polymer chains adsorbed on the nanofiller surface and quantitative evaluation of the interphase zone of nanofiller arise as important matters [146,147]. Graphene and GO offer a remarkable new opportunity to understand the adsorption behaviour of polymers that could open up a wide range of applications, including nanocomposites, healthcare, biosensing and semiconductors [19,20]. In the last decade, various studies have focused on understanding the surface adsorption of the polymer on the fillers to understand the surface of the nanocomposites, which is an important aspect of the materials, which must be understood.

According to previous studies [74,169,188,189] were discussed in section 2.6.2, the PEG and PEO are strongly restricted between the GO or RGO nanosheets but are adsorbed on the graphene. The finding matches results of other studies that focused on the adsorption of PEO on to other nanoparticles. The PEO can be strongly restricted through hydrogen bonding by layers of montmorillonite [190], fluoromica-based clay [191], smectite clay [193], or a hematite and alumina surface [192].

Protocols with different parameters are needed, such as different mixing times, washing procedures, mixing ratios of materials and the molecular weight of PEG, to improve the adsorption behaviour of polymers onto GO nanosheets. These significant factors have not been systematically addressed before but could offer an improved understanding of the polymer adsorption behaviour and reduce this knowledge gap.

The semicrystalline polymer PEGs, with various molecular weights, were selected as the model polymer in this chapter to investigate the effect of GO on the adsorption behaviour of the polymer. GO was firstly prepared, then mixed with the PEG using different parameters, as mention above. The adsorption amount and properties of PEG/GO nanohybrids were intensively investigated using various characterization techniques, such as the Fourier transform infra-red (FT-IR) spectroscopy, X-ray diffraction (XRD), thermogravimetric analysis (TGA), differential scanning calorimetry (DSC), optical light microscopy (OLM), scanning electron microscopy (SEM) and atomic force microscopy (AFM).

3.2 Experimental section

3.2.1 Materials

Graphite powder (≤20 μm), potassium permanganate ($KMnO_4$), sodium nitrate ($NaNO_3$), hydrogen peroxide, sulfuric acid (H_2SO_4) (analytical grade, 99%), hydrochloric acid (HCl, 35%) and poly(ethylene glycol)s with different molecular weights (Mw) of 960, 10000 and 100000 were purchased from Sigma-Aldrich Company, UK. It is noted that PEGs H-(O-CH_2-CH_2)$_n$-OH of higher molecular weights should be termed as PEOs [172]. For simplicity, PEG is used for both PEGs and PEOs in this work.

3.2.2 Synthesis and purification of graphene oxide

Graphite oxide was synthesized from graphite powder by a modified Hummer's method [25]. The resulting graphite oxide was washed five times with HCl and distilled water at 1:4 a ratio

to remove the metal ions [82]. Additional several washings with distilled water only were applied to raise the pH to 5.4. The graphite oxide was dispersed in distilled water for 24 hours using a magnetic stirrer then sonicated in a sonication bath (Fisherbrand, 230 V, 50 Hz for 30 minutes) to exfoliate graphene oxide into single nanosheets. After that, GO was centrifuged at 6000 rpm for 30 min to remove the unexfoliated graphite oxide. The resulting GO suspension was lyophilized in a Labconco FreeZone benchtop freeze dryer and stored in powder form in a desiccator before use as shown in Figure 3-1.

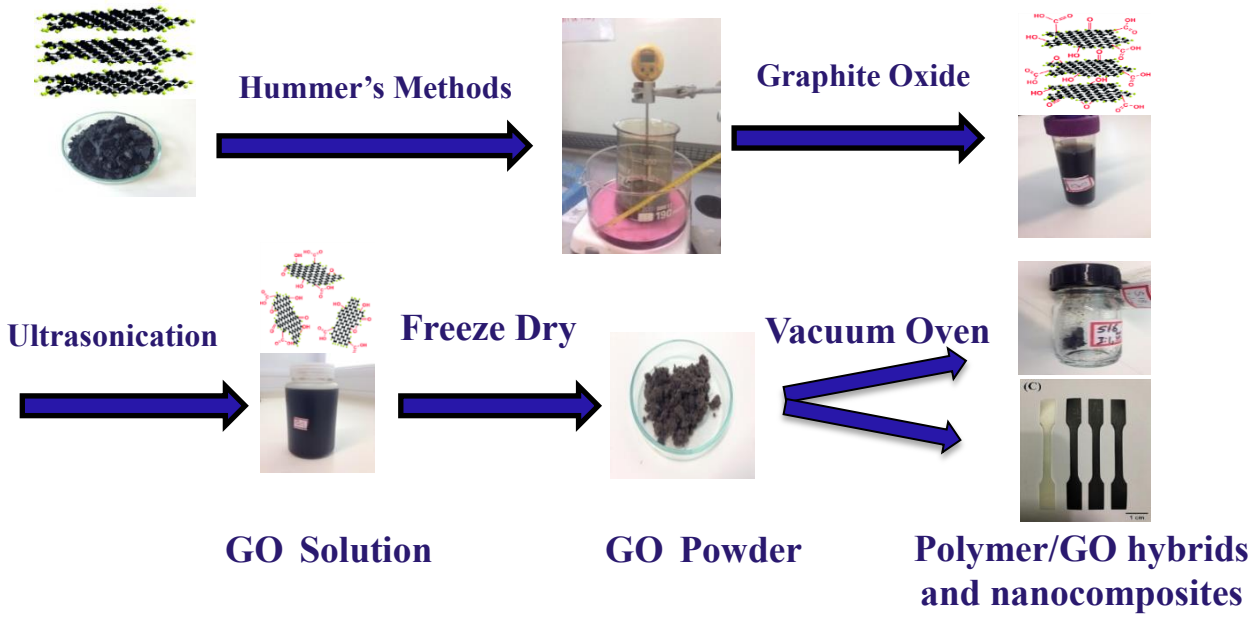

Figure 3-1: Synthesis and purification of graphene oxide and samples using modified Hummer's method.

3.2.3 Surface adsorption of poly(ethylene glycol) onto graphene oxide

Various formulations and methods were used to prepare PEG/GO nanohybrid including different mixing times, molecular weights, material ratios and washing procedures. Firstly, the PEG was dissolved in distilled water with a concertation of 4.2 wt/vol %. The GO was dispersed with a concentration of 0.1 wt/vol % in distilled water. Both PEG solution and GO suspension were mixed together at room temperature using a magnetic stirrer to prepare the samples as shown in Table 3-1. Samples were dried for 15 hours at 40 ^{o}C under 0.1 MPa

pressure in a vacuum oven until the weight mass of samples became constant. PEG samples without GO were prepared in parallel as controls. The samples were kept in a desiccator under vacuum.

Codes were created to help identify the samples. Letters N, h and w in the codes of Table 3-1 refer to nanomaterials of PEG/GO, mixing hour and washing time. Unless otherwise stated, the molecular weight of the polymer was 10K, the mixing ratio of PEG:GO was 3:1 and the washing time was 2. For example, N72h means the mixing hour was 72 hours, and N100k-1.5-24h means the molecular weight of PEG was 100K, the mixing ratio of PEG:GO was 1.5 and the mixing time was 24 hours.

Table 3-1: The preparation methods and sample denotations of PEG/GO hybrid nanomaterials.

Sample ID	**Polymer**	**Mixing Ratio**		**Mixing**	**Washing**
	Molecular Weight	**PEG**	**GO**	**Time / h**	**Number**
N1h	10K	3	1	1	2
N3h	10K	3	1	3	2
N6h	10K	3	1	6	2
N12h	10K	3	1	12	2
N24h	10K	3	1	24	2
N72h	10K	3	1	72	2
N144h	10K	3	1	144	2
N192h	10K	3	1	192	2
N1k-1.5-24h	1K	1.5	1	24	2
N10k-1.5-24h	10K	1.5	1	24	2
N100k-1.5-24h	100K	1.5	1	24	2
N-1.5-192h	10K	1.5	1	192	2
N-1.5-192h-0w	10K	1.5	1	192	0
N192h-0w	10K	3	1	192	0
N72h-0w	10K	3	1	72	0
N24h-0w	10K	3	1	24	0

3.2.4 Characterization

Fourier transform infrared spectroscopy (FTIR) spectroscopy is an analytical method that provides the facility to directly monitor the vibrations of the functional groups with ambient temperature operation. “Infrared” refers to any electro-magnetic radiation falling in the region from 0.7 mm to 1000 mm, whereas, the most attractive for chemical analysis are located in the region between 2.5 mm and 25 mm (4000 to 400 cm^{-1}). FTIR is the preferred method of infrared spectroscopy, which is a technique used to obtain an infrared spectrum of emission or absorption of a liquid, solid or gas. An FTIR spectrometer simultaneously collects high-spectral-resolution data over a wide spectral range. This technique lets through a beam containing many different wavelengths of light at once, and measures the total beam intensity. Then, the beam is modified to contain a different combination of wavelengths, giving a second data point. This process is repeated many times. Afterwards, a computer takes all this data and works backwards to infer how much light there is at each wavelength. When IR radiation is passed through a sample, some radiation is passed through (is transmitted) and some absorbed by the sample. The resulting signal at the detector is a spectrum representing a molecular ‘fingerprint’ of the sample. The usefulness of infrared spectroscopy arises because different chemical structures (molecules) produce different spectral fingerprints. The organic chemicals consist of a relatively few similar parts, combined in different ways, by comparing how other molecules containing the same types of parts are known to react. These parts of organic molecules are called functional groups. Functional groups are specific atoms, ions, or groups of atoms having consistent properties. A functional group makes up part of a larger molecule. For example, -OH, the hydroxyl group that characterizes alcohols, is an oxygen with a hydrogen attached. Different functional groups produce bond absorptions at different locations and intensities on the IR spectrum. Recognizing where the absorptions generated by the common functional groups occur and there are table lists of the locations and intensities of absorptions produced by typical functional groups could help to identify or recognize the

specific functional groups [226]. FTIR spectroscopy with a resolution of 1 cm^{-1} was performed using a Perkin Elmer Spectrum 100 with the attenuated total reflectance in the wavenumber region of 4000 to 400 cm^{-1}. The samples were directly test using attenuated total reflection (ATR), which is used a property of total internal reflection resulting in an evanescent wave. A beam of infrared light is passed through the ATR crystal in such a way that it reflects at least once off the internal surface in contact with the sample. This reflection forms the evanescent wave which extends into the sample. ATR is a sampling technique conjunction with FTIR spectroscopy that enables samples to be scanned directly without further preparation in a different state, such as, solid or liquid [227].

The atomic and molecular structure of a crystal was determined by X-ray technique that now a common technique to identify the study of crystal structures and spacing between lattice planes (hkl Miller indices). This interplanar spacing (dhkl) is the distance between parallel planes of atoms or ions, where the X-ray diffractometers consist of three basic elements: an X-ray tube (cathode), an X-ray detector and a sample holder. A X-ray tube is generated these X-rays that is filtered to produce monochromatic radiation, collimated to concentrate and directed toward the sample. The interaction of the incident rays with the sample produces constructive interference (and a diffracted ray) when conditions satisfy Bragg's Law.

$$n\lambda = 2dsin\theta \qquad (3\text{-}1)$$

Where n means a positive integer and λ means the wavelength of the incident wave. The waves are scattered from lattice planes separated by the interplanar distance d. The path difference between two waves undergoing interference is given by $2dsin\theta$, where θ is the scattering angle. XRD samples are acceptable in many forms, depending on the availability of the material and the type of analysis to be performed. The samples those were prepared and explained in section 3.2.3 where directly tested by the X-ray diffraction that was achieved

using a STOE STADI P (CuIP) with an irradiation wavelength of 0.154 nm. Measurements were taken from 2 – 100^{o} (2θ) with a scanning speed of 10^{o} min^{-1} at 40 kV and 35 mA. Interlayer distances of PEG/ GO hybrid nanocomposites ($d_{PEO/GO\ hybrid\ nanocomposites}$) were obtained by using equation (3-1)

Thermogravimetric analysis (TGA) is technique measured the change of sample mass as a function of time or temperature, under a controlled environment with respect to gas atmosphere, flow rate, crucible type and heating rate, etc. A TGA consists of the furnace and a sample pan, which is supported by a precision balance. That pan is heated or cooled during the experiment by the furnace. During the heating, the mass of the sample is monitored under a sample purge gas to control the sample environment. This gas may be inert or a reactive gas that flows over the sample and exits through an exhaust [228]. Therefore, the prepared samples were performed directly using on a Perkin Elmer Pyris 1 TGA. The samples were heated from 25 to 600 °C with a ramp rate of 10 °C min^{-1} under nitrogen gas at a flow rate of 20 ml min^{-1}.

Thermogravimetric analysis (TGA) result was used to determine the amount of PEG in the PEG/GO sample. The adsorbed amount of PEO in the PEO/GO nanohybrid materials was determined from sample-residue analysis at 550 °C, whereas the free water amount determined at 100 ^{o}C, was removed from the results (curve) for GO, PEO and all samples, which means all the samples was recalibrated before calculating the adsorption amounts. For instance, the GO curved shifted to up by 13.5% after removing the amount of water that evaporated at 100 ^{o}C, see the appendix of chapter 3 figure A3-2. This calculation method was applied in all sections in this study. The equation below was derivative and applied to calculate the adsorbed amount of PEG in the samples.

$$\frac{y}{x} = \frac{a}{(1-a)} \qquad (3\text{-}2)$$

$$S = ax + (1 - a)y \quad (3\text{-}3)$$

Where S, x and y are the weight percentage of the mass decomposition ratio of the sample, polymer and GO, respectively.

Differential Scanning Calorimetry (DSC) is a thermal analysis technique that measured the difference in the amount of heat required to increase the temperature of a sample and reference. That is measured as a function of temperature. The reference and sample, both, are maintained at nearly the same temperature throughout the experiment. Generally, the DSC temperature program for is designed to analysis the sample holder temperature that increases linearly as a function of time, where a well-defined heat capacity over the range of temperatures must require of reference sample for scanned, whereas the changes in the samples, which is a known mass, heat capacity are tracked as changes in the heat flow during heated or cooled. This allows the detection of transitions such as glass transitions, melts temperature, curing and phase changes during the experimental. The DSC experiments were carried out directly on a Perkin Elmer DSC6 with two consecutive heating cycles from 30 °C to 90 °C. Each cycle consisted of a heating scan and cooling scan, where the temperature of heating scans was from 30 °C to 90 °C and cooling scan was from 90 °C to 30 °C with a ramp rate at 10 °C min^{-1} under the flow of nitrogen gas as the flow rate of 20 ml min^{-1}. The heat capacity changing in the second heating cycle was used for analysis.

Optical light microscopy (OLM) is often referred to as light microscope, is a type of microscope that uses a visible light and a system of lenses to magnify images of small samples, where most of the OLM are compound microscopes, which consist of two lenses at least. The image produced by the objective lens that is then magnified again by the eyepiece lens, which acts as a simple magnifying glass. The samples were prepared by dispersing the GO in distilled water using a stirrer for 24 h and a sonication bath for 30 minutes. A few drops of GO suspension were dropped on a glass substrate and then was left in the air to dry

for overnight at room temperature. The PEG was melted on the GO using the vacuum oven at 80 ^{o}C for an hour. This sample represented the N-72h-0w, which showed 38 wt.%. Therefore, this ratio was divided for two to consider the adsorption of PEG on one side of GO. The samples were examined using a Nikon Eclipse LV150 microscope in order to reveal PEG crystalline structure on the GO nanosheets,

Scanning electron microscopy (SEM) is basically a topographic technique, where a focused electron beam scans over the surface of the sample and the reflected electrons were collected with a detector to create an image of the surface of the sample. By doing this in a raster pattern across the surface an image is formed, pixel by pixel. The electrons were generated and focused by the column called the primary electrons. These electrons in the beam interact with the sample, producing various signals, they generate backscattered electrons, secondary electrons, auger electrons, cathodeluminescence and X-ray photons, where the backscattered electrons are analysed to provide information about the surface topography and composition. All the samples in this study were placed on an aluminium stub after coating the samples using a gold sputter coater (Emscope SC500A) and were conducted on an inspect F scanning at voltage 5 kV. SEM was pursued by FEI Company.

The atomic force microscope (AFM) is one kind of scanning probe microscopes (SPM) that was designed to measure local properties, for instance, friction, height and magnetism. The SPM raster-scans the probe scans over a small area of the sample for achieving an acquired image. AFM operates by measuring the force between a probe and the sample. The probe is a sharp tip, tall pyramids between a 1 - 6 µm with an end radius of 15 - 40 nm. The AFM samples were prepared by dropping one or two drops of the samples that suspension before placed on a freshly cleaved mica surface. The sample was left in the fresh air to dry for overnight. This Atomic force microscopy images were taken by using a Veeco Dimension 3100 atomic force microscope with an Olympus AC160TS probe with tapping mode at 0.5 Hz.

3.3 Results and Discussion

3.3.1 Characterization of graphene oxide

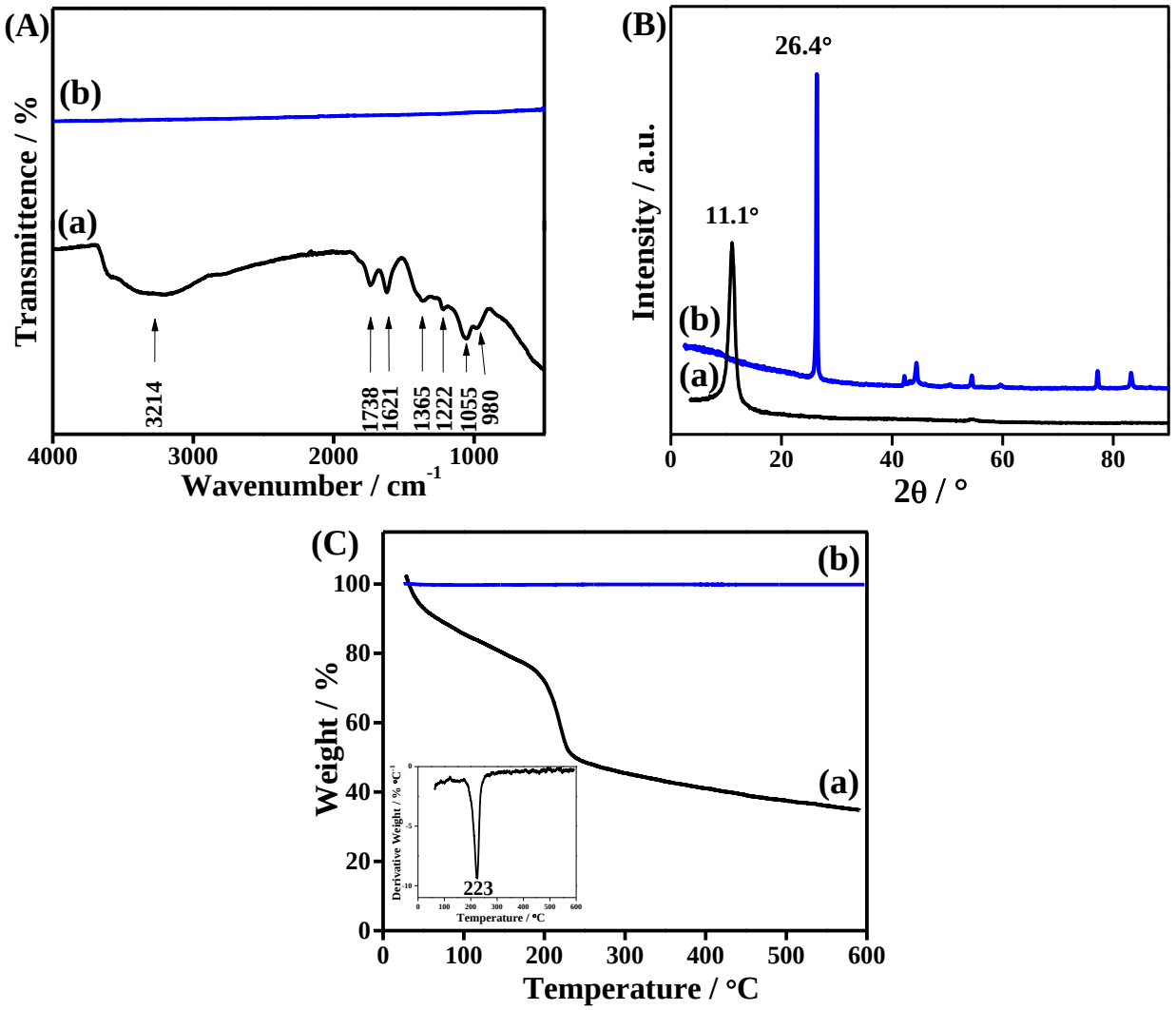

Figure 3-2: (A) FTIR spectra, (B) XRD traces, and (C) TGA curves of (a) GO and (b) graphite.

Figure 3-2 shows the FTIR, XRD and TGA results of the GO nanosheets, which were prepared by oxidizing the graphite using a modified Hummers method [25], followed by exfoliation, in contrast to the control sample graphite. In Figure 3-2 (A), GO nanosheets showed new characteristic peaks at 3214, 1738, 1621, 1365, 1222, 1055 and 980 cm^{-1} wavenumbers corresponding to O-H (free water) stretching, carbonyl C=O stretching,

aromatic ring C=C skeletal vibrations, -C-H bending, C-OH stretching, epoxy C−O−C stretching and C-O stretching functional groups, respectively [25,229].

In Figure 3-2 (B), A sharp X-ray diffraction peak of graphite was presented at 2θ = 26.4° corresponding to the (002) peak with an interlayer spacing of 0.33, nm in agreement with the literature value [188,229], whereas this (002) peak shifted to 2θ = 11.1° during the strong oxidation of graphite to synthesis GO1, indicating an interlayer spacing of 0.79 nm which, in line with other studies [25,229]. Figure 3-2 (C) shows the thermal degradation of GO that constituted 31 wt.% of the total dry mass between 150 - 250 ^{o}C, due to the degradation of epoxide, hydroxyl, carbonyl and carboxyl functional groups [229]. The peak degradation temperature of the GO was located at 223 ^{o}C as shown in Figure 3-2 (C). These characterization results confirmed that the GO nanosheets were successfully prepared.

3.3.2 The effect of mixing times

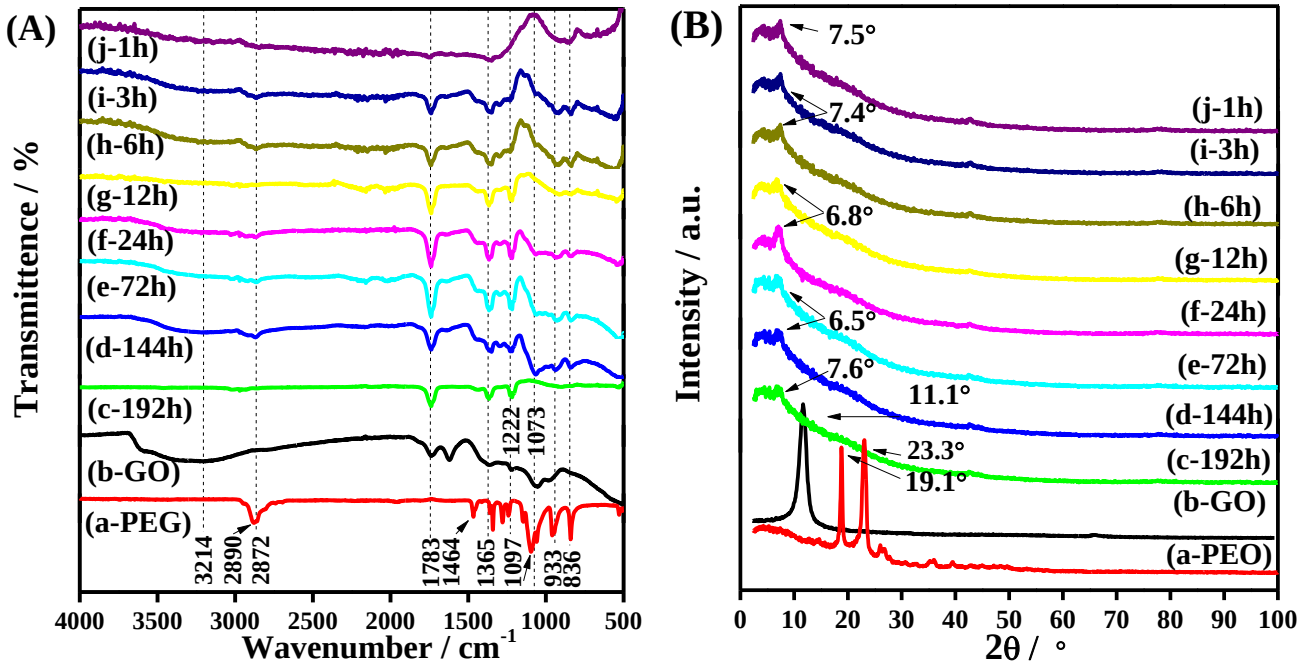

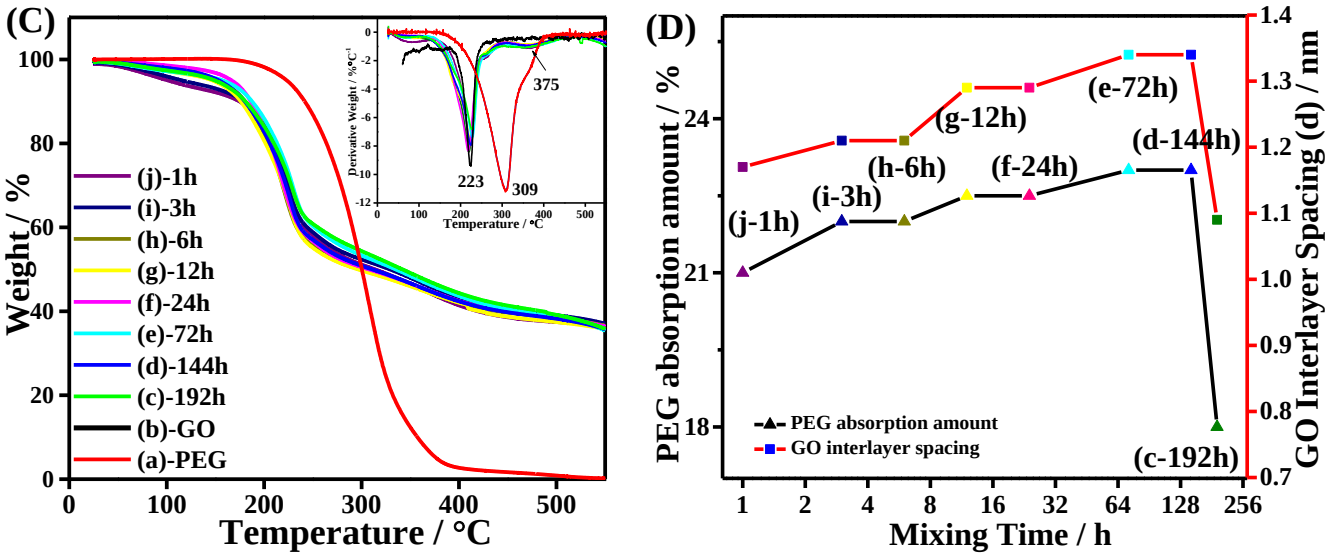

Figure 3-3: (A) FTIR spectra, (B) XRD traces, (C) TGA curves and (D) the PEG absorption amount on GO nanosheets and GO interlayer spacing for various mixing times of (a) 10k PEG, (b) GO, (c) 192h, (d) 144h, (e) 72h, (f) 24h, (g) 12h, (h) 6h, (i) 3h and (j) 1h.

A series of PEG/GO hybrid nanomaterials with different mixing times were prepared to investigate the effect of mixing time on the adsorption behaviour of the PEG onto GO nanosheets. Figure 3-3 shows the series of samples that were prepared by mixing the 10k PEG with GO using 3:1 as the ratio for eight different mixing times in the range from 1 h to 192 h, with two wash procedures. In Figure 3-3 (A), the FTIR spectra of the PEG showed the functional group peaks, which were C-H stretching at 2890 cm^{-1}, C-H bending at 1464 and 1343 cm^{-1}, C–OH or C-O stretching at 1222 cm^{-1}, C-O-C stretching at 1097 cm^{-1} and $–CH_2–CH_2–$ stretching at 933 - 863 cm^{-1} (for a pure PEO's helical conformation) [126,230].

The FTIR spectra of PEG/GO nanomaterials illustrated the most characterization peaks of the adsorbed PEG and GO. The strong absorption peaks from PEG were presented at 1738 cm^{-1}, 1365 cm^{-1}, 1222 cm^{-1} and 1073 cm^{-1} of C=O, COOH, C-O and C-O-C, respectively, This shifting of the functional group suggested absorption of PEG onto GO nanosheets, such as the C-H peaks presented small shitting and vibration at 2872 cm^{-1}. Hydrogen bonding is considered the major factor in the interaction between the GO

nanosheets and PEG, where the hydrogen bond led to improvement in the PEG adsorption behaviour [126]. The intermolecular hydrogen bonding between the ether group such as C–O–C sites of PEG chain interact with polar functional groups, such as COOH and -OH of GO [231], for instance the FTIR peak of the PEO presented the C-O-C stretch group at 1106 cm^{-1} to 1055 cm^{-1} as formation of hydrogen bonds interaction in agreement with literature [232]. These absorption peaks confirmed the adsorption of the PEG onto the GO nanosheets, which clearly presented in all hybrid nanomaterials except the N1h sample. The N1h sample presented without the peaks at 2872, 1222 and 933 - 863 cm^{-1} of the PEG as well as at a 1073 cm^{-1} peak, which was related to PEO. These peaks occurred again in the hybrid nanomaterials with stronger intensity with an increase in the mixing time from 3h to 144 h samples (N3h to N144h).

The absorption peaks of PEG exhibited higher increase in the intensity with increasing mixing time, from 3 h to 72 h. This suggested improving in the PEG amount in the hybrids, whereas the absorption peaks' intensity decreased after increasing the mixing time from 72 h to 192 h. The 192 h was the longest mixing time in this study. That showed the reduction of the number of absorption peaks and the peak intensity of absorption PEG in this sample. That indicated a reduction in the adsorption polymer of these samples, whereas N1h samples demonstrated low absorption peaks of PEG, due the lower mixing time.

Figure 3-3 (B) shows the diffraction peaks of PEG, However, the reflection of (120) and (032) appeared at $2\theta = 19.1°$ and $2\theta = 23.52°$ as were usually reported in the literature [233]. The (002) GO peak shifted from $2\theta = 11.1^{o}$ of GO to 7.5^{o}, 7.4^{o}, 6.8^{o}, 6.5^{o} and 7.6^{o}, corresponding to the interlayer spacing that increased from 0.79 nm of GO to 1.17, 1.21, 1.29, 1.34 and 1.09 nm of N1h, N3h N6h, N12h N24h, N72h N144h and N192h, respectively. Increasing the ratio of polymer between the GO nanosheets shifted the GO diffraction peak and increased the distance of GO interlayer spacing. N192h exhibited the lower interlayer spacing compared to other samples in agreement with FTIR results, which showed a reduction

the intensity of the characteristic peaks of PEG. The interlayer spacing increased by 0.55 nm with an increased mixing ratio from 1 h to 144 h, whereas it decreased by 0.25 nm with an increased mixing ratio from 144 h to 192 h.

Figure 3-3 (C) shows the thermal degradation behaviour of PEG, GO and their hybrid nanomaterials. The PEG was thermally stable in the range of 30 ^{o}C to 170 ^{o}C. Between 200 ^{o}C to 400 ^{o}C, the mass of PEG lost 79 wt.% then up to 99 wt.% at 550 ^{o}C due to the degradation of the PEG backbone. The mass of hybrid nanomaterials was significantly reduced by 39 wt.% between 150-250 ^{o}C, which was related to the degradation of the oxygenated functional groups of the GO. Moreover, between 250 - 420 ^{o}C, the samples lost 19 wt.% of its mass attributable to the degradation of the polymer in hybrids. The total loss of the hybrid mass was 65 wt.% at 550 ^{o}C due to the presence of GO. Between the 250 - 420 ^{o}C, the thermal behaviour of hybrid nanomaterials was improved by the contribution of the hydrogen bonding between the polymer and GO. The thermal behaviour showed significant improvements up to 52.3% at 550 ^{o}C due to the GO content.

The peak degradation temperature (T_d) was at 223 ^{o}C and 309 ^{o}C of GO and PEG, respectively. These Td values were shifted in the hybrids and each hybrid presented two T_d values. First, the Td of the hybrids shifted from 223 ^{o}C to between 224 - 229 ^{o}C, which was related to the degradation of the functional group of GO, whereas the second T_d improved notably from 309 ^{o}C of PEG to a range between 372 - 378 ^{o}C. The incorporation of the GO led to this enhancing the T_d values, as shown in Figure 3-3 (C) and improved the non-oxidative thermal stability of hybrids compared to thermal behaviour neat PEG in agreement with the literature [234].

Figure 3-3 (D) illustrates the absorption amounts of PEG compared to the interlayer spacing distance of the GO nanosheets of the nanohybrids, which were calculated from XRD spectra and TGA results respectively, as a function of the increased mixing time. The

absorption amount of PEG increased slightly from 21 to 23 (± 0.0015) wt.% with an increase in the mixing time from 1 h to 144 h and was reduced to 18 wt.% of the 192 h mixing time. The results showed an increase in the interlayer space of GO nanosheets that due to the increase of the intercalated polymer in the samples. The reduced absorption amount at 192 h suggested that the PEG intercalated via weak physical bonds, which could be removed by the long mixing time.

3.3.3 The effect of molecular weights

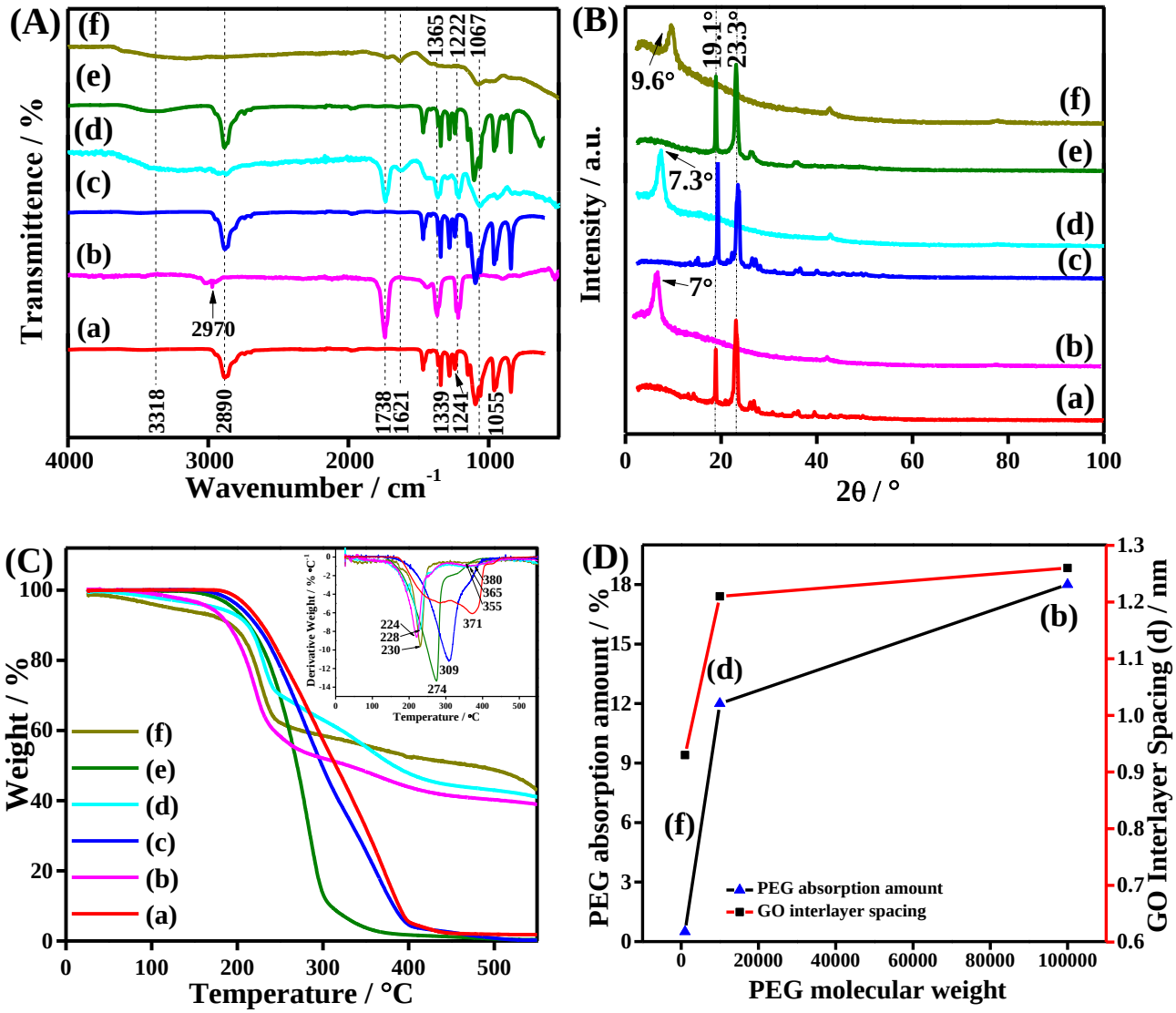

Figure 3-4: (A) FTIR spectra, (B) XRD traces, (C) TGA curves and (D) PEGs absorption amounts and GO interlayer spacings of (a) 100k PEG, (b) N100k-1.5-24h, (c)10k PEG, (d) N10k-1.5-24h, (e) 1k PEG and (f) N1k-1.5-24h hybrids.

Figure 3-4 shows the effect of polymer molecular weight on the adsorption behaviour of PEG onto the GO nanosheets. Three different molecular weights, i.e. 1k, 10k and 100k, of PEG were used for preparing three PEG/GO hybrids, N1k-1.5-24h, N10k-1.5-24h and N100k-1.5-24h. Figure 3-4 (A) shows the FTIR spectra of the PEGs and hybrids. N1k-1.5-24h showed the same peaks of GO functional groups, with only small features of 1k PEG, whereas N10k-1.5-24h and N100k-1.5-24h presented the main functional group peaks of both PEGs and GO with clear changes in the peak positions and intensity. For instance, the -C-H bending shifted from 1339 to 1365 cm^{-1} and 1241 to 1222 cm^{-1}, whereas the C-H stretching shifted from 2890 to 2970 cm^{-1} of the N100k-1.5-24h.

The hydrogen bonding between the C-H or C–O–C groups of PEO chains and COOH or –OH of GO nanosheets led to these shifts of peaks. The absorption peaks of PEG presented intensely in the hybrids such as C-H stretching at 2872 cm^{-1}, C-O at 1738 cm^{-1}, -C-H bending at 1365 cm^{-1}, C-OH stretching at 1222 cm^{-1}. The most interesting aspect of these peaks vibration intensity was a considerable increase in molecular weight from 1k to 100k of the N10k-1.5-24h, which probably means a higher polymer molecular weight shows a higher absorption ratio of the polymer in the hybrids [189].

In Figure 3-4 (B), the XRD traces of the hybrids shifted the diffraction peaks compared to that of GO. The (002) peak of GO shifted from $2\Theta = 11.1^{o}$ to 9.6^{o}, 7.3^{o} and 7^{o} corresponding to the increase in the interlayer spacing from 0.79 nm to 0.93, 1.21 and 1.26 nm for N1k-1.5-24h, N10k-1.5-24h and N100k-1.5-24h nanohybrids, respectively. These shifts implied the intercalation of the PEG ratio into the GO nanosheets. Generally, it was observed that the hybrids, which contained higher molecular weights, showed a higher intensity of the (002) peak and larger interlayer spacing compared with other nanohybrids containing lower molecular weight PEGs. XRD peak intensity of samples suggested a higher degree of order and concentration within the stacks as a function of the polymer molecular weight [189,235]. This is in agreement with the FTIR results discussed above. The hydrogen

bonding between the functional groups of GO and PEG helped the intercalation of the PEG in between GO nanosheets. The interlayer spacing showed a substantial increase of 47% for the confined 100k PEG between the GO nanosheets compared to GO, and a 33% for an increase in the PEG molecular weight from, 1k to 100k.

The TGA curves in Figure 3-4 (C) showed more mass loss for the hybrids that contained 10k and 100k PEG compared to the N1k-1.5-24h with 1K PEG. The loss of mass was 31.7 wt.%, 38.3 wt.% and 26.2 wt.% between 150 - 250 ^{o}C, whereas the total mass losses were 38.9 wt.%, 41.1 wt.% and 42.7 wt.% at 550 ^{o}C for N1k-1.5-24h-2w, N10k-1.5-24h-2w and N100k-1.5-24h-2w, respectively. This former was related to the degradation of the oxygenated functional groups of GO. The latter correlated to the degradation of the PEG. The ratio of degradation the mass samples increased by 9.7% when increasing the molecular weight from 1k to 100k. This finding supports the increase of the interlayer spacing due to the increasing molecular weight of PEG.

Each hybrid also presented two values of the peak degradation temperature, which exhibited higher than the GO and PEG values. The first Td of the GO shifted from 223 ^{o}C to 224, 228 and 230 ^{o}C, whereas the T_d of the PEGs shifted from 274, 309 and 371 ^{o}C to 355, 365 and 380 ^{o}C of 1k, 10k, 100k, N1k-1.5-24h, N10k-1.5-24h and N100k-1.5-24h, respectively. The Td of the hybrids exhibited a clear enhancement of the values, where the first T_d degradation was presented in the range 170 - 250 ^{o}C due to releasing the oxygen functional groups of GO, which are associated with increasing the thermal behaviour of the samples. The second of the T_d values related to the degradation of PEGs, which showed an improvement in the values, due to the contribution of GO in the hybrids in comparison with neat PEGs.

Figure 3-4 (D) shows the PEG absorption amount between the GO nanosheets and the interlayer spacing between the GO nanosheets, which were calculated from TGA curves and

XRD traces, respectively, as a function of increasing PEG molecular weight. The PEG absorption amount exhibited a significant increase from 1 wt.% to 16 wt.% then to 18 wt.% when the PEG molecular weight was increased from 1k to 10k then 100k for N1k-1.5-24h-2w, N10k-1.5-24h-2w and N100k-1.5-24h-2w, respectively. These results showed a notable increase by 1700% of the absorption of the PEG ratio, even when reducing the PEG mixing ratio from 3 to 1.5 in these hybrids in agreements with the XRD results that indicated increasing the GO interlayer spacing from 0.79 nm of the GO to 0.93 nm, 1.21 nm and 1.26 nm of the N1k-1.5-24h-2w, N10k-1.5-24h-2w and N100k-1.5-24h-2w, respectively as shown in Figure 3-4 (D). This increase in the interlayer spacing was directly related to the increases in the absorption ratio of PEG between the GO nanosheets in the samples. Similar to an increase, the molecular weights showed a major difference in the absorption ratio of PEG in the hybrids.

Generally, the above characterization results demonstrated that an increase in molecular weight of PEG brought a higher absorption amount of the PEG between GO nanosheets, where the free energy in the polymer chain significantly increased with the longer polymer chain to achieve a perfectly (higher free - energy) planar conformation [189,236]. Meanwhile, the GO surface had an abundance of oxygen functional groups, which resulted from the high oxidizing of graphite [189]. The chemically reactive sites on the GO, with free energy in the PEG chain, led to strong hydrogen bond interaction between the polymer and GO nanosheets. The hydrogen bond is considered the main factor in absorbing the polymer chains between the GO nanosheets [189]. This increased the absorption polymers between the GO nanosheets. Similar conclusions were reached in a study by Nelson and Cosgrove [237], who found that increasing the molecular weight of PEO led to an increase in the hydrodynamic thickness of the adsorption layer of PEO on Laponite clay. The molecular weight is presented as an important factor for improving the PEG absorption behaviour.

3.3.4 The effect of mixing ratio of polymer to graphene oxide and wash procedure

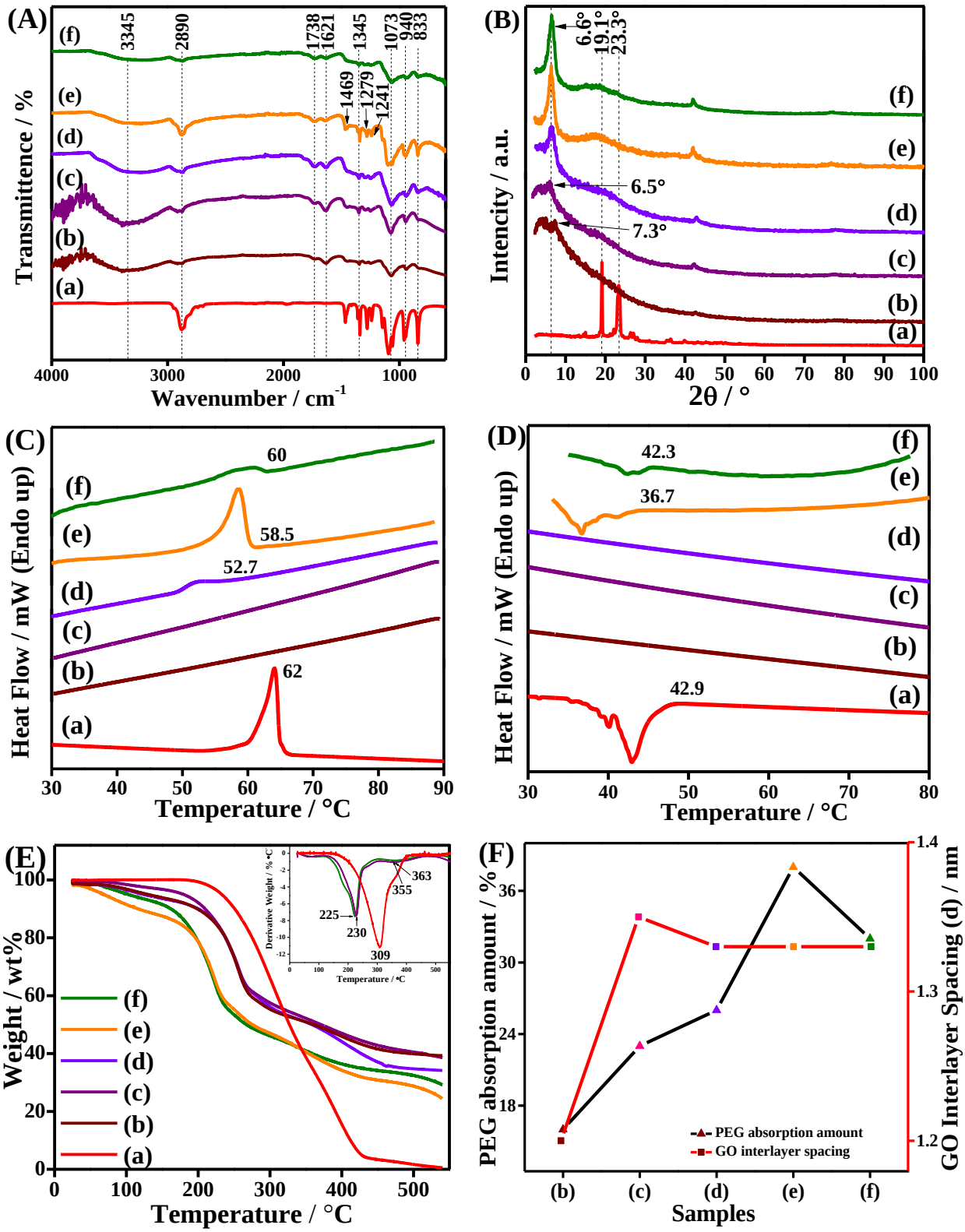

Figure 3-5: (A) FTIR spectra, (B) XRD traces, (D) second DSC heating scan and (E) second DSC cooling scan, (E) TGA curves and (F) PEG absorption amounts and GO interlayer spacings of the (a) 10k PEG compared with the (b) N-1.5-192h, (c) N-1.5-192h-0w, (d) N192h-0w (e) N72h-0w and (f) N24h-0w.

In this part, methods were applied that extracted from the first two sections' method, where results showed that the long mixing time and reducing the mixing ratio decreased the PEG adsorption. This increased very significantly molecular weight. Therefore, the methods started by applying: no further washing procedure, increasing the mixing ratio of the PEG:GO from 1.5:1 to 3:1 and decreasing the mixing time twice from 192 h to 72 h and 24 h, as shown in Table 3-1.

In Figure 3-5 (A), the most functional groups of the GO and PEG presented in the FTIR spectra of the hybrids, were those, such as O-H, C=O, C=C and C-H of GO with a clear reduction in the intensity of some adsorption peaks of PEG compared with the neat PEGs. Those, in turn, were related to the interaction between ether groups of PEG and oxygen functional group of GO nanosheets that presented from the formation of intermolecular hydrogen bonds between the polar functional groups, such as COOH and –OH groups on the GO with C-H or -O- groups of PEO. For instance, the peaks at 2890 $cm^{-1}$of C-H, 1345 cm^{-1} of C-OH , 1073 $cm^{-1}$of C-O-C, 940 cm^{-1} of C-O and 833 cm^{-1} of C-H, which were related to PEG, clearly confirmed the strong adsorption of PEO after applying no further washing procedure. This corresponded to an increase in the adsorption PEG concentration in the N192h-0w. Applying no further washing procedure of the samples was an important factor that increased the peaks intensity that related to an increase in the concentration of the PEG onto GO nanosheets. The washing procedure was associated with breaking the weak physical bond that attached the PEG on the surface of the GO nanosheets. Therefore, no further washing procedure helped to keep the absorption PEG on the GO nanosheets surface of N-1.5-192h-0w compared to the N-1.5-192h.

Increasing the mixing ratio of PEG from 1 to 3 showed an additional increase in the peak intensity that was clear in the C-H and C=O and C-O functional groups, whereas the O-H functional groups were seen to reduce the intensity peaks of the N192h-0w compared to the N-1.5-192h-0w. All the above parameters, which were no future washing procedure and 3:1

mixing ratio mixing time, were applied to further samples with the additional factor that involved reducing the mixing time twice from 192 to 72 then 24 h. Appling these factors together showed a notable increase in the intensity of functional group peaks, especially the N72h-0w. The N72h-0w presented the highest intensity of the adsorption PEG peaks, which combined to present interestingly new adsorption peaks of PEG at 1469, 1279 and 1241 cm^{-1}, which was exhibited for the first time and only with these hybrids compared to other hybrids.

Figure 3-5 (B) shows the shifting of the (002) peaks of GO from 11.1^{o} to 7.3^{o} of N-1.5-192h. Applying no further washing procedure was associated with another important shift of the XRD peak from 7.3^{o} to 6.5^{o} corresponding to an increase the interlayer distance from 0.79 nm of GO to 1.2 nm then 1.35 nm of the N-1.5-192h and the no washing samples N-1.5-192h-0w, respectively. This interlayer space distance was considered the biggest of the GO in the current study compared to the other samples. The shifting of the XRD and increase in the GO interlayer space confirmed the increase in the confined PEG between the GO nanosheets. Applying no washing procedure meant that the attached polymer on the GO nanosheets surfaces and showed a significant shift in the crystalline peak of the hybrids.

After reducing the mixing time from 192h to 72h, then to 24h, the XRD peak of nanohybrids shifted from 11.1^{o} of GO to 6.6^{o} corresponding to an increase in the interlayer space of 0.79 to 1.33 nm that showed increasing the amount ratio of confined polymer between the GO nanosheets, whereas an interesting peak appeared between 14^{o} - 24^{o} for the first time in this study, which was represented by attaching the PEG on the GO nanosheets surface of the N192h-0w. This peak of PEG confirmed the adsorbed PEG on the GO nanosheets, whereas the intercalated PEG peak between the GO nanosheets was amorphous due the strong governed of the GO nanosheets. This amorphous PEG produced an increase in the interlayer spacing of GO nanosheets, as discussed above, whereas the adsorption PEG peak presented a clearer, wider and higher intensity when reducing the mixing time to 72 h of the N72h-0w compared with N192h-0w and N24h-0w.

Increasing the PEG mixing ratio and reducing the mixing time were associated with the increase of both ratios of the confined polymer between the GO nanosheets and the adsorbed PEG on the GO nanosheets surface, the latter of which presented the peaks of semicrystalline PEG for washing samples only. The polymer was strongly restricted between the GO nanosheets. Appling no further washing procedure, the increase in the mixing ratio of PEG and reduction the mixing time showed notable improvement in adsorption behaviour, where the interlayer spacing increased by 56 nm compared to GO, whereas it increased by 0.15 nm of a hybrid without washing procedure.

Figure 3-5 (C) and (D) showed the second heating and second cooling cycles of the PEG and hybrids. In Figure 3-5 (C), the 10k PEG curve exhibited a sharp melting peak at 62 ^{o}C. In the hybrids, the crystalline peak of PEGs disappeared in all samples from both the effect of the mixing time and polymer molecular weight sections as shown in Figure A3-1 (see appendix of chapter 3). Because the long mixing time and washing procedure were associated with removing the adsorbed polymer from the GO nanosheet surface in these hybrids, whereas the 2D-layers GO strongly geometric restricted the remind PEG as amorphous [189]. Therefore, most of the polymers are confined between the GO nanosheets as absorbed polymers, in agreement with Wang et al. [230], who reported that XRD crystalline peaks were presented in the PEG/GO hybrids with ratio of PEGs more than 60 wt.% adsorption ratio [230]. Also, it matched the finding of the Barroso-Bujans, and co-authors [74,169,188,189], which that showed no sign of melting peaks for the PEO/GO and PEO/RGO hybrid nanomaterials.

Abroad melting peak at 52.7 ^{o}C was present after increasing the PEG:GO mixing ratio from 1.5:1 to 3:1 and applying no washing procedure, where this melting peak confirmed the adsorption of PEG on the GO nanosheets surface of the N192h-0w. Reducing the mixing time from 192 h to 72 h presented a sharp and significant melting peak at 58.5 ^{o}C of the N72h-0w, which was the biggest melting enthalpy compared to other hybrids. The DSC result of N72h-

0w confirmed the FTIR and XRD results, which showed the higher intensity peaks of the adsorbed PEG in this sample. However, further reducing the mixing time to 24 h exhibited shifting of the melting peak area to 60 ^{o}C, which presented a broad DSC peak of the N24h-0w. The DSC results of no washing hybrids confirmed the XRD results, which showed the crystalline peaks of the adsorption PEG. Generally, the melting transition peaks of the hybrids were shifted toward lower values comparing with PEG 10k. The decreasing in the melting peak (T_m) of the samples were related to the contribution of the high amount of GO nanosheets that showed more heterogeneous nucleation sites in the hybrids [189]. Moreover, the adsorption PEO is considered as free surface attached and repulsive interfaces that enhanced the chain mobility and reduced T_m [126]**.**

The chain motions of the PEG were restricted due to the stronger interactions with the 2D GO nanosheets with a higher specific surface area than the interaction between polymer particles. This led to a reduction in the melting temperatures of the hybrids. A decrease in the T_m value was reported in the nanocomposites with an increase the graphene ratio [74,169]. However, applying the increased mixing ratio of the PEG, no further washing procedure and reduced mixing time presented the melting peaks of the PEG for the first time in the hybrids and showed an important enhancing of the melting temperature from 52.7 to 60 ^{o}C of the nanohybrids.

Table 3-2 summarizes the melting peak temperature (T_m), melting enthalpy (ΔH_m), crystalline peak temperature (T_c), crystalline enthalpy (ΔH_c) and crystallinity. The percentage of crystallinity (X_c) of the PEO as bulk or in nanohybrids were calculated from the following equation (3-1) [238]:

$$X_c = \Delta H_m (T_m)/(1-wGO)\Delta H^o_m (T^o_m) \quad (3\text{-}4)$$

where ΔH_m (T_m), ΔH^o_m (T^o_m) and w are the specific heat enthalpy of melting of the hybrids, the 100% crystalline of PEO (205 J g^{-1}) [224] and the mass fraction of GO in composites, respectively.

Table 3-2: The DSC heating and cooling scan temperatures summary of PEGs and the hybrid nanocomposites.

Samples Temperature ^oC	PEG 10k	N192h-0w	N72h-0w	N24h-0w
T_m	62.2	52.7	58.5	60
ΔH_m J g^{-1}	141	6.5	15.6	9.2
T_c	42.9	22.8	36.7	42.3
ΔH_c J g^{-1}	138	0.019	0.94	0.08
Crystallinity (X_c) %	69	12	20	14

In Figure 3-5 (E), the TGA results showed the adsorption amount of the PEG on the GO nanosheets. The results confirmed that most of the PEGs were confined between the GO nanosheets of the samples from N1h to N-1.5-192h-0w because these hybrids presented without any sign of the XRD and DSC peaks of the adsorption PEG with no washed hybrids. The adsorption amount of PEG exhibited a significant increase from 16 wt.% of N-1.5-192h to 23 wt.% of N-1.5-192h-0w without applying washing procedure, whereas increasing the PEG mixing ratio to GO from 1.5:1 to 3:1 of N192h-0w showed another increase from 23 wt.% to 26 wt.% compared to the N-1.5-192h-0w that presented of the XRD and DSC melting peaks of the adsorbing polymer of this sample, where the N192h-0w presented both of the absorbed polymers between the GO nanosheets and adsorbed them on the GO nanosheets surface at the same time.

Moreover, the mixing time was reduced from 192 h to 72 h, then to 24 h without washing procedure. Polymer adsorption amounts presented a significant enhancement from 23 wt.% to 38 wt.%, while reducing the mixing times from 192 h to 27 h, whereas it was reduced

again to 32 wt.% when reducing the mixing time to 24 h of the N192h-0w, N72h-0w and N24h-0w, respectively. The best adsorption polymer ratios and higher intensity peaks exhibited N72h-0w with 72 h mixing time, which was the optimum mixing time, in compared to the other hybrids. The N72h-0w strongly agreed with the FTIR, XRD and DSC results of this sample, given above.

The peak of degradation temperature (T_d) in Figure 3-5 (E) showed a thermal stability of the samples within the range 30 ^oC to 130 ^oC. The first T_d of hybrids shifted from 223 ^oC of GO to 225 ^oC of all the three washing hybrids, whereas it shifted to 230 ^oC or non-washed hybrids. While, the second T_d significantly improved from 309 to 355 ^oC and 363 ^oC, where all three used no washing hybrids, when releasing the oxygen functional groups into the graphene oxide nanosheets indicated for decreasing the mass ratio in the samples in the first section, the samples showed an improvement in thermal stability behaviour due to an increase in the residual carbon of the samples in the range 400–550 ^oC by the contribution of GO.

The no further washing procedure results observed two main important findings. Firstly, the rapid PEG adsorption reached 24 h mixing time. Secondly, the PEG adsorption was considerably enhanced by up to 65% compared to the samples that were washed and not washed at the same 72 h mixing time, mixing ratio and molecular weight. The PEG attached to the GO nanosheets surface with physical bonds. This weak physical interaction was easily lost even with a weak external effect, as clearly presented when applying the long mixing time 192 h or the washing procedure or both. For examples, using both the long mixing time 192 h and washing procedure showed a reduction the adsorption amount of the PEG to 18 wt.% of the N192 samples and vice versa.

The attached PEG interacted with the GO nanosheets in two main positions confined between the GO nanosheets and adsorbed on the GO nanosheets surface. For instance, N-1.5-192h-0w presented 23 wt.% as the total ratio of the PEG in this sample, obtained by TGA

results. This samples presented without any sign of the semicrystalline PEG peaks in the diffraction behaviour, glass and melting transition, whereas the XRD peaks were shifted by the confined PEG between the GO nanosheets. This finding confirmed that all PEG ratios in this sample were confined between the GO nanosheets.

In comparison, applying no further washing procedure, increasing only the mixing ratio of PEG to GO from 1.5:1 to 3:1 and reducing the mixing time shifted of the diffraction peak of GO and significant crystalline peaks of PEG in XRD traces. This finding presented two XRD peaks; the first was related to GO and was shifted by the confined PEG between the GO nanosheets and the second peak related to the adsorption PEG on the GO surface, whereas the melting peaks also corresponded to absorbing the PEG on the GO nanosheets surface. This finding confirmed the two type of attachment of the PEG in this sample. Firstly, the confined PEG between the GO nanosheets showed the shifted XRD peaks of the GO and represented the main ratio of PEG. Secondly, the adsorbed PEG on the GO nanosheets showed the crystalline and melting peaks. According to these findings, the PEG in the washed samples was confined between the GO nanosheets, whereas the other samples presented two attaching types of PEG.

Generally, PEG was successfully adsorbed on the GO nanosheet surface in the non-washed hybrids, where the adsorption amount was improved by 44% without further washing procedure, 13% through increasing the mixing ratio of the PEG, 46% through reducing the mixing time for 192 h to 72 h and 73% for applying all these parameters together.

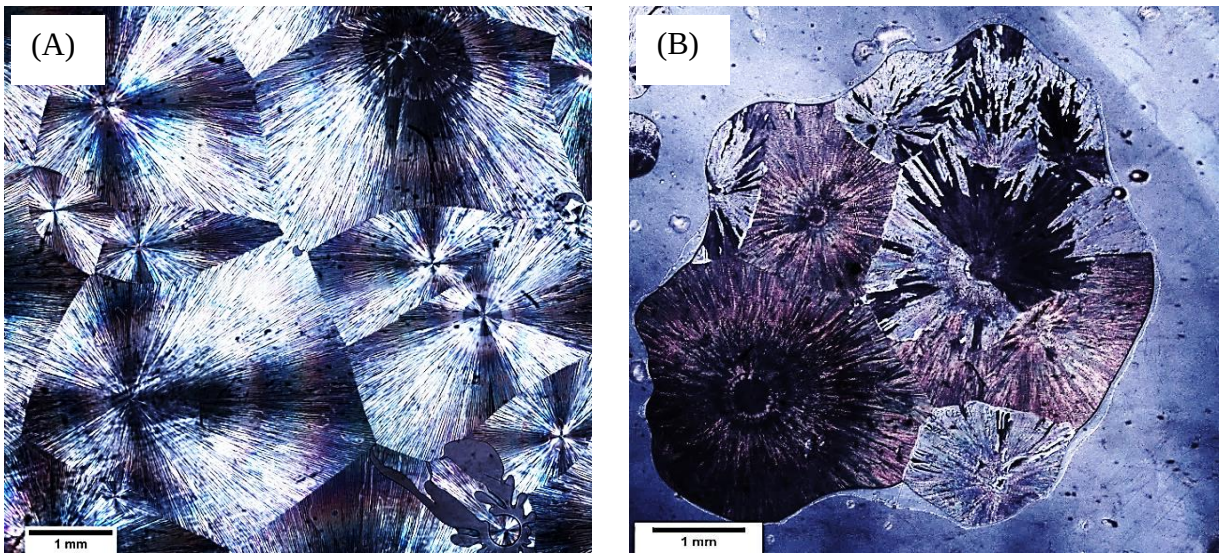

Figure 3-6: Optical light microscopy (OLM) images of (A) PEG 10k and (B) N72h-0w.

The effect of GO on the PEG crystalline behaviour is an important issue that was further investigated by preparing the transparency sample similar to N72h-0w hybrids as shown in Figure 3-6. Nucleation and crystal growth is the two-stage of the crystal formation that influences by the nanofillers. These nanofillers are effective nucleating agents on the linear growth rate and the crystallization rate of polymer in matrix [239]. The significant influence of the interface interaction of GO nanosheets could restrict the PEG crystallization, in agreement with the literature [240]. Tong et al. [240] reported that the PEG spherulite growth rate was slower during the crystallization of polymers on the surface of GO nanosheet.

The OLM images clearly indicate that the neat PEG crystallite size was not showed large difference than PEG on GO nanosheets as shown in Figure 3-6. This could relate to the weak interaction between the PEG and GO using melting methods, whereas these results different from the DSC results, which showed a reduction in the melting temperature peak from 62 ^{o}C to 58 ^{o}C and crystallinity of N72h-0w, compared to neat PEG. A similar phenomenon with GO/polyurethane composites was reported by Cai et al. [223], where the crystal size of polyurethane was smaller, with the incorporation of GO, where the growing of crystallizing on the nucleation agents led to changes the polymer properties, such as thermal,

mechanical, optical and physical, through the incorporation of inorganic fillers [240,241]. The load transferring efficiency from the semicrystalline polymer to the filler depended on the interfacial interaction between the filler and matrix properties [242].

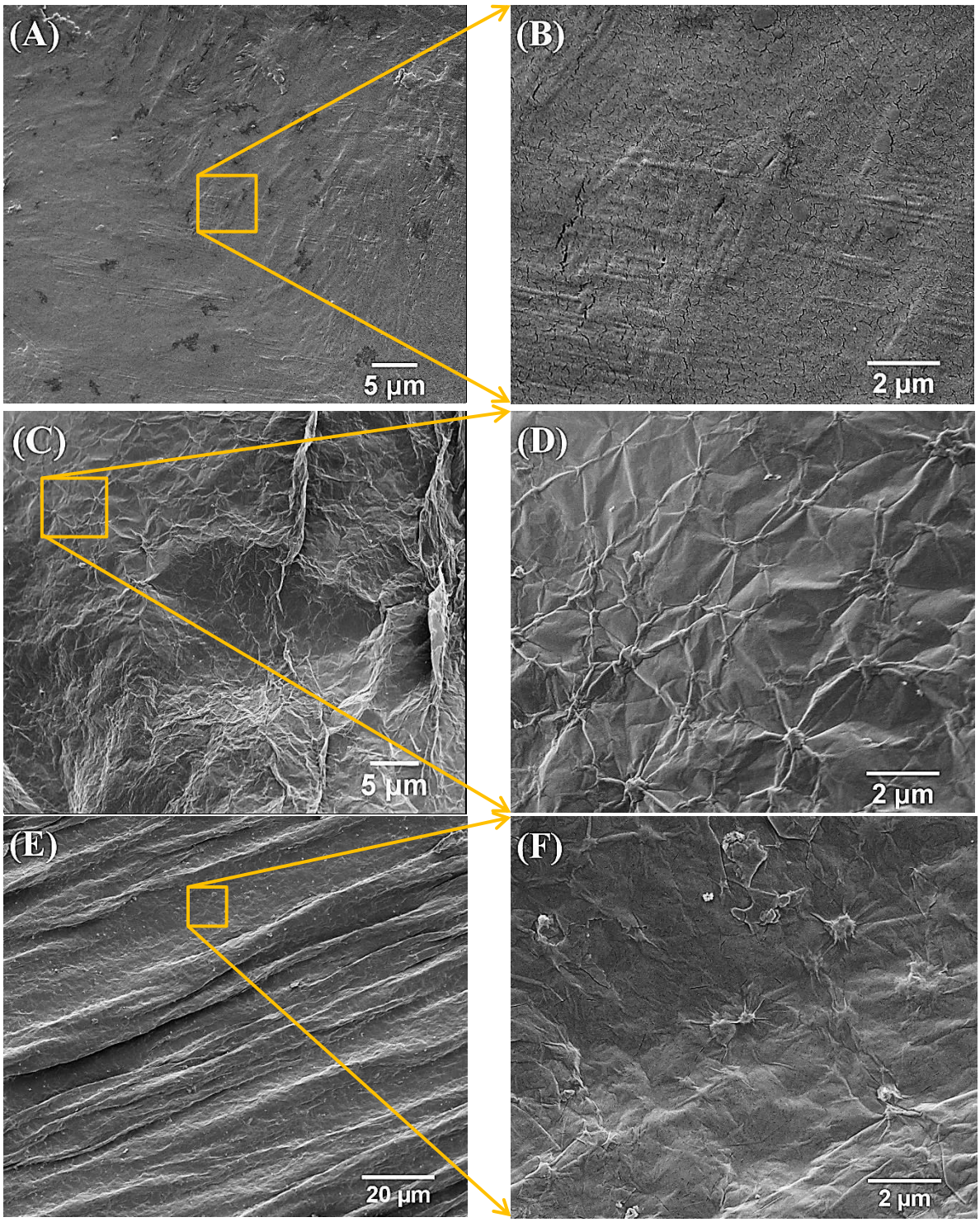

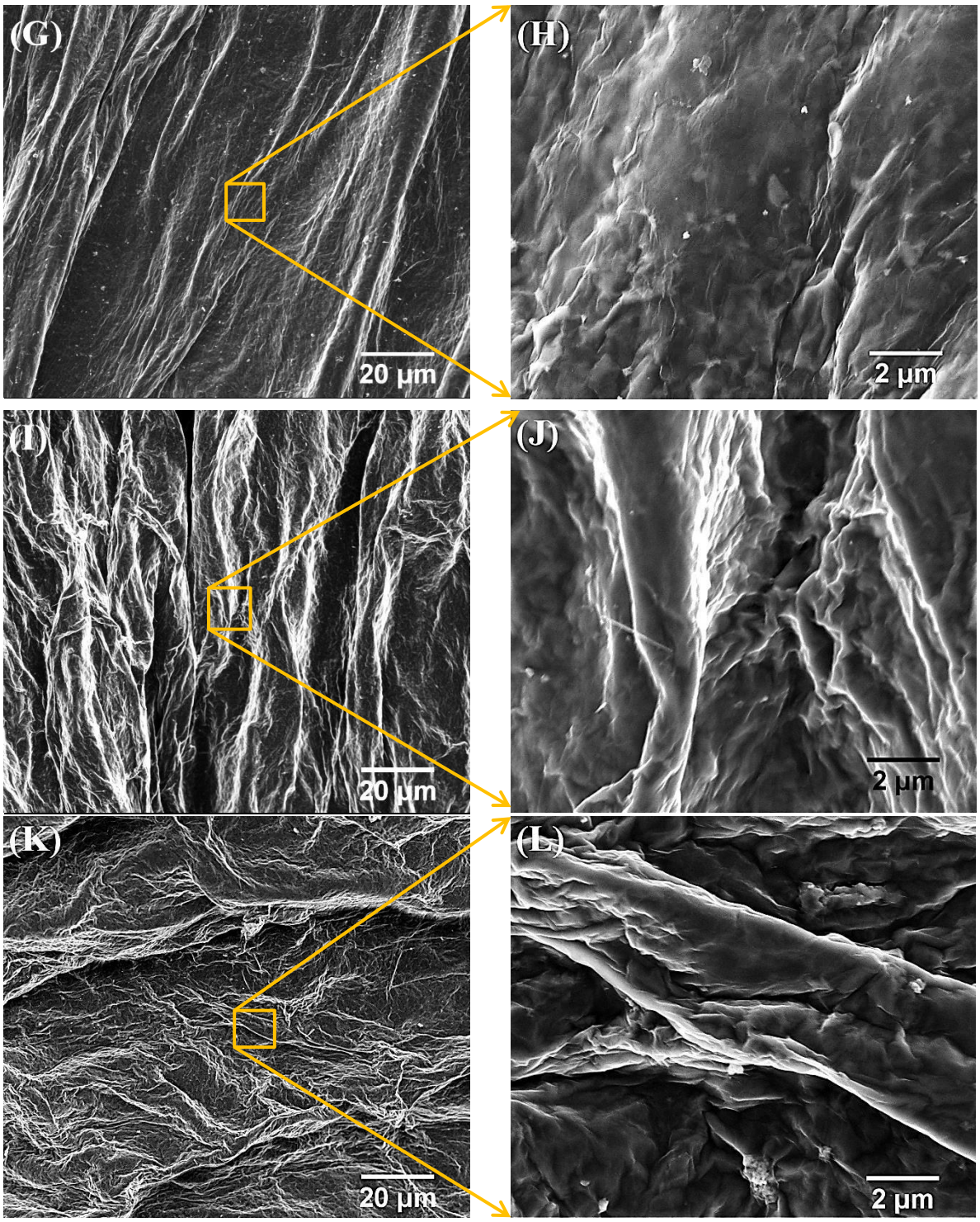

Figure 3-7: SEM images of the fracture surface of (A and B) GO sheet, (C and D) 10k PEG, (E and F) N192h, (G and H) N192h-0w, (I and J) N72h-0w and (K and L) N24h-0w.

Figure 3-7 shows SEM images of the fracture surfaces of GO, 10k PEG, N192h, N192h-0w, N72h-0w and N24h-0w, respectively. The images illustrate the changing of the fracture surface of nanohybrids compared to the GO and PEG. Figure 3-7 (A and B) presented

a smooth surface with many small cracks on neat PEG, whereas Figure 3-7 (C and D) clearly showed the flaky morphology surface of GO. The fracture surface of N192h presented differently to both PEG and GO, where the fracture surface observed shrinkage behaviour in Figure 3-7 (E), whereas the magnified image in Figure 3-7 (F) showed similar behaviour, as of the GO nanosheets were covered by thin layer of PEG because the long mixing time and washing procedure removed most of the adsorption PEG from the GO surface.

However, in Figure 3-7 (G and H), the flaky fracture surface was turned into densely packed sheets of the N192h-0w surface because the polymer covered most of the GO nanosheet surface. Moreover, the adsorbed PEG was clearly observed on the GO nanosheets surface of N72h-0w as shown in Figure 3-7 (I and J). N24h-0w showed much shrinkage on the surface due to the absorption of the PEG on the covering GO nanosheets. The PEG presented clearly on the GO nanosheets as an attachment particle of PEG. The SEM image clearly showed the N24h-0w presenting more polymer compared to N192h in agreement with TGA results. The SEM image strongly supported and agreed with the above results that presented the best adsorption amount of PEG on GO nanosheets (38 wt.%) and the sharp DSC melting peaks at 58.2 ^{o}C of N72h-0w, compared to other hybrids.

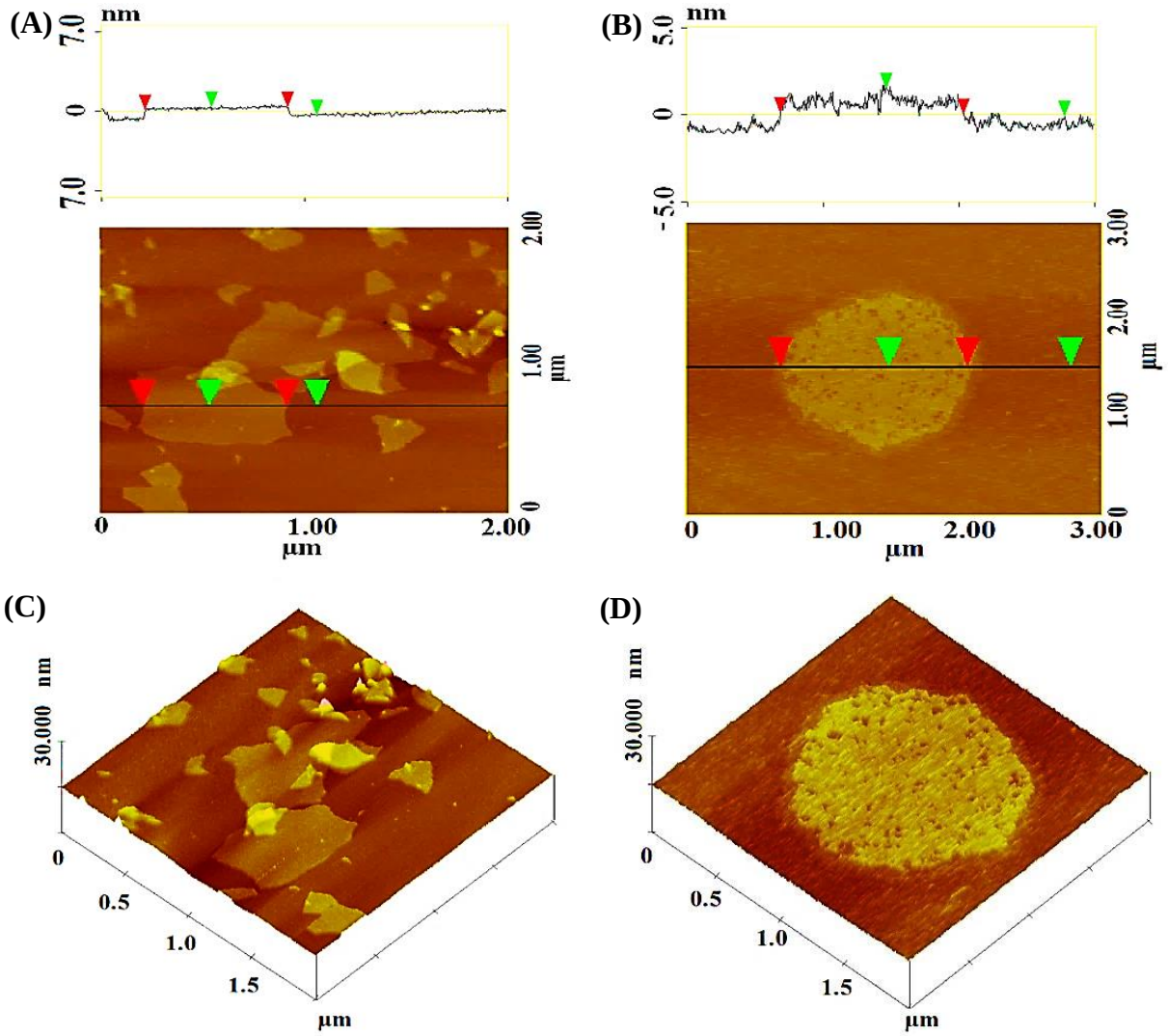

Figure 3-8: 2D and 3D AFM images of the (A, C) GO nanosheets and (B, D) N192-0w.

In Figure 3-8, the 2D and 3D AFM images characterised the morphology and thickness of GO and N192-0w. Figure 3-8 (A) shows the single sheets of GO with an average thickness of 0.77 nm, which was close to XRD results. The AFM image showed different shape and size of GO nanosheets that were between 1840 nm to 150 nm. In Figure 3-8 (B), the surface roughness of N192-0w with a wrinkle structure is revealed. The thickness increases from 0.77 nm of GO to 1.58 nm of the N192h-0w due to adsorbed PEG onto the GO nanosheets, where the thickness of adsorbed PEG was 0.405 nm on each side of the GO nanosheet. The 3D AFM image also revealed that the surface of the GO nanosheets is smooth, as shown in Figure 3-8 (C), whereas the rough structure with wrinkle structure presented with

the absence of beads on the hybrid surface, proving that PEG was adsorbed on the GO nanosheets, as shown in Figure 3-8 (D). These AFM images presented other clear evidence and support the results above, showing successful adsorption of PEG on the GO nanosheets.

3.4 Conclusions

The adsorption behaviour of the polymer onto GO nanosheets is very important for understanding the interfacial interaction effect of GO nanosheets on the structures and properties of nanohybrids. A serial of hybrids was prepared using methods with different parameters, such as mixing time, polymer molecular weight, mixing ratio and washing procedure. The FTIR results confirmed the successful preparation of GO and the absorption of PEG on GO nanosheets. The XRD peak of GO shifted due to the intercalation of PEGs between GO nanosheets and presented the XRD peaks of absorption PEG of not-washed hybrids. The not-washed hybrids only presented a melting temperature of PEG. The thermal behaviour of the hybrids was improved due to the incorporation of GO nanosheets.

The absorption PEG accrued rapidly, whereas the long mixing time such as 192 h shows a negative role on the absorption polymer behaviour. The higher molecular weight significant improved the absorption amount from 0.8 wt.% to 18 wt.%. All the washed samples have only confined intercalated polymers between the GO nanosheets, indicating the long mixing time and two washing procedure were associated with removing the adsorbed polymer from the GO surface due to weak Van der Waals and hydrogen interaction.

Increasing the polymer mixing ratio essentially improved the absorption amount of PEG, which increased from 16 wt.% to 26 wt.%. Without future washing procedure, the adsorption polymer amount was enhanced from 16 wt.% to 23 wt.%. Reducing the mixing time was another important factor for improving the adsorbed polymer. Applying these parameters at the same time succeeded in achieving the adsorbing polymer and increasing the

adsorption amount up to 38 wt.%. This investigation showed significant factors that can influence the interfacial interaction between the polymer and GO and how this could be improved. The optical microscopy image confirmed the reduction of the crystallite size of the PEG, where GO restricted the PEO chain. The SEM images showed the N72h-0w presenting better adsorption behaviour of PEG compared to other samples. The AFM images presented strong evidence of 0.405 nm of the PEG adsorbed on each side of the GO nanosheet. The absorption amount was increased by up to 1700% when increasing the PEG molecular weight from 1k to 100k.

Overall, the PEG was successfully adsorbed on the GO nanosheet surface and the adsorption amount was improved by 46% through reducing the mixing time for 192 h to 72 h, by 44% without a further washing procedure, by 13% through increasing the mixing ratio of the PEG and 73% for applying all these parameters together.

Chapter 4: Effect of the polymer functional group on the adsorption behaviour of polymer/graphene oxide nanosheets

4.1 Introduction

According to the previous chapter, various parameters strongly affected the surface adsorption behaviour of the polymer and other important factors that could bring a better understanding including the functional groups of the polymer matrix, which significantly affect the compatibility of the nanofiller with the polymer matrix, and the properties of polymer/graphene oxide nanocomposites [204]. A stable and homogeneous dispersion is required of the nanofiller in the polymer matrix to produce good interfacial interactions, which is dependent on this compatibility [199]. According to the review in section 2.7.2, most of the investigations have been focused on functionalizing the graphene nanofillers to improve the homogeneity of the filler dispersion [200].

This work aims to investigate the effect of functional groups of polymers on their adsorption behaviour onto GO nanosheets. Polymers with similar backbones but having different functional side groups were used as the polymer models, namely poly(methyl methacrylate) (PMMA), poly(methyl methacrylate-co-methacrylic acid) (PMMA-co-MAA), and poly (methacrylic acid) (PMAA). The possessing method was optimised from the third chapter by considering the best parameter and results. GO was firstly prepared and then mixed with these polymers separately, in order to prepare the polymer/GO hybrids. The resulting samples were characterised by various techniques, such as FTIR, XRD, TGA, DSC, SEM and a drop shape analyser (contact angle measurement) (CA).

4.2 Experimental section

4.2.1 Materials

Natural Graphite powder (≤150 μm), PMMA $(C_5O_2H_8)_n$ (35000 Mw), PMMA-co-MAA $[-CH_2C(CH_3)(CO_2CH_3)-]_m[-CH_2C(CH_3)(CO_2H)-]_n$ (34000 Mw), PMAA $(C_4H_6O_2)_n$ (10000-15000 Mw) and N,N-dimethylformamide (DMF, 98.8% w/w) were purchased from Sigma-Aldrich company, UK. Other materials were the same as used in the previous chapter in section 3.2.1.

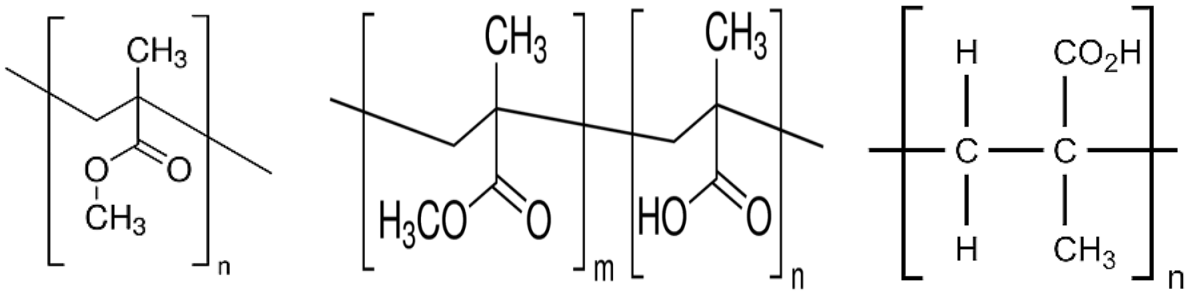

(A) **(B)** **(C)**

Figure 4-1: The repeat unit of (A) PMMA, (B) PMMA-co-MAA and (C) PMAA.

4.2.2 Synthesis and purification of graphene oxide

This was described in the previous chapter in section 3.2.2.

4.2.3 Surface adsorption of polymers onto graphene oxide nanosheets

Three polymers, PMMA, PMMA-co-MAA and PMAA with different functional groups were mixed with the GO nanosheets. Firstly, the polymer was dissolved in DMF at a concentration of 4.2 wt/vol %, whereas the GO was dispersed in DMF with a concentration of 0.1 wt/vol %. Secondly, it was stirred for 72 h by a magnetic stirrer at room temperature then centrifuged for 20 min at 8793 g-force to remove the excess solvent. Two samples were prepared from each polymer, which one was further washed with DMF and the other was not washed. The hybrids were dried for 15 hours at 40 ^oC under 0.1 MPa pressure in a vacuum oven until the weight of samples became constant. The same method was applied to all the prepare

polymer/GO hybrid samples. The preparation methods and sample denotations of hybrids are summarized in Table 4-1.

Table 4-1: The preparation methods and sample denotations of hybrids.

Samples ID	Mixing Ratio P:GO	Mixing Time	G-force / Time g/ min	Further Washing
PMMA/GO-w **PMMA-co-MAA/GO-w** **PMAA/GO-w**	3 : 1	72 h	8793/ 20	Yes
PMMA/GO **PMMA-co-MAA/GO** **PMAA/GO**	3 : 1	72 h	8793/ 20	No

4.2.4 Characterization

Contact angle measurement is one of the most sensitive techniques used to analyse the outer layer of polymer surfaces [251]. The more hydrophilic material surface has a low contact angle [229,252]. The contact angle is formed by the intersection of the liquid-solid interface and the liquid-vapour interface of a liquid drop resting on a flat, horizontal solid surface. The Young of the contact angle defines the relationship between the surface tension of the liquid and that of the solid as well as the interfacial tension between the phases. From the wetting processes were described by this relationship the Young contact angle θ in formula [243]:

$$cos\,\theta = \frac{\sigma_s - \gamma_{sl}}{\sigma_l} \qquad (4\text{-}1)$$

where σ_s, σ_l and γ_{sl} mean the surface tensions σ of the solid, liquid and the interfacial tension, respectively. The prepared samples was placed directly to measure the contact angle using a drop shape analyser (contact angle), which is a model type DSA100 (KRUSS, Germany) at 21 ± 0.5 ^{o}C and a relative humidity of 50%. Images of 2 μL distilled water droplets on the membrane surface were captured after reaching a constant value. The data were recorded ten times every 3 seconds after the water drop was placed upon the membrane

surface. The average value of these ten measurements was recorded. Other characterization procedures were explained in the previous chapter in section 3.2.4.

4.3 Results and discussion

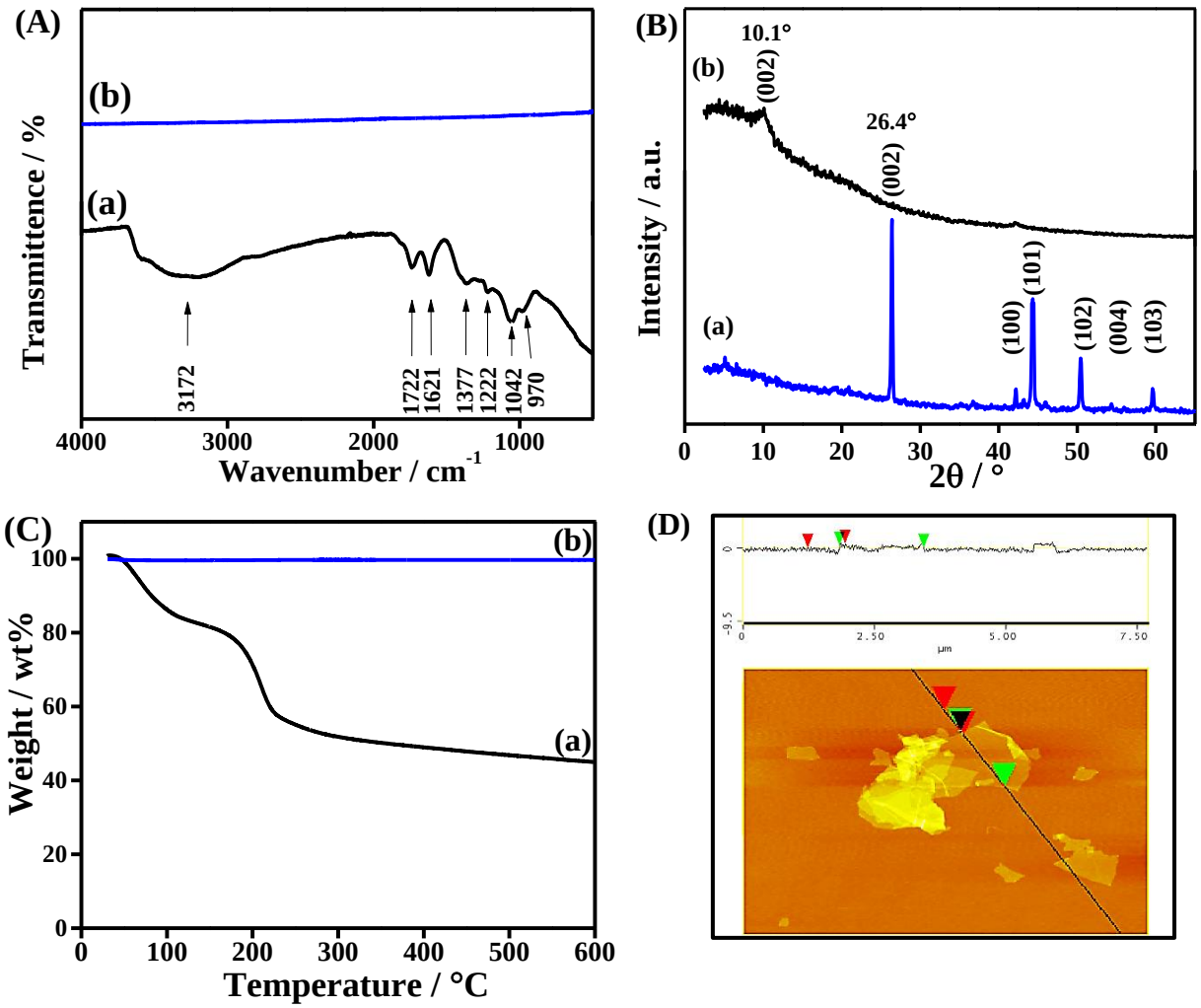

Figure 4-2: The characterization of graphite and GO: (A) FTIR spectra, (B) XRD traces and (C) TGA curves of (a) GO and (b) graphite. (D) AFM image of GO.

Figure 4-2 (A) shows the FTIR spectra of GO nanosheets compared with graphite. New functional groups presented of GO due to oxidizing the graphite using modified Hummer's method [25]. GO illustrated new functional groups peaks on the graphene oxide, which were at 3172, 1726, 1621, 1378, 1222, 1042 and 970 cm^{-1} wavenumbers, corresponding to O-H

stretching (free water), COOH stretching, C=C stretching, C-O stretching, O-H bending, C-O-C stretching and C-O cm^{-1} stretching functional groups, respectively [25,244]. In Figure 4-2 (B), The XRD pattern corresponding to graphite μm provided strong peaks at the (002), (100) (101), (102), (004) and (103) peaks, which represent perpendicular the of natural graphite hexagonal planes with (c-axis) direction and impurity ratio, that matched the literature results [245,246]. The (002) peak of natural graphite shifted from $2\theta = 26.4°$ to $2\theta = 10.1°$ corresponding to interlayer spacings of 0.33 nm and 0.87 nm of graphite and GO respectively, in agreement with the literature [25,244]. The interlayer spacing increased due to the attachment of the functional groups on the GO nanosheets.

TGA results in Figure 4-2 (C) shows the thermal degradation of GO compared to graphite, where the GO lose about 23% of the total dry mass between 180-220 ^{o}C due to the degradation of the epoxide and hydroxyl, carbonyl and carboxyl groups [244]. The GO presented the derivative weight peak at 67 ^{o}C and 217 ^{o}C, which corresponded to a loss of O-H group and oxygen functional groups during the main degradation of the mass, respectively [19,229]. The AFM image shows the morphology and thickness of GO nanosheets. The lateral size of the GO nanosheets was between ~200 nm to 1660 nm to the average thickness was 0.88 nm, which was close to XRD results. The GO nanosheets were successfully prepared, as confirmed by characterization results above.

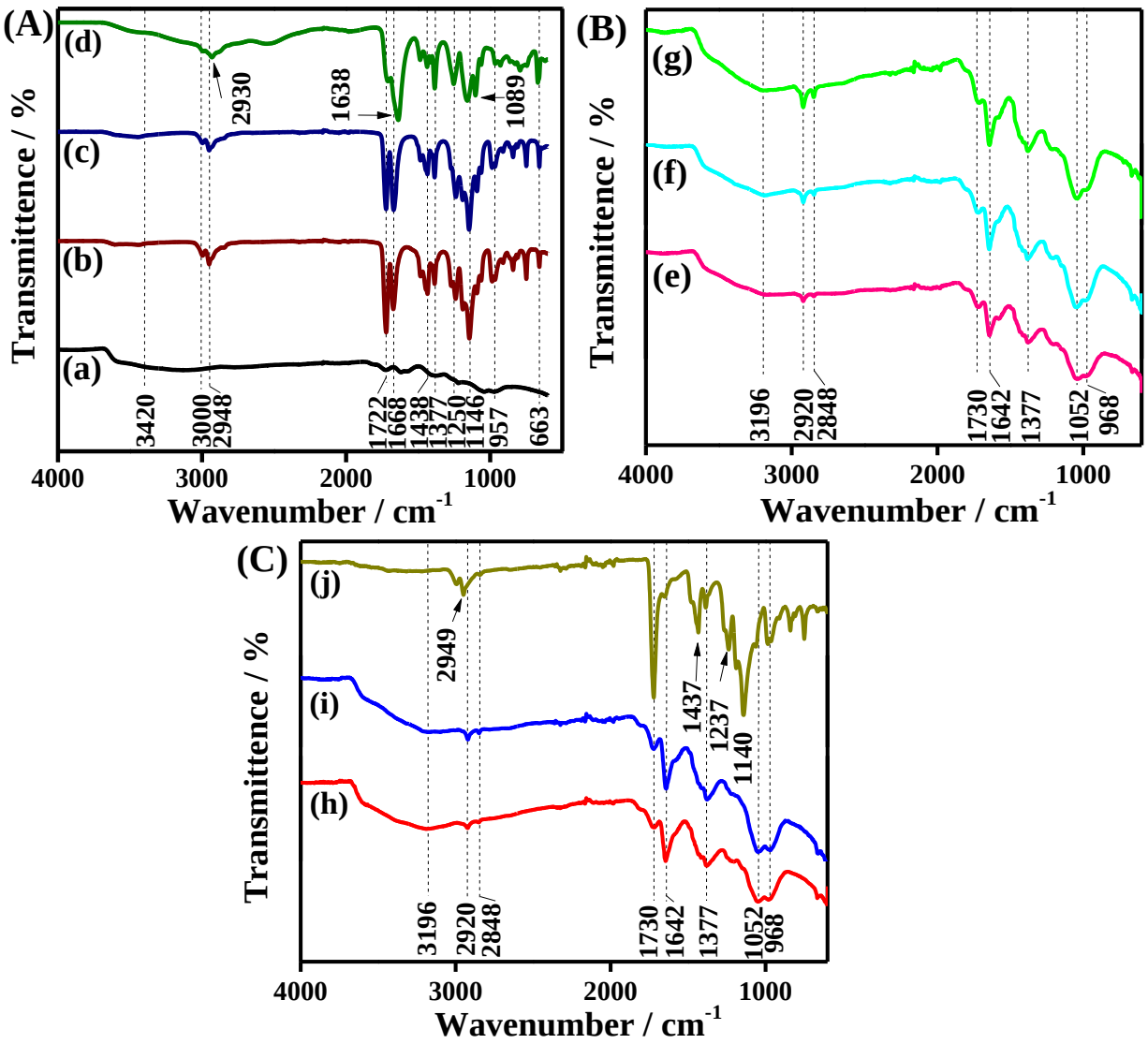

Figure 4-3: FTIR spectra of polymer/GO hybrids:(A) polymers (a) GO, (b) PMMA, (c) PMMA-co-MAA, (d) PMAA), (B) washed samples ((e) PMMA/GO-w, (f) PMMA-co-MAA/GO-w, (g) PMAA/GO-w)) and (C) non-washed samples ((h) PMMA/GO, (i) PMMA-co-MAA/GO and (j) PMAA/GO)).

Figure 4-3 (A) shows the FTIR spectra of the polymers and GO nanosheets. The bonds CH_3, COOH, C=C, C-H, C-O-H, C-O-C, C-O and -C-H of 3000 - 2948, 1722, 1668 - 1384, 1377, 1250, 1146, 957 and 663 cm^{-1} wavenumbers, respectively presented of the PMMA and PMMA-co-MAA polymers. PMMA-co-MAA in curve c illustrated the same FTIR spectra behaviour of PMMA in curve b. that was related to the former consists of PMMA and few amount of MAA unit as a 1:0.016 weight ratio of PMMA:MAA units,

whereas the most characterization peaks of PMAA illustrated at different peak positions compared to the other two polymers. For instance, the bonds O-H, C-H, C=C and C-O presented at 3420, 2930, 1638 and 1089 cm^{-1} in curve d.

Figure 4-3 (B) shows FTIR spectra of the hybrid nanomaterials, which prepared from mixing polymers with GO. These samples were washed to remove the excess polymer. The hybrid nanomaterials illustrated characterization peaks that related to both GO and polymers, where the general behaviour of the washed samples is similar to GO behaviour, for instance, a broad peak of the O-H and C=O bonds appeared in the washed hybrid nanomaterials, which are related to the GO, whereas the polymer presented adsorption peaks of polymers onto GO nanosheets, where the most of these adsorption peaks significantly shifted from 3000 to 2920, 2948 to 2848, 1668 to 1642 and 1438 to 1377 cm^{-1} of all washed hybrid nanomaterials compared to neat polymers in Figure 4-3 (A). This shifting in the adsorption peaks of polymers was related to physical interaction between polymers and GO nanosheets, in addition to the strong bond peaks of absorption polymers that presented at 2920, 1730, 1642, 1377 and 1052 cm^{-1} in the hybrid nanomaterials, which other confirmed of the successful adsorption of the polymers onto GO nanosheets. These peaks displayed the strong intermolecular interactions (hydrogen bonding) between C-H or COOH of methacrylate group of PMMA and with polar functional groups, such as C=O and -OH of GO, for instance, the peaks at 2848, 1642 and 1377 cm^{-1}. Interestingly, the vibration intensity was notably increasing of the polymers contained addition functional groups, which were PMMA-co-MAA/GO-w and PMAA/GO-w, compared with PMMA/GO-w of the curve (g), (f) and (e), respectively. PMAA/GO-w demonstrated the highest intensity of the adsorption peaks of PMAA than other two polymers.

Another important finding that the adsorption peaks of polymers significantly reduced in vibration intensity compared with peaks of neat polymers in Figure 4-3 (A). That supposes the washing procedure influenced the intensity peaks of the adsorption polymer onto the GO

nanosheets. It suggested remove of the most adsorption polymers from GO nanosheets during the washing procedure, but a clear sign of adsorption polymers still onto GO nanosheets.

Therefore, further samples were prepared without washing procedure to investigate that effect on the adsorption amounts of polymer on GO nanosheets as shown in Figure 4-3 (C). The FTIR spectra of hybrid nanomaterials exhibited strong adsorption peaks of polymer on GO nanosheets. That led to significant increase in the vibration of the most bond peaks compared to the washed samples in Figure 4-3 (B). The PMMA-co-MAA/GO exhibited the higher intensity of adsorption bond peaks compared with PMMA/GO expect O-H bond, whereas the PMAA/GO presented without O-H bond peak, which is related to GO.

In addition, C-H bond shifted from 2930 to 2949 and 1377 to 1437 cm^{-1} of PMAA/GO compared with PMAA. The PMMA/GO and PMMA-co-MAA/GO illustrated the same behaviour of their washed samples with increasing of the vibration of bonds, whereas PMMA/GO presented the highest intensity vibration of the adsorption peaks at 2949, 1730, 1437, 1237 and 1140 cm^{-1} than other samples. That indicated a strong physical interaction between GO and PMMA, for instance, the stretching vibration of the C=O bond of carboxylic acid groups in the range of 1730 cm^{-1} and other bindings of C-O, C-O-C and C-OH vibrations were recognized after adsorption on GO nanosheets. This peak in the spectrum for PMAA was much stronger than those in spectra PMMA/GO and PMMA-co-MAA/GO. This indicated better absorbance of PMAA onto the GO nanosheets compared to other samples in both cases washing and not washed hybrids.

Interestingly, the O-H group presented in all washed hybrid nanomaterials, whereas in the not washed samples, it was significantly reduced with functional polymer, where it clear presented of PMMA/GO curve (h), whereas it reduced of PMMA-MAA/GO curve (i) and totally disappeared of PMAA/GO (j). The similar phenomena were presented with vibration intensity of the bond peaks of adsorption polymers, where it was increased of polymer with

the additional functional group. For instance, PMMA-co-MAA showed the higher intensity of than PMMA even with a low ratio of MAA group of the former, whereas the PMAA with MAA group showed the best vibration of the adsorption bond peaks on GO nanosheets among all samples in both cases. Generally, these characterization results confirmed the successful adsorption of the polymers onto the GO nanosheets. The PMAA/GO hybrid showed a number of functional groups and the highest intensity of functional peaks, which suggested a higher degree of order and concentration within the stacks as bonds of PMAA onto GO nanosheets [189,235].

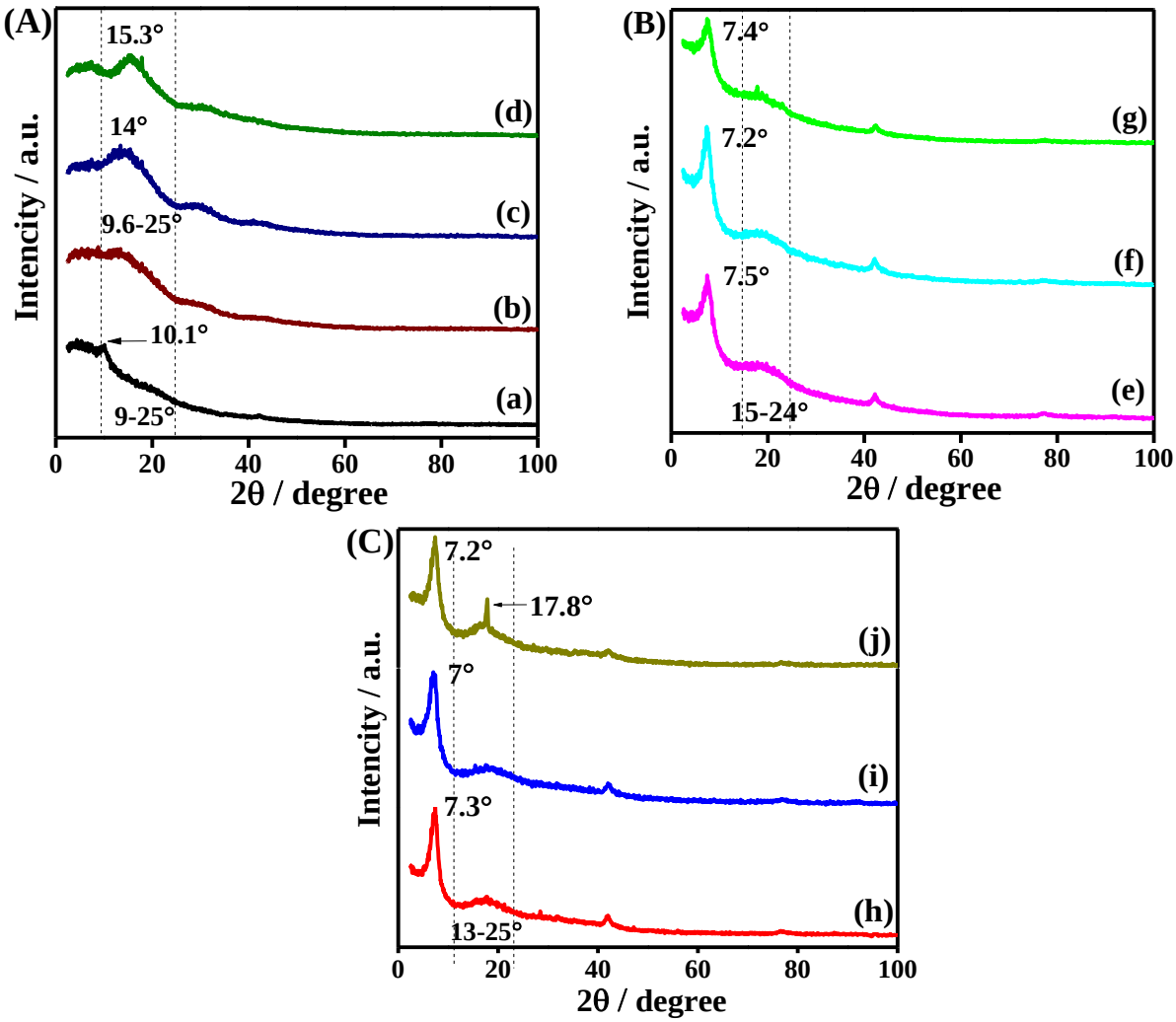

Figure 4-4: XRD traces of polymer/GO hybrids:(A) polymers ((a) GO, (b) PMMA, (c) PMMA-co-MAA, (d) PMAA), (B) washed samples (e) PMMA/GO-w, (f) PMMA-co-MAA/GO-w, (g) PMAA/GO-w) and (C) non-washed samples (h) PMMA/GO, (i) PMMA-co-MAA/GO and (j) PMAA/GO).

Figure 4-4 (A) shows the XRD traces of GO and polymers. The PMMA presented amorphous behaviours between 9.6^{o} - 25^{o}, whereas PMMA-co-MAA and PMAA exhibited crystalline peaks at 14^{o} and 15.3^{o}, respectively. Figure 4-4 (B) illustrates the hybrid nanocomposites that were washed with DMF after mixed GO and polymers. Each washed sample presented two XRD peaks. The first peak was related to (002) GO, which shifted from 10.1^{o} to 7.5^{o}, 7.2^{o} and 7.4^{o} corresponding to increasing in the interlayer space from 0.87 nm of the GO to 1.10, 1.15 and 1.12 nm of PMMA/GO-w, PMMA-co-MAA/GO-w and PMAA/GO-w respectively, whereas the significant second-wide was linked to adsorbed polymers on the surface of GO nanosheets. The later peaks reduced from 9 - 25^{o} to 15 - 24^{o} for all samples. The shifting in the interlayer space of GO nanosheets depended on the increase in the amount of the confined polymer between the GO nanosheets. That means the intercalated polymers between the GO nanosheets led to increasing the distance between GO nanosheets, whereas reduced the area of adsorption peaks of polymers was related to the washing procedure. It removed the most of the polymer from GO nanosheets in agreement with FTIR finding in Figure 4-3 (B).

Appling no further washing procedure on the samples showed a significantly improve in the XRD result as shown in Figure 4-4 (C), where the hybrid nanomaterials also presented two different XRD peaks for each sample, whereas the interlayers space shifted to higher value due to increase in the amount of the confined polymer between GO nanosheets. The crystalline peak, which related to (002) GO, shifted from 7.5^{o} to 7.3^{o}, 7.2^{o} to 7^{o} and 7.4^{o} to 7.2^{o} corresponding to the increase in the interlayer space from 1.10 to 1.13, 1.15 to 1.18 and 1.12 to 1.15 nm of the PMMA/GO, the PMMA-co-MAA/GO and the PMAA/GO respectively, compared to washed hybrid nanomaterials in Figure 4-4 (B). The confined polymer amounts between the GO nanosheets were the main factor involved in this shifting of the crystalline peak of GO to a different position. The area of the second crystalline peak increased from 15^{o} - 24^{o} to 13^{o} - 25^{o} as well as an increase in the intensity of the peaks. This

was another interesting finding that resulted from an increase in the physical attachment of the polymer on the surface of GO nanosheets.

The interlayer space of GO, distance area of adsorption polymers and intensity of peaks increased among the samples in both washed and not washed procedure. That suggested the different amount of absorption polymer between GO nanosheets and adsorption polymer on the surface of GO nanosheets. Therefore, the PMMA-co-MAA/GO showed the biggest interlayer space, which means the highest amount of the confined polymer between GO nanosheets. Even at the low amount of additional functional groups of MAA in the PMMA-co-MAA, that presented a significant shift in the peak position of both absorbed and adsorbed polymer compared with PMMA/GO. It showed more physical interaction with the functional groups of GO, whereas the MAA unit of PMAA showed the most physical bond attaching of PMAA to the surface of GO nanosheets, where the only PMAA/GO exhibited a higher crystalline peak of adsorbed PMAA at 17.8^{o}. This confirmed the best attachment of adsorbed PMAA on the surface of GO nanosheets in agreement with strong adsorption peaks of C=O, C-H and C-O-H of PMAA/GO, which presented in the FTIR spectra curve (j) in Figure 4-3 (C).

Interestingly, the hybrid nanomaterials, which contained polymers with functional groups, exhibited the better absorption and adsorption polymer amount compared with the sample contained PMMA. The amount of adsorbed polymer was influenced by the washed procedure, where no future washing increased the interlayer space by 0.03 nm of functional polymers and improved the peaks area of the adsorbed polymer by 45%, as well as the peaks intensity compared to the washed hybrid nanomaterials. That means the washing procedure reduced the amount of both confined and adsorbed polymers onto the GO nanosheets in strong agreement with the FTIR findings, which showed a reduction in the peaks vibration of the bonds in Figure 4-3 (B).

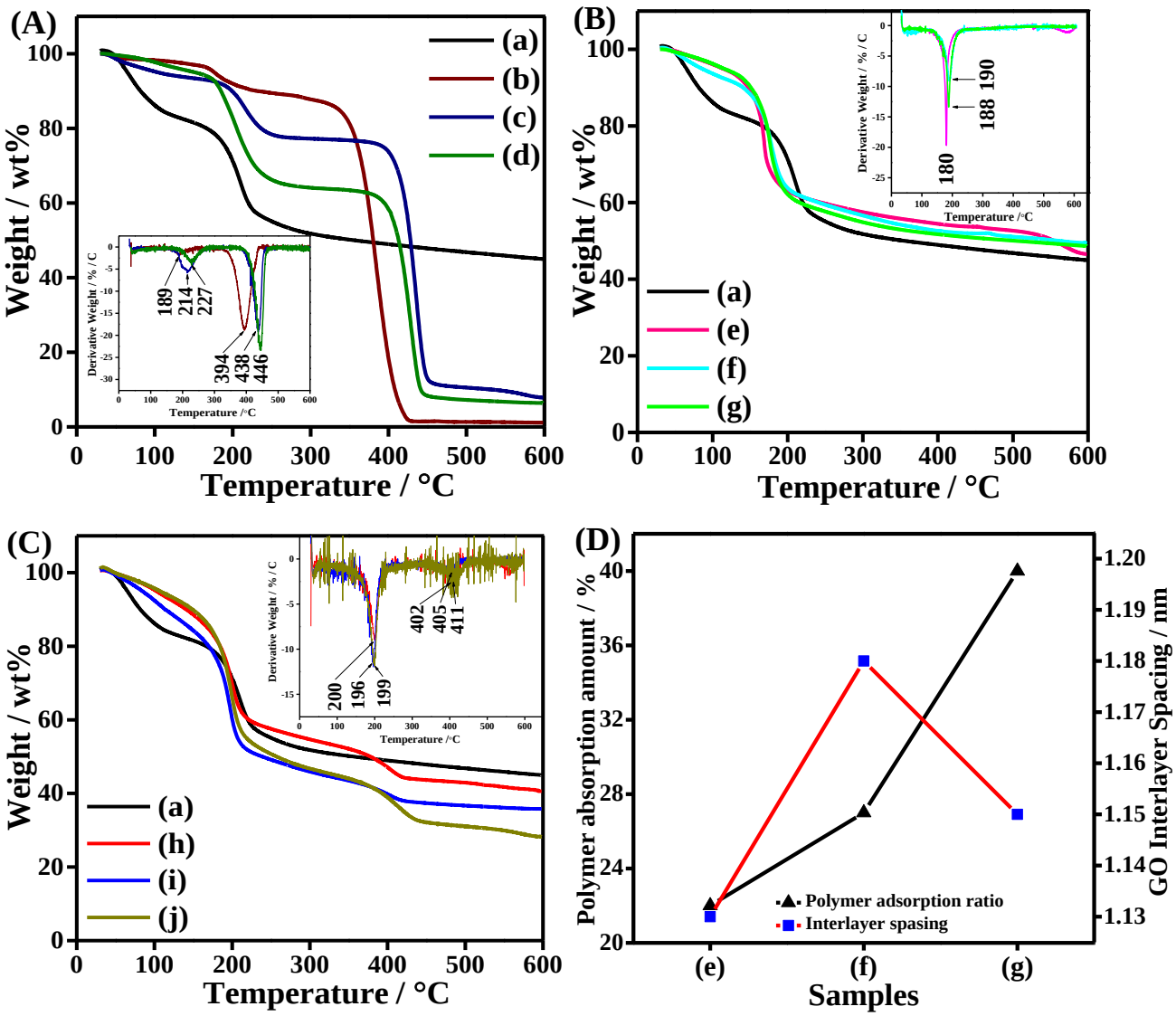

Figure 4-5: TGA curves of polymer/GO hybrids: (A) neat materials, (B) washed samples, (C) non-washed samples, the inserts are derivative thermogravimetric (T_d) curves and (D) The polymer adsorption amount and GO interlayer spacing of (a) GO, (b) PMMA, (c) PMMA-co-MAA, (d) PMAA, (e) PMMA/GO-w, (f) PMMA-co-MAA/GO-w, (g) PMAA/GO-w, (h) PMMA/GO, (i) PMMA-co-MAA/GO and (j) PMAA/GO.

In Figure 4-5 (A), the thermal degradation of the polymers presented two segments degradation. The first and second degradation segments of the polymers were between 150 - 250 ^{o}C and 300 - 470 ^{o}C with two temperature values of peak degradation (T_d), where the first and second T_d were 189, 214, 227 ^{o}C and 394, 438 and 446 ^{o}C, which were related to the

degradation of the oxygen functional groups and the main mass of PMMA, PMMA-co-MAA and PMAA, respectively. PMMA-co-MAA and PMAA with additional functional groups showed a higher degradation amounts than PMMA, especially in the second segments.

Figure 4-5 (B) shows thermal degradation behaviour of the hybrid nanomaterials after washed. It was similar to that of GO behaviour with one segment degradation, showing T_d values of 180, 188 and 190 ^oC of PMMA/GO-w, PMMA-co-MAA/GO-w and PMAA/GO-w, respectively. The adsorption polymer value presented lower than 10 wt.% of washed samples. These results suggested the washing procedure of the samples using DMF removed the most polymers on to the GO nanosheets in the samples, especially the absorption polymer on the surface of GO nanosheet, whereas the other amount of polymer intercalated between GO nanosheets. This TGA results strongly agreed with XRD and FTIR result of washed samples in Figure 4-3 (A) and Figure 4-4 (B) respectively, which observed the same phenomena.

Further samples were prepared with the same method but without washing procedure steep. The TGA result of the not washed samples illustrated in Figure 4-5 (C). These showed notable differences in the degradation behaviour of hybrid nanomaterials. It presented two different segments of the degradation samples between 150 - 250 ^oC and between 350 - 450 ^oC, respectively. These degradation behaviours of not washed samples were similar to the polymers behaviours, whereas the washed samples were similar to GO behaviour.

The hybrid nanomaterials gradually degraded after 450 ^oC to lose of the mass 59.5 wt.%, 64 wt.% and 72 wt.% at 600 ^oC of PMMA/GO, PMMA-co-MAA/GO and PMAA/GO, respectively. It illustrated two T_d values. In the first segments, the T_d shifted from 189, 214 and 227 ^oC to 200, 196 and 199 ^oC, whereas in the second segments, the T_d shifted from 394, 438 and 446 ^oC to 402, 405 and 411 ^oC of the PMMA/GO, PMMA-co-MAA/GO and PMAA/GO, respectively. Those degradation sediments were related to degradation the residual oxygen functional groups between GO and the polymers and degraded the remind

polymer in the samples, respectively. The thermal degradation was substantially improved in the second sediment due to the contribution of the GO by the carbon bonds compared to the neat polymers.

Also, the samples that contained polymers with additional functional groups, which were PMMA-co-MAA/GO and PMAA/GO, showed more degradation mass of the oxygen functional group compared to PMMA/GO. More degradation of mass means more functional groups formed between these functional polymers and GO. This resulted from the better interaction between the functional groups of the polymer and GO nanosheets. These samples showed a significant increase in degradation mass up to 7.5% and 21% of PMMA-MAA/GO and PMAA/GO respectively, compared with the PMMA/GO sample and washed samples. That showed a better adsorption amount of PMAA onto GO nanosheets, which agreed to XRD results, which showed an increase in the peaks area of adsorption polymer in Figure 4-3 (C).

The adsorption amounts of the polymers were calculated from the TGA results in Figure 4-5 (D). It showed an increase to 22 wt.%, 27 wt.% and 40 wt.% of the PMMA/GO, PMMA-co-MAA/GO and PMAA/GO, respectively compared to the washed samples. The small ratio of MAA unit of PMMA-co-MAA showed a significant enhancement in the adsorption ratio of 23 for PMMA-co-MAA on the GO nanosheets whereas it was considerably improved up to 82% for the PMAA compared with PMMA. The polymer with additional functional groups showed the better interaction between the functional groups of both polymers and GO led to a better adsorption ratio than PMMA.

These TGA findings were strongly supported by the XRD results, which showed an increase in the interlayer spacing of the GO in the hybrids from 0.87 nm to 1.13, 1.18 and 1.15 nm for the PMMA/GO, the PMMA-co-MAA/GO and the PMAA/GO compared to GO interlayer spacing. PMAA/GO showed a reduction in the interlayer spacing, whereas it

illustrated the best adsorption ratio. This means the most of the mass of adsorption PMAA adsorbed on the surface of GO compared to the confined PMMA that between GO nanosheets. This explains the decrease in the interlayer spacing of GO in PMAA/GO as shown in Figure 4-5 (D).

Generally, the incorporation of the functional group of the polymers offered significant improvements in the adsorption amount of functional polymer due to the physical bonding interaction. This well interacted between the functional group of polymers and the oxidizing groups of GO. The PMAA/GO hybrid presented the best adsorption ratio due to the physical bonds interaction that attached PMAA into the GO nanosheets surface in agreement with FTIR spectra in Figure 4-3 (C) curve (j) and the literature [247].

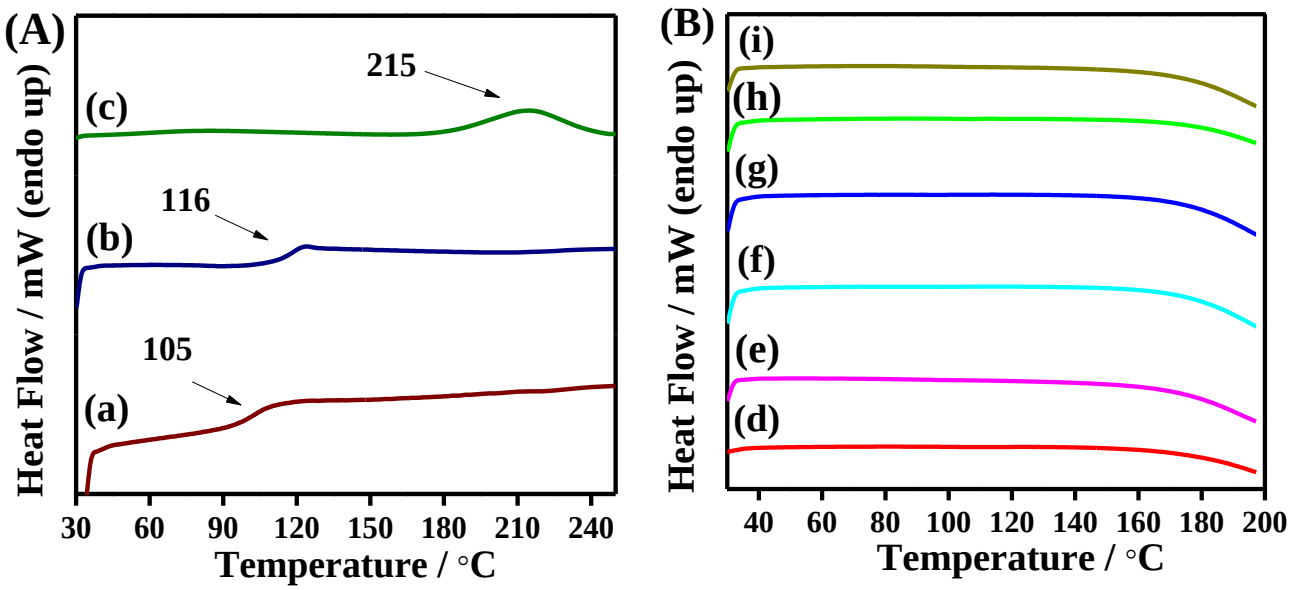

Figure 4-6: DSC second heating curves of (A) polymers and (B) samples of the (a) PMMA, (b) PMMA-co-MAA, (c) PMAA, (d) PMMA/GO-w, (e) PMMA/GO, (f) PMMA-co-MAA/GO-w, (g) PMMA-co-MAA/GO, (h) PMAA/GO-wand (i) PMAA/GO.

Figure 4-6 shows the second heating cycle of the polymers and hybrids that were characterized using the DSC. In Figure 5 (A), the glass transition temperature (T_g) of the polymers presented at 105 ^oC, 116 ^oC and 215 ^oC of the PMMA, PMMA-co-MAA and PMAA, respectively. These results were very similar to the published values for polymers, where Fu et al. [248] reported T_g at 105.2 ^oC of PMMA and 213 ^oC for PMAA, whereas the T_g of the PMMA copolymer is expected to increase. This was dependent on the feeding ratio and the effect of polar MAA units that interacted with the MMA units due to the formation of the hydrogen bonds.

The polymers showed a clear T_g value due to the chain segments mobility of macromolecules in the amorphous phase, whereas the hybrids presented without a clear sign of glass transition of the polymers. Generally, the solvent blending process provides physical interactions between the fillers and polymers matrix [249], where the physical bond formed between the GO nanosheets and matrix polymers [249], which increased the T_g of the hybrids [250]. According to the TGA results, the mass ratio of GO these samples was higher than the polymers which mean more hydrogen bonds formed, further restricting the movement of polymer chains during the interaction between the oxidizing group and C=C in the GO nanosheets with functional groups of neat polymers [249,250]. The interfacial interactions of the GO intensified the restriction of the mobility of the polymer chains that interpreted the T_g [249]. This presented the hybrid nanomaterials without any sign of the glass transition, as shown in Figure 4-6 (B) which is in agreement with the literature [251].

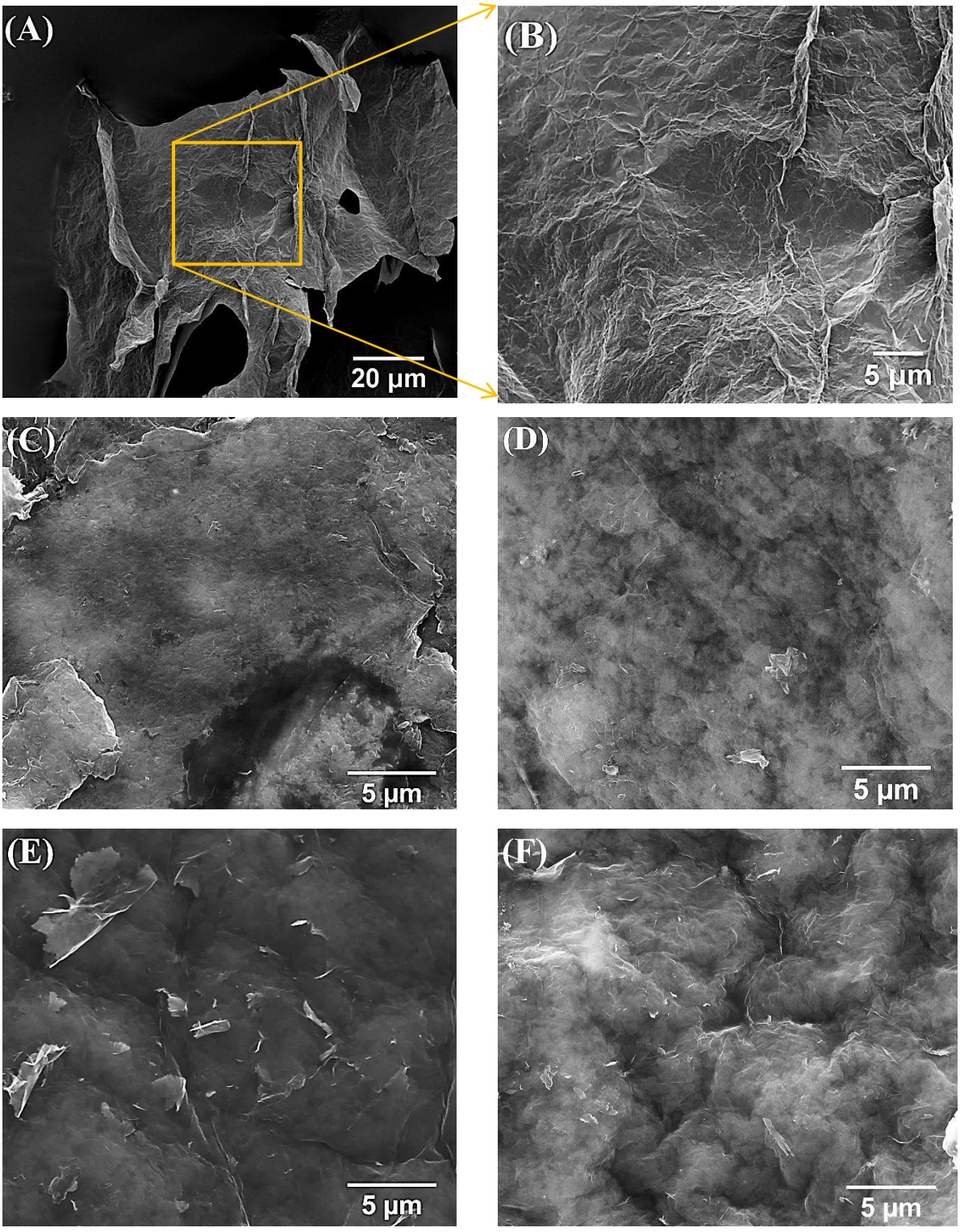
(A)
20 μm
(B)
5 μm
(C)
5 μm
(D)
5 μm
(E)
5 μm
(F)
5 μm

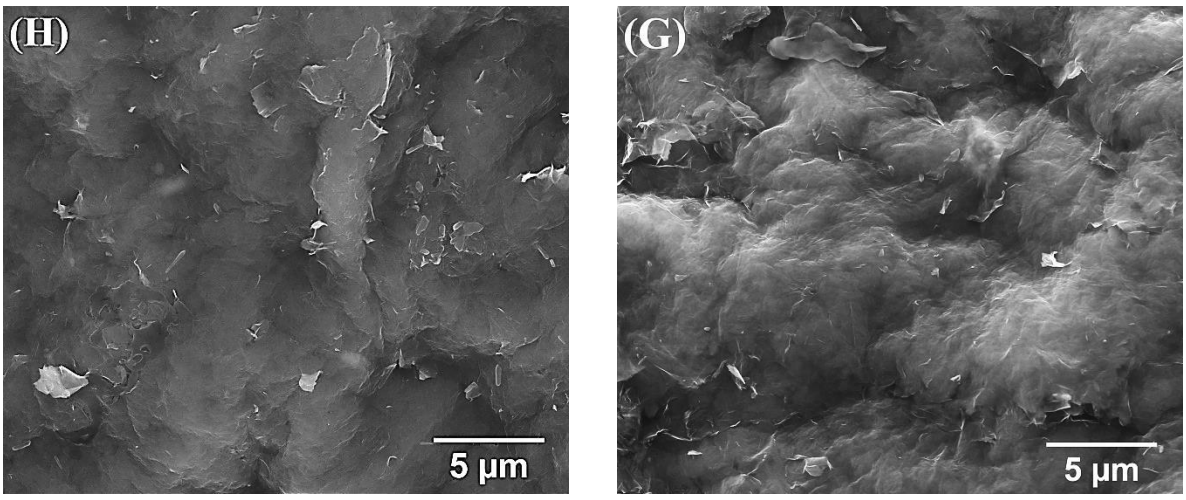

Figure 4-7: SEM images of (A and B) GO, (C) PMMA/GO, (D) PMMA/GO-w, (E) PMMA-co-MAA/GO, (F) PMMA-co-MAA/GO-w, (G) PMAA/GO and (H) PMAA/GO-w.

In Figure 4-7, SEM images showed a change in the fracture surface of hybrid nanomaterials. The GO nanosheets exhibited a flaky fracture surface as shown in Figure 4-7 (A and B). In Figure 6 (C), PMMA/GO-w demonstrated a flaky fracture surface similar to the GO nanosheets, whereas PMMA-co-MAA/GO-w and PMAA/GO-w hybrids showed a densely packed surface with some flakes of GO nanosheets that clear presented on the hybrid nanomaterials surface as shown in Figure 4-7 (E and G). The SEM images observed that the washing producer removed the most of adsorbed polymer on the surface of GO nanosheets, where the GO nanosheets represented on the surface of the washed samples in strong agreement with TGA results, which showed a significantly reduce in the mass ratio of adsorbed polymer to lower than 10 wt.% of washed samples as discussed in Figure 4-5 (B).

Appling washing procedure led to reduction the adsorption amount of polymer and present the flak of GO on the surface on the washed samples, whereas, applying no further washing procedure for the hybrids tended to change the flaky fracture surface to a densely packed surface of the PMMA/GO in Figure 4-7 (D), where the PMMA partially covered GO nanosheets and only some of the edges of GO nanosheet observed in these not washed PMMA/GO compared to washed PMMA/GO-w. The functional PMMA-co-MAA and PMAA

showed a significant covering of most GO nanosheets during the adsorption of these polymers onto GO nanosheet surface as shown in Figure 4-7 (F and H), where the PMMA-co-MAA/GO and PMAA/GO showed a different fracture surface. Those were a wrinkled and crumpled profile with the highest thickness of adsorbed polymer layers like hills onto the GO nanosheets surface in comparison with the PMMA/GO. PMMA/GO showed a flat fracture surface with a lower thickness of adsorbed PMMA.

The SEM images clearly observed that the PMMA-co-MAA and PMAA with additional functional groups offered better physical interactions. This led to improving the adsorption behaviour compared with PMMA. The PMAA/GO, which contained the MAA unit, showed the thickest layer of adsorbed polymer compared to other polymers. Those finding confirmed the TGA finding that presented the best adsorption ratio of PMAA onto the GO nanosheets.

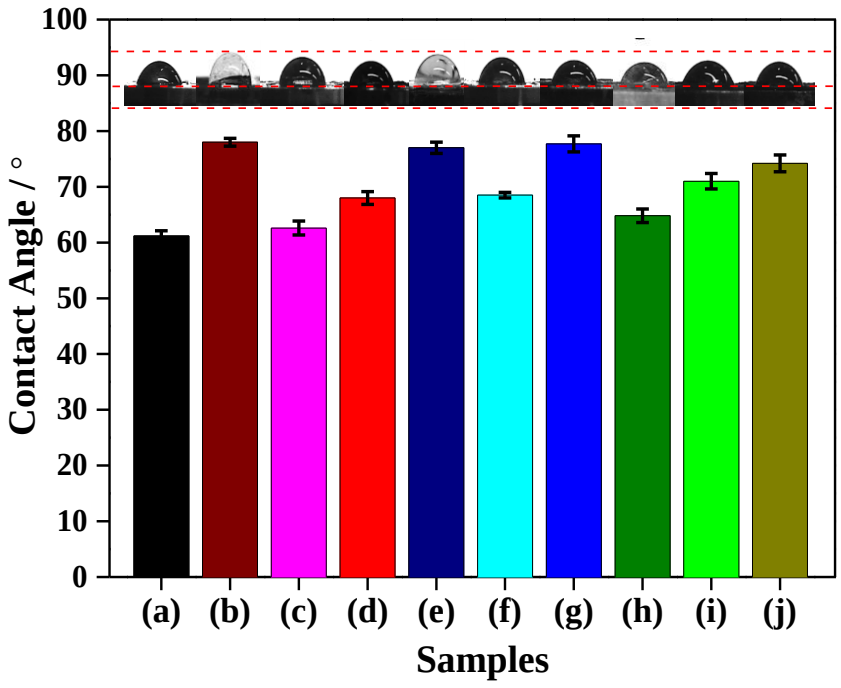

Figure 4-8: Water contact angles measurements: of (a) GO, (b) PMMA, (c) PMMA/GO-w, (d) PMMA/GO, (e) PMMA-co-MAA, (f) PMMA-co-MAA/GO-w, (g) PMMA-co-MAA/GO, (h) PMAA, (i) PMAA/GO-w and (j) PMAA/GO. The inset is photographs of water droplets on each sample.

Figure 4-8 shows the measurement of contact angles of GO, polymers and hybrids that investigated the relative hydrophobic/hydrophilic nature of the samples. The contact angle of GO was 61.2 (± 0.9) ^{o}. It is more hydrophilic in nature due to the O-H, COOH and other oxidizing functional groups that covalently attached to the surface of GO nanosheets [229,252].

The contact angle of PMMA was 78 (± 0.7)^{o} in agreement with the literature [253], whereas the contact angle of PMMA-co-MAA was 77.3 (± 1) ^{o}. The PMMA-co-MAA exhibited the slightly lower value of the contact angle than the PMMA. The PMMA-co-MAA is the PMMA with the methoxy acid groups (MAA) which provide more numbers of –COOH functional groups in the polymer chain [254,255]. The water contact angle of PMAA was measured at 64.8 (± 1.2)^{o}. However, to the best of our knowledge, the contact angle surface properties of PMMA-co-MAA/GO, PMAA and PMAA/GO hybrids film have not been reported.

The contact angle decreased from 78 (± 0.7)^{o} to 62.6 (± 1.25) ^{o} and 77 (± 0.7) ^{o} to 68.5 (± 1.2)^{o} for the PMMA/GO-w and PMMA-co-MAA/GO-w respectively, whereas it increased from 64.8 (± 1.2)^{o} to 71 (± 1.4)^{o} for the PMAA/GO-w compared to the polymers values. The incorporation of the functional groups of GO turned the samples to more hydrophilic, where the washing procedure removed the adsorbed polymer, which is more hydrophobic than the GO nanosheets surface. It associated to represent GO flake on the surface of samples as shown in the SEM images in Figure 4-7. This led to reductions the contact angle values. This result matched the TGA results, which significantly decreased the adsorption polymers using the washing procedure, whereas the FTIR showed broad O-H peaks, C-O and other oxidizing peaks in the washed hybrids.

No further washing procedure led to increasing the contact angle values from 62.6 (± 1.25)^{o} to 68 (± 1.15)^{o}, 68.5 (± 1.2)^{o} to 77.8 (± 0.5)^{o} and 71 (± 1.4)^{o} to 74.2 (± 1.5)^{o} for

PMMA/GO, PMMA-co-MAA/GO and PMAA/GO, respectively. PMMA showed a decrease in the contact angle of 24.6% and 14.7% of both the washed and non-washed hybrids compared to PMMA. The incorporation of GO nanosheets tended to make both PMMA samples more hydrophilic and increased the functional groups of GO on the surface of the hybrids compared to neat PMMA.

The FTIR results of PMMA/GO supported these findings, for instance, the PMMA curve presented a broad O-H functional peak with other oxygen functional groups, where the PMMA/GO consisted of 78 wt.% of GO, which was a higher ratio than PMMA according to the TGA result, Those led to reducing the contact angle value due to the nature hydrophilic of GO nanosheets. These results matched the work of Zinadini et al. [252], they reported a decrease in the value of contact angle from 65.2^{o} to 55.3^{o} of the polyethersulfone matrix nanofiltration membrane by increasing the ratio of GO and agreed with other researchers results [229,256].

PMMA-co-MAA/GO-w also illustrated a decrease in the contact angle of 12.8% due to the washed procedure of sample, whereas it increased by 1.2% for not washed nanohybrid compared to PMMA-co-MAA. The SEM image showed the PMMA-co-MAA covered most of the surface of GO nanosheets during the strong hydrogen interaction between the functional group of the PMMA-co-MAA with the functional group of GO in the PMMA-co-MAA/GO hybrids. Therefore, the contact angle value of this sample presented very closely the value of PMMA-co-MAA neat. PMAA exhibited a significant increase in the water contact angle of 9.6% and 14.5% of both washed and not washed samples, respectively compared to neat PMAA. These results were supported by the FTIR finding, where PMAA/GO presented without any sign of O-H functional group, as discussed before in Figure 4-3 (C) curve (j).

PMMA-co-MAA/GO and PMAA/GO presented an increase in the contact angle in comparison to its polymers. The increasing contact angle was related to strong hydrogen bonds interaction between the functional groups of the polymer and GO. For instance, the interaction of the hydrogen bond between the -COOH groups of the MAA unit in both of these polymers and the oxygen groups of GO led to the creation of a network-like structure, where a hydrophobic character of samples predominates. The same phenomena were reported by Rajender and Suresh [195], their result exhibited an increase in the water contact angle of PMMA from 69^{o} to 82^{o} with 2.33 wt.% of incorporation of functionalized graphene sheets (FGS). They considered this increase to be related to the interaction that creates a network-like structure as C-composites between the PMMA with FGS in which the hydrophobic character of FGS predominates [195]. Interestingly, this interaction between GO and PMMA-co-MAA and PMAA turned the hybrid nanomaterials to hydrophobic behaviour compared to PMMA/GO. The contact angle value of the PMAA/GO showed the biggest changed compared to other hybrids. Generally, no further washing procedure associated with significant improvements in the contact angle of 8.6%, 13.5% and 4.5% for all the not washed samples in comparison to the washed samples.

4.4 Conclusions

A proper functional group is an important key for good compatibility and fine dispersion of the nanofillers in polymer/GO nanocomposites. PMMA, PMMA-co-MAA and PMAA were used as the polymer models that have the similar backbone structure as PMMA, but with side functional groups. These were used to investigate the effect of the polymer functional groups on the adsorption behaviour onto GO nanosheets. GO was prepared using a Hummer's method, and then mixed with the polymers in DMF by solution blending method. These prepared as PMMA/GO, PMMA-co-MAA/GO and PMAA/GO hybrid nanomaterials were investigated before and after washing procedure.

The results showed the successful preparation of polymer/GO hybrid nanomaterials. The main characterization of the polymers and GO nanosheets confirmed the adsorption of the polymer onto GO nanosheets, whereas the washing process provided a direct influence of all the characterization of the samples. The washing process removed most of the adsorbed polymers on the surface of GO nanosheets and small amount of confined polymers in the interlayer space between the GO nanosheets, The adsorption amount of the polymers onto the GO nanosheets was reduced to less than 10 wt.% of the polymers by the washing process, where most of the remaining polymers were confined between the GO nanosheets, indication a strong restriction applied by GO nanosheets.

The interlayer spacing of GO nanosheets in non-washed samples was increased by 2.7% due to the presence of confined polymer between the GO nanosheets. That led to the shift of the XRD peaks to lower values. For the significant diffraction peaks attributed to the adsorbed polymer on the surface of GO nanosheets, the intensity increased by of 45% compared with washed samples. The amount of adsorbed polymers increased to 22 wt.%, 27 wt.% and 40 wt.% for the PMMA/GO, PMMA-MMA/GO and PMAA/GO respectively. With a moderate amount of MAA unit, PMMA-co-MAA achieved an improvement up to 23 of the adsorption amount on GO nanosheets, whereas PMAA exhibited the best adsorption, raising the polymer adsorption amount by up to 82%, compared to PMMA, which has no MAA unit. MAA unit provided a notable enhancement in the polymer adsorption on GO nanosheets due to the strong electrostatic interaction.

The neat polymers demonstrated a clear glass transition, whereas the polymers in polymer/GO hybrids presented no sign of glass transition due to the contribution of the GO nanosheets. That was because GO restricted the molecular mobility of polymers chains caused by the interactions of GO nanosheets with polymers. SEM images provided significant confirmations of the polymer adsorption onto GO nanosheets that observed significant evidence on the best thickness of adsorbed PMAA onto GO nanosheets. Thanks to the

hydrophilic nature of MAA unit, the water contact angle of the hybrid nanomaterials containing MAA was enhanced by 1.2% and 14.5% after mixing with GO of PMMA-co-MAA/GO and PMAA/GO respectively. In contrast, the water contact angle of PMMA/GO was reduced by 14.7%.

Generally, the functional groups showed a significant influence and had a direct effect on the polymer adsorption behaviour of the hybrids properties even at a low amount. These results showed a significant influence of the functional groups on the adsorption behaviour of polymers/GO nanohybrid properties, which is an important insight and will be helpful for the investigation of the interfaces in polymer/GO nanocomposites, as well as for monitoring the surface characteristics of GO nanosheets.

Chapter 5: Preparation and new separating methods for different-size graphene oxides using centrifugal and sonication methods

5.1 Introduction

The previous chapters provided some information associated with the understanding the adsorption behaviour of polymers onto GO in a matrix. GO is abundant with oxygen-functional groups [257]. This makes GO an interesting candidate for processing of bulk polymer/GO nanocomposites for industrial application [199,218,258] because of its computability with a range of polymer matrix [257]. GO sheet-like nanoparticles have an effective length scale that can reach between several hundreds of nanometers [146] and several microns [211]. The determination of the aspect ratio for these nanoparticles is very important in terms of evaluating the efficiency of stress transfer. Controlling the size of the fillers is an important factor that could provide the significant information on interfacial interaction, which can lead to a better understanding of the size effect on the properties of the nanoparticles distribution of a broad size of regularly fillers led to indefinite results [219]. This could offer a wide range of applications, such as structural engineering energy [259] and health [219,260].

However, few investigation [217–219] have been reported on separating the size of GO particles, as received well in the previous chapter in section 2.8. Most of the existing reported studies involved high power sonication, long sonication duration, and complicated procedures to prepare various size GOs, which have resulted in many defects and a broad distribution size of GO particles because all of the parameters have not been considered that may have a direct effect on the results to avoid the defects. Therefore, a preparation of different size of GO particles with narrow distributions, and their effect on the properties of

nanocomposites need urgently be addressed, because an engineered size is required to achieve a high-performance from nanocomposites properties [152,211–215,219,260,261].

In order to fill the knowledge gap in this field, a separation of narrow distribution size GO particle is studied in this chapter; and two main objectives were the focus in this study. The first was to investigate the relationship between graphite flake size and the resulting GO size, where two graphite flakes with different sizes were selected to prepare GOs by a modified Hummer's method [25]. The second objective was to separate different size of GO particles with narrow distributions from the selected GO by developing separation methods. Using the low power sonication and a short sonication time was expected to avoid or reduce the defects, so the combination of low-power sonication, centrifugal speed and centrifugal duration were investigated, as means to separate the as-prepared GO. Dynamic light scattering (DLS) and atomic force microscopy (AFM) were used to characterize and confirm the dimensions of the obtained size of GO particles.

5.2 Basics of centrifugation

Centrifugation is one of the popular techniques widely used in biology, biochemistry, evaluation of suspensions, medicine and pharmacy. Centrifugal techniques involve separating particles from different surrounding media or other particles by relative centrifugal force (RCF) [262]. The suspension in a liquid of different particles, especially large in size, settles down over time due to gravity, whereas other particle sizes, namely medium and especially small size, stay suspended at all in such a solution. However, a long-timeframe is required to separate the suspension particle in some applications, such as medicine. Therefore, centrifugal force (RCF) is required to separate most particles. This particle could settle to the bottom under high centrifugal force. The RCF moves the particle at a certain speed away from the axis of rotation [263], which is determined by the distance of the particles from the centre of

rotation and the rotation speed (rpm) of the centrifuge. The RCF can be calculated from equation (5-1).

$$\mathrm{RCF} = 11.17\, \mathrm{r_{max}}\, (\mathrm{rpm}/1000)^2 \qquad (5\text{-}1)$$

Here, r means the radius of the circle of rotation. Different factors can affect the centrifugal force, such as the mass of the object, the angular velocity of rotation and the radius of the circle, which play important roles in the separation of particles. The RCF force is also usually called g-force [264].

Increasing the effective gravitational force precipitates the particles descent to the bottom of the tube. The precipitate particles are called pellets or sediment and the remaining solution is supernatant. The latter is quickly removed from the tube using a pasteur pipette without disturbing the precipitate [265].

The particle size or the densities of the supernatant determine the rate of separation because the higher density or larger size of particles settles quickly compared to other particles, which are smaller sizes. This movement of the sedimentation of particles is explained by the Stokes equation [263,266], which calculates the velocity of the sediment utilizing five parameters [266] and describes the movement of a sphere in a gravitational field [263].

$$\mathrm{V} = (d^2(\rho - L)\ 3\, g) \,/\, (18\, \eta) \qquad (5\text{-}2)$$

where V means the sedimentation rate or velocity of the sphere, d means the sphere's diameter, ρ means particle density, L means the medium density, g is gravity and η means the viscosity of the medium.

The rate of particle sedimentation is proportional to Stokes equation, example that the particle size; it becomes zero if the particle and medium have the same density or are

proportional to the difference in their densities; it increases if the gravitational force is increasing; and it decreases if the medium viscosity is increasing [263].

Simple filtration techniques separate the particle at the bottom with a size above 5µm, while if the size is less, then it follows Brownian motion. This motion is considered to be the rotation of the body mass as a circular path of the radius at a specific velocity. This applies a strong centrifugal force to separate the particles. The particle is affected by the force in a radial direction, as explained in the equation below [263]:

$$F = mv^2/r \quad (5\text{-}3)$$

where F means centrifugal force, m means the mass of body and v means the velocity of the body.

The same particle effect occurs as a result of gravitational force (G), which is affected by acceleration due to gravity (g), as given by the formula below:

$$G = mg \quad (5\text{-}4)$$

where the centrifugal effect (C) is the ratio between the gravitational force (G) and the centrifugal force (F), given in the formula below:

$$C = F/G = v^2/gr = kD\,n^2 \quad (5\text{-}5)$$

By substitution of $v = 2\pi$ r n, where $k = 2\pi^2/g$, which is constant, D = 2r, a maximum diameter of the centrifuge, which measures from the centre of the centrifuge to the top of the centrifuge tube, and n = the speed of centrifuge rotation.

Manipulating the speed and the diameter of the centrifuge helps isolate particle by size. Different centrifugal separation methods are explained in the literature [262,263,265–267].

5.3 Experimental part

5.3.1 Materials

All other materials were the same as used in the previous chapter in section 3.2.1.

5.3.2 Synthesis and purification of graphene oxide

This was described in the previous chapter in section 3.2.2.

5.3.3 Separation of graphene oxide particle sizes

GO1 and GO2 were dispersed in the distilled water for 24 h with 0.002/20 mg ml^{-1} concentration, which is appropriate concentration to test using DLS in this study. Both GOs were sonicated in a sonication bath for a different period of time up to 5 h. Different g-forces were applied from 137 g up to 11138 g on the GO samples for a series of times, from 10 seconds up to 4.5 h, using (Eppendorf Centrifuge 5804, fixed angle rotor FA-45-6-30 with radius 12.3 cm and 50 ml tube). The methods were discussed in detail in the results and discussions section. The samples are mostly clear without dust for accurate measurements of particle sizes. Values centrifugal forces (g) were calculated for the selected centrifuge rotor radiuses, and the centrifugal effect depends on the centrifugal speed, as shown in

Table **5-1**.

Table 5-1: g-force values and centrifugal effect against the centrifugal speed (revolutions per minute, rpm)

Centrifugal speed/ rpm	g-force / g	Centrifugal effect
1000	137	$9*10^{8}$
3000	1237	$0.8*10^{10}$
4500	2782	$1.8*10^{10}$
6000	4950	$3.2*10^{10}$
8000	8793	$5.7*10^{10}$
9000	11138	$7.3*10^{10}$

5.3.4 Characterization

An X-ray photoelectron spectroscopy (XPS) was carried out using a Kratos Ultra instrument with a monochromatic aluminium source. Survey scans were collected between 1200 to 0 eV binding energy at 160 eV pass energy and 1.0 eV intervals. In addition, high-resolution C1s, O1s, and N1s spectra were collected, as specified, over an appropriate energy range at 20 eV pass energy and 0.1 eV intervals. The analysis area was between 300 and 700 µm. The data collected was calibrated in intensity using a transmission function characteristic of the instrument (determined using software from NPL) to make the values instrument independent. The data were calibrated for binding energy by making the main carbon peak C 1s at 285.0, and correcting all data for each sample analysis accordingly.

Dynamic light scattering (DLS) analysis is a non-invasive technique for determining the size distribution of particles in a solution or suspension [268]. During the random motion of these particles, the scatter incoming laser light intensity fluctuates in time. The DLS particle size measurements depend on the Stokes-Einstein equation that assumes all the particles are spherical and there are no particle-particle interactions. The equation measured the hydrodynamic diameter of the particle size, which is the diameter of a sphere that diffuses in the same way as the sample [268].

$$d_h = K_B\, T / 3\pi\, \eta\, D_t \qquad (5\text{-}6)$$

where d_h means hydrodynamic diameter particle size, D_t means the translational diffusion coefficient found by DLS, K_B means Boltzmann's constant, T means thermodynamic temperature and η means dynamic viscosity. This method has been described previously in the literature [269]. Hydrodynamic Diameter is "the diameter of a hard sphere that diffuses at the same speed as the particle or molecule being measured" [268], which depends on the size of the particles (core), ions concentration in the medium surface and surface structure.

To introduce the DLS data, Figure 5-1 shows an example, where Figure 5-1 (A) deduced three axes: the x-axis introduces the lognormal size of differential particle size distribution that is the hydrodynamic radius (h_d) of the particles size in nanometre diameters. It is the percentage of particles of the total that is within a specified size range. The y1-axis (left side) represents the intensity of particle size, and the y2-axis (right side) is signed to the cumulative particle size distribution. The latter is found by the accumulation of differential distribution [270]. Each sample had 10 runs to get the hydrodynamic diameter and the samples were repeated twice for reproducible results.

Figure 5-1 (B) presents the multimodal distribution that explains the size and intensity (number) of particle size as well as the ranges of particle sizes in the samples [270,271]. For instance, the sample presented a broad distribution of the hydrodynamic diameters because this sample had three different ranges of various particle sizes as shown in Figure 5-1 (A) and vice versa.

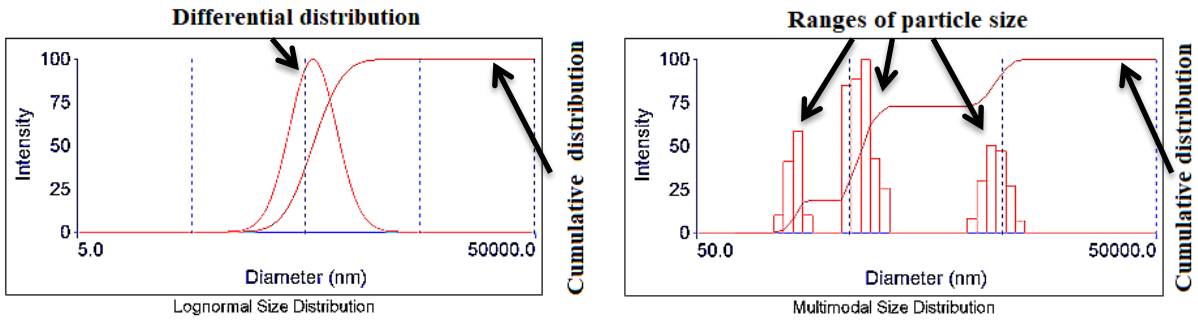

Figure 5-1: DLS illustration of data processing to introduce the results in each curve.

DLS used a Brookhaven 90Plus to measure the GO particle size. The features of particle sizing from <1 nm to 6 µm, accommodates a wide concentration range for easy sample preparation, multimodal and unimodal size distribution software, two scattering angles and a 35 mW laser with a high sensitivity detector. Each sample measured for 10 runs and the

combined diameter was the average of all the raw data; treating all the individual runs as one long run with a standard error. Other characterization techniques procedures were explained in the previous chapter in section 3.2.4.

5.4 Results and discussion

5.4.1 Characterisation of graphene oxide

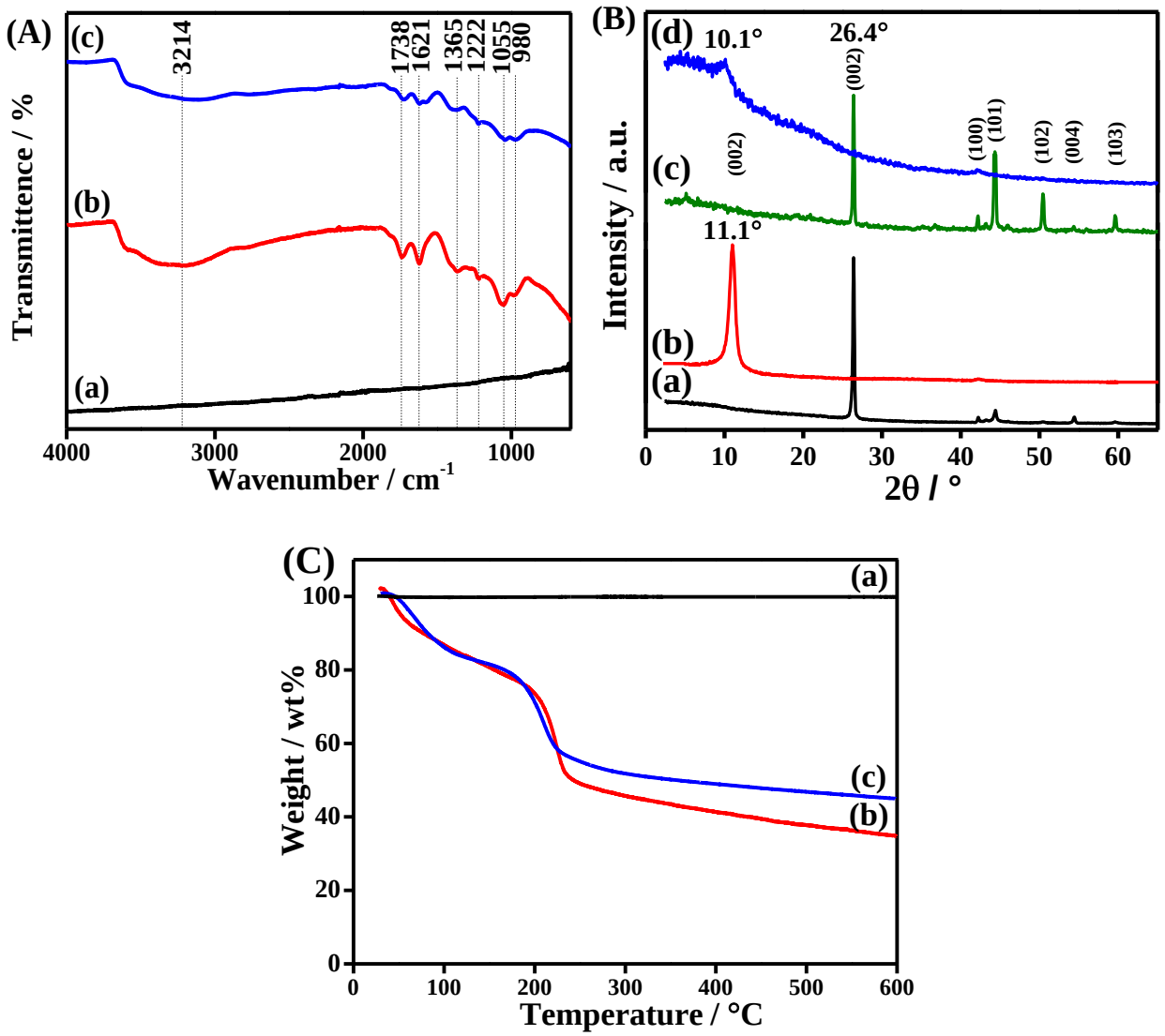

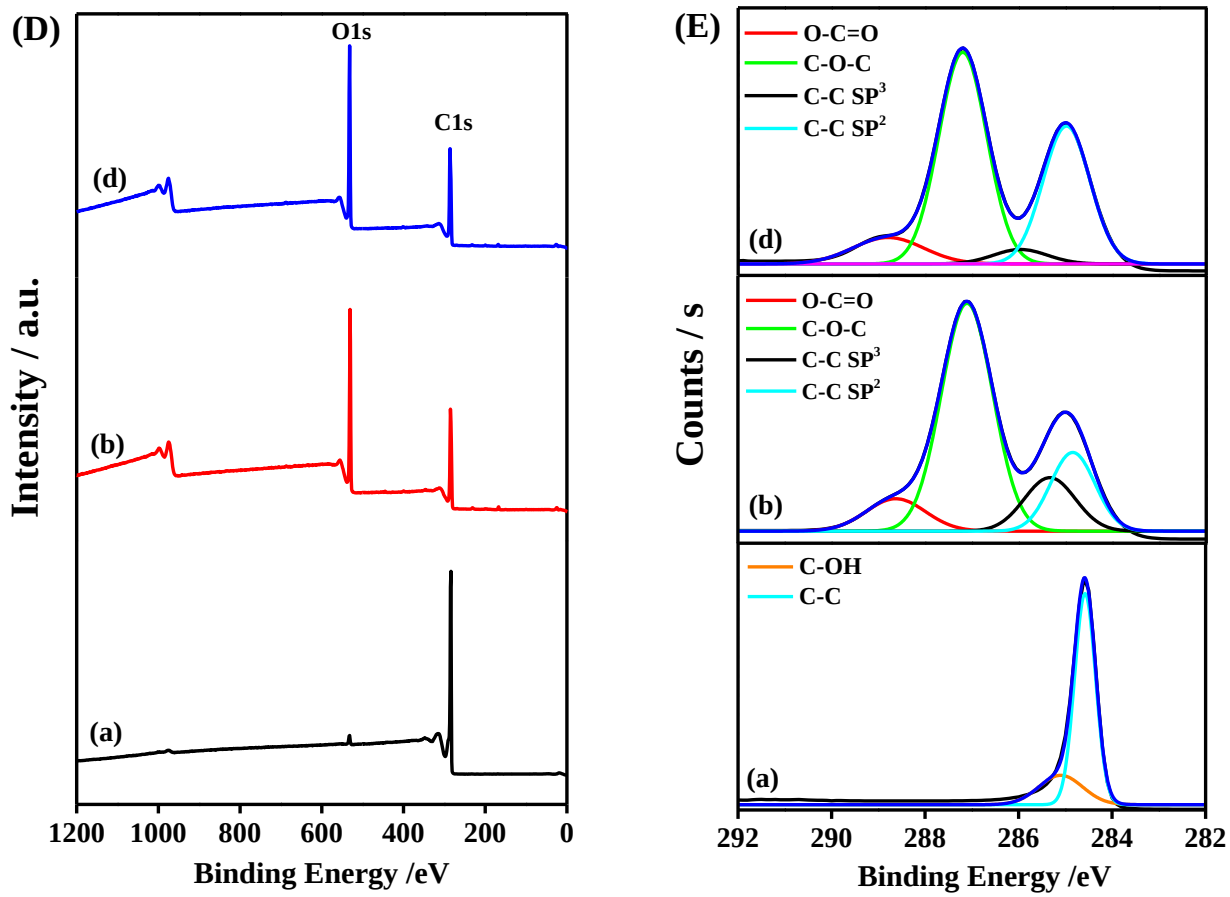

Figure 5-2: (A) FTIR spectra, (B) XRD traces, (C) TGA curves, (D) XPS survey spectra and (E) C1s core level XPS spectra of (a) graphite (size ≤20 μm), (b) GO1 and (c) graphite (size ≤149 μm) and (d) GO2.

The FTIR, XRD, TGA and XPS results of the GO1 and GO2 nanosheets were shown in Figure 5-2. The strong oxidation of graphite produced both GO1 and GO2 nanosheets with new oxygen functional groups, such as the O-H (free water) stretching, carbonyl C=O stretching, aromatic ring C=C stretching, -C-H bending, C-OH stretching, epoxy C−O−C stretching and C-O stretching functional groups, respectively, at 3214, 1738, 1621, 1365, 1222, 1055 and 980 cm^{-1} wavenumbers, respectively [25,244], as shown in Figure 5-2 (A). X-ray diffraction exhibited the (002) peak of both graphite's at $2\theta = 26.4°$ in corresponding to an interlayer spacing of 0.33 nm in agreement with the literature [188,244], The XRD pattern corresponding to graphite ≤150 μm provided other strong peaks at the (101) and (102) peaks,

representing the perpendicularity of natural graphite hexagonal planes with (c-axis) direction and impurity ratio, which matched the literature results [245,246], On the other hand, graphite ≤20 μm presented differently at peak intensity, due to the synthesis process. This (002) peak shifted to 2θ = 11.1° and 10^{o} for GO1 and GO2, corresponding to the interlayer spacing of 0.79 nm and 0.88 nm, respectively, as shown in Figure 5-2 (B). The shifting in XRD peaks resulted from the attachment of oxygen functional groups on the GO nanosheets surface, which increased the interlayer spacing between GO layers. TGA results in the Figure 5-2 (C) illustrated a different thermal behaviour of GO1 and GO2 compared with the graphite, with 31 wt.% and 23 wt.% loss of the total dry mass between 150 - 250 ^{o}C of GO1 and GO2 respectively, due to the degradation of epoxides [272], hydroxyl, carbonyl and carboxyl groups [244].

To determine the elemental composition and chemistry of the material surface, an X-ray photoelectron spectroscopy was used, which indicated the oxygen to carbon functional groups levels of synthesized GO. Figure 5-2 (D) shows the survey 1s spectrum, presenting carbon, oxygen, nitrogen and sulfur containing functional groups of GO.

Table 5-2: Atomic concentrations of O1s, C1s and their ratios obtained by XPS survey spectra.

Sample ID	Elements (at%)		O/C ratio
	O1s	C1s	
Graphite	1.6	98.4	0.16
GO1	30.7	67.3	4.45
GO2	30.1	68.2	4.41

Table 5-2 summarises the atomic concentrations of O1s and C1s, and their ratios of graphite, GO1 and GO2. The results exhibit an increase in the oxygen content of the GO1 and GO2 from 1.6% to 30.7% and 30.1% respectively, after the chemical oxidation of the

graphite. This presents a notable increase in the oxygen to carbon ratio, from 0.16% up to 4.45%, and the introduction of the oxygen functional groups with large amounts on the surface of the GO. Oxidizing the graphite was clearly confirmed by the XPS results during the chemical oxidation, as shown in Table 5-2 and Figure 5-2 (D and E).

Figure 5-2 (E) shows the different functional groups between graphite and the GOs that formed on their surface, basal or edge plane during the chemical oxidation. Figure 5-2 (E) shows the O1s peak of GO, which was higher than the C1s peak of GO due to the strong oxidation of the graphite, whereas the C1s atomic concentration values determined the oxygen to carbon ratio in both GOs and graphite. The C1s spectrum of GO presented four bands, corresponding to the functional groups, as shown in Table 5-3.

Table 5-3: XPS analysis summary of the binding energy observed in C1s spectra for graphite, GO1 and GO2 samples.

Sample ID	**C1s peak assignment with corresponding B.E (eV)**			
	C-C / SP^2	**C-C / SP^3**	**C-O-C**	**O-C=O**
Graphite	284.57	284.79	285.05	-
GO1	284.8	285.4	287.09	288.6
GO2	284.9	285.9	287.2	288.7

Table 5-3 summarises the different binding energies (B.E.) with their peak assignments of C1s de-convolution spectra. These results presented de-convoluted core level C1s spectra of GO functional groups. These results matched the functional group obtained from FTIR. It is a further confirmation of the GO structure formation, compared to graphite. The slight differences in results between GO1 and GO2 were related to the slight difference in the diffraction structure between the natural and synthesise graphite.

Sonication-centrifugal based methods were applied to separate a uniform particle size of GO using various sonication timeframes at low power, and different centrifugal speeds for

various times. Both GOs were dispersed only in distilled water. The particle sizes of both GOs were characterized by DLS, whereas AFM was used to measure the physical dimensions of GO particles. This could provide significant evidence of DLS data on particle size. AFM measurements were for a single sheet of a particle size that separated, rather than the hydrodynamic diameter of the GO particles sizes, which was given by DLS. All the hydrodynamic diameters of GO particle sizes were measured by DLS in nanometre unit (nm).

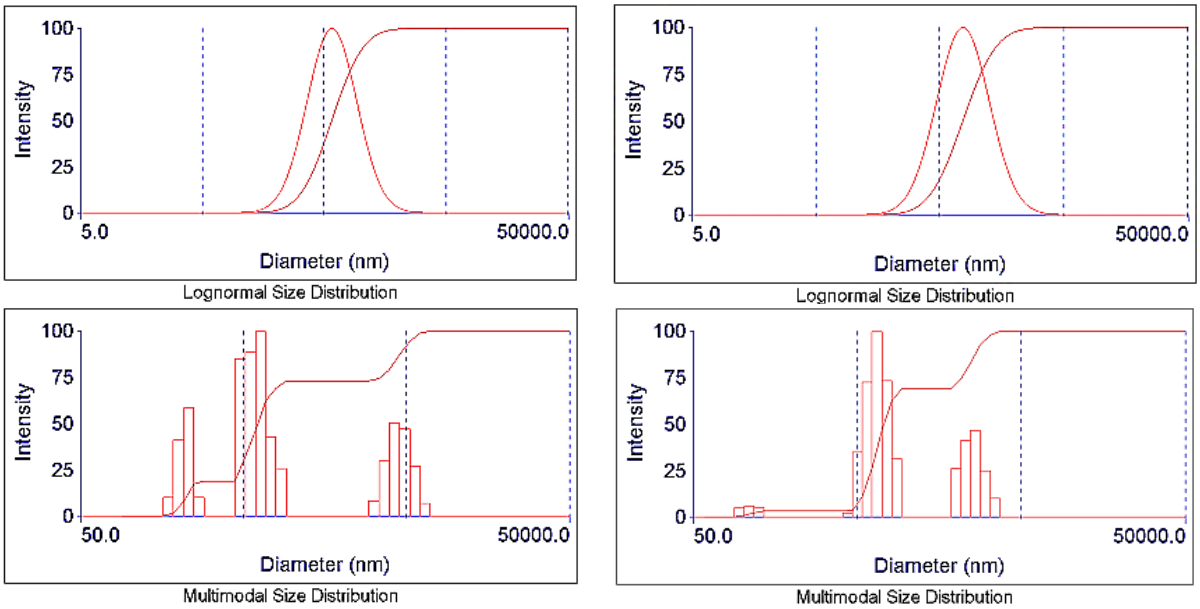

(A) **(B)**

Figure 5-3: The hydrodynamic diameters of sediment samples were sonicated for 30 minutes of (A) GO1 and (B) GO2.

The DLS provides two types for results of each sample: the top figure introduces the average hydrodynamic diameters of distribution particles, whereas the bottom curves induced a range of hydrodynamic diameters of particle size.

In Figure 5-3 (A and C, top), which introduces the average hydrodynamic diameters of distribution particles, a broad average hydrodynamic diameter of 1860 nm and 1517 nm of the of GO1 and GO2 sediments it illustrated, respectively. Figure 5-3 (A and B, bottom) shows

that both GOs induced a broad distribution size of particle with different intensity, where the GOs curves illustrated three ranges of the hydrodynamic diameters of the particle size between (198-633, 571-1131 and 1449-3128) nm, in contrast to ranges between (189-349, 571-1183 and 1501-2993) nm sized particles in GO1 and GO2, respectively. This means these samples had various ranges of GO size, which explains a broad distribution size of hydrodynamic diameters in the top figures.

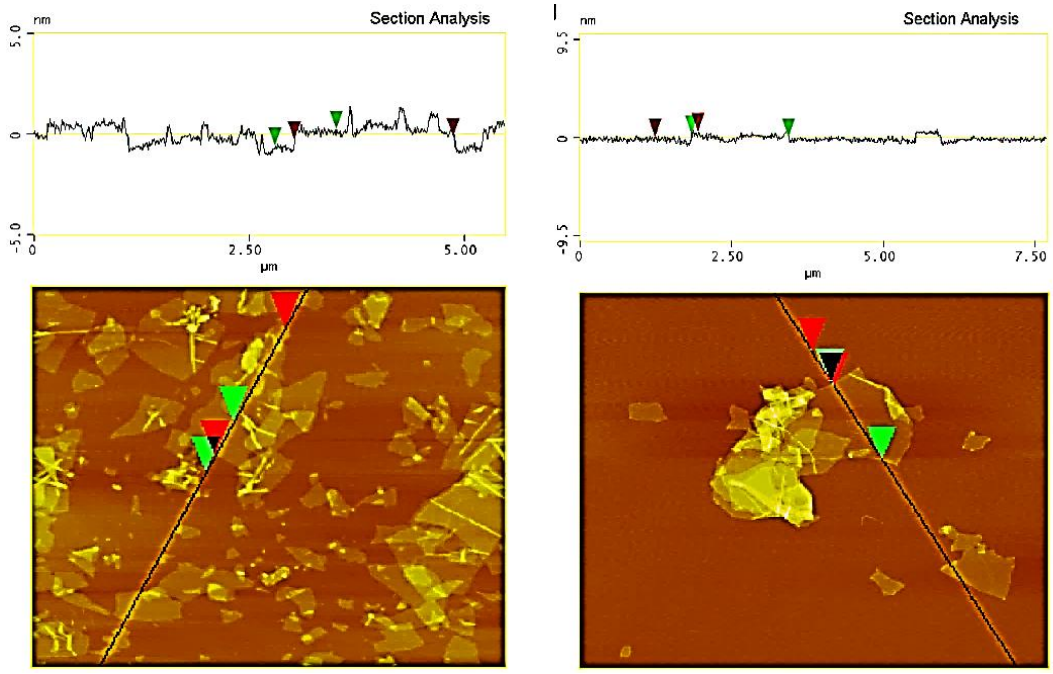

(A) **(B)**

Figure 5-4: AFM images of (A) GO1 and (B) GO2.

Figure 5-4 (A and B) showed the physical dimensions of particle sizes of GO1 and GO2 that were characterized by AFM, respectively. The thickness of the GO nanosheets was 0.8 nm and 0.88 nm, whereas the surface sizes of nanosheets were between ~300 up to 1900 nm and ~200 up to 1700 nm of GO1 and GO2, respectively. The AFM results showed very similar results to the average hydrodynamic diameter data obtained by DLS, which presented

abroad hydrodynamic diameters and three range of sizes for both GO samples as shown in Figure 5-3 (A and B).

Various parameters were applied to cover the investigation, which involved separating the sizes of GO particles, such as a range of low power sonication times, different centrifugal speeds and centrifugal times. Achieving narrow distribution size with one range of GO particles is the main aim of each method. In all experiments, the GO1 and GO2 nanosheets were dispersed in the distilled water for 24 h by stirring, before sonication and centrifugal. Appling these methods separated two immiscible liquids of the suspension of GO. These were the settlement of GO nanosheets at the bottom (B), which contains denser particles of GO, moving away from the axis of the centrifuge, and the supernatant at the top (T), where the is less-dense particles of the mixture that move towards the axis [263]. The DLS test was carried out on both parts of the GO.

5.4.2 Separation of graphene oxide

5.4.2.1 Separation of the large-size of graphene oxide particles

This part focuses on the separation of the large-sizes of GO particles at the bottom of the centrifuge tubes, which occurred faster than other particles, with a high centrifugal force and shorter centrifugal times. One sonication time for 30 minutes was applied to the dispersion of both GOs. It was centrifuged at 4950 g centrifugal force a series of times, namely 10, 22, 45 and 60 seconds, as shown in Table 5-4. The lowest centrifugal time, 10 seconds was selected as a flash centrifugal time to separate the largest particle sizes only with a higher centrifugal force at 11138 g, but the centrifugal force only reached 2782 g at this time, whereas it reached 11138 g at 22 seconds, which was used as the second centrifugal time.

Table 5-4: Separation methods and the hydrodynamic diameters and their ranges (r) (nm) of the sediment samples centrifuged for 30 minutes and centrifuged at 4950 g.

Samples ID	h_d, r / nm	Centrifugal time / second			
		10	22	45	60
GO1	h_d	2156	2085	2015	1902
	r	(743-1064, 5812-8359)	(507-594, 2256-3340)	(706-982, 3686-5131)	(872-1348, 5929-8401)
GO2	h_d	2031	1705	1696	1660
	r	(572-718, 2393-3487)	(1032-1445, 5102-7770)	(944-1323, 5098-7766)	(1421-1470)

Table 5-4 summarizes the hydrodynamic diameters of the both sediment samples and the ranges of the hydrodynamic diameters for both GOs at 60 minutes sonication times. The DLS data showed a slight changing between the results, due to a gradual increase in the centrifugal time from 10 to 60 seconds. This was related to precipitating the large-size particles first and was followed by smaller-size particles, thus reducing the average number of hydrodynamic diameters.

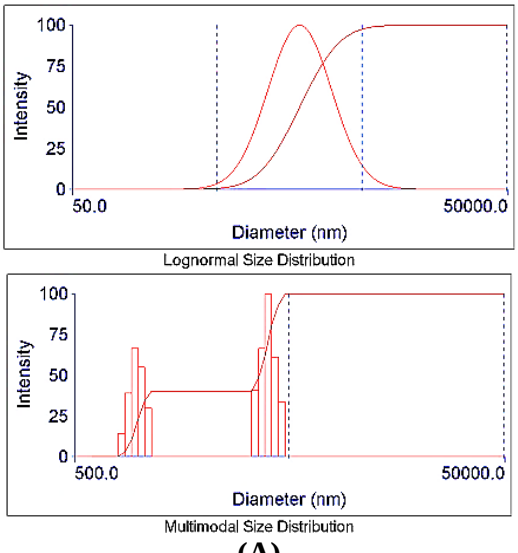

(A)

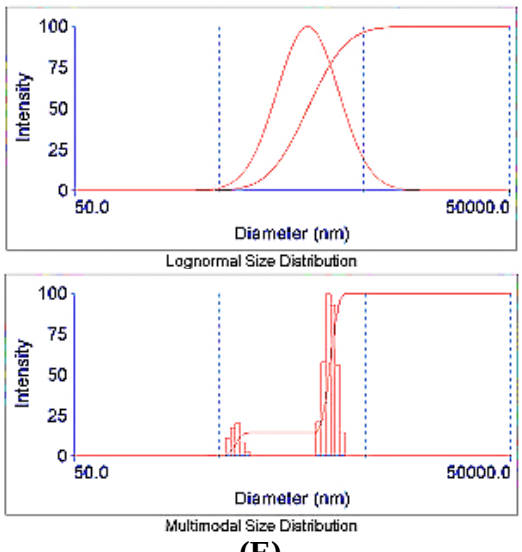

(E)

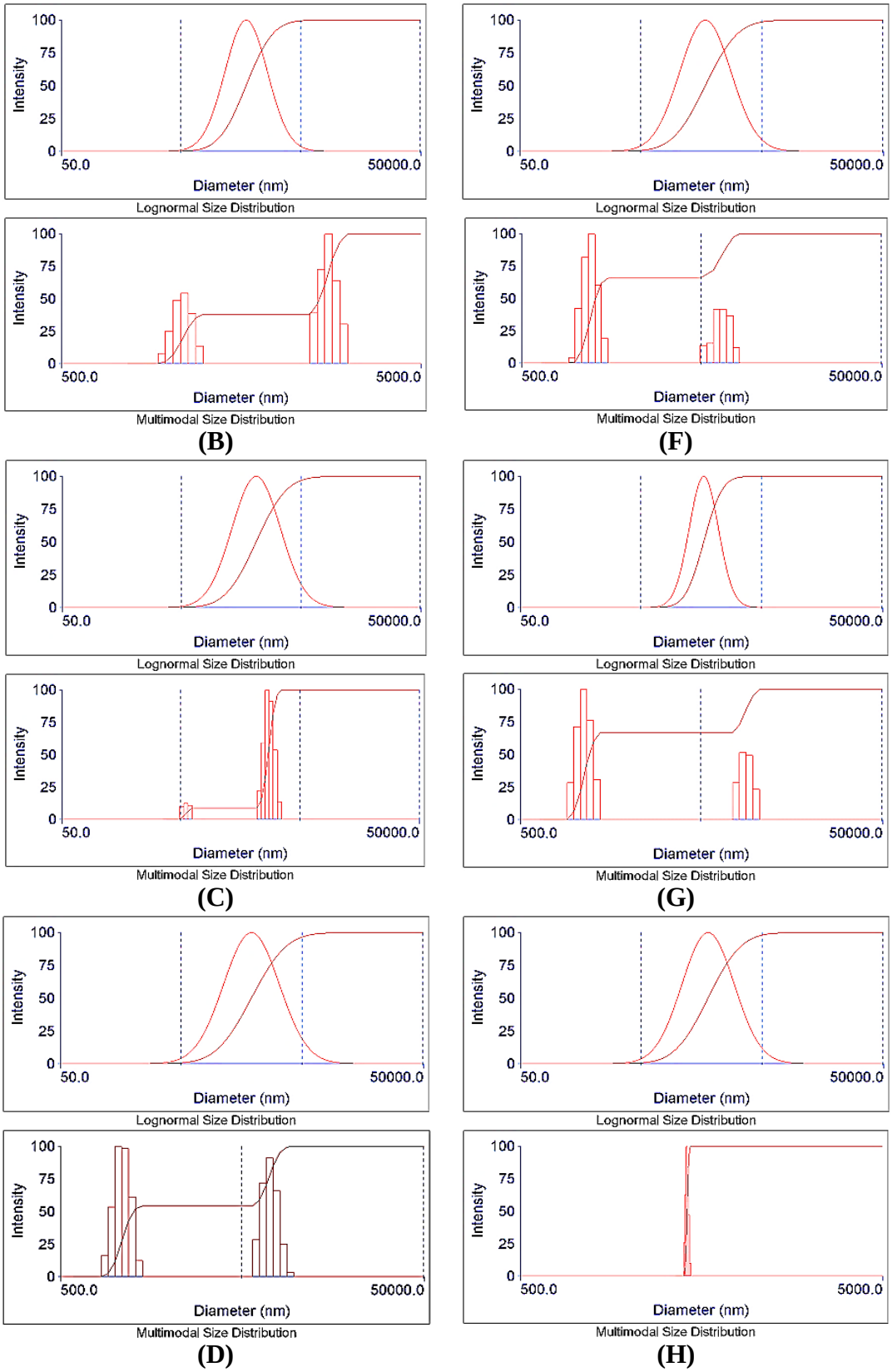

Figure 5-5: The hydrodynamic diameters of sediment samples sonicated for 30 minutes and centrifuged at 4950 g for different times of (A) GO1 for 10 seconds, (B) GO1 for 22 seconds, (C) GO1 for 45 seconds, (D) GO1 for 60 seconds, (E) GO2 for 10 seconds, (F) GO2 for 22 seconds, (G) GO2 for 45 seconds, and (H) GO2 for 60 seconds.

The DLS curves in Figure 5-5 (H) only show one uniform narrow distribution and one range of hydrodynamic diameters size of the GO2 sample at 1660 nm. This was sonicated and centrifuged for 60 seconds, whereas all other samples provided a broad distribution and two different ranges of hydrodynamic diameters, as shown in Table 5-4 and Figure 5-5. The second range could relate to the smaller- or larger-sized particles, which might be attracted by larger-size particles, due to their movement under centrifugal force.

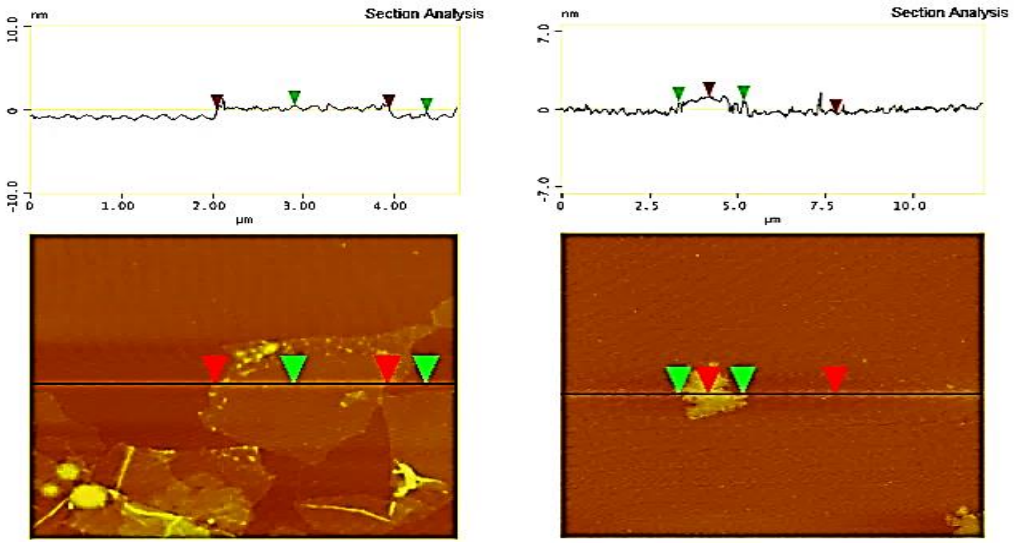

(A) **(B)**

Figure 5-6: The hydrodynamic diameters of sediment samples sonicated for 60 minutes and centrifuged at 4950 g for 60 seconds of (A) GO1 and (B) GO2.

The samples in Figure 5-5 (D and H) were selected to be characterized by AFM because the GO2 sample presents narrow hydrodynamic diameters with only one range and the GO1 sample was selected for comparison. All AFM samples were selected for the same reasons in this study. The AFM images in Figure 5-6 show the lateral dimensions that presented 1894 nm and 1874 nm of GO1 and GO2, respectively, which are different from the DLS in Table 5-4 because the DLS considers all the particles in a spherical shape as discussed

previously. Interestingly, the AFM image of GO1 sample illustrated two ranges of particle size that is similar to the DLS results in Figure 5-5 (D).

As indicated in the results above, this method was developed by adding two more sonication times to become three sonication times, which were 30, 60 and 220 minutes. Also, the centrifugal force was increased from 4950 g to 11138 g in order to achieve a better understanding of its effect. The separation methods and the sediment GO results are summarized in Table 5-5 and Table 5-6, whereas the average hydrodynamic diameter curves are shown in Figure 5-7, Figure 5-9 and Figure 5-10.

Table 5-5: The separation methods and the hydrodynamic diameter (nm) and ranges (r) (nm) of the particle size of sediment samples centrifuged at 11138 g.

Samples ID	**Sonication time / minutes**	**h_d, r / nm**	**Centrifugal time / second**			
			10	**22**	**45**	**60**
GO1	**30**	**h_d r**	1785 (1805-1864)	1611 (1540-1667)	1438 (1437-1466)	1385 (1267-1278)
	60	**h_d r**	0	1434 (1348-1493)	1250 (1149-1276)	1199 (1165-1223)
GO2	**30**	**h_d r**	1531 (1435-1616)	1475 (1424-1532)	1220 (1081-1297)	1190 (1219-1252)
	60	**h_d r**	0	1388 (1284-1427)	1237 (1157-1276)	1102 (470-574, 1277-1560)

In Table 5-5, the DLS results show reduction in the average hydrodynamic diameter of both GOs due to an increase in the sonication time from 30 to 60 minutes for all centrifugal times, where the samples that were sonicated for 30 minutes and centrifuged for 10 seconds precipitated large-sized particles in the bottom of the centrifuge tube, whereas at 60 minutes

sonicated time and centrifuged at the same time, no sediment materials presented at the bottom of the centrifuge tube.

Another important finding is that the average distribution of the hydrodynamic diameter of particle sizes significantly decreased with not only the effect of long sonication time but also with an increase in the centrifugal times and speeds for both GOs, compared to the first centrifugal speed, at 4950 g. These results showed that the g-force forces the large-sized particles to settle at the bottom first, followed by smaller-sizes particles, according to their density or size [263], as shown in Table 5-5.

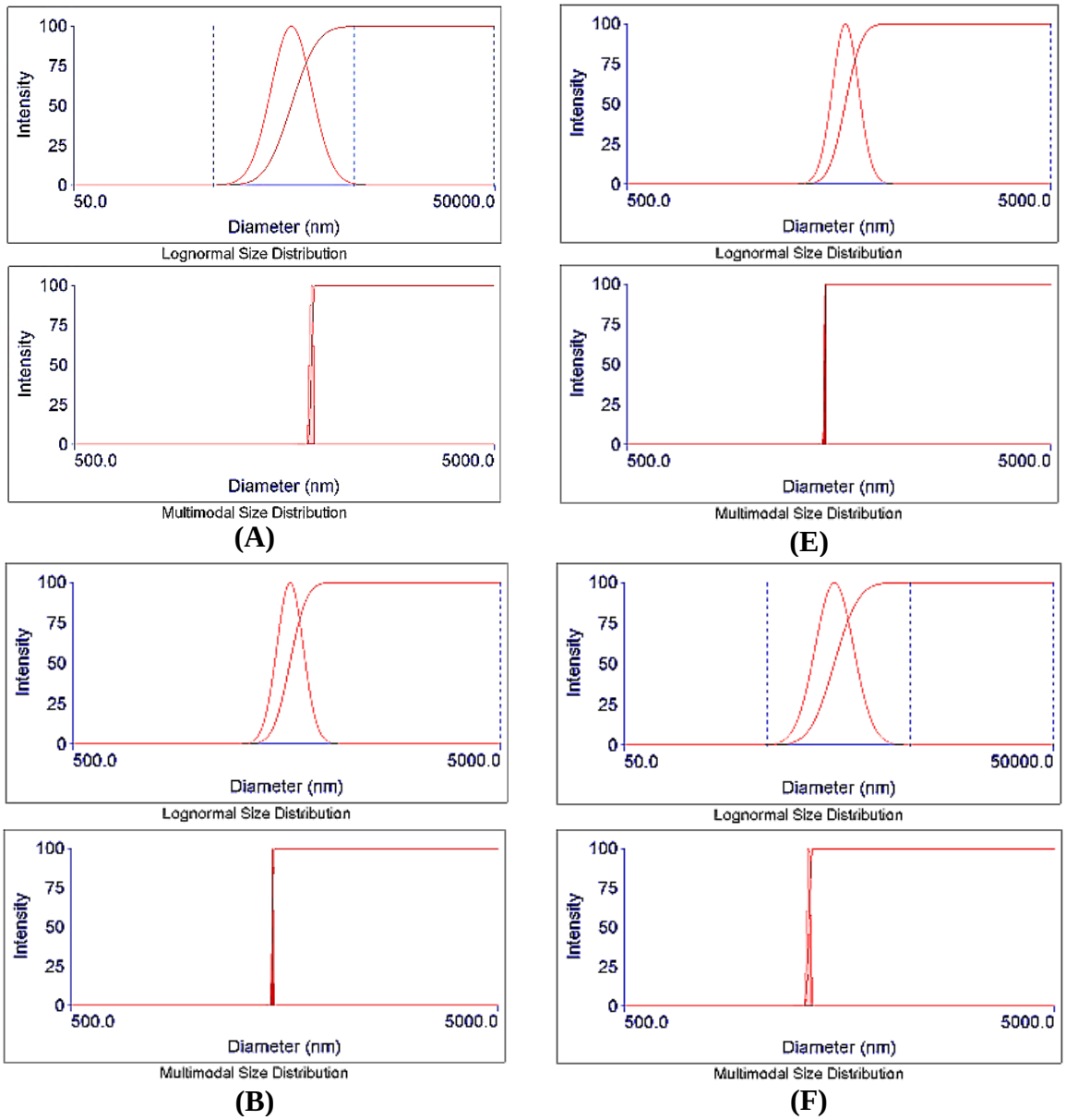

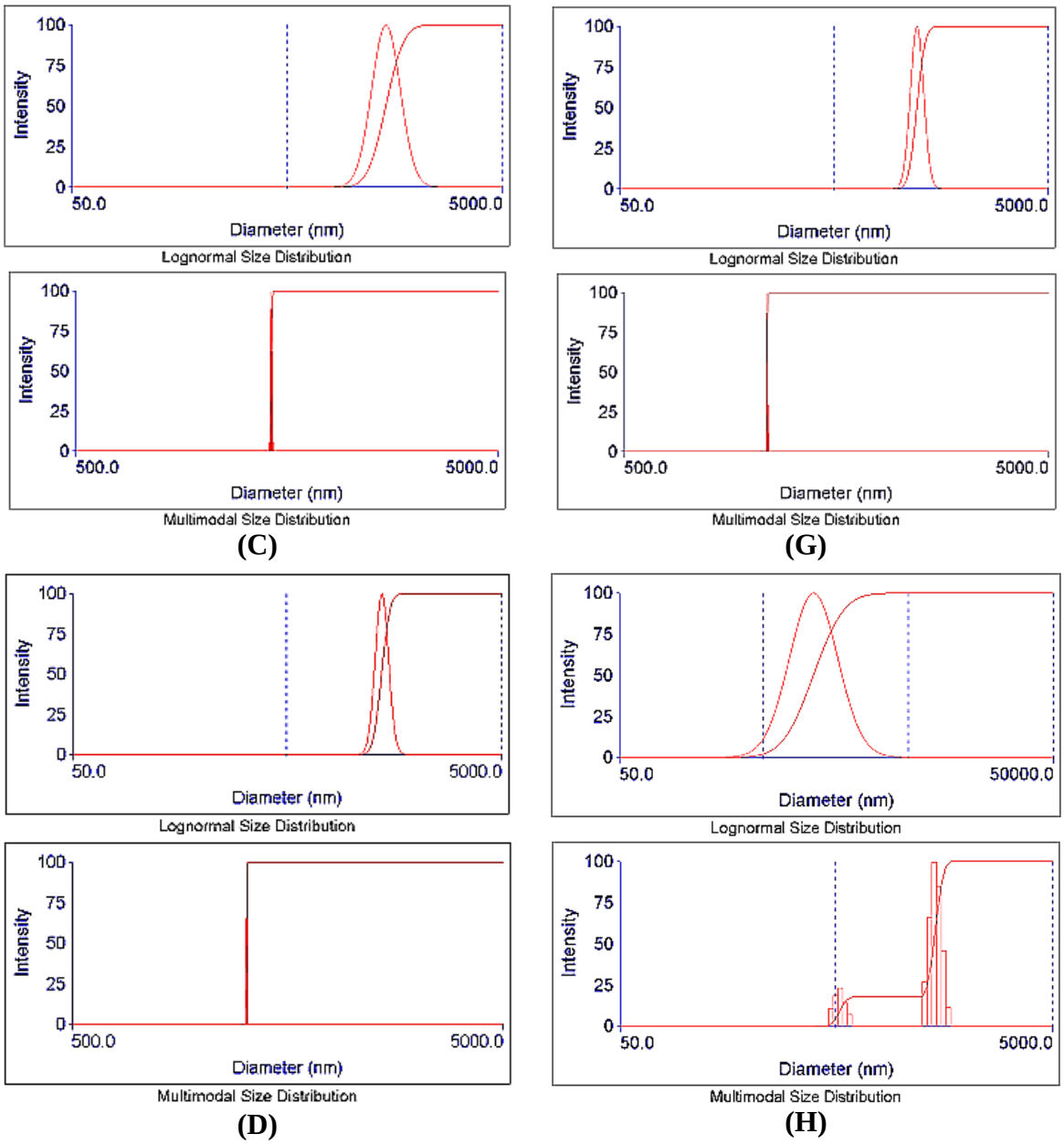

Figure 5-7: The hydrodynamic diameters of sediment samples sonicated for 30 minutes and centrifuged for different times at 11138 g of (A) GO1 for 10 seconds, (B) GO1 for 22 seconds, (C) GO1 for 45 seconds, (D) GO1 for 60 seconds, (E) GO2 for 10 seconds, (F) GO2 for 22 seconds, (G) GO2 for 45 seconds, and (H) GO2 for 60 seconds.

At 30 minutes sonication time, the DLS curves showed one narrow distribution and one range of hydrodynamic diameters of all the samples expected the GO2 sample that was sonicated for 60 seconds as shown in Figure 5-7 (H). The later samples presented a broad

hydrodynamic diameter with two ranges. The hydrodynamic diameters showed different distributions among the samples, which were related to the range of the particles.

The higher centrifugal force at 11138 g applied a strong force for the very short time of 10 seconds each, which only settled down the large-sized particles to the bottom of the centrifuge tube, whereas other particle sizes stratify the other various size suspension at the top part of the tube of the centrifuge. Interestingly, this method showed perfect separation of most samples. These presented a narrow distribution with one range of hydrodynamic diameters, for all GO1 samples, whereas GO2 presented a narrow distribution of hydrodynamic diameters, with one range for three out of four GO2 samples. Interestingly, the centrifugal force illustrated a significant enhancement in the separation of particle size compared to the same samples that were sonicated for 30 minutes with a lower centrifugal force, which was 4950 g, as shown in Figure 5-5.

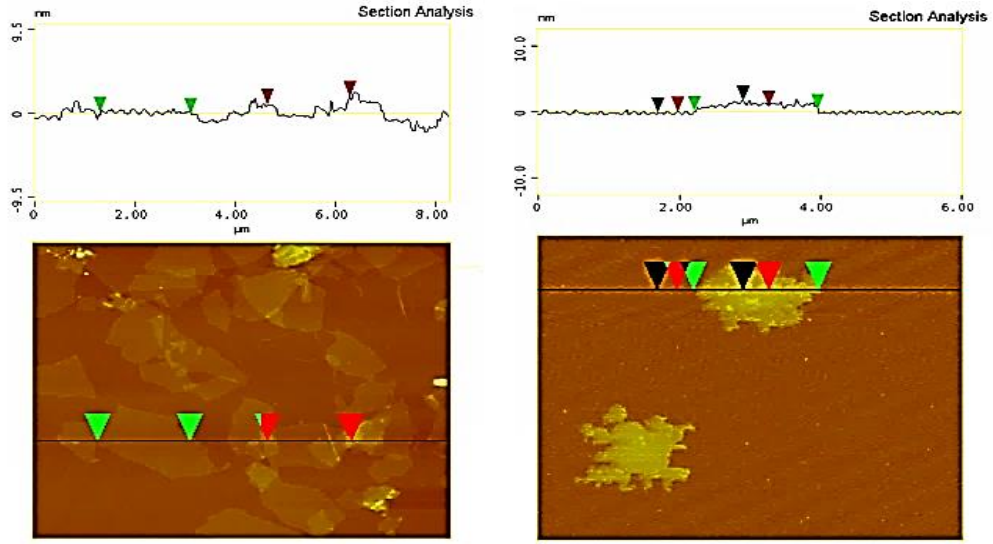

(A) **(B)**

Figure 5-8 : AFM images of (A) GO1 and (B) GO2 sonicated for 30 minutes and centrifuged for 10 seconds at 11138 g.

Figure 5-8 shows the AFM images of the selected GO samples that were sonicated for 30 minutes and centrifuged for 10 seconds, illustrating the average sizes of 1912 nm and 1746 nm of GO1 and GO2 nanosheets, respectively. The AFM image of GO1 demonstrated some medium-sized particles between 1200 - 1450 nm that were attracted by the large-sized particles. These medium-sized particles observed among the large sizes could explain the difference in the distribution of hydrodynamic diameters between the samples. For instance, the DLS results of the GO1 showed a slight broad distribution of hydrodynamic diameters in the GO2 sample, as shown in Figure 5-7 (A and B). However, some smaller-sized particles may be attracted to the large-sized particles at the bottom, as shown in the sample in Figure 5-8 (A) that were not presented clearly in the DLS result, which could overlap with the large-sized particles. More measurements of the above AFM images for both samples were available in the appendix of chapter 4.

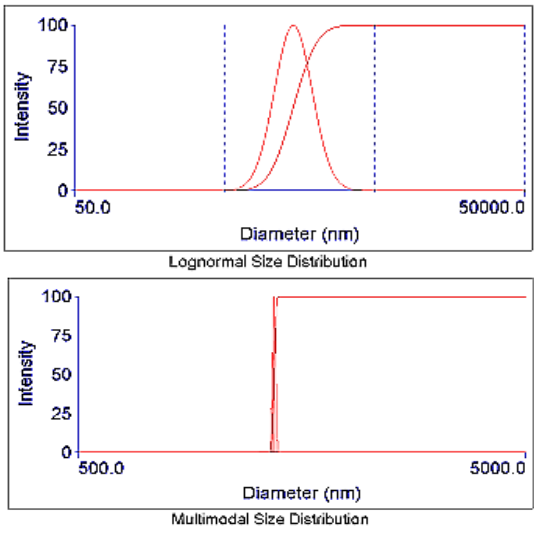

(A)

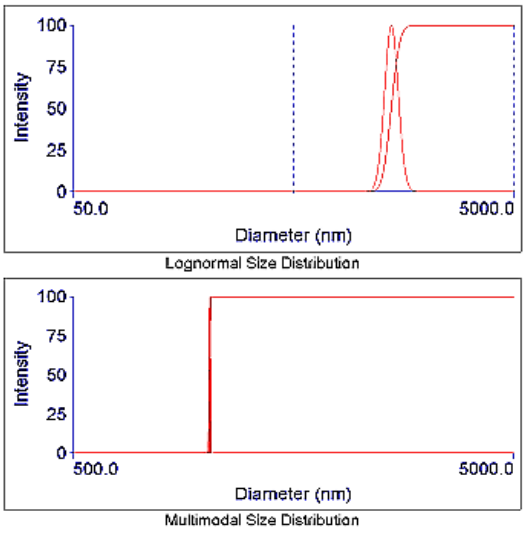

(D)

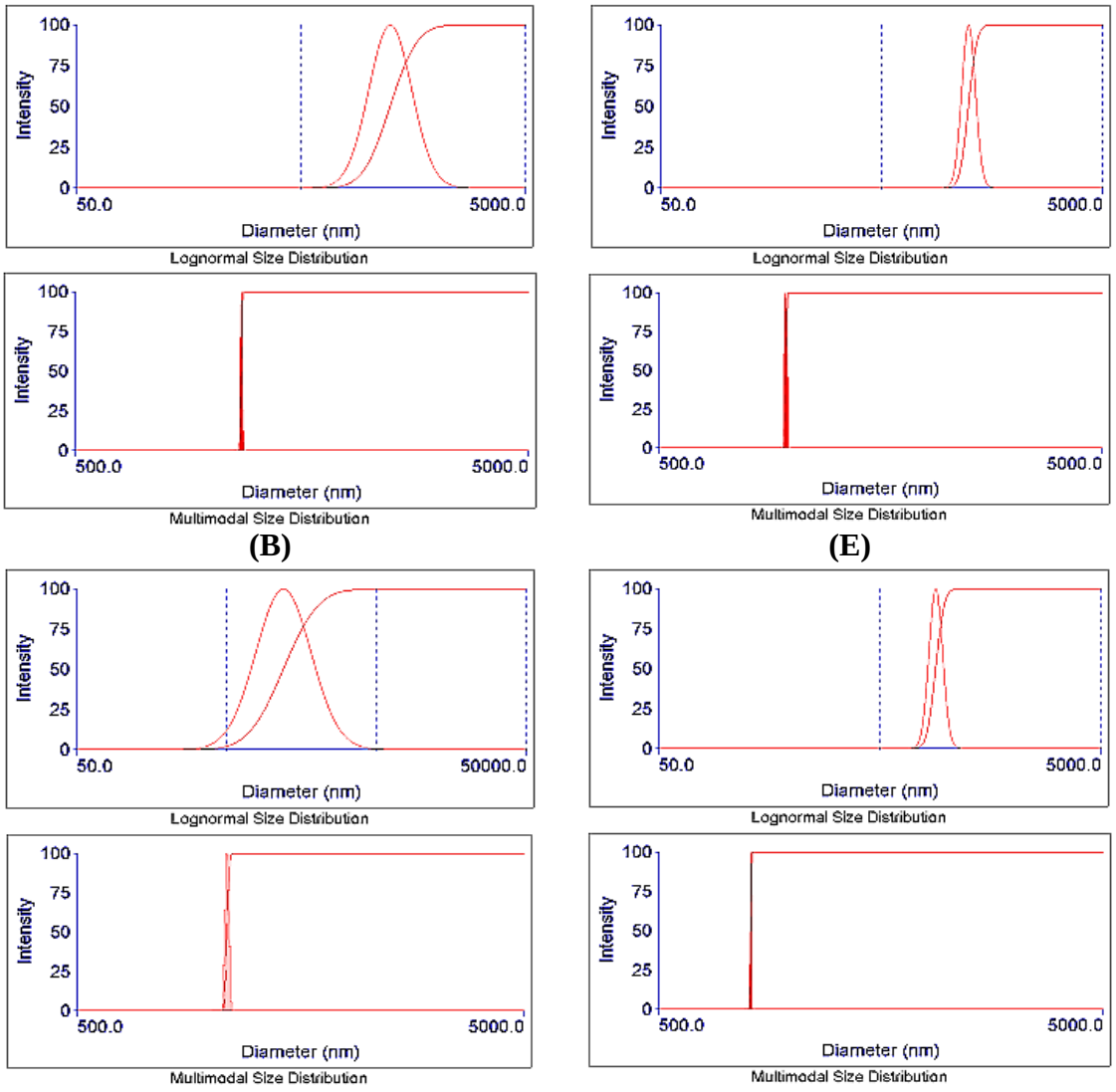

Figure 5-9: The hydrodynamic diameters of sediment samples sonicated for 60 minutes and centrifuged for different times at 11138 g of (A) GO1 for 22 seconds, (B) GO1 for 45 seconds, (C) GO1 for 60 seconds, (D) GO2 for 22 seconds, (E) GO2 for 45 seconds and (F) GO2 for 60 seconds.

At 60 minutes sonication time, centrifuging the samples for 10 seconds did not precipitate any GO materials in the bottom of the centrifuge tube for both of the GO samples. In Figure 5-9 (A, B and C), GO1 and GO2 showed one uniform range and narrow distribution of hydrodynamic diameters, with one range for the all samples of both GOs, whereas the distribution of hydrodynamic diameter curves observed different width peaks for these samples. This showed a close particle size in terms of one uniform range.

Table 5-6: Separation methods and the hydrodynamic diameters (nm) and their ranges (r) (nm) of sediment samples sonicated for 220 minutes and centrifuged at 11138 g.

Samples ID	h_d, r / nm	Centrifugal time / second	
		90	**180**
GO1	h_d **r**	1193 (1157-1271)	962 (287-430, 1152-1559)
GO2	h_d **r**	1148 (1130-1153)	895 (798-911)

Applying a longer sonication time of 220 minutes under a higher centrifugal force at 11138 g for 180 and 300 seconds reduced the hydrodynamic diameter of particle compared to other samples, as shown Table 5-6.

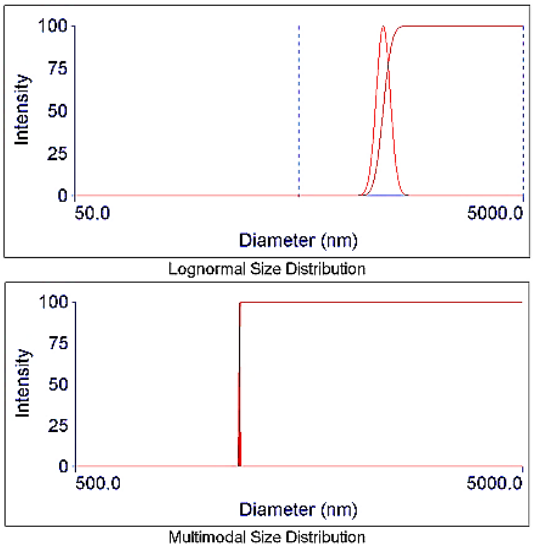

(A)

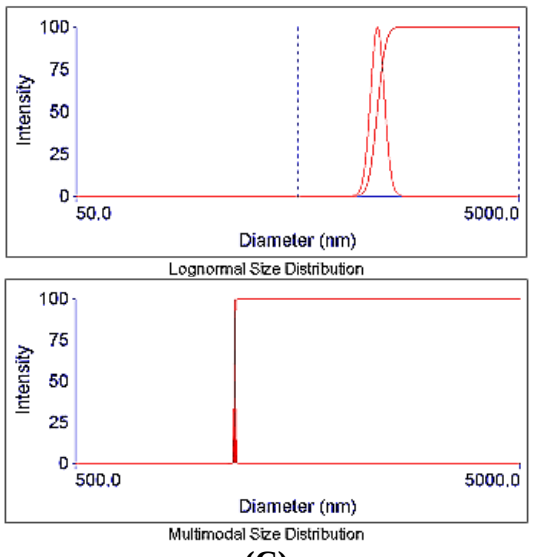

(C)

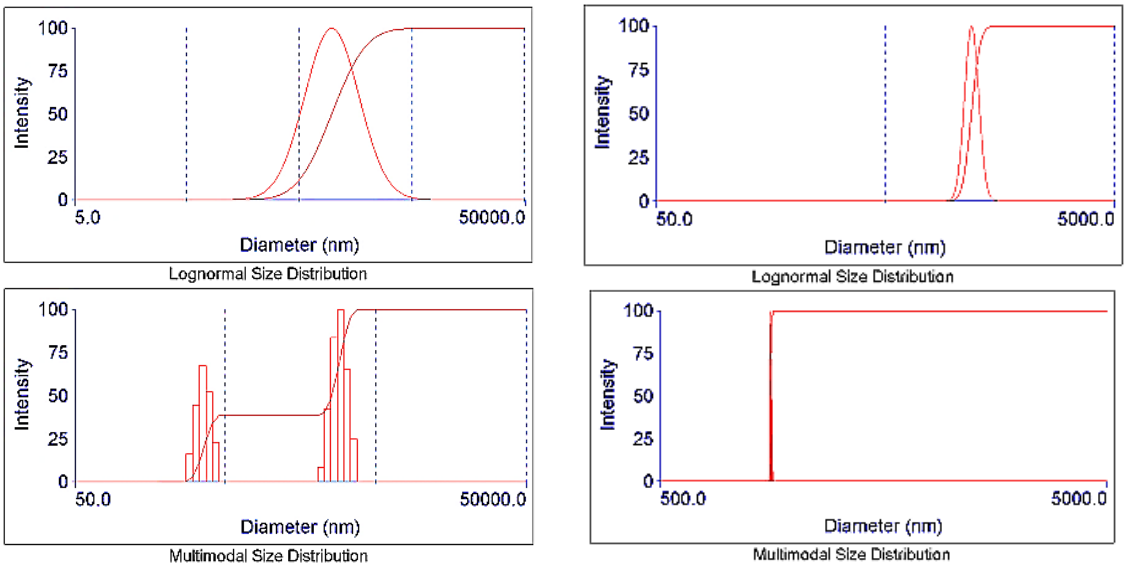

(B) **(D)**

Figure 5-10: The hydrodynamic diameters of sediment samples sonicated for 220 minutes and centrifuged for different times at 11138 g of (A) GO1 for 90 seconds, (B) GO1 for 180 seconds, (C) GO2 for 90 seconds and (D) GO2 for 180 seconds.

The longest sonication time for 220 minutes with longer centrifugal times for 180 minutes observed good separation results of medium-sized of GO particles. These DLS results presented one uniform range and narrow distribution size of hydrodynamic diameters with only one range, as shown in Figure 5-10 (A and C) compared to the 60 minutes sonication times of GO1. GO1 and GO2, showing a perfect separation of the hydrodynamic diameter all the samples except GO1, which was centrifuged for 180 seconds. The latter exhibited broad hydrodynamic diameter. This was related to the second range of the smaller-sized particles that were precipitated by attraction to the larger-sized particles, as shown in Figure 5-10 (B).

However, increasing the sonication time reduced the particle size, meanwhile, the centrifugal force and time were associated to reduce the particle size through attracting the small particles with some of the large-sized particles, where the latter pulled the smaller-sized particles toward the bottom of the centrifuge tube under centrifugal force during the

movement. Therefore, these reasons were considered the keys to reducing hydrodynamic diameters.

Table 5-7: The summary of hydrodynamic diameters (nm) of the separation methods for large particle size with a series of sonication time, centrifugal force and time.

Sonication time / minute	**30**		**30**		**60**		**220**	
Centrifugal force / g	**4950**		**11138**		**11138**		**11138**	
Centrifugal time / second	**GO1**	**GO2**	**GO1**	**GO2**	**GO1**	**GO2**	**GO1**	**GO2**
10	2105	2031	1785	1531	0	0	-	-
22	2085	1705	1611	1475	1434	1388	-	-
45	2015	1696	1438	1220	1250	1237	-	-
60	1902	1660	1385	1190	1199	1102	-	-
90	-	-	-	-	-	-	1193	1148
180	-	-	-	-	-	-	962	895

Table 5-7 summarizes the DLS date of the average distribution of hydrodynamic diameters for the separation of the large-sized of GO particles. Increasing the sonication time from 30 to 60 and then to 220 minutes significantly decreased the particle sizes, from 2156 and 2031 to 962 and 1102 nm of both GO1 and GO2, respectively. Additionally, the other important factors were the centrifugal force and time, where the results showed the significant effect of forcing the particles to settle down. This force was clearly seen in the large-sized particles, whereas it slightly decreased when reducing particle increasing the centrifugal forces, depending on the particle density or size, where smaller-sized particles require a higher centrifugal force and longer centrifugal time. For instance, the hydrodynamic diameters reduced slightly with an increase in the centrifugal time from 60 to 90, then to 180 seconds.

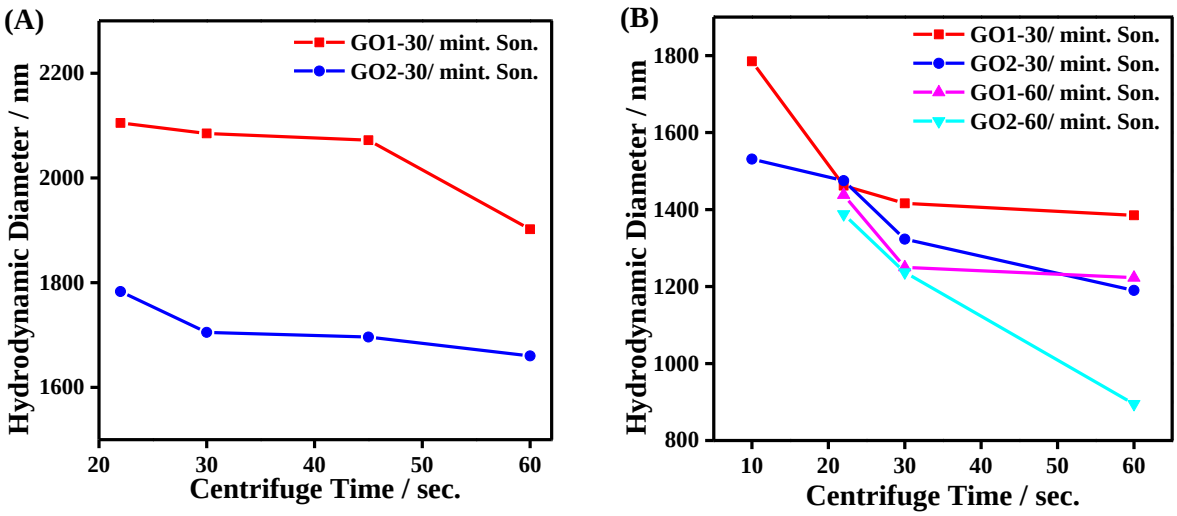

Figure 5-11: The effect of sonication time on the behaviour of average hydrodynamic diameter with different centrifugal times of GO samples sonicated for (A) 30 minutes with centrifugal force at 4950 g and (B) 30 and 60 minutes at 11138 g.

Figure 5-11 shows the behaviour of the hydrodynamic diameter of GOs after the effect of sonication time, which reduced the hydrodynamic diameter of GOs, with an increase in sonication, centrifuged force and times. Figure 5-11 (A) demonstrates the reduction of GO particles size with an increase in centrifugal force and time, due to the precipitation of the large particle first that followed by the smaller and so on. Increasing the sonication time from 30 to 60 minutes decreased the size of GO particles, where the 10 seconds centrifugal time did not precipitate any particle sizes for either GO, as shown in Figure 5-11 (B). The precipitation of particles depended on the applied force of the centrifuge. These forces moved the particles at a certain speed toward the bottom. Large-sized particles could precipitate at the short centrifugal time under a low or high force to settle at the bottom, whereas to precipitate the medium and smaller-sized particles, a higher centrifugal force and longer centrifugal time were required, according to their density or size [263].

The most interesting element in this part of the process was the significant separation of the large particle size for various sizes above more than 1 µm, with a uniform size.

Uniform size is the most significant issue for a broad application. Also, a longer sonication time showed a reduction in GO particle size when increasing the sonication time in agreement with the literature, whereas in this study, a lower power of sonication succeeded to reduce the particle size of GO without any defects, even with a long sonication time compared to the literature [217,218], in which defect was seen when using the high power and long-time of sonication.

The value of the DLS data was the average of the hydrodynamic diameter of particles, and that could give a value in the range of this average. Another important issue was the behaviour of the particles that could change depending on the factors, which was used to separate the particles, as discussed. These results observed good methods of separating large-sized particles but the mass ratio of these samples was low. Also, this part gave clear evidence and understanding to the effect of sonication time, which could help in graphene applications. Another important finding was the centrifugal force. It showed a notable effect on separation the GO particle size when this was increased from 4950 to 11138 g, which is not fully understood and needs to be investigated at a wide range of speeds. The next part focuses on separating the medium- and small-sized GO particles using the effect of centrifugal force in.

5.4.2.2 Separation of medium-sized particles of graphene oxide

Separating the medium- and small-sized particles is the main focus in next two parts; firstly, it looks at ways of separating the medium-sized of GO particles from the sediments in the centrifuge tube, while small-sized particles were separated from the top part at the bottom of the tube in the second part. The effect of centrifugal force and time were used as the main factors in both parts. Ranges of centrifugal forces were applied for several centrifugal times on GO samples after sonicated for different timeframes in each separation method.

In the separation of the medium-sized particles, the same centrifugal speeds were used, but with higher sonication time at low power. This long sonication time reduces the hydrodynamic diameter of GO particles [218], which made the precipitation of the GO particles more difficult. This design could bring a better understanding of the effect of centrifugal speeds as an important parameter for separating GO particle sizes. The separation method of samples was stopped after precipitating the samples. Therefore, methods were developed by applying the same four centrifugal forces, namely 137, 1237, 4950 and 11138 with various centrifuge timeframes that started at 1 minute and went up to 90 minutes and were sonicated for 220 minutes, as shown in Table 5-8.

Table 5-8: Separation methods and effect of different centrifugal forces on the sediment samples that sonicated for 220 minutes.

Centrifugal force / g	Centrifugal time / minute					
137	1	5	15	30	45	90
1237	1	5	15	30		
4950	1	5				
11138	1	5				

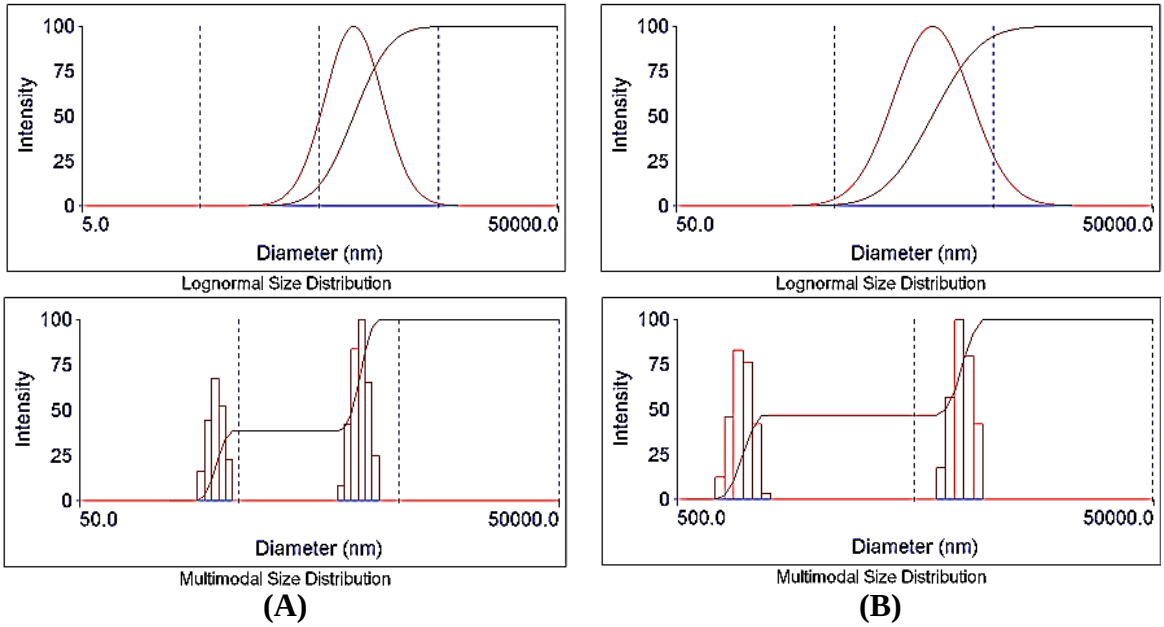

Figure 5-12: The hydrodynamic diameters of bottom samples sonicated for 220 minutes and centrifuged for 90 minutes at 137 g for of (A) GO1 and (B) GO2.

At 137 g centrifugal force, centrifugal the sample with 1, 5, 15, 30 and 45 minutes did not precipitate any particles of either GO to the bottom of the centrifuge tubes, while the long sonication time reduced sizes of GO particles. Also, applying a low centrifugal force and time did not provide enough force to settle the particles down. However, the particles centrifuged for 90 minutes exhibited a hydrodynamic diameter of 962 nm of GO1 and 1465 nm of GO2, illustrated a broad distribution of hydrodynamic diameters with two ranges (287-430, 1152-1559) nm and (756-1080, 1408-1548) nm, of GO1 and GO2 particle size, as shown in Figure 5-12 (A and B), respectively.

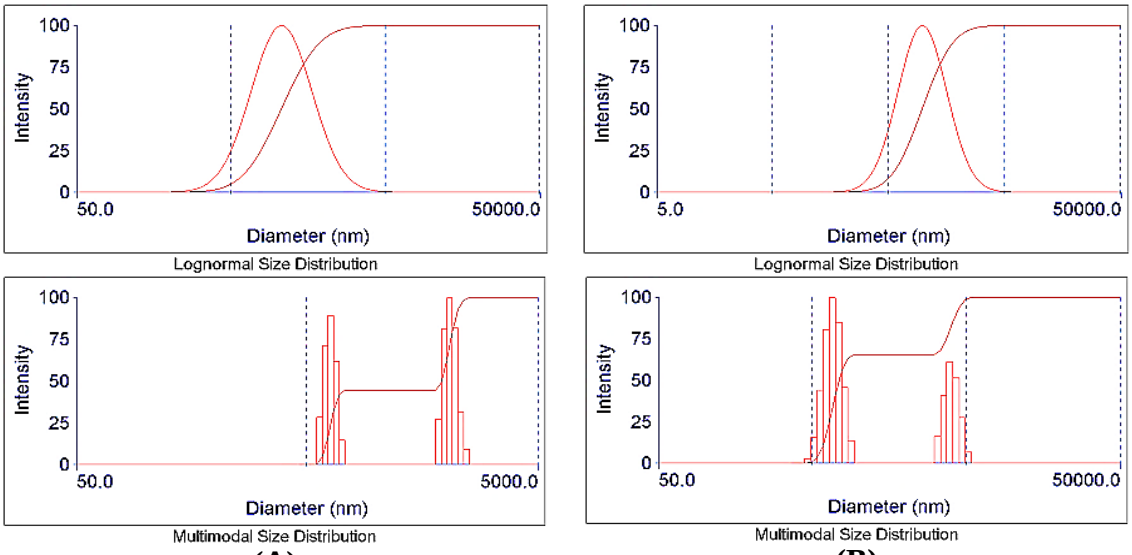

Figure 5-13: The hydrodynamic diameters of bottom samples sonicated for 220 minutes and centrifuged at 1237 g for 60 minutes of (A) GO1 and (B) GO2.

At 1237 g centrifugal force, the sample centrifuged for 1, 5 and 15 minutes and presented also without any precipitation of GO particles at the bottom of the centrifuge tubes, whereas it settled down at 30 minutes, which showed 1060 nm and 971 nm for GO1 and GO2, respectively. It provided a broad distribution of hydrodynamic diameters of both GO samples as shown in Figure 5-13. These samples showed two ranges, at (564-707, 847-1115)

and (509-688, 842-1094) nm, accordingly. The GO particle precipitated at 30 minutes in this method after increasing the centrifugal force from 137 to 1237 g. These results showed the clear influence of an increase in the centrifugal force at the same centrifugal time.

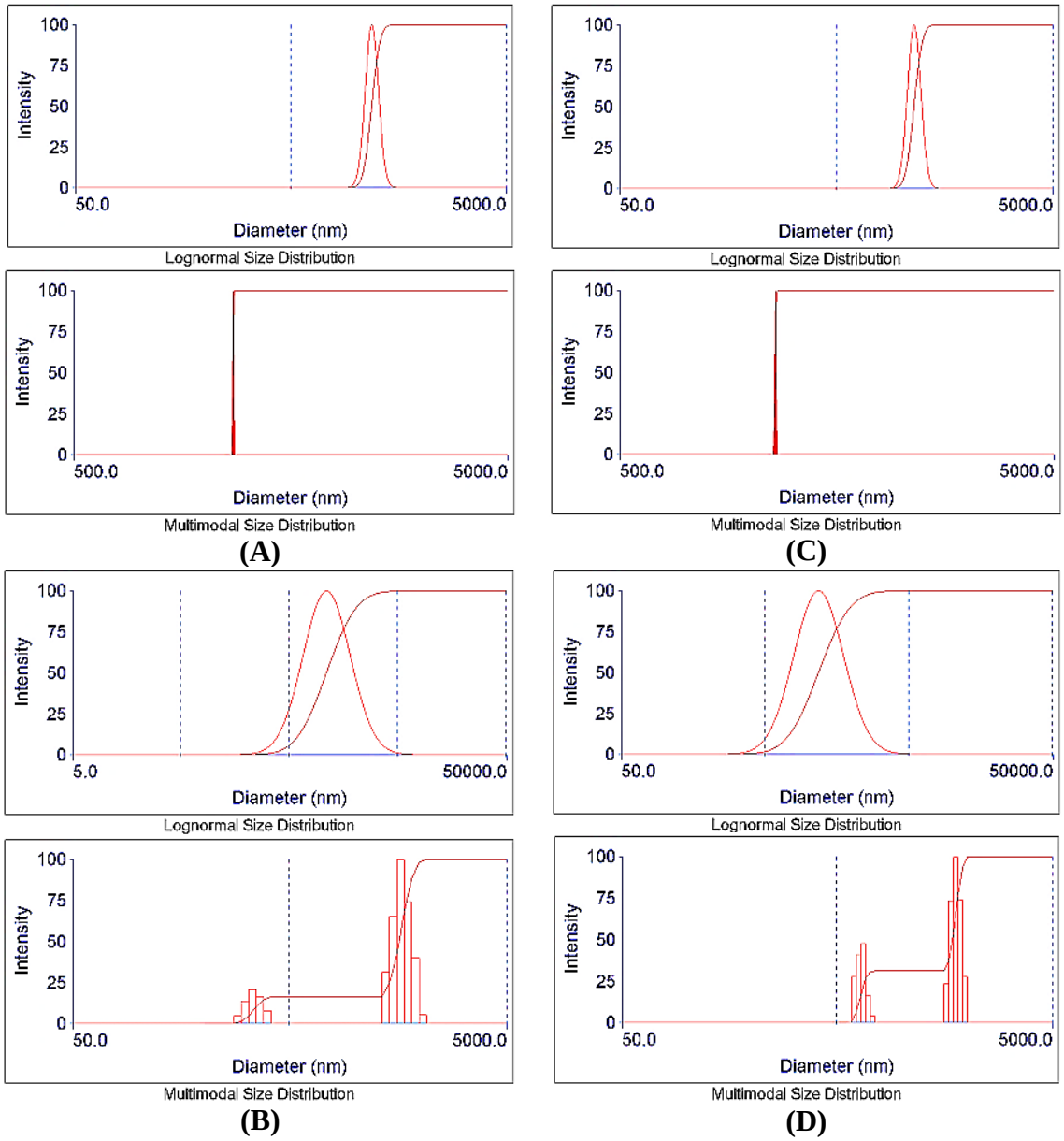

Figure 5-14: The hydrodynamic diameter of sediment samples sonicated for 220 minutes sonication and centrifuged for different times at 4950 g of (A) GO1 for 5 minutes, (B) GO1 for 15 minutes, (C) GO2 for 5 minutes and (D) GO2 for 15 minutes.

At 4950 g centrifugal force, the separation of GO particles was precipitated at the bottom of the centrifuge tubes at 5 and 15 minutes. The DLS curved demonstrated the narrow distribution of hydrodynamic diameter of the GO particles sizes, at 1193 nm and 1148 nm, whereas it illustrated a broad distribution size at 1097, 1015 for 5 and 15 minutes timeframes for GO1 and GO2, respectively. Both GO samples that precipitated at 5 minutes presented one range of hydrodynamic diameter (1157-1171) and (1130-1153) nm, whereas increasing the centrifugal for 5 minutes demonstrated two ranges of particle size (310-393, 893- 1145) and (596-727, 1002-1059) nm, as shown in Figure 5-14 (A, C and B, D), respectively. This illustrates another improvement in the separation of one uniform range and narrow distribution size of hydrodynamic diameter, where the results confirmed the positive effect of an increase in the centrifugal force.

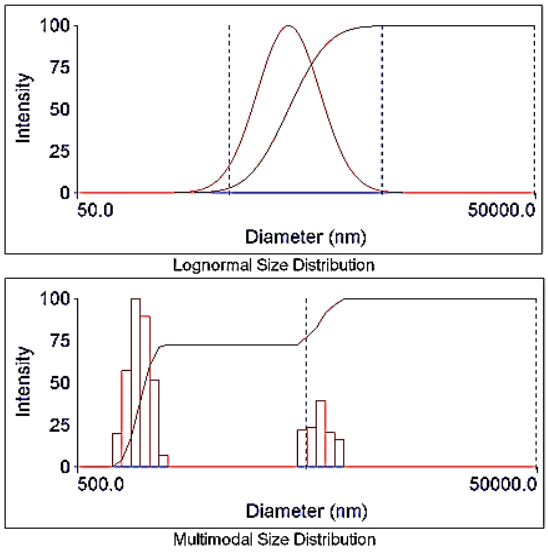

(A)

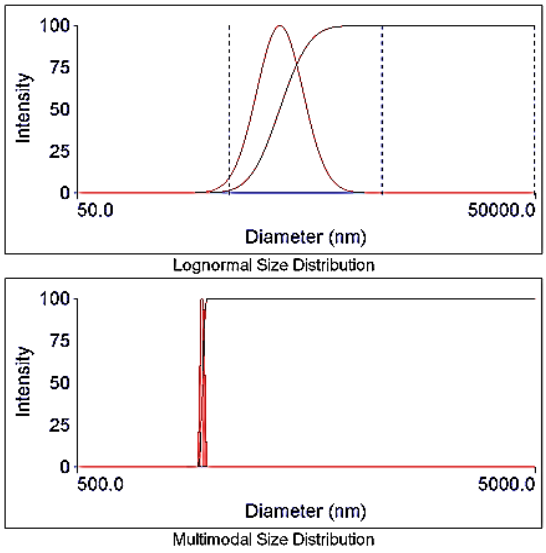

(C)

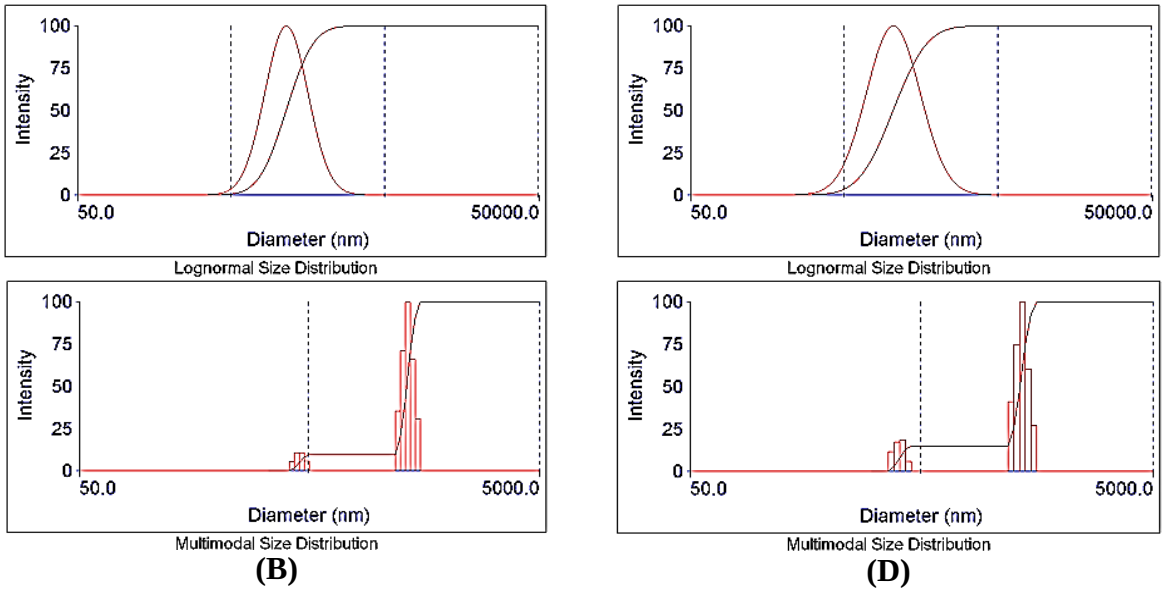

Figure 5-15: The hydrodynamic diameter of sediment samples sonicated 220 minutes and centrifuged at 11138 g for different times of (A) GO1 for 1 minute, (B) GO1 for 5 minutes, (C) GO2 for 1 minutes and (D) GO2 for 5 minutes.

At 11138 g centrifugal force, the sediments of GO particles instead at 1 and 5 minutes at the bottom of the centrifuge tubes. GO1 samples exhibited a reduction in the hydrodynamic diameter from 1218 nm to 1047 nm when increasing the centrifuge timeframe from 1 to 5 minutes, whereas the GO2 samples exhibited a slightly lower value between these centrifuge times, at 1067 and 1042 nm for 1 and 5 minutes, respectively. Figure 5-15 shows a broad distribution of hydrodynamic diameters, with two ranges of the samples (745-1144, 4762-69114), (418-486, 1210-1481) and (313-466, 910-1141) nm, except for the GO2, with 1067 nm that had only one range of particles between (923-1157) nm when centrifuged for 1 minute.

Table 5-9: The summary of the hydrodynamic diameters (nm) of the separation methods for a medium particle size of different centrifugal force for a series times and 220 minutes sonication time.

Centrifugal time / minute	Centrifugal force / g							
	137		1237		4950		11138	
	GO1	GO2	GO1	GO2	GO1	GO2	GO1	GO2
1	0	0	0	0	0	0	1218	1067
5	0	0	0	0	1193	1148	1047	1042
15	0	0	0	0	1097	1015	-	-
30	0	0	1060	971	-	-	-	-
45	0	0	-	-	-	-	-	-
90	962	1465	-	-	-	-	-	-

Applying these methods succeeds in separating the medium-size particles between 1465 and 962 nm of GO, as summarized in Table 5-9. Applying a long sonication timeframe reduced particle size, making the precipitation of these particles more difficult, requiring more centrifugal forces and times. This helped us to investigate and understand the effect of centrifugal force for various timeframes on separation particle size. Increasing the centrifugal speed (force) presented one of the main factors and a significant effect on the separation of GO particle sizes.

5.4.2.3 Separation of the small-sized of graphene oxide particles

In the separate of the small-sized particles, different separation methods were applied to separate it from the top part of the tube of the GOs samples, where four different centrifugal forces of 137, 1237, 4950 and 11138 g were applied for three various centrifugal times of 10, 45 and 90 minutes for both GO1 and GO2. All the GO samples were sonicated for 30 minutes.

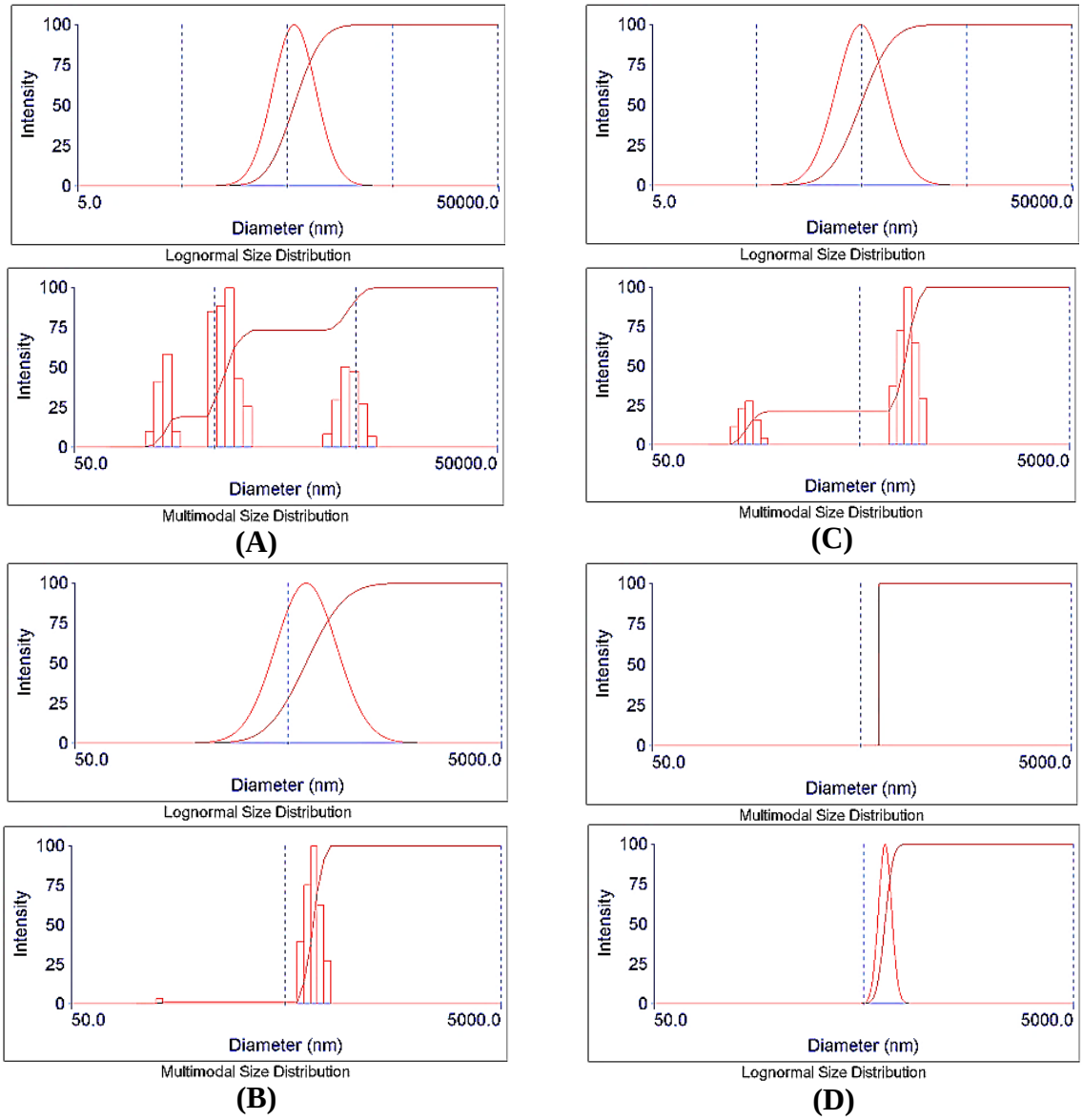

Figure 5-16: The hydrodynamic diameters of top samples sonicated for 30 minutes and centrifuged for three different times at 137 g of (A) GO1 for 45 minutes, (B) GO1 for 90 minutes, (C) GO2 for 45 minutes and (D) GO2 for 90 minutes.

At 137 g centrifugal force, the 10 minutes centrifugal time did not precipitate or separated out any GO particle sizes in the bottom of the centrifuge tubes of either GO samples, where a low centrifugal force and time provided low power to precipitate the GO particles but kept it suspended in the solution. At 45 minutes centrifugal time, Figure 5-16 (A and C) shows a broad hydrodynamic diameter of 574 and 483 nm for GO1 and GO2,

respectively. The low centrifugal speed for a longer centrifugal time attracted differently-sized particles toward the bottom of the centrifuge tube, providing more than one range of particle sizes. where GO1 samples reported three ranges of hydrodynamic diameters (171-264, 473-846 and 2617-2953) nm, where the latter range of size might be dust on the samples, whereas GO2 demonstrated two ranges of particle sizes, at (135-173 and 711-992) nm. These particles size ranges lowered the hydrodynamic diameter to lower values.

At 90 minutes centrifugal time, GO1 showed a broad hydrodynamic diameter of 610 and GO2 illustrated a narrow hydrodynamic diameter of 634 nm of GO1 and GO2 as shown in Figure 5-16 (B and D), respectively. These samples observed one range of particle size at (583-658) and (600-680) nm, respectively, except one size of the smaller particle, which presented in the GO1 samples at 128 nm, as shown in Figure 5-16 (B). A longer centrifugal time provided a strong factor that attracted all the large-sized particles to precipitate down, followed by other smaller particle sizes, and so on, which left the smallest particle sizes suspended in the top part of the solution compared to samples that centrifuged for 45 minutes, as shown in Figure 5-16 (A and C).

Table 5-10: Separation methods and the hydrodynamic diameters (nm) and ranges (r) (nm) of the particle size of the top samples that sonicated for 30 minutes and centrifuged for three different times at 1237 g.

Samples ID	**$h_{d,\,r}$ / nm**	**Centrifugal time / minute**		
		10	**45**	**90**
GO1	**h_d** **r**	706 (295-407, 1370-2052)	644 (359-505, 1969-2766)	505 (256-305, 867-1093)
GO2	**h_d** **r**	753 (100-188, 572-1081, 2805-5296)	563 (202-269, 689-1142)	482 (348-554, 4999, 7934, 8907)

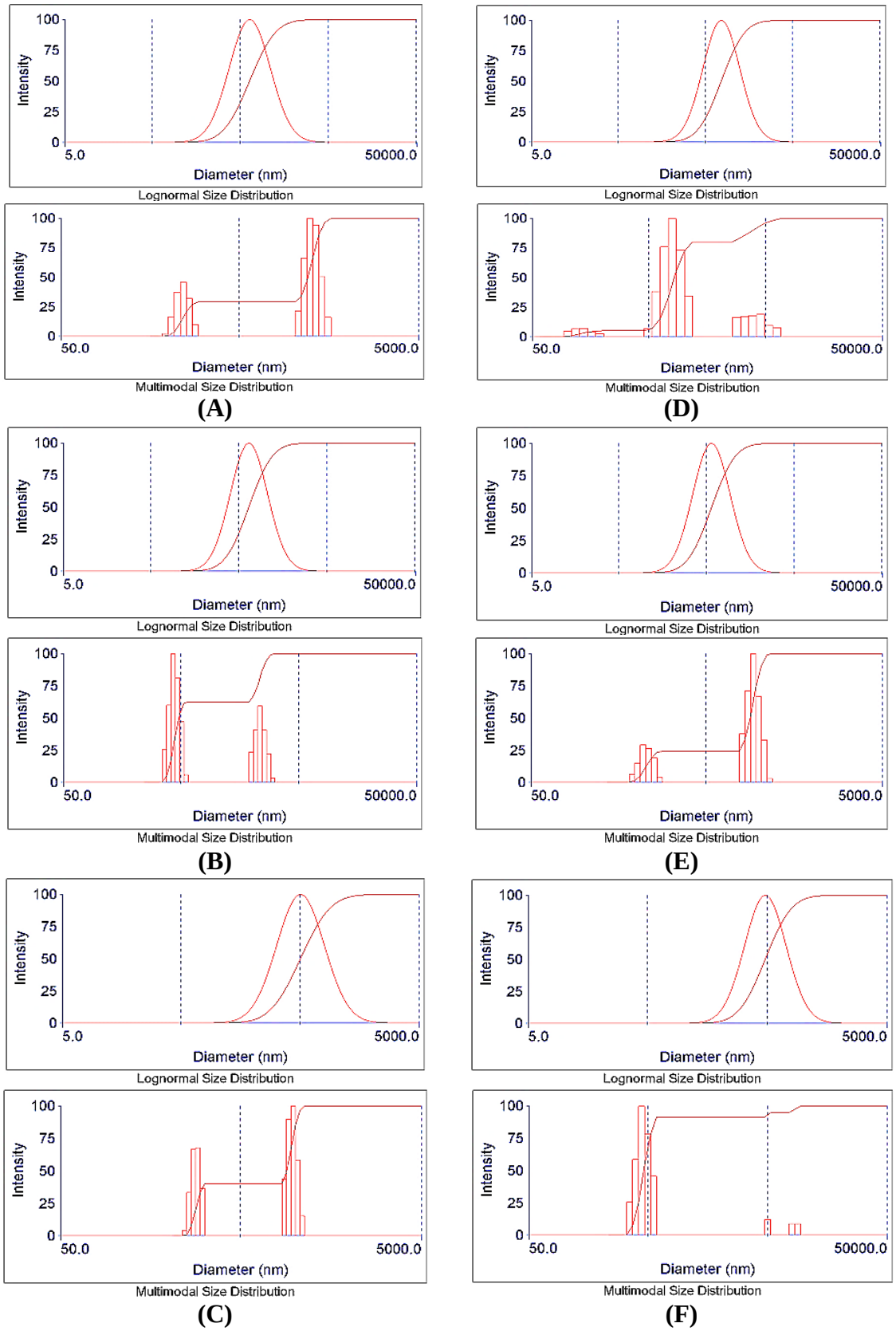

Figure 5-17: The hydrodynamic diameters of top samples sonicated for 30 minutes and centrifuged for different times at 1237 g of (A) GO1 for 10 minutes, (B) GO1 for 45 minutes, (C) GO1 for 90 minutes, (D) GO2 for 10 minutes, (E) GO2 for 45 minutes and (F) GO2 for 90 minutes.

At 1237 g centrifugal force,

Table **5-10** shows a decrease in the hydrodynamic diameters of both GO samples with an increase in centrifugal times. In Figure 5-17, both GOs in this method demonstrated a broad distribution of the hydrodynamic diameters, with more that one range of both GO1 and GO2 that centrifuged for 10, 45 and 90 minutes, as shown

Table **5-10** and Figure 5-17. These different ranges of particle sizes turned the hydrodynamic diameters into a broad distribution. However, the effect of increasing centrifugal time clearly reduced the hydrodynamic diameters. Most of the hydrodynamic diameters of both GOs in this method contained different particle sizes, expect the GO2 sample, as shown Figure 5-17, which was centrifuged for 90 minutes, and contained a very small ratio of the large-sized particles, as shown in Figure 5-17 (F).

Table 5-11: Separation methods, the hydrodynamic diameters (nm) and their ranges (r) (nm) of top samples that sonicated for 30 minutes and centrifuged for three different speeds at 4950 g.

Samples ID	**h_d, r / nm**	**Centrifugal time / minute**		
		10	**45**	**90**
GO1	**h_d** **r**	703 (243-605, 1828-3193)	495 (231-328, 934-1234)	469 (214-292, 865-1377)
GO2	**h_d** **r**	584 (221-288, 889-1239)	446 (245-338, 1227-1694)	394 (181-219, 607-783)

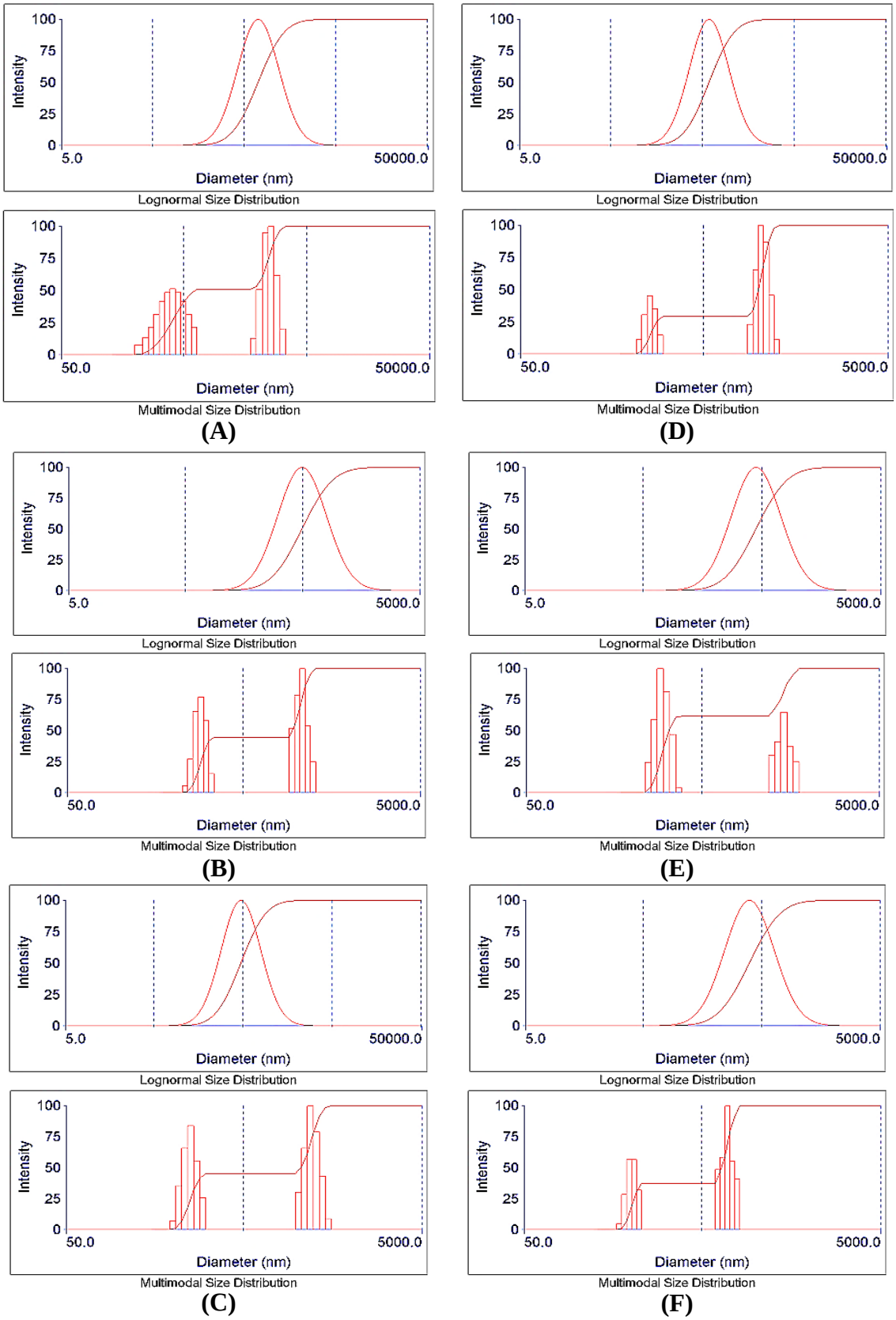

Figure 5-18: The hydrodynamic diameters of top samples sonicated for 30 minutes and centrifuged for three different times at 4950 g of (A) GO1 for 10 minutes, (B) GO1 for 45 minutes, (C) GO1 for 90 minutes, (D) GO2 for 10 minutes, (E) GO2 for 45 minutes and (F) GO2 for 90 minutes.

At 4950 g centrifugal force, Table 5-11 shows a reduction of the hydrodynamic diameters that decreased from 703 to 495 then to 469 nm, and 584 to 446 then to 394 nm for GO1 and GO2 samples, respectively, where hydrodynamic diameters of the particle size gradually decreased with an increase in the centrifugal times and force that increased the applied force on the particle sizes of GO. These samples exhibited two ranges of separation particle sizes that explained a broad distribution of the hydrodynamic diameters, as shown in Figure 5-18.

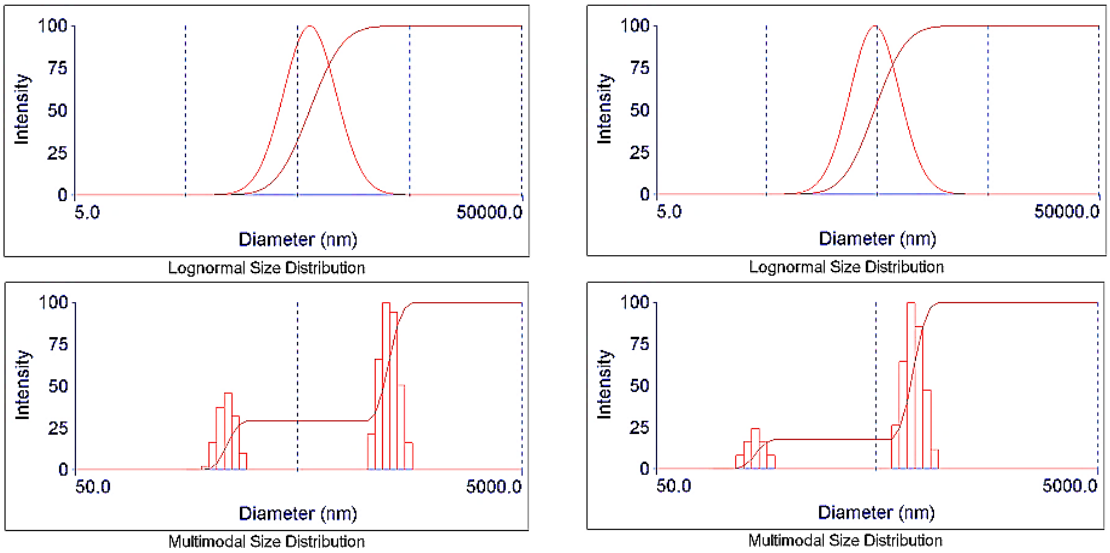

Figure 5-19: The hydrodynamic diameters of top samples sonicated for 30 minutes and centrifuged for 90 minutes at 11138 g of (A) GO1 and (B) GO2.

At 11138 g centrifugal force, both GO samples were centrifuged for 90 minutes, as shown in Figure 5-19, which illustrates a broad average distribution of hydrodynamic diameters of GO1 and GO2 samples at 634 nm and 468 nm, respectively. This did not give a fully uniform hydrodynamic diameter particle size in spite of using a high centrifugal speed and different times. It presented two ranges of hydrodynamic diameters in both samples, at (223-281, 1056-1557) and (129-165, 607-911) nm, respectively. The samples comprised

small-sized particles with low ratios of smallest-sized particles suspended on the top part. Where the precipitation of particle size is dependent on their size and density this became more difficult, given the nanosize of the GO particles, even with higher centrifugal speeds and longer centrifugal times, as shown in Figure 5-19.

Table 5-12: The summary of the hydrodynamic diameters (nm) of the separation methods for small particle size under different centrifugal force for three different centrifugal times and 30 minutes sonication.

Centrifugal time / minutes	**Centrifugal force / g**							
	137		**1237**		**4950**		**11138**	
	GO	**GO2**	**GO1**	**GO2**	**GO1**	**GO2**	**GO1**	**GO2**
10	0	0	706	753	703	584	-	-
45	574	483	644	563	495	446	-	-
90	610	634	505	482	469	394	634	468

Table 5-12 summarizes the DLS results of separating of the smaller-sized particles. Increasing the centrifugal speed provides an important factor for separating the particle size; for instance, the centrifugal force at 137 g did not precipitate any materials, whereas this was precipitated after increasing the centrifugal force at the same time. Increasing the centrifugal force forced all the large- and small-sizes particles to precipitate in samples at the bottom of the tube and left the small-sized particles at the top of centrifugal speed. Also, the longer centrifugal time reduced the particle size by precipitating the larger particle size and keeping the smallest particle suspending in the solution. The hydrodynamic diameters presented with two ranges that may be related to smallest-sized particles required a higher centrifugal force. However, the methods succeeded in separating small-sized particles lower than 1 µm to 394 nm without defects using a green method, with a low sonication power for a short period of time.

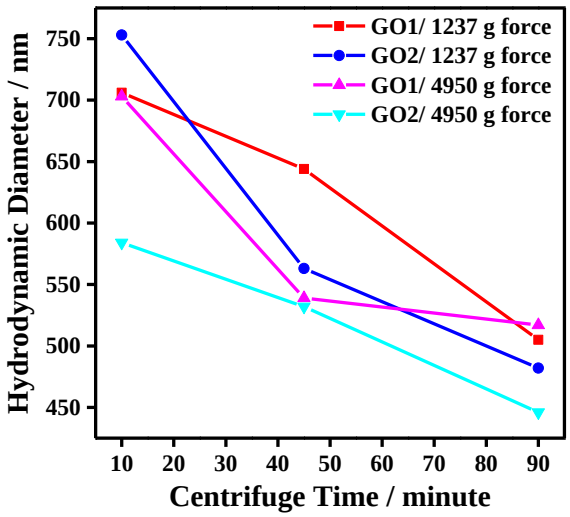

Figure 5-20: The effect of centrifugal times on the average hydrodynamic diameters of GO particles under different centrifugal forces.

Figure 5-20 demonstrates the behaviour of the average hydrodynamic diameters of the GO particle sizes with various centrifugal times, as a function of centrifugal force. These samples were centrifuged for two forces, 1237 and 11138 g, which provided a clear influence on the separation of GO particle sizes. Increasing the centrifugal speed and times decreased the particle size of both GOs. The centrifugal force settled the particles down that depending on the size or density of the particle. Therefore, increasing the centrifugal speed and time on the GO samples applied a more continuous force that precipitated more sizes of GO particles. This kept only the smallest particle size in the suspended and dropped down the large particle size. Most of the hydrodynamic diameters of both GOs in this method contained different particle sizes.

5.4.2.4 Separation of differently-sized particles graphene oxide from the same sample

To separate small-and large-sized particles from the same GO sample, both the effects of sonication time and centrifugal speeds were applied.

At 60 minutes sonication time, two different centrifugal forces, one low, at 137 g, and one high, at 11138 g, were applied to separate large- and small-sized of GO particles for the same sample that was centrifuged for 180 minutes, as shown in Table 5-13.

Table 5-13: Separation methods and the hydrodynamic diameters of top and bottom GO samples that sonicated for 60 minutes and centrifuged for 180 minutes at 137 and 11138 g.

Samples ID	**h_d, r / nm**	**Centrifugal force / g**			
		137		**11138**	
		T	**B**	**T**	**B**
GO1	**h_d r**	641 (316-733, 1180-1498)	2030 (402-544, 1992-2174)	335 (110, 262-399, 7498)	912 (688-985, 1593-1899)
GO2	**h_d r**	577 (449-604, 679-890)	1520 (1064-1732)	395 (284-442)	830 (723-879)

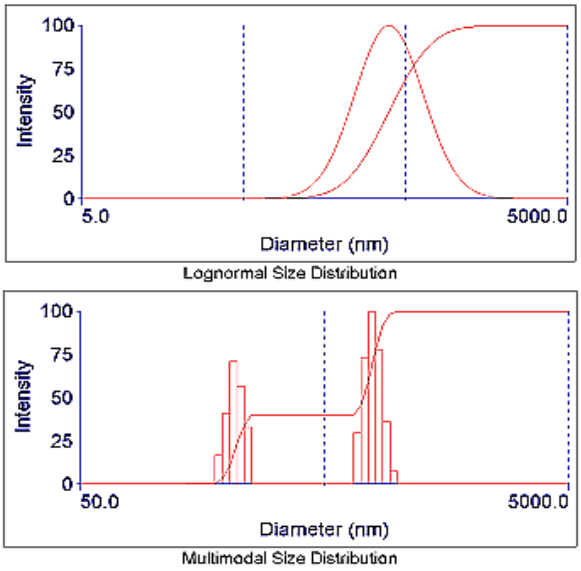

(A)

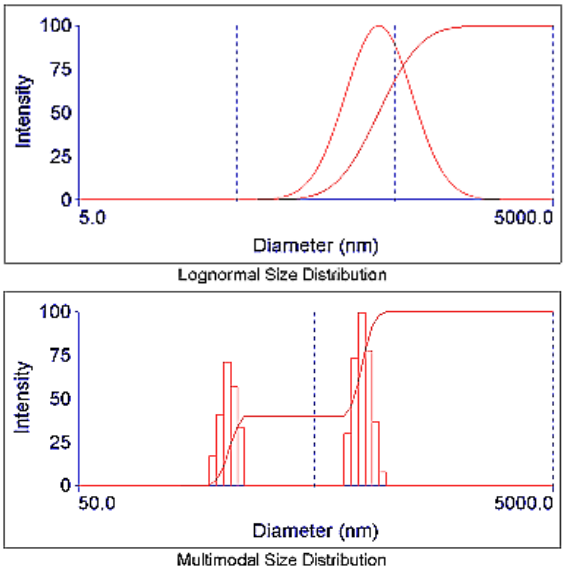

(E)

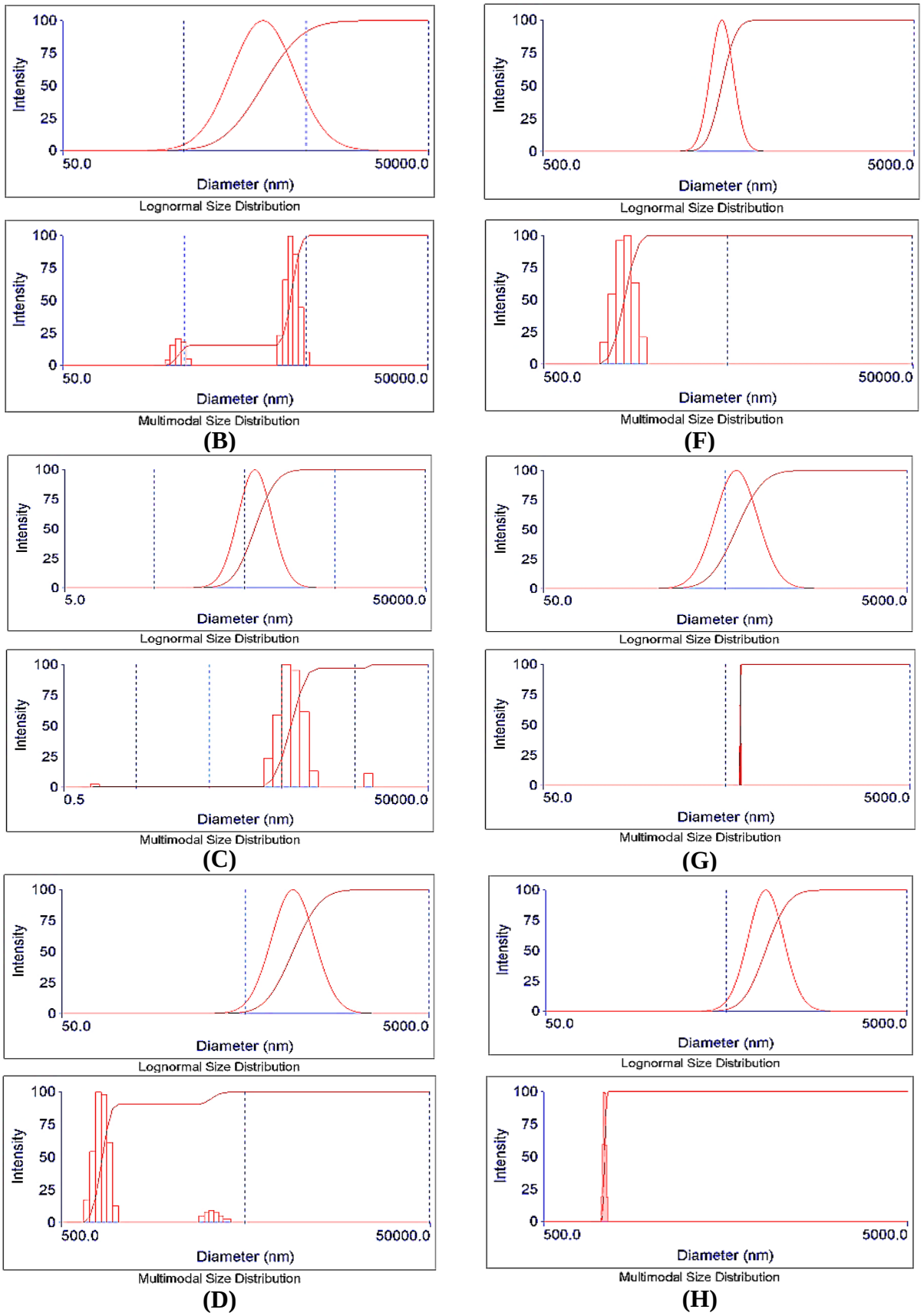

Figure 5-21: The hydrodynamic diameters of Top and bottom samples sonicated for 60 minutes and centrifuged for 180 minutes of (A) GO1 top centrifuged at 137 g, (B) GO1 bottom centrifuged at 137 g, (C) GO1 bottom centrifuged at 111138 g, (D) GO1 bottom

centrifuged at 111138 g, (E) GO2 top centrifuged at 137 g, (F) GO2 bottom centrifuged at 137 g, (G) GO2 top centrifuged at 111138 g, and (H) GO2 bottom centrifuged at 111138 g.

For the top part of the samples, applying a centrifugal force of 137 g presented a broad average distribution of the hydrodynamic diameters of the top samples, 641 nm and 577 nm, which decreased to 335 nm and 395 nm due to an increase in the centrifugal force to 11138 g of GO1 and GO2, respectively, as shown in Table 5-13. Increasing the centrifugal force from 137 to 11138 successfully precipitated and attracted most the large- and medium-sized particles to the bottom of the tube, whereas it left the small-sized particles suspended at the top of the tube. Therefore, centrifuging the samples under a lower force provided two ranges of particle size because this force attracted only the large-sized particles and left the small-sized and some of the medium-sized particles suspended at the top of the centrifuge tube, as shown in Figure 5-21 (A, E, C and G), accordingly.

For the bottom part of the samples, the centrifugal force 137 illustrated hydrodynamic diameters of 1630 and 1520 nm, whereas this was significantly reduced to 912 and 830 nm with an increase in the force to 11138 g of GO1 and GO2 as shown in Figure 5-21 (A, E, C and G), respectively. The low centrifugal force effectively precipitated only the large-sized particles at the bottom of the centrifuge tube as shown in Figure 5-21 (B and F), whereas the high centrifugal force precipitated other particle sizes with the large-sized particles, where this high centrifugal force drove the large particles down quickly and pulled the small particles in their way toward the bottom of the centrifuge tube, as shown in Figure 5-21 (D and H). GO1 samples presented two ranges of particle size, therefore the hydrodynamic diameters presented a broad distribution excepting two samples of GO2 as shown in Figure 5-21 (B, C, F and H) and Table 5-13. The result showed good separation methods of large- and small-sized particles using low and high speeds.

From the results above and comparisons among the effect factors, such as sonication times, centrifugal speeds and times, along centrifugal time of up to 4.5 h and a sonication time f up to 5 h were selected to develop the methods and achieved other ranges of hydrodynamic diameters. In this method, a high g-force of 11138, and three different centrifugal and sonication times were applied to separate the top and bottom parts of same samples for GO1 and GO2, as shown in Table 5-14.

Table 5-14: Separation methods, the hydrodynamic diameters (nm) and their ranges (r) (nm) of the GO samples that sonicated for 60 minutes and centrifuged for various times at 11138 g.

Centrifugal Time / h	**Samples ID**	**h_d, r / nm**	**Top GO**			**Bottom GO**	
			Sonication time / h			**Sonication time / h**	
			1	**3**	**5**	**1**	**3**
1.5	**GO1**	**h_d r**	637 (164-212, 1072-	404 (93, 133-749)	385 (209-304, 726-779)	1082 (917-1323)	1014 (575-914, 1223-
	GO2	**h_d r**	516 (490-548)	395 (184-242, 679-894)	290 (139-196, 312-387)	1261 (710-816, 1262-1298)	850 (801-893)
3	**GO1**	**h_d r**	664 (177-692)	378 (130-371)	335 (164-309, 433-564)	952 (855-984)	912 (688-985, 1293-
	GO2	**h_d r**	446 (248-427, 1108-	386 (232-350, 423-564)	254 (139-191, 233-371)	1051 (981-1194)	830 (728-749)
4.5	**GO1**	**h_d r**	390 (291-448)	360 (277-431)	-	-	-
	GO2	**h_d r**	334 (133-218, 353-497)	210 (119-174, 297-423)	- -	- -	- -

In Table 5-14, the top and bottom parts of both GO samples illustrated a decrease in the hydrodynamic diameters of particles with an increase in the sonication times. Increasing

the sonication time from 1 h to 3h, then to 5 h decreased the hydrodynamic diameter. For instance, at 1.5 h centrifugal time, the hydrodynamic diameter reduced from 637 to 385 nm, with an increase the sonication time from 1 h to 5 h, and so on, of both GO samples in the top part of the tube. These findings supported the previous results and strongly agree with the literature [218] results. Most the samples showed a broad distribution of hydrodynamic diameters with two ranges, as shown in Table 5-14. Increasing centrifugal speed times demonstrated another important factor in separating particles by size, when precipitating the large- and medium-sized particles to the bottom during the time with applying g-force, which kept the very small-sized particles suspended at the top part of the centrifuge tube only. Interestingly, a reduction in particle sizes observed with an increase in both centrifugal speeds and sonication times. It exhibited a particle size of around 210 nm, as shown in Table 5-14. For instance, the particle size reduced from 637 to 390 nm for GO1 and from 664 to 334 nm of GO2 at 1 h sonication time for the top materials, whereas it reduced from 1082 to 952 nm and from 1261 to 1051nm at 1h sonication for the bottom samples, as shown Table 5-14.

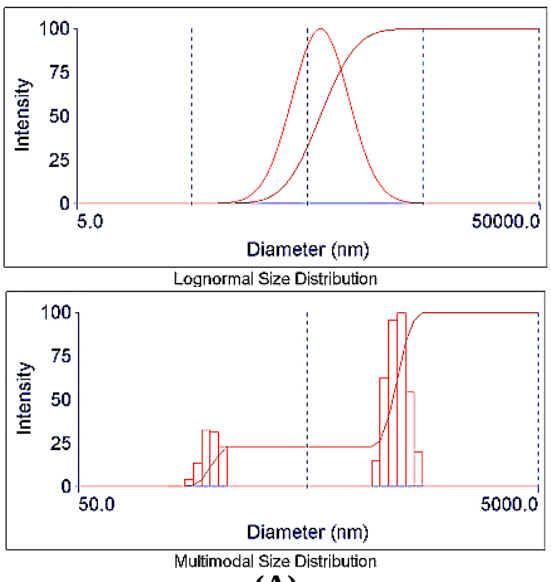

(A)

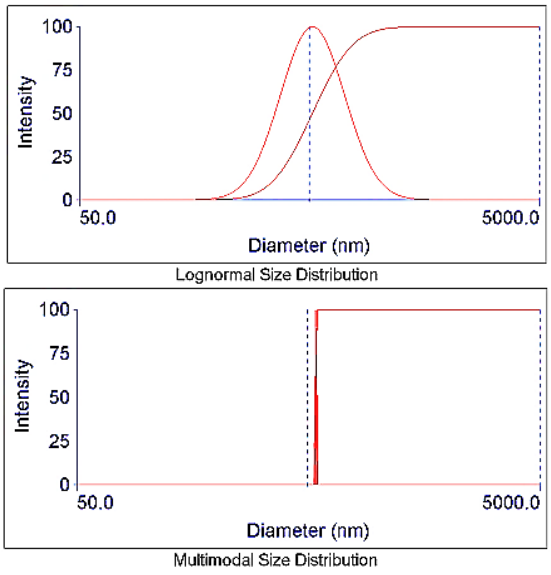

(F)

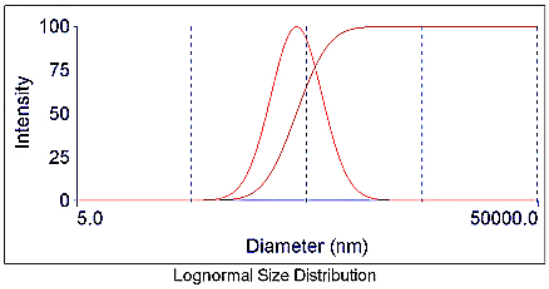

Lognormal Size Distribution

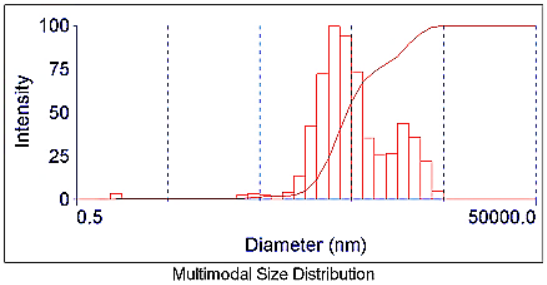

Multimodal Size Distribution

(B)

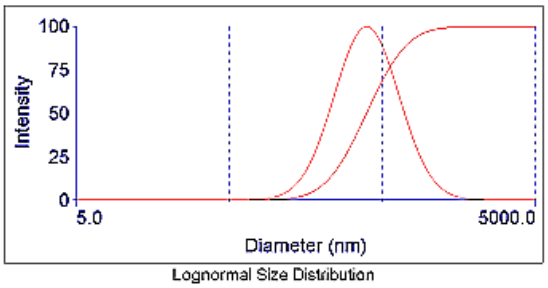

Lognormal Size Distribution

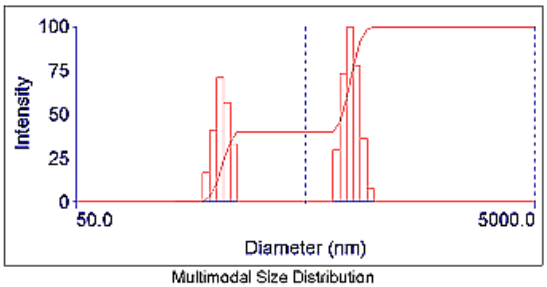

Multimodal Size Distribution

(G)

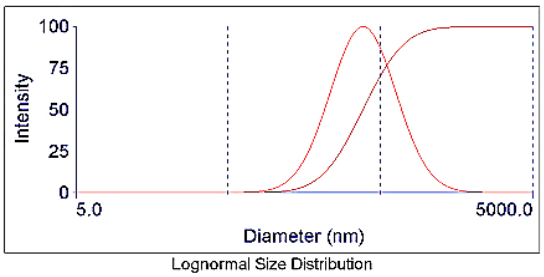

Lognormal Size Distribution

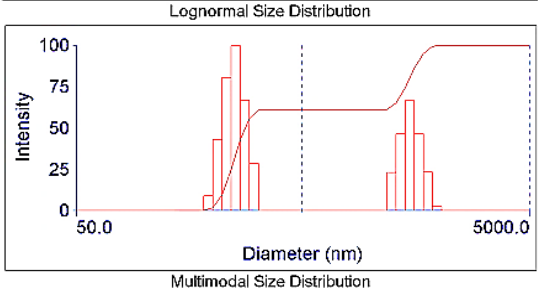

Multimodal Size Distribution

(C)

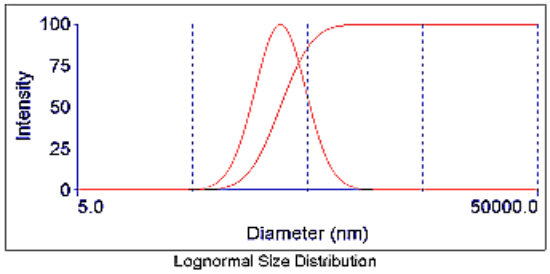

Lognormal Size Distribution

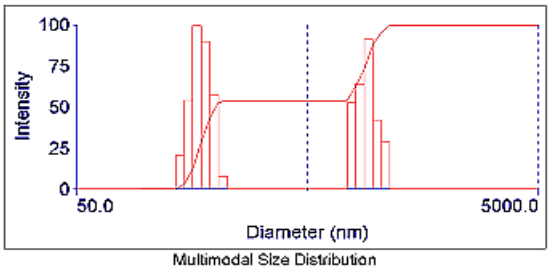

Multimodal Size Distribution

(H)

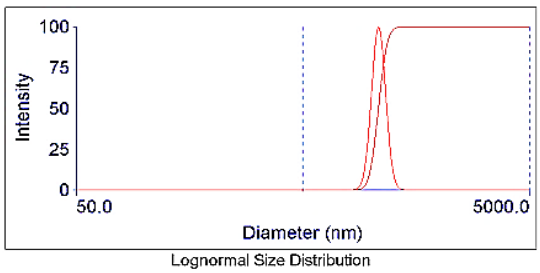

Lognormal Size Distribution

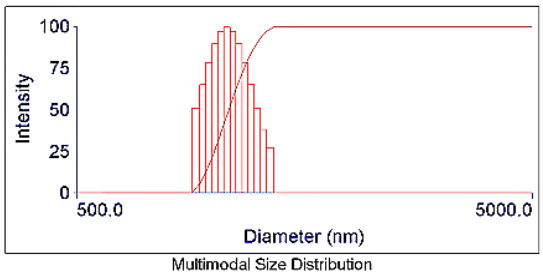

Multimodal Size Distribution

(D)

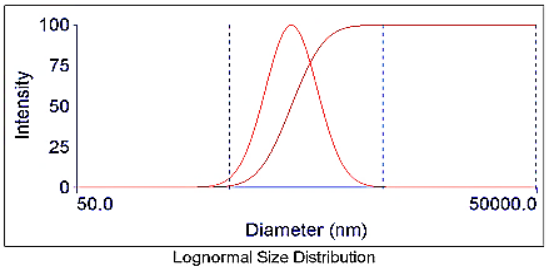

Lognormal Size Distribution

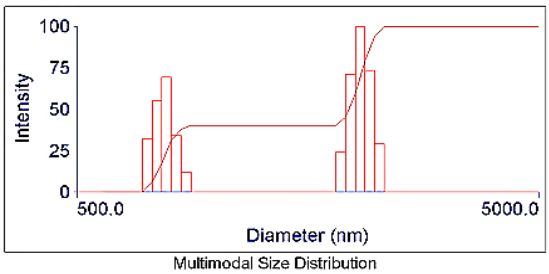

Multimodal Size Distribution

(I)

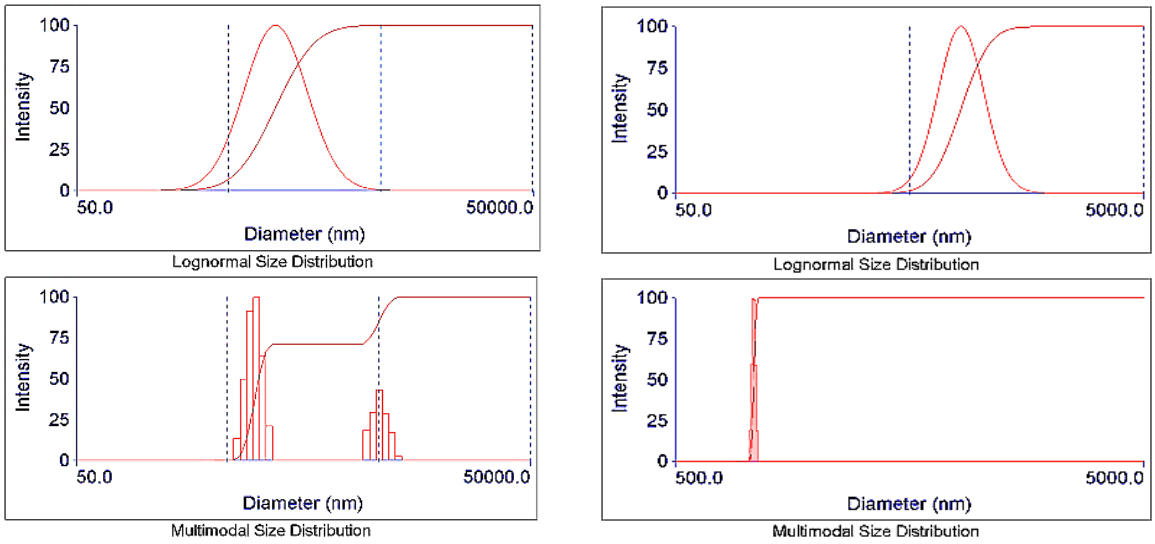

(E) **(J)**

Figure 5-22: The hydrodynamic diameters of samples centrifuged for 1.5 h at 11138 g and sonicated for three different times of (A) GO1 top sonicated for 1 h, (B) GO1 top sonicated for 3 h, (C) GO1 top sonicated for 5 h, (D) GO1 bottom sonicated for 1 h, (E) GO1 bottom sonicated for 3 h, (F) GO2 top sonicated for 1 h, (G) GO2 top sonicated for 3 h, (H) GO2 top sonicated for 5 h, (I) GO2 bottom sonicated for 1 h and (J) GO2 bottom sonicated for 3 h.

Most of the top and bottom parts of samples demonstrated a broad average distribution of the hydrodynamic diameters, with two ranges except for one sample from each part of both GOs, which were sonicated for 1 h and 3 h for both GOs, as shown in Figure 5-21 (B, D, F and J). These samples with one uniform range demonstrated good separation results for the smallest hydrodynamic diameters of 390 and 360 nm of GO1, whereas the GO2 presented 210 nm as the smallest particle size but with two ranges. The samples sonicated for 5 h also reduced the hydrodynamic diameters to about 335 nm for GO1 and 254 nm for GO2 but with two ranges because a longer sonication time could break the flake into smallest parts.

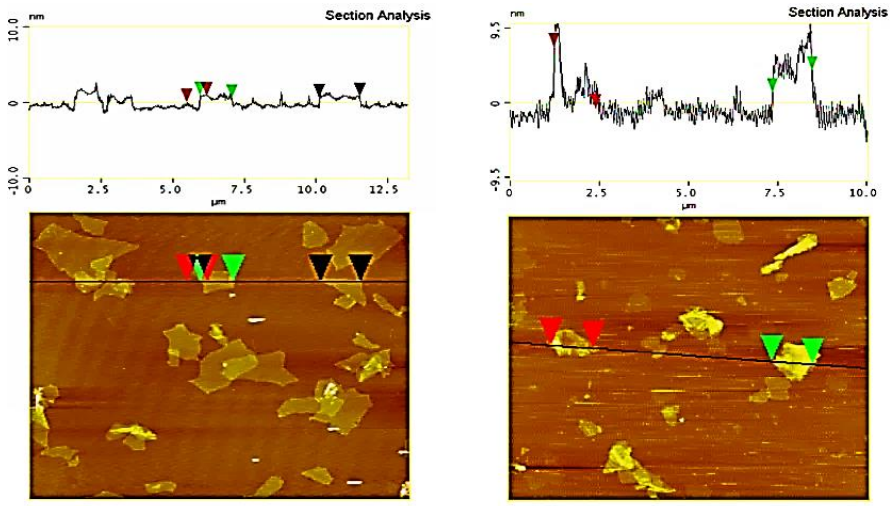

(A) **(B)**

Figure 5-23 : AFM images of the bottom samples sonicated for 1 h and centrifuged for 1.5 h at 11138 g of (A) GO1, (B) GO1.

Figure 5-23 (A and B) shows the AFM images of the GO1 and GO2 samples that were sonicated for 1h and centrifuged for 1.5 h at 11138 g, respectively. This represents the samples in Table 5-14 (D and I), accordingly. The AFM image of GO1 exhibiting the average lateral size was around 1110 nm. These images illustrate close ranges of particle sizes, in strong agreement with DLS findings, which have shown the average hydrodynamic diameter of 1082 nm with a range between (917-1323) nm, as shown in Figure 5-22 (D).

Figure 5-23 (B) shows the average of lateral size ~1200 nm of GO2 samples in the range of these particles between 1068 nm to 1320 nm, in agreement with DLS results of this sample, where the DLS results observed 1261 nm of the average distribution of hydrodynamic diameter that also presented two ranges between (710-816 and 1262-1298) nm, as shown in Figure 5-22 (I). This method provided a good separation method for the average medium-sized particles and even included some larger-sized particles because it was difficult to avoid the attraction of small particles by the large-sized particles.

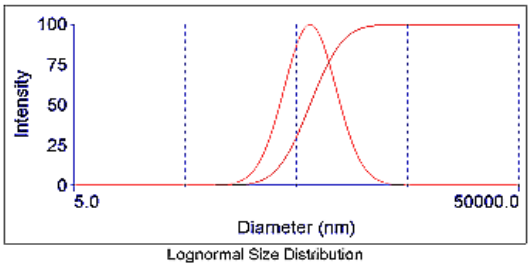

Lognormal Size Distribution

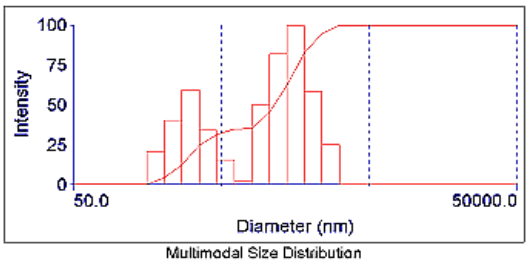

Multimodal Size Distribution

(A)

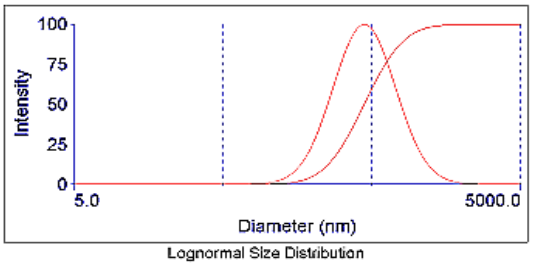

Lognormal Size Distribution

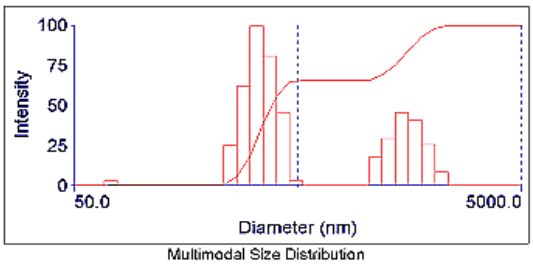

Multimodal Size Distribution

(F)

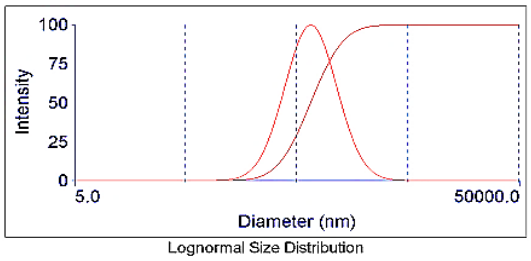

Lognormal Size Distribution

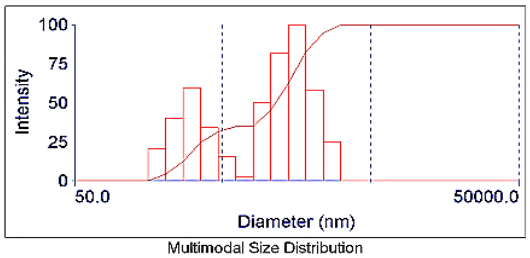

Multimodal Size Distribution

(B)

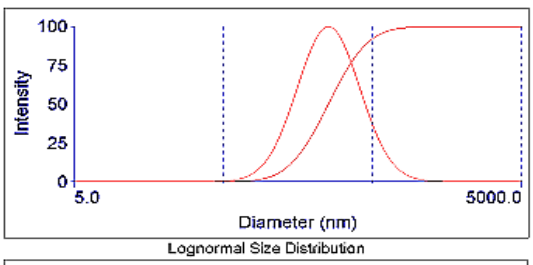

Lognormal Size Distribution

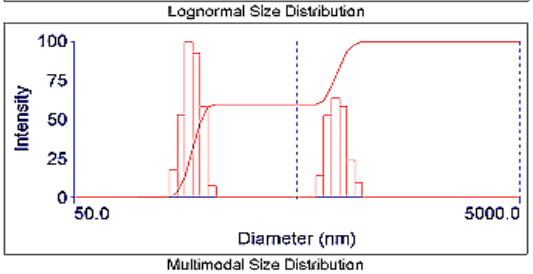

Multimodal Size Distribution

(G)

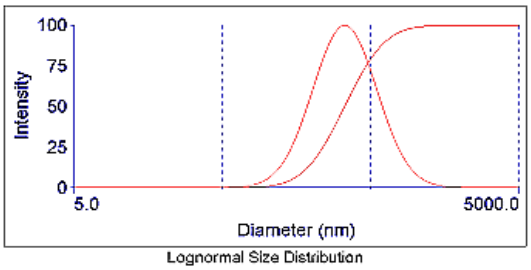

Lognormal Size Distribution

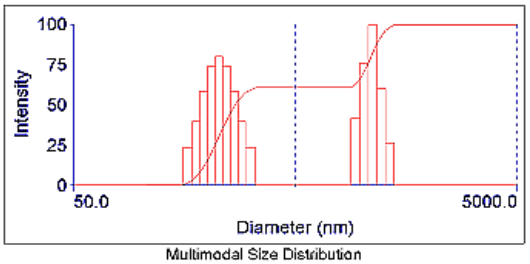

Multimodal Size Distribution

(C)

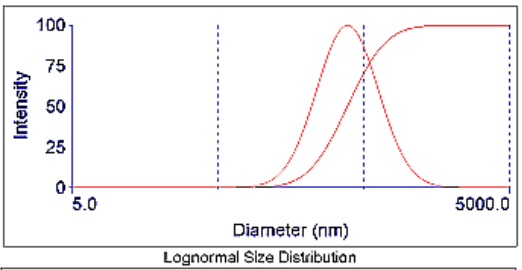

Lognormal Size Distribution

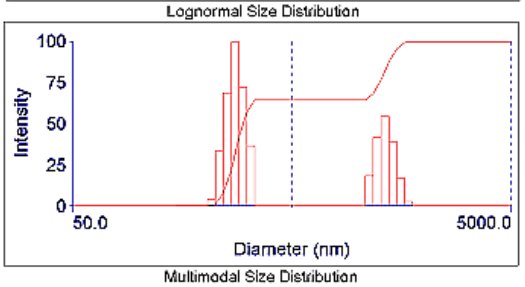

Multimodal Size Distribution

(H)

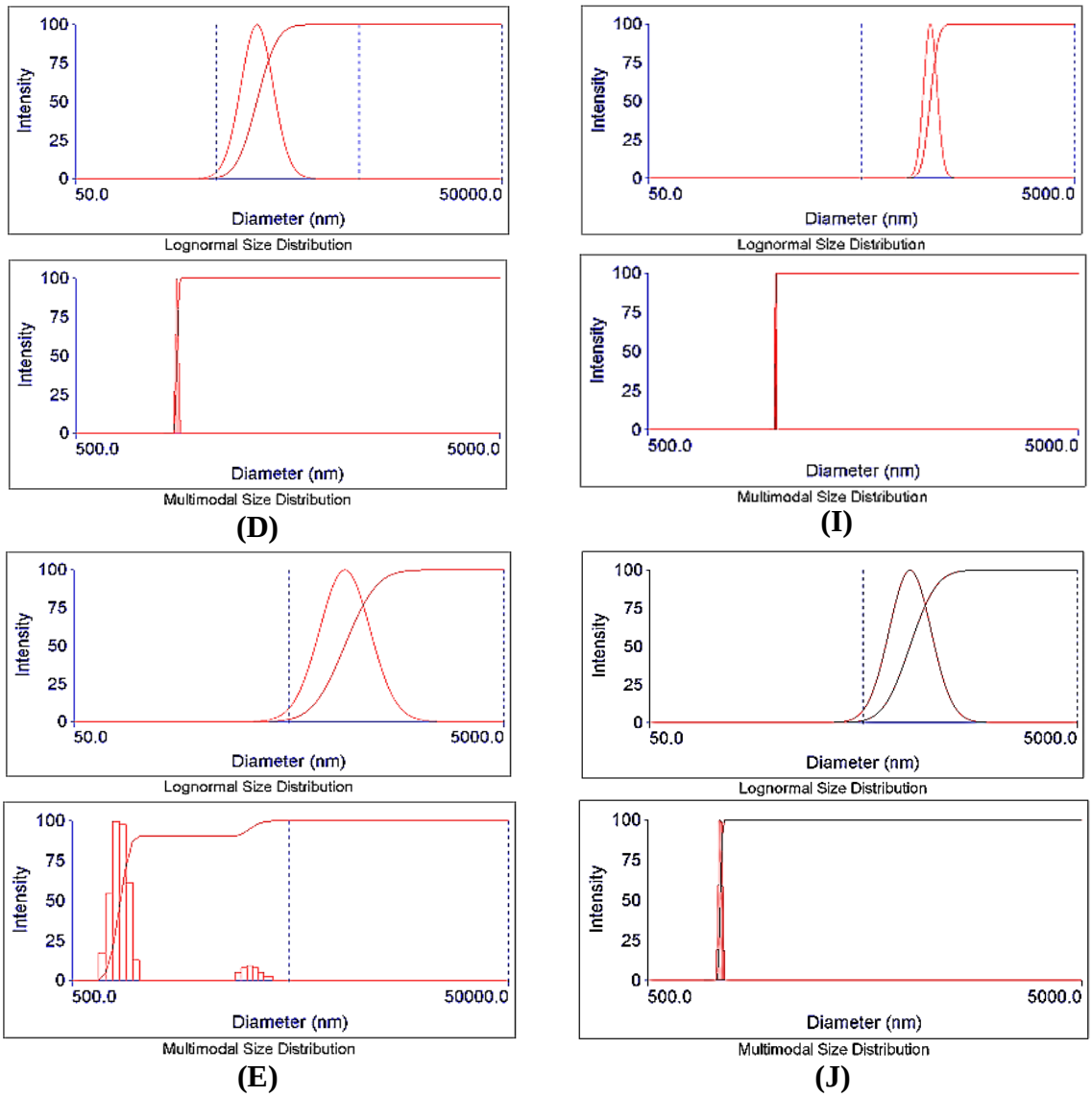

Figure 5-24: The hydrodynamic diameters of samples centrifuged for 3 h at 11138 g and sonicated for three different times of (A) GO1 top sonicated for 1 h, (B) GO1 top sonicated for 3 h, (C) GO1 top sonicated for 5 h, (D) GO1 bottom sonicated for 1 h, (E) GO1 bottom sonicated for 3 h, (F) GO2 top sonicated for 1 h, (G) GO2 top sonicated for 3 h, (H) GO2 top sonicated for 5 h, (I) GO2 bottom sonicated for 1 h and (J) GO2 bottom sonicated for 3 h.

Figure 5-24 shows the hydrodynamic diameter of the top and bottom parts of GO samples that centrifuged for 3 h at 11138 g centrifugal force and sonicated for three different times. Increasing the centrifugal speed from 1.5 to 3 h provided a reduction in the average distribution of hydrodynamic diameters, compared to with the result of the samples in

Figure 5-22. The GO1 samples exhibited a narrow distribution of hydrodynamic diameters, with one range of three out of five samples, whereas the only two samples of GO2 sample observed a good separation and other samples demonstrated two ranges of particle size.

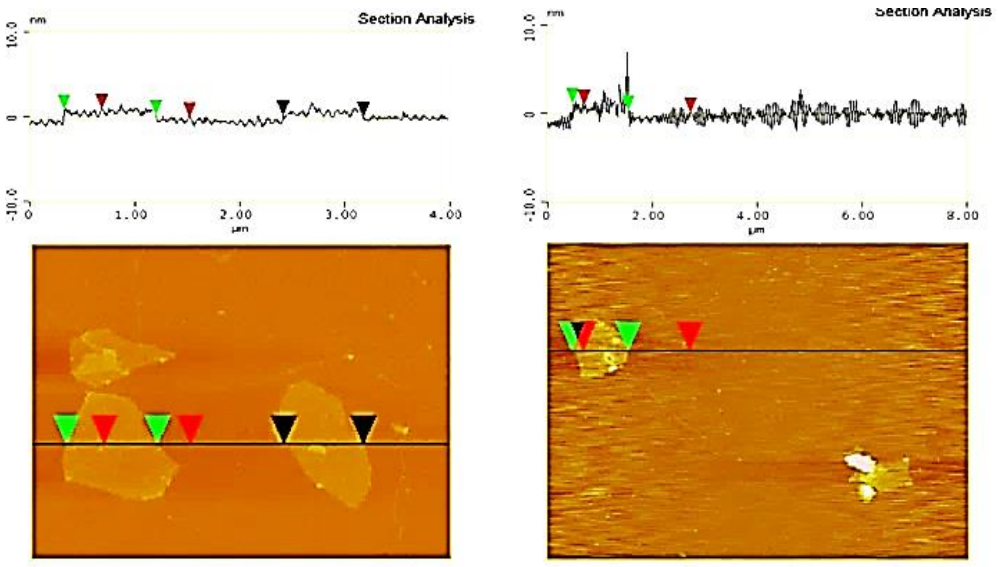

(A) **(B)**

Figure 5-25: AFM images of the bottom samples sonicated for 3 h and centrifuged for 3 h at 11138 g of (A) GO1, (B) GO2.

Figure 5-25 shows the AFM images of GO samples were sonicated for 3h and centrifuged for 3 h at 11138 g of GO samples, as shown in Table 5-14. GO1 particle size exhibited an average hydrodynamic diameter of 912 nm by the DLS, whereas it was presented between 875 to 766 nm by the AFM results, as shown in Figure 5-25 (A) and Table 5-14.

Figure 5-25 (B) shows the particle sizes of GO2, which were between 959 nm and 810 nm by AFM, in the same range as the average hydrodynamic diameter of the GO2 particle size of 830 nm, which was measured by DLS, as shown in Table 5-14 and Figure 5-25 (J).

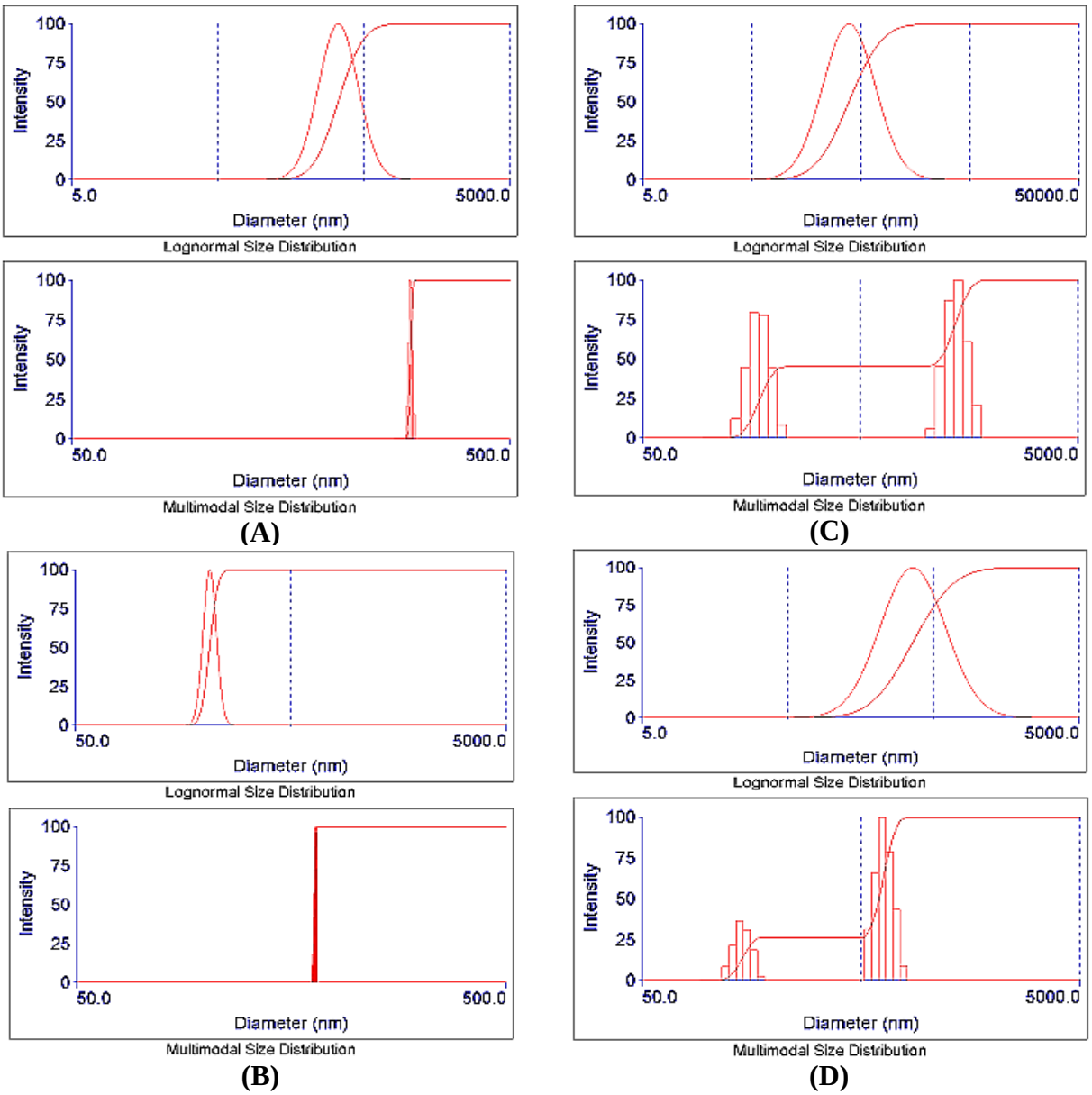

Figure 5-26: The hydrodynamic diameters of samples centrifuged at 11138 g for 4.5 h and sonicated for different times of (A) GO1 top sonicated for 1 h, (B) GO1 top sonicated for 3 h, (C) GO2 top sonicated for 1 h and (D) GO2 top sonicated for 3 h.

Figure 5-26 illustrates the narrow distribution of hydrodynamic diameters of the GO1 samples. These samples presented one range of the hydrodynamic diameters that sonicated for 1 and 3 h and centrifuged for 4.5 h. This sample observed the best separation of the small-sized particles, as shown in Figure 5-26 (A and B). The GO2 samples exhibited two ranges of hydrodynamic diameters that turned the hydrodynamic diameters into a broad distribution.

However, GO2 samples that sonicated for 3 h and centrifuged for 4.5 h provided the smallest-sized particles that were separated in this study.

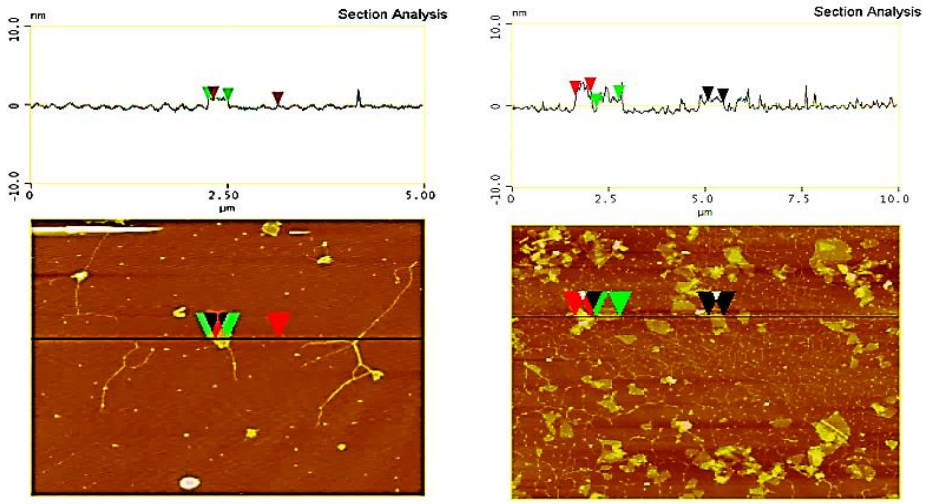

(A) **(B)**

Figure 5-27: AFM images of the top samples sonicated for 3 h and centrifuged for 4.5 h at 11138 g of (A) GO1 and (B) GO1.

Figure 5-27 shows the top GO samples that were sonicated for 3 h and centrifuged for 4.5 h at 11138 g centrifugal force. GO1 presented 360 nm as the average distribution of the hydrodynamic diameter of the GO1 sample by DLS, as shown in Table 5-14. Interestingly, the AFM measurements of most GO1 particles were in the range between 300 and 400 nm, as shown in Figure 5-27 (A). This was strongly identical to the hydrodynamic diameter value. This sample also contained a few particles that were slightly large, up 586 nm or smaller. Figure 5-27 (B) shows the particle sizes of GO2 that presented between 293 and 205 nm. This sample also contained a few particles that were slightly large, up to 410 nm. These particle sizes were the smallest particles sizes that were separated in this study, which exhibited very good agreement with the DLS results, as shown in Table 5-14.

Most of the AFM results for selected samples presented one range of the hydrodynamic diameter of the GO particles. They confirmed and supported the DLS results that showed successful separation methods, which separated various ranges of particle size from 210 to 2000 nm. For more information, see the supplementary information (SI). The difference in the results between the DLS and AFM results was related to the mechanism of DLS, which considers all particles to be spherical, as explained previously.

Table 5-15: The summary of the hydrodynamic diameters (nm) of the separation methods for large, medium and small particle from the top and bottom materials of the same sample at the same time for two different centrifugal force and three sonications and centrifugal time.

Centrifugal speed / g		**137**	**11138**			**137**	**11138**	
Centrifugal Time / h	**Samples ID**	**Top GO**	**Top GO**			**Bottom GO**	**Bottom GO**	
		Sonicate time / h						
		1h	**1h**	**3h**	**5h**	**1h**	**1h**	**3h**
1.5	**GO1**	-	637	404	385	-	1082	1014
	GO2	-	516	395	290	-	1261	850
3	**GO1**	641	664	378	335	2030	952	912
	GO2	577	446	386	254	1520	1051	830
4.5	**GO1**	-	390	360	-	-	-	-
	GO2	-	334	210	-	-	-	-

Table 5-15 summarizes DLS data of the average distribution of hydrodynamic diameters of the top and bottom materials for the separation of the large-, medium- and small-sized GO particles. This table induced reduction of the particle size by manipulating the parameter to get the required size. These provided important and easy methods to separate different sizes of GO, started from nanosize and moving to microsize. Increasing the sonication time to 5 h exhibited a significant reduction of the particle size, without any defects

due to the low power of sonication. Centrifugal force was an important factor in forcing the particles to the bottom of the tube of the centrifuge, even where a low force was applied, which successfully separated the large-sized particles as well as the medium-sized ones, while increasing the centrifugal force.

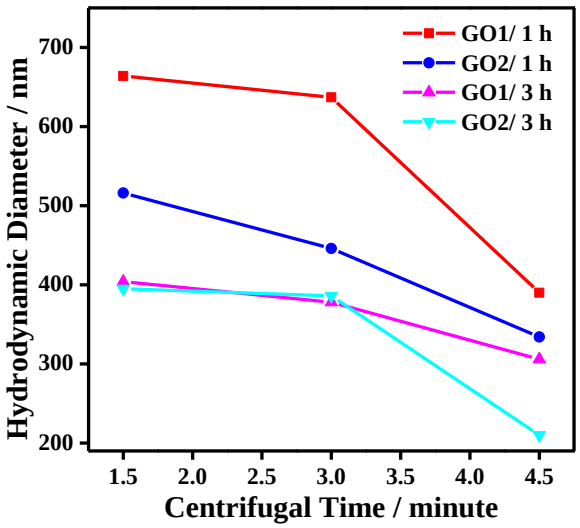

Figure 5-28: The effect of the different centrifugal and sonication times on the average hydrodynamic diameter of GO particles.

Figure 5-28 summarises the DLS results of the effect of three different centrifugal times and three different sonication times on separation of the hydrodynamic diameters' behaviour of both GOs. Increasing the centrifugal time decreased the particle size of the suspension GO in the top part of the tube. The centrifugal force attracted most of the large and medium particle sizes with different times. This depends on the particle size and density. Increasing the time of both centrifugal and sonication reduced the particle size, where the particle size was larger for the samples that were sonicated for one hour than the samples sonicated for 3 hours. It was clear that the sonication time decreased the size of the particles. Therefore,

manipulating these factors could enable the separation of the required particles sizes for GO particles.

5.5 Conclusions

GO synthesized from graphite using a modified Hummer's method has a broad distribution size. The size of GOs showed a weak relation with the size of graphite flakes used. Sonication and centrifugal were employed to separate the as-synthesized GO to produce non-defective GOs with different average sizes.

The GO size decreased when increasing the sonication time, centrifugal force and centrifugal time. A series of particle sizes started at ~200 nm, at the lower end, and went up to ~2000 nm through ~ 600, 800, 500, 1200, 1450, 1600 and 1800 nm, as confirmed by DLS and AFM were obtained. These methods are an eco-friendly, without using any chemical or thermal modifications. Additionally, this method reduced the defects that resulted from using very long of sonication or centrifugal time, such as fold in the edge, which did not present in the AFM images in this study. This method can save GO materials, and reduce the time and cost of separating GO, and will greatly facilitate the separation of GO for a range of applications.

Chapter 6: Effect of graphene particle size on adsorption behaviour of poly(ethylene oxide) and mechanical properties of their nanocomposites

6.1 Introduction

The separation method chapter, deduced a narrow distribution of GO particle sizes, which could help examine another important factor of GO, namely the effect of particle size. This could have a direct effect on the interfacial interactions in addition to other factors, such as the surface area to volume and aspect ratio, and plays an important role in adsorption behaviour of polymers onto GO sheets. Understanding this factor will enable us to obtain a stronger interfacial interaction between the filler and matrix, and higher reinforcements in polymer/GO nanocomposites by transferring the load more effectively from the polymer matrix to the nanoparticles [146,152,212].

Most of the previous studies have focused on the dispersion of GOs and the interfacial interaction between GOs and the polymer matrix. These studies [220–224] did not consider other parameters that could strongly affect the properties of nanocomposites, as reviewed well in previous chapter in section 2.8. In fact, the particle size and the effective length scale of the fillers play an important role, strongly influencing the reinforcement of the mechanical properties of polymer nanocomposites. Recently, this significant subject has attracted attention by theoretical investigation [152,212], whereas only one important experimental investigation has focused on the effective length scale of graphene particle and another [217] has investigated the effect of two particle sizes of GO on the mechanical properties. Hence, the size of graphene particle should be considered, as a way of achieving a high-profile interface interaction and effective stress transfer [152,212,214–216], as reviewed in previous chapter in section 2.8. The influence of graphene/GO particle size on polymer adsorption behaviour and the mechanical properties of polymer/GO nanocomposites have not yet been

fully understood. The formation of a strong interfacial interaction between GOs and the polymer matrix still needs to be investigated as an urgent issue for a full understanding of the particle size effect on the interfacial interaction between filler and polymer matrix, and how that effect on the properties of the polymer/GO nanocomposites [225].

The objectives of this study are to investigate the influence of the particle size and particle size dispersion of GO on the adsorption behaviour and the mechanical properties of PEO/GO nanocomposites, where three particle sizes, large (≥1800 nm), medium (~1000 nm) and small (≤400 nm), of GO that were prepared in chapter three and selected in this chapter. These nanocomposites were characterized using various techniques, such as FT-IR, XRD, TGA, DSC, tensile testing, nanoindentation, SEM and OLM.

6.2 Experimental work

6.2.1 Materials

High molecular weight poly(ethylene oxide) H-(O-CH_2-CH_2)$_n$-OH (5 × 10^6 Mv) was purchased from Sigma-Aldrich Company, UK. Other materials were the same as those used in the previous chapter in section 3.2.1.

6.2.2 Synthesis and purification of graphene oxide

This was described in the previous chapter in section 3.2.2.

6.2.3 Surface adsorption of poly(ethylene oxide) onto graphene oxide

The method was used in this part, reviled in the previous chapter in section 4.2.3. Five samples were prepared in solution pending method, as PGO1 and PGO2, which contained a broad distribution sizes of GO1 and GO2 particles, respectively, whereas PGO1-L, PGO1-M and PGO1-S contained GO1 with different particle sizes, which was 1894, 1086 and 360 nm, respectively. PEO samples without GO were prepared in parallel as controls. The samples were kept in a desiccator under vacuum.

6.2.4 Preparation of bulk poly(ethylene oxide)/graphene oxide nanocomposites

GO with 2.0 wt.% loading ratio was selected to reinforce the PEO matrix in the nanocomposites. According to the literature [222,225,249], which reported a good reinforcement of GO at this loading with different polymer matrixes. Briefly, PEO was dissolved in distilled water (3 g in 100 ml). 2.0 wt.% of GO was added to the mixture after sonication for 30 minutes. The PEO/GO solution was mixed for an hour then sonicated for 30 minutes. The mixture was mixed again for 2 h and then sonicated again for 30 minutes. After this, it was mixed for 72 h before being cast in the petri-dish and dried for 72 h at 40 ^{o}C, in a vacuum. Five nanocomposites were prepared using the same method, PEO mixed with a broad distribution size of GO2 and GO1 to prepare PGO2 and PGO1, respectively. Another three samples were prepared using three different particle sizes of 1894, 1086 and 360 nm of PGO1-L, PGO1-M and PGO1-S, respectively. All the samples were kept in a desiccator under vacuum.

6.2.5 Characterization

Tensile Young's modulus and tensile strength of bulk PEO/GO nanocomposites were measured using a universal mechanical test machine (Hounsfield, UK). Tensile testing is called as tension testing that is a fundamental material science test, where the sample is subjected to a controlled tension until failure. The tensile test was carried out with a 1000 N load and the speed of the cross-head was 20 mm min^{-1}. The specification of the samples was according to the standard (EN ISO 527-2) with "dog bone" shaped specimens (n = 6; width: 3.25 mm, gauge length: 25 mm, thickness: 0.23 – 0.25 mm). Nanoindentation was performed using a Hystitron Triboscope TS70 nano-mechanical interface, with a DI Dimension 3100 AFM (Veeco). A Berkovich (three-sided pyramid) diamond indenter tip was used in the experiments at room temperature. The indent process was set up as 3*3 indents in three different positions, which two of them were near to the edge on both sides of each sample and

the third in the middle. The position ident had fixed depths at 195 nm. Other characterization procedures have been explained in the previous chapter in section 3.2.4.

6.3 Result and discussion

6.3.1 Effect of graphene oxide particle sizes on the adsorption behaviour of poly(ethylene oxide)

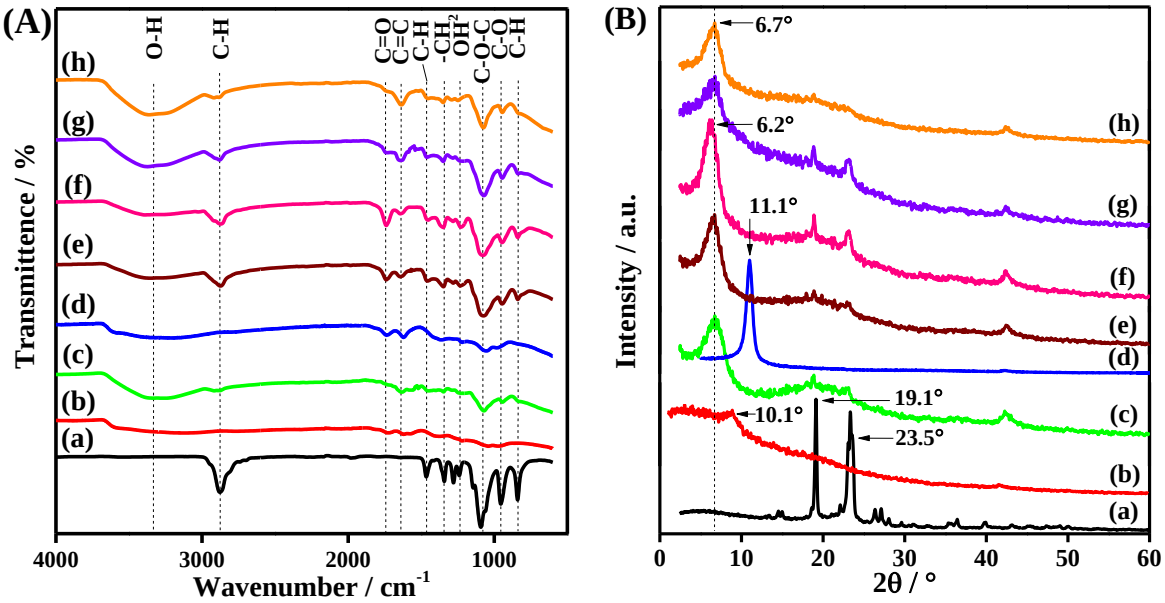

Figure 6-1: (A) FTIR spectra and (B) XRD traces of (a) PEO, (b) GO2, (c) PGO2, (d) GO1, (e) PGO1, (f) PGO1-L, (g) PGO1-M and (h) PGO1-S.

The FTIR spectra of the PEO, GO1, GO2 and nanocomposites showed the presence of different types of oxygen functional groups as shown in Figure 6-1 (A). The FTIR spectra for both GO1 and GO2 nanosheets were discussed before in chapter three and four in section 3.3.1 and 4.3, respectively. The FTIR spectra of hybrid nanomaterials indicated strong adsorption peaks of PEO on the GO nanosheets, such as stretching and bending of C-H and C-O-C groups. In addition, the some of the hybrid nanomaterials that contained a broad and narrow distribution of the GO particle presented -CH_2-CH_2- peaks at 956 - 841 cm^{-1}, which is related to a pure PEO's helical conformation [186,273]. This corresponded to strong hydrogen

bonds interactions between these groups of PEO and oxygen groups of GO, such as C=O and O-H groups. Increasing in the vibration intensity of the adsorption bond between the nanocomposites indicated to an increase in the adsorption amount of PEO onto the GO nanosheets, such as C-H, C=O and C-O-C bond groups. These adsorption peaks introduced a significant increase in their intensity using one narrow range of particle size of GO, especially for PGO1-L that contained larger particle sizes of GO.

Interestingly, the reducing the particle size from 1894 nm to 1086 nm and then to 360 nm led to a reduction the vibration intensity of C-H, C=O, $-CH_2$ and C-O-C of PGO1-M and PGO1-S compared with PGO1-L. Moreover, the PGO1-M and PGO1-S demonstrated an increase in the C=C peak, which was related to not exfoliated or aggregated the GO in addition to these samples presented without the C-H bond peak at 841 cm^{-1}, which related to the PEO. This indicated to these samples probably have a lower amount of adsorbed PEO on the GO surface, where the nanosize particle of GO showed higher intensity peaks of C=C bands in the FTIR results that could restrict the PEO chain between the GO nanosheets compared with PGO1, PGO1-L and PGO1-M.

Figure 6-1 (B) shows the XRD traces for PEO and both GO1 and GO2 nanosheets were discussed before in section 3.3.1 and 4.3, respectively. The hybrids presented two crystalline peaks; the first and second peaks were related to GO nanosheets and PEO, respectively. In PGO2, which contained a broad sizes distribution of GO2, the (002) GO2 peaks shifted from 10.1^{o} to 6.7^{o}, corresponding to the confining of the PEO between the GO nanosheets, which led to an increase in interlayer spacing from 0.83 nm to 1.24 nm, whereas the (002) GO1 peaks shifted from 11.1^{o} to 6.7^{o}, corresponding to an increase in interlayer spacing from 0.79 to 1.24 nm of all other samples that contained GO1 as a broad and narrow size distribution, except for the PGO1-L. The PGO1-L, that contained the narrow distribution of the large size of the GO1 particles, showed a shift from $2\theta = 11.1°$ to 6.2^{o}, with an increase in the interlayer space from 0.79 nm of GO1 to 1.34 nm. The interfacial interaction between

the polymer and GO nanosheets shifted the GO peaks in the samples due to the intercalated PEO between GO nanosheets. This increase the interlayer spacing distance was dependent on the absorbed ratio of PEO between the GO nanosheets.

The second crystalline peaks present in the hybrid confirmed the adsorption of PEO onto the GO nanosheets. These firstly presented in samples with a broad distribution of GOs, which were PGO2 and PGO1. These samples exhibited wide crystalline peaks with very small features of adsorption of PEO onto GO nanosheets, whereas the intensity of these peaks slightly increased for PGO1 compared to PGO2. These adsorption peaks became sharper and without a wide crystalline peak for the samples that contained narrow distribution size of the GO particles, except for PGO1-S, where this XRD adsorption peaks of GO became very small and difficult to note, given the wide crystalline peak presented again. Decreasing the particle size of GO from 1894 to 1086 nm, then 360 nm of the PGO1-L, PGO1-M and PGO1-S, respectively, reduced the intensity of the adsorption peaks of PEO.

Using narrow distribution size of the GO particle showed higher interlayer spacing of GO nanosheets and significant two crystalline peaks of adsorbed PEO in the hybrid nanomaterials compared to those with samples containing a broad distribution size of the GOs particles, whereas hybrids containing microsized (1894 nm) of GO particles demonstrated sharper and clearer crystalline peaks of adsorbed polymer than a hybrid that contained smaller sizes, especially nanosized GO particles. This means the larger particle sizes adsorbed more polymers due to the large size of GO particles that are abundant in functional groups, providing more interfacial interaction with PEO. This offered an opportunity to adsorb the polymer onto the surface, as shown in Figure 6-1 (B).

These XRD results showed clear peaks of PEO that resulted from absorbing and adsorbing the PEO with different amounts onto GO nanosheets in the hybrids. The changes in the interlayer spacing distance were related to the amount of the absorbed PEO between the

GO nanosheets. These XRD peaks of adsorbed PEO on the GO nanosheets confirmed and supported the FTIR results, which observed changes in the vibration intensity of adsorption peaks with a reduction in the GO particle sizes in the samples. It is clear that the distribution and size of the GO particles play important roles by providing different interaction sites and different intensity peaks. This offered an opportunity to tailor the physical interaction between PEO and GO. The changing in the intensity of peaks of the samples confirmed the interfacial interaction and adsorption of the PEO onto GO nanosheets. Hydrogen bonding is considered the main interaction factor between the hydrophilic groups of GO nanosheets and the oxygen sites of PEO chain [126,274].

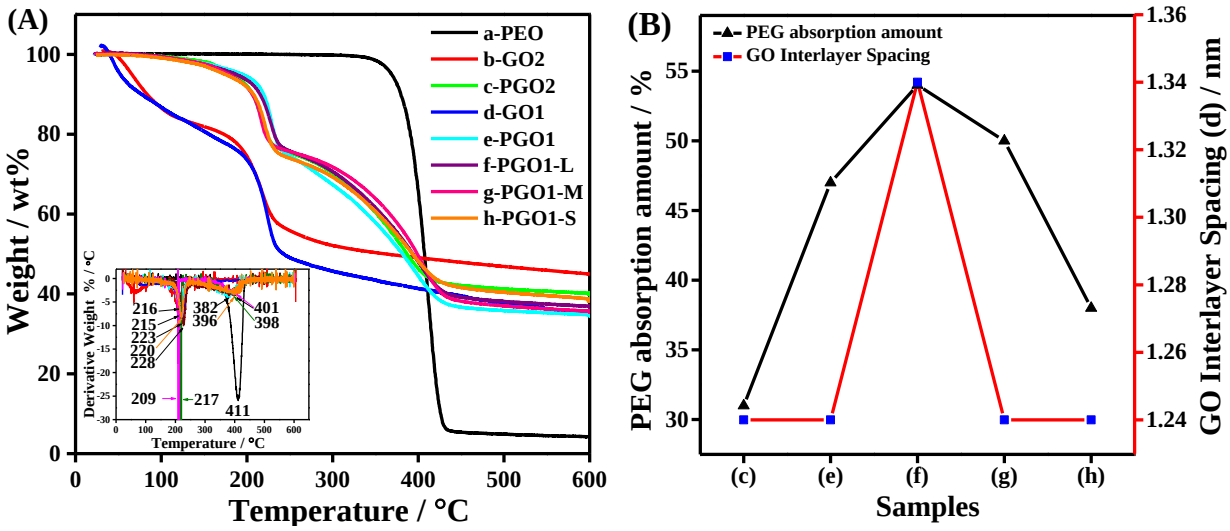

Figure 6-2: (A) TGA curves of samples and (B) PEO adsorption amounts and interlayer space of (a) 5000K PEO, (b) GO2, (c) PGO2, (d) GO1, (e) PGO1, (f) PGO1-L, (g) PGO1-M and (h) PGO1-S.

In the TGA curves of PEO, both GOs and all samples shown in Figure 6-2 (A), PEO exhibited a stable thermal behaviour from room temperature to 295 ^{o}C. Between 350 to 450 ^{o}C, the PEO sharply degraded, losing 96 wt.% of the mass in one degradation sediment at 600 ^{o}C. Both GOs gradually released the O-H groups at 100 ^{o}C, whereas between 150 - 250 ^{o}C,

GO1 and GO2 lost 21.6 wt.% and 26.16 wt.% of the mass, respectively during the release of epoxide, hydroxyl, carbonyl and carboxyl functional groups as CO and CO_2 gases in one sediment degradation. The mass ratio gradually reduced to 65 and 55 wt.% of GO2 and GO1 at 600 ^{o}C, respectively.

The hybrids presented significant degradation behaviour that was different from the original components, combining GO and PEO thermal behaviours, where the samples exhibited stable thermal degradation from room temperature to 150 ^{o}C. Afterwards, hybrids presented two main degradation segments. Firstly, between 150 - 350 ^{o}C, where the mass of samples degraded by 22.7, 21.6, 23.2, 23.9 and 23.7 wt.%, due to the release of the functional groups, which were related to the GO, whereas between 350 - 450 ^{o}C, the second main degradation stage illustrated the reduction of the mass of 18.4, 22.4, 25.7, 21.2 and 19.1 wt.% for the PGO2, PGO1, PGO1-L, PGO1-M and PGO1-S samples, respectively. The degradation of the functional groups between the GO and PEO then degraded the remaining PEO, which was the cause of the loss of mass in both segments.

The samples' degradation behaviour showed a significant improvement in the thermal behaviour of PEO, resulting from the interaction and contribution of the GO with PEO in the hybrids. The degradation behaviour reduced sharply between these two main stages, whereas after the second degradation sediment, the mass of the sample degraded gradually for the residual of PEO in the samples. At 600 ^{o}C, the proportions of mass loss of the samples were 96, 55, 60, 63, 63.3, 68, 64 and 63.3 wt.% of the total mass of the PEO, GO2, PGO2, GO1, PGO1, PGO1-L, PGO1-M and PGO1-S, respectively.

The incorporation of narrow distribution size of the GO particles in the hybrids introduced better degradation behaviour than the samples that contained a broad distribution size of GO. This means the samples with narrow distribution contained higher adsorption values of the PEO, whereas the mass ratio of PGO1-L demonstrated the highest degradation

amount of their mass than other samples with a narrow distribution and smaller size of the GO particle. One of the most significant findings was that the large-sized of GO particles exhibited an increase in the adsorption polymer amounts onto the GO nanosheets' surfaces, where the surface energies and functional groups of GO on the surface were required for better polymer adsorption. Large particle of GO provided more attachment sites and surface energy, which is associated with better interaction of PEO, as confirmed by the FTIR results, whereas the reduction of the aspect ratio of GO particles reduced thermal stability, even that the samples with narrow distribution it showed better thermal stability than hybrids containing a broad distribution size of GO particles in agreement with the FTIR, XRD and DSC results.

The original components of samples illustrated one degradation peak (T_d), whereas the samples exhibited two T_d as shown in Figure 6-2 (A). These T_d peaks were 411, 216 and 223 ^oC of PEO, GO2 and GO1, whereas first and second T_d peaks exhibited at 215, 382 and 228, 396 and 217, 398 and 209, 396 and 220, 401 ^oC of the PGO2, PGO1, PGO1-L, PGO1-M and PGO1-S, respectively, as shown in Figure 6-2 (A). Releasing the epoxy [272], hydroxyl, carbonyl and carboxyl functional groups of GO [244] caused the first T_d degradation behaviour of hybrids, whereas the second degradation peaks were related to a reduction of T_d value, which was related to the degrading of the physical bond interactions between abundant oxygen functional groups of GO nanosheets with ether groups of PEO and the degradation of the remaining polymers in the hybrid nanomaterials.

The TGA curves were used to calculate the PEO absorption amount, which exhibited 31 wt.% absorption polymer amounts in the PGO2 and 47 wt.%, of the PGO1, whereas this amount increased to 54 wt.%, 50 wt.% and 38 wt.% of the PGO1-L, PGO1-M and PGO1-S. Interestingly, the adsorption ratio increased from 47 to 54 wt.%, when using one uniform size of the separated GO, especially the microsize of GO, then decreased to 38 wt.% with a reduction in the particle size of GO from microsize to nanosize, as shown in Figure 6-2 (B). Interestingly, this study presented the crystalline peaks of PEO with ratio 47 wt.% that was

less than what reported by Wang, et. al. [230], they reported of no crystalline peak of PEO with a ratio less than 60 wt.%.

The distribution and size of GO particle played an important role to improve the polymer adsorption behaviour when using narrow distribution size and large size of GO particle (1886 nm) induced the best adsorption behaviour compared to other two particle size. The TGA finding confirmed the FTIR and XRD results that showed an increase in intensity bonds, while interlayer spacing and crystalline peaks confirmed an increase in the adsorption ratio of PEO when increasing in the particle size or using the narrow distribution of the GO nanosheets or both of them.

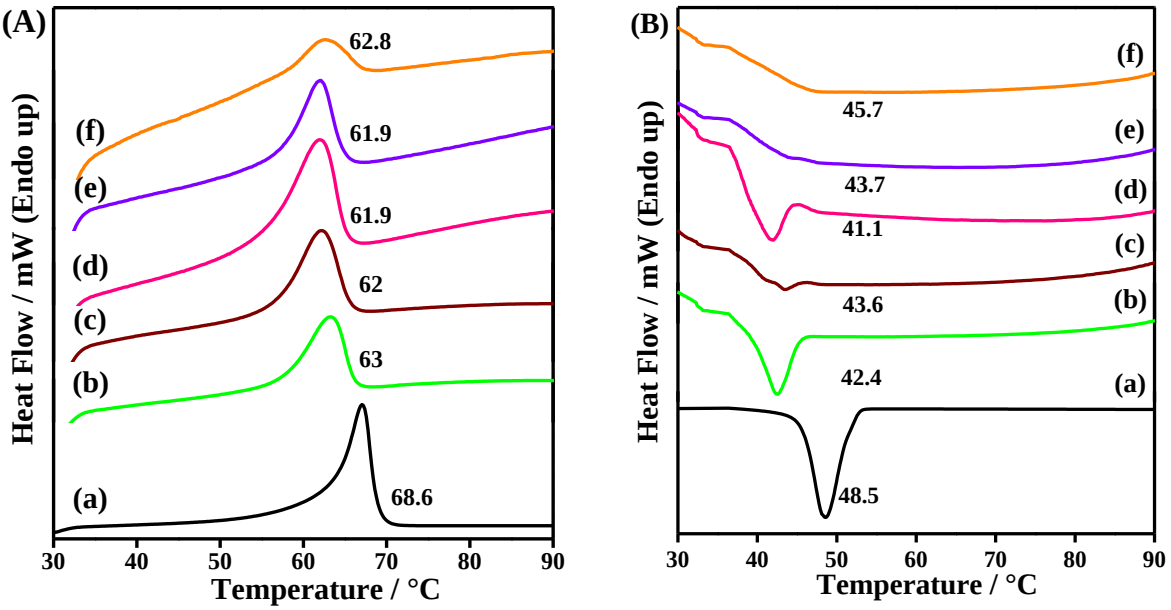

Figure 6-3: DSC heating (A) and DSC cooling (B) scans of (a) PEO, (b) PGO2, (c) PGO1, (d) PGO1-L, (e) PGO1-M and (f) PGO1-S.

Figure 6-3 (A) shows the second DSC heating and cooling cycle of the PEO and hybrids. The melting temperature (T_m) of the PEO presented at 68.6 ^oC. This T_m reduced to 63 ^oC for the PGO2 hybrids, and to 62 ^oC for the PGO1. The contribution of the broad

distribution size of both GO particles in these samples turned T_m of the adsorbed for PEO to lower values compared to the PEO crystalline peak. The confined polymer was restricted between the GO nanosheets, whereas only the adsorbed polymer on the surface of GO nanosheets melted, due to the physical interaction between free surface and repulsive interfaces. This increased the chain mobility of PEO and reduced the melting temperature [126].

The narrow distribution size of the GO1 particle shifted T_m of PEO to 61.9 ^oC of the PGO1-L and PGO1-M. These hybrids exhibited sharper melting peaks, providing the higher amount of PEO because it contained the microsized particles of GO, which were 1894 nm and 1086 nm, respectively. The samples presented the same T_m but the intensity of the peaks was different. This was related to the adsorption concentrations of PEO on the GO nanosheets. The large sizes of GO1 particles provided a bigger nanosheets surface, which means more surface energies. These led to better physical interactions and adsorption of PEO onto the GO nanosheets [189]. This peak turned out to be wide, with a lower intensity, at 62.8 ^oC melting temperature for PGO1-S, which contained a smaller-narrow sized distribution of GO particles of 360 nm. Generally, the T_m decreased for all samples. This caused an increase in the free volume that increased the mobility of the polymer chain, which was resulted from decreasing the particle size as shown in Figure 6-3 (A) in agreement with the literature [275].

The absorbed PEO on the GO nanosheets was able to crystallize and showed more mobility during the heating as a free surface attachment in agreement with the FTIR and TGA results, which showed an increase in the intensity of the functional groups and thermal behaviour of the PEO in the hybrids with narrow distribution size and an increase in the particle sizes of the GO and vice versa. This matched other studies [126,276], which reported a decrease in the T_m of the nanocomposites with an increase in the ratio of graphene. Increasing the intensity of the peaks was related to an increase in the concentration of the adsorption PEO and fast transition. This was increased by using the GO particles separated by

size, whereas the nanosized of GO particle restricted the PEO chain between the GO nanosheets that presented clear in FTIR results, which showed higher intensity peaks of C=C bands of not exfoliated or aggregated GO nanosheets, compared to PGO1, PGO1-L and PGO1-M.

The second DSC cooling scan cycle of PEO and samples is shown in Figure 6-3 (B). The crystalline temperature (T_c) of the PEO is clearly presented at 48.5 ^oC, whereas the T_c of the samples shifted to 42.4, 43.6 and 41.1 ^oC of the PGO2, PGO1 and PGO1-L. Crystallisation transitions presented at 43.7 and 45.7 ^oC of the PGO1-M and PGO1-S, respectively. The GO contributions restricted the confined PEO, thus reducing the time of re-crystallisation of the chain PEO. This caused a low internal chain order as a result of their being less time to stretch the attached molecules to the crystal, meaning less time for the relaxation of attached molecules toward the full extension and rearrangements at the crystal surface in agreement with the literature [277]. The melting temperature (T_m), melting enthalpy (ΔH), crystallization temperature (T_c) and crystallinity (C) are shown in Table 6-1. The percentage of crystallinity (X_c) was calculated using the equation (3-1).

Table 6-1: DSC result summary of PEO and the hybrid nanomaterials.

Sample ID	T_m ^oC	ΔH_m J g^{-1}	T_c ^oC	ΔH_c J g^{-1}	X_c %
PEO	67	152	48.5	149.7	74
PGO2	63.2	14.4	42.4	5.6	23
PGO1	62	16.1	43.6	0.55	18
PGO1-L	61.9	17.4	41.1	2.18	16
PGO1-M	61.9	6.8	43.7	-	7
PGO1-S	62.8	3.5	45.7	-	4

The T_m, ΔH_m, T_c, ΔH_c and X_c of the PEO were influenced by GO, as shown in Table 6-1. All the results were lower than for the PEO, which could be explained by an increase in the conformational flexibility in the adsorbed PEO sample. The presence of GO

provided a significant reduction of T_m, T_c, ΔH_m and ΔH_c, where the loss of packing constraints and configurational entropy came from the decrease of reachable PEO chain, which was configured close to an impenetrable wall [278]. This showed a strong effect on the response of the thermal behaviour in the polymer phase [278], in agreement with The results reported in the literature [74].

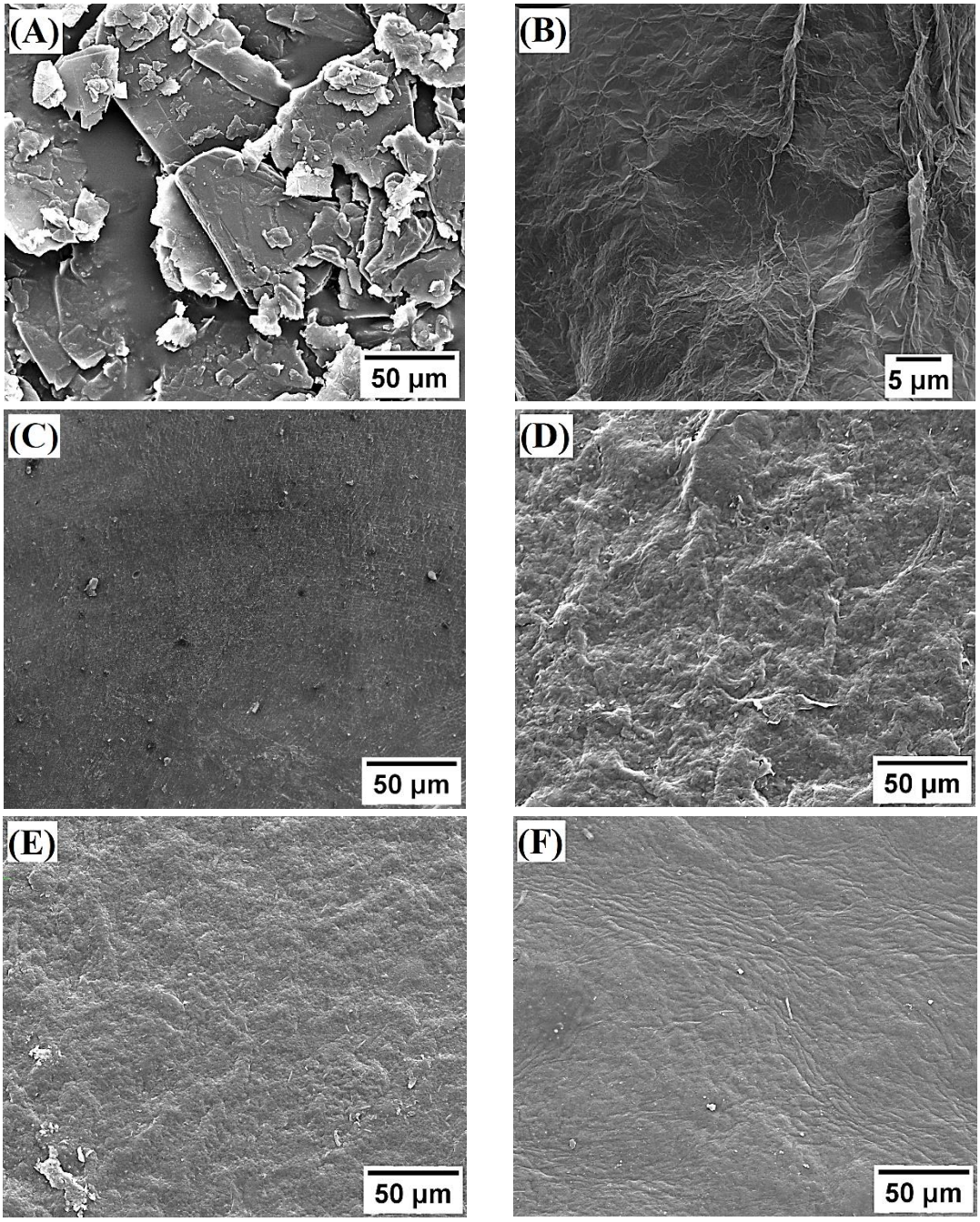

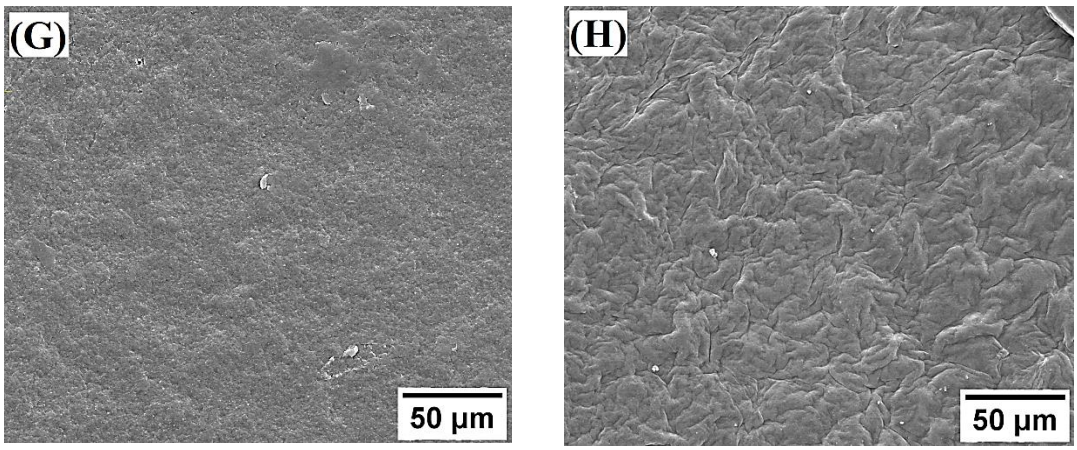

Figure 6-4 : SEM images of the fracture surface of (A) graphite (B) GO sheet, (C) PEG, (D) PGO2, (E) PGO1, (F) PGO1-L, (G) PGO1-M and (H) PGO1-S.

The fracture surface of the graphite, GO and samples are shown in Figure 6-4 using SEM. In Figure 6-4 (A), graphite platelets showed the stacking graphitic sheets and a typical multilayer structure, whereas GO exhibited a flaky morphology surface, as shown in Figure 6-4 (B), where the fracture surface demonstrated a flat surface in addition to small cracks in the surface of PEO, as shown in Figure 6-4 (C). All samples presented densely packed surface without the flaky surface, providing good adsorption of PEO onto the GO nanosheets, due to the interaction and adsorption of PEO onto the GO nanosheets surface.

In Figure 6-4 (D and E), the hybrids presented a rough and shrinkage fracture surface that different from the PEO and GO surfaces, especially the samples that included a broad distribution size of GO particles, whereas PGO1-L demonstrated a different fracture surface. This was a very flat and without flaky or shrinkage of the fracture surfaces compared with the other samples, especially PGO2 and PGO1. Using the narrow distribution size of GO particles, especially the samples containing microsized GOs, presented a significant change in the fracture surface, with a homogeneous and uniform surface, whereas this turned again to a slightly rough surface due to the reduction of the narrow distribution size of GO particles, from 1894 to 1086 nm of the PGO1-M, as shown in Figure 6-4 (F and H), respectively. The

rough surface with shrinkage behaviour presented a greater decrease in the narrow distribution size of GO particles from 1086 to 360 nm of PGO1-S, as shown in Figure 6-4 (H).

Decreasing the particle size of the GO increased the rough and shrinkage behaviour of the fracture surface in the samples, whereas SEM images clearly exhibited that the sample contained the large-sized separated of GO particles illustrated a fracture surface that was more homogeneous and reduced the shrinkage behaviour in the fracture surface of PGO1-L. In addition, it showed a flat surface and better adsorption of PEO on the GO of PGO1-L, in agreement with DSC and TGA results above, which showed better adsorption amounts of the samples with microsized GO nanosheets.

6.3.2 The effect of graphene oxide particle size on the mechanical properties of poly(ethylene oxide)

6.3.2.1 Characterization of bulk poly(ethylene oxide)/graphene oxide nanocomposites

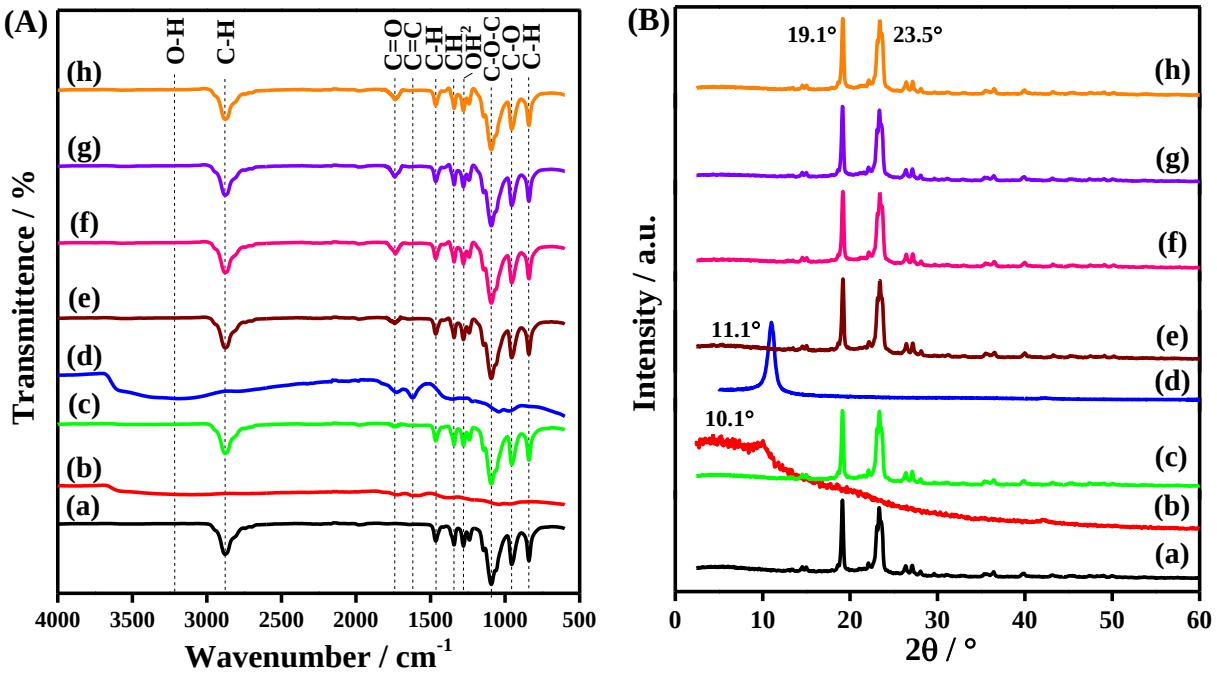

Figure 6-5: (A) FTIR spectra and (B) XRD traces of (a) PEO, (b) GO2, (c) PGO2, (d) GO1 (e) PGO1 (f) PGO1-L, (G) PGO1-M and (h) PGO1-S.

Figure 6-5 (A) shows the FTIR spectra of the PEO, GO1, GO2 discussed the earlier chapter in section 6.3.2. The FTIR spectra of bulk PEO/GO nanocomposites presented a peak at 1621 cm^{-1} corresponding to C=O stretching vibration of GO and depicts interfacial interactions (hydrogen bonding) between COOH or C=O group of GO with C-O-C or -OH of PEO [220]. This indicates a stronger interaction between the PEO and all the particles separated by size, as one uniform size of GO1 compared to a broad distribution size of GO particles. This phenomenon has also been reported for PEO/GO nanocomposites by other researchers such as Han et al. [279], Cao et al. [220] and Jagtap et al. [224]. Other functional groups of GO nanosheets were covered or overlapped by PEO spectra [279]. Another interaction or overlap could be formed between C-O-C stretching at 1092 cm^{-1} of PEO in the nanocomposites displayed a formulation of the hydrogen bond with –OH group of GO, in agreement with the literature [224,232].

Figure 6-5 (B) shows the XRD traces of PEO in, GOs, as discussed in the earlier chapter section 6.3.1. In PEO/GO nanocomposites, the diffraction peaks of PEO presented clearly in all nanocomposites, whereas the characteristic peak of GO was hard to detect. The exfoliation of GO in the PEO/GO nanocomposites, which led to the loss of the periodic order of GO, where a similar finding of polystyrene/thermal reduce GO nanocomposites was reported by Han et al. [279].

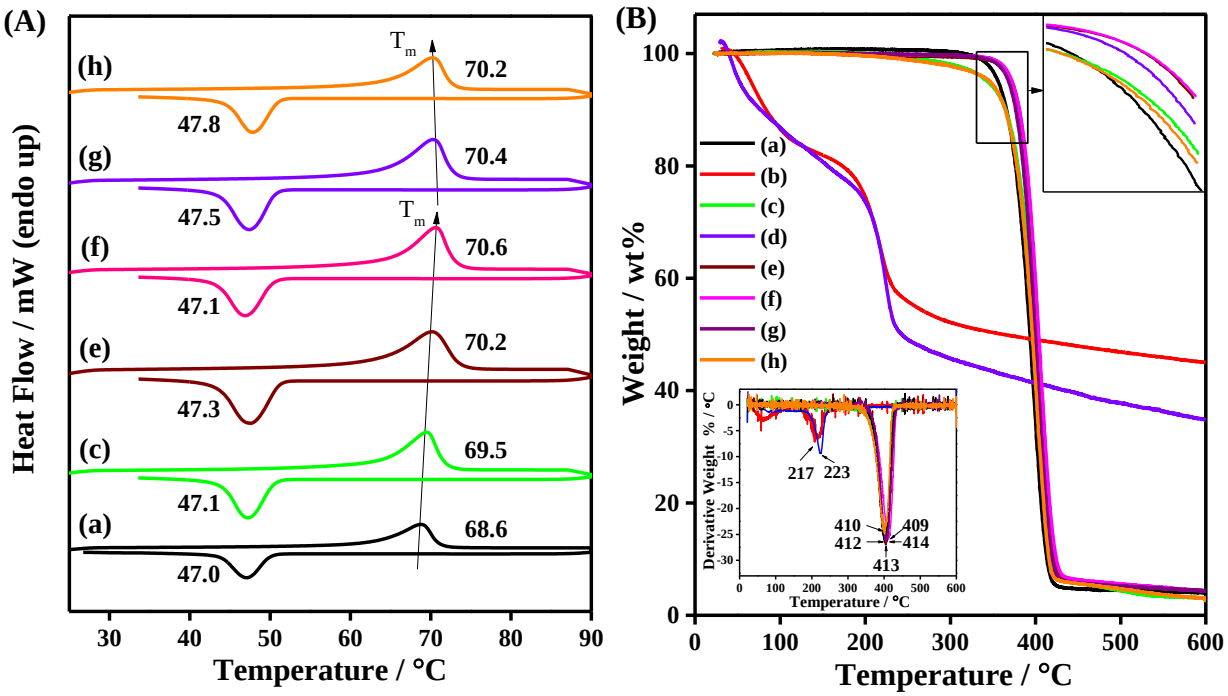

Figure 6-6: (A) second DSC heating and cooling scans and (B) TGA curves of (a) PEO, (b) GO2, (c) PGO2, (d) GO1 (e) PGO1 (f) PGO1-L, (g) PGO1-M and (h) PGO1-S.

The second heating and second cooling scans in Figure 6-6 (A) showed a clear melting temperature (T_m) of the PEO and nanocomposites. The DSC curve of PEO presented a T_m at 68.6 ^oC, as usually reported in the literature [236]. This melting peak was increased to 69.5 and 70.2 ^oC, by using a broad distribution size of GO particle for PGO1 and PGO2, respectively. This enhancement of T_m results is related to the contribution of GO in the nanocomposites, related to the interaction between the blending water-soluble polymers and GO. This was significantly restricted of the chains mobility of PEO at an interface, where a PEO matrix interface could restrict chain mobility. This gives a reasonable improvement in the thermal and mechanical behaviour [146], an improvement in the thermal behaviour even with non-covalent bonding formed between the components, where not only did the simple aqueous blending process lead to the formation of a high level of strong hydrogen bonds between the water-soluble and GO but also polar polymers and the higher content of oxygen groups in GO can do that [249], whereas the T_m was reduced of the adsorbed PEO on the GO

nanosheets that were related to considering the adsorped PEO onto the GO nanosheets as free surface attached that repulsive and away from the strong interfacial interaction which led to improving the chain mobility and reduced T_m [126].

T_m improved from 68.2 ^oC of PEO to 70.6, 70.4 and 70.2 ^oC when using narrow distribution size of the GO1 particle for PGO1-L, PGO1-M and PGO1-S, respectively. The nanocomposites with narrow distribution size of the GO particles showed better results from the both of PGO1 and PGO2, which contained a broad distribution size of both GO particles. Applying different size of the GO1 particle provided another enhancement, especially, in terms of the large-size particles. It provided the highest improvement of T_m values for PGO1-L compared to other samples, whereas even where T_m was reduced with the reduction of particle size from microsize to nanosize. This increase in of T_m depended on the strength of the interaction between the particle of GO and PEO matrix, where this altered mobility at the interphase region of PEO chains could extend away from the interface to a range from hundreds of nanometers [148] or microns [211], this according to the effective length scale of the GO particle and that depends on the particle size of the nanofiller [146]. This may lead to the formation of a network of the interphase polymer through creating a large volume of polymer, which brings a change in the polymer viscoelastic behaviour. This could manifest an increase of T_m for polymer nanocomposites at low nanofiller loadings [280].

The crystalline temperature (T_c) of PEO was increased from 47.0 ^oC to 47.3 and 47.1 ^oC with a contribution of a broad distribution size of GO particles for PGO1 and PGO2 nanocomposites respectively, as shown in Figure 6-6 (A), whereas the incorporation of separately sized of GO particles with PEO enhanced the T_c of PEO from 47.0 ^oC to 47.1, 47.4 and 47.8 ^oC of PGO1-L, PGO1-M and PGO1-S, respectively. Increasing the T_m and T_c indicated a strong interfacial interaction between the PEO and GO, in agreement with FTIR results. Similar behaviour reported an increasing in T_c by 5 ^oC of [222,249] with the incorporation of 2.0 wt.% of GO. Meanwhile, the heat fusion (ΔH_f) value of PEO decreased

from 173.1 J g^{-1} to 155.3 and 149.2 J g^{-1}**.** Also, the crystallinity (X_c) reduced from 84% to 75% and by 72% of PGO1 and PGO2, respectively, due to the contribution of a broad distribution size of GO particles. The incorporation of the narrow distribution size of GO particle showed slight decreases of ΔH_f from 173.1 J g^{-1} to 168.7, 151.3 and 149.3 J g^{-1}, whereas X_c reduced from 84% to 81%, 73% and 72% of PGO1-L, PGO1-M and PGO1-S, respectively, compared to the cooperative of a broad distribution size of GO particles.

The GO plays an important role of a nucleating agent and promotes improvements in the T_m and T_c and has influence values of ΔH_m and X_c of the PEO. PEO was formed to form a physically crosslinked structure with nanoparticles, which have strong interfacial interactions, in the PEO nanocomposites [281] that restrict the crystallization growth of the polymer due to an increase in the crosslink density with GO content [282].

The ΔH_c of PEO were increased from 138.4 J g^{-1} to 148.5, 146.6, 142.5, 141.4 and 141.3 J g^{-1} of PGO1, PGO2, PGO1-L, PGO1-M and PGO1-S, respectively. This finding agreed with the results Lee et al. [283], who reported a decrease in the crystallinity of polyurethane after adding functional graphene. Meanwhile, Wang and co-authors [225] observed a reduction in the crystalline size of poly(caprolactone) (PCL) with the addition of 2.0 wt.% GO using polarized light microscopy [222]. The crystallinity (X_c) of the polymer as bulk or in nanocomposites was calculated using the formula (3-1):

Table 6-2: DSC and TGA results of PEO and PEO/GO nanocomposites.

Temperature ^oC	**Sample ID**					
	PEO	**PGO1**	**PGO2**	**PGO1-L**	**PGO1-M**	**PGO1-S**
T_m	68.6	70.1	69.5	70.6	70.4	70.2
ΔH_m J g^{-1}	173.1	155.3	149.2	168.7	151.3	149.3
T_c	47.0	47.3	47.1	47.1	47.5	47.8
ΔH_c J g^{-1}	138.4	148.5	146.6	142.5	141.4	141.3
X_c %	84	75	72	81	73	72
T_d	409	413	411	414	414	412

Figure 6-6 (B) shows the TGA curves of the PEO, GO1, GO2 were discussed earlier in section 6.3.1. The thermal behaviour of nanocomposites observed the similar behaviour of PEO with an improved, where the degradation of nanocomposites started at 345 ^{o}C, except PGO2 and PGO1-S, which showed earlier degradation at 180 ^{o}C. At 600 ^{o}C, PEO and samples lost massed of 3.8, 2.9, 4.1, 4.7, 4.2 and 4.2 wt.% for the PEO, PGO2, PGO1, PGO1-L, PGO1-M and PGO1-S, respectively.

This degradation behaviour of nanocomposites resulted from releasing the epoxy [272], hydroxyl, carbonyl and carboxyl functional groups [244], whereas, graphene can impose a strong interfacial interaction with a polymer chain that leads to a restriction of the mobilization of the macromolecules of PEO with homogeneous heating. This slight improvement in the thermal stability of PEO/GO confirms again the interactions between GO and PEO. This observed different degradation behaviour of the samples as shown in the top right corner of Figure 6-6 (B).

The peak of degradation temperature (T_d) of GO1 and GO2 presented at 223 and 217 ^{o}C, respectively. It slightly decreased from 409 ^{o}C of PEO to 413, 412, 414, 414 and 411 ^{o}C of PGO1, PGO2, PGO1-L, PGO1-M and PGO1-S. The lower T_d values of GOs was related to increasing of the contribution of oxygen function groups of GO and interaction between the PEO and GO. This led to degrading the samples at a lower temperature as shown in Figure 6-6 (B). However, the contribution of 2.0 wt.% GO nanosheets enhanced the T_m by 1.5, 2, 1.8 and 1.6 ^{o}C of PGO1, PGO1-L, PGO1-M and PGO1-S, respectively. These samples presented better thermal behaviour than other nanocomposites, except PGO2, which showed a decrease of 0.9 ^{o}C.

PGO1-L contained larger sizes of the GO particle and provided more resistance to the thermal degradation of PEO, where the large size of GO exhibited more interaction sites and

surface energy. The high surface area and the oxygen functionalities of graphene allow good dispersion with better and more intimate interaction with polar polymers, such as PEO. This led to better physical interactions between the COOH group of GO with the ether group of PEO [185], creating a percolated domain of strong interphase interaction between the polymer and graphene that introduced a dramatic influence on thermal and mechanical properties even at low loadings [94]. PGO1-S was more degraded of mass with the reduction in particle size that led to a reduction in the effective length scale and decreased the crosslinking between the GO and PEO matrix. Generally, using one uniform size of GO generated better interaction, the thermal behaviour of PEO/GO nanocomposites, especially the microsize particle, compared to a broad distribution size of GO particles, for reinforcing the PEO matrix.

6.3.2.2 Mechanical properties of bulk poly(ethylene oxide)/graphene oxide nanocomposites

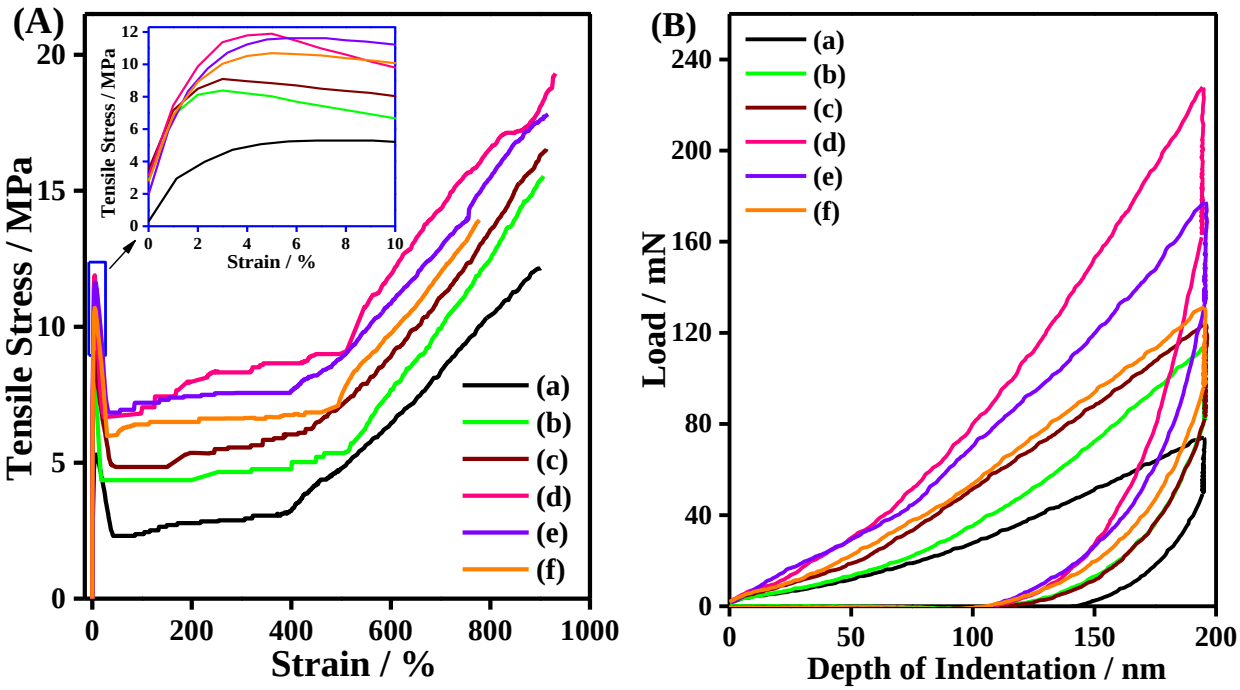

Figure 6-7: (A) Representative tensile stress-strain curves and (B) nanoindentation curves of (a) PEO, (b) PGO2, (c) PGO1, (d) PGO1-L, (e) PGO1-M and (f) PGO1-S.

Representative tensile stress-strain curves of PEO and nanocomposites are depicted in Figure 6-7 (A). The PEO presented a ductile, yield and deformation behaviour with 162 MPa, 5.2 MPa, 12.1% and 901% of Young's Modulus, tensile strength, yield strain and elongation at break, respectively. These values of PEO were in the same range of those reported in the literature or slight higher [282]. The deformation behaviour of PEO may relate to fine slips that changed the orientation of lamellar planes in relation to the direction of macromolecular chains of the semicrystalline polymer [284]. Fine chain slips are most possibly detected at the ultra-high molecular weight of polyethylene (PE) at the yield point, which causes lamellar thinning, confirming the basic similarity between the micromechanical behaviour of linear and branched PE, as reported in the literature [285].

According to the results in Figure 6-7 (A) of PGO2 and PGO1, the nanocomposites exhibited ductile and deformation behaviours as PEO, where the nanocomposites exhibited the same behaviour of PEO. This behaviour of the nanocomposites can be related to slippage of polymer chains by good dispersion of the GO nanosheets that induced the stress concentrations under tensile stress, where this should enhance the ductility by releasing the tensile stress of the PEO molecules during extension [282,286,287]. The same phenomenon was reported by Chang et al. when reinforcing PEO using contents of 1, 3, 5 and 7 wt% GO nanosheets [282]. These mechanical properties, namely Young's Modulus, ultimate tensile strength, yield strain and elongation at break, of PEO, significantly improved to 273, 220 MPa and 9.1, 8.3 MPa and 16.5%, 15.6% and 912%, 908% respectively, of PGO1 and PGO2 as shown in Table 6-3. GO is abundant in the oxygen functional groups on the surface that could easily interact polar polymer. Therefore, GO could offer simultaneous improvements in mechanical properties of the matrix due to its mobility and possible delamination under tensile stress [288]. The similar behaviour was reported by Wan and Chen [238] and Wang et al. [225], who reported different reinforcing ratios of up to 2.0 wt.% of GO into poly(ε-caprolactone). Moreover, Jagtap et al. [224] reported the same performance of the PEO at a

low loading ratio of 0.5 wt.%, of graphene. Table 6-3 summarises Young's Modules, ultimate tensile strength, yield strain, and elongation at break results.

Table 6-3: Mechanical properties of PEO and PEO/GO nanocomposites.

Sample ID	Tensile test				Nanoindentation	
	Young's Modules (E_c) / MPa	**Tensile strength (σ_c) / MPa**	**Yield strain / %**	**Elongation at break / %**	**Young's Modulus / GPa**	**Hardness / MPa**
PEO	162 ± 15	5.2 ± 0.22	12.1 ± 0.25	901 ± 60	1.7 ± 0.10	20 ± 6
PGO1	273 ± 17	9.1 ± 0.10	16.5 ± 0.30	912 ± 7.9	2.0 ± 0.10	100 ± 3
PGO2	220 ± 18	8.3 ± 0.07	15.6 ± 0.51	908 ± 14.9	1.9 ± 0.12	80 ± 5
PGO1-L	614 ± 18	11.9 ± 0.28	19.3 ± 0.34	931 ± 9.9	4.6 ± 0.08	230 ± 4
PGO1-M	494 ± 17	11.6 ± 0.05	17.8 ± 0.39	913 ± 11.4	2.2 ± 0.14	120 ± 3
PGO1-S	346 ±16	10.7 ± 0.18	13.9 ± 0.52	778 ± 18.4	2.0 ± 0.05	110 ± 2

GO1 and GO2 with abroad distribution size were used to investigate their effect on the mechanical properties melt in PEO, which According demonstrated better reinforcement of PGO1 than GO2. Therefore, GO1 was selected to separate out three different particle-sized, as discussed earlier in this study, to reinforce PEO in further studies. The narrow distribution size of the GO1 particles were ≥1894, ~1086 and ≤360 nm that were large, medium and small. Each particle size with a loading ratio of 2.0 wt.% was mixed with PEO to preparing the PGO1-L, PGO1-M and PGO1-S and investigated the effect of particle size on the mechanical properties, as shown in Figure 6-7 (A).

The incorporation of one separated size of GO1 particle enhanced Young's modulus, tensile strength, yield strain and elongation at break results by 614, 494, 346 MPa and 11.9, 11.6, 10.7 MPa and 19.3, 17.8, 13.9% and 931, 913% respectively, despite that the elongation at the break of PGO1-S exhibited reduction to 778%, compared to the PEO results. These findings suggested the possible delamination and mobility of the one size of GO particles and

better interfacial interaction with a PEO matrix. This increased the yield strain compared to nanocomposites a broad distribution size of GO particles.

The results clearly show that Young's modulus of the nanocomposites was enhanced by 297, 200 and 125% of PGO1-L, PGO1-M and PGO1-S respectively, whereas it improved up to 173% when using one size of GO particle as shown in Figure 6-7 (B). The tensile strength and yield strain presented notable increase by 128%, 123%, 105% and 59%, 47%, 15%, of PGO1-L, PGO1-M and PGO1-S, respectively. The tensile strength and yield strain enhanced by 36% and 17% respectively, when using narrow size of GO particle, especially of the bigger particles of GO compared to a broad distribution size of GO particle, whereas the PGO1-L, which contained the biggest size of GO1 particles, exhibited the best mechanical properties compared to other smaller particle size and the samples with a broad distribution size. The PGO1-M showed the second best mechanical results. PGO1-S, which contained the nanosize particle of GO, provided an improvement in mechanical properties, except for the elongation at break, which was reduced. This could be attributed to restrictions on the movement of the polymer chains by the small aspect ratio of graphene and re-stacking of the graphene sheets together via the van der Waals force.

Even the mechanical properties reduced with redaction the particle size but it exhibited better reinforcement than those samples reinforced with abroad distribution size of the GO particles, except for elongation at the break value of PGO1-S. The nanosized of GO particles demonstrated an efficient interfacial stress and transfer of the load between the GO parties and PEO matrix because the GO nanosheets presented isotropic reinforcement of the geometry in more than one direction [222]. Addition, each particle has an effective length on the nanometer scale that can reach between several hundreds of nanometers to microns and it strongly depends on the size of the particle [146,211]. Therefore, the larger size of the GO particle exhibited a higher value of effective length scale that led to stronger interfacial interaction and better transfer to stress between GO and PEO under tensile stress.

The quality of the reinforcement of the nanocomposites is often described as being relevant to the critical length, where the strain is reduced from plateau level toward the fibre (particle) ends and is lower for stronger interfaces [289]. The strain of the flake plateau of graphene increases to about 90% of that distance over about 1.5 μm from the edge of the graphene flake for reinforcement of high-density polyethylene [213]. Therefore, in the case of the PGO1-S sample under elongation and stress, the nanoparticle size did not provide enough effective length scale between the GO particle itself and polymer, which led to a lack of transference of the load between the GO particle and the PEO chain, and earlier cracks due to interfacial interaction of failure. This reduction in the mechanical properties and elastic behaviour strongly agreed with the literature in many cases; decreasing the flake size [290], the short flakes or not completely exfoliated flakes provide relatively weaker reinforcement of the matrix [291], such as a reduction of tensile strength [223], whereas Gong et al. [80] pointed out the good reinforcement requires large lateral graphene particles [213].

Nanoindentation is a technique to measure mechanical properties of materials using nanosized or microsized indenters [223]. Figure 6-7 (B) shows the nanoindentation curve of PEO, GO and nanocomposites. The depth of the indent was fixed at 195 nm. The PEO (curve a) needed to load 74 mN to reach the 195 nm depths. This load of PEO was significantly increased to 124 and 114 mN of PGO1 and PGO2, which contained a broad distribution size of both GO particles. This improvement was related to the strong physical interaction between the GO nanosheets and PEO matrix as discussed before.

In comparison, the incorporation of narrow distribution size of GO particle demonstrated higher increases in the load value to 228, 177 and 131 mN of PGO1-L, PGO1-M and PGO1-S. This refers to more efficient interfacial interaction and transfers to the load between the narrow distribution size of GO particle and PEO matrix. Interestingly, the narrow distribution size of GO particles presented stronger reinforcement of the PEO matrix compared to a broad distribution size of GO particle, especially the PGO1-L, where the large

particle exhibited the highest resistance to the applied load by the nanoindenter by transferring the load between the nanofiller and the polymer matrix. This resistance resulted from the large effective length scale of the large nanofillers, which led to a strong interaction between the nanocomposites components compared to other particle sizes of GOs.

Both hardness and elastic modulus results of the materials were also shown in Table 6-3, which was 1.7 GPa and 20 MPa for PEO, respectively. These values showed improvement to 2.0, 1.9 GPa and 100, 80 MPa with the incorporation of a broad distribution size of GO1 and GO2 particles in PGO1 and PGO2, respectively. The abundant oxygen functional groups on the GO surface and using this process succeeded to achieve an excellent dispersion of GO in the PEO matrix. The effective Young's modulus of the monolayer GO was 207.6 GPa, which is a similar to that of several GO layers [146,292]. This led to strong interfacial interaction via hydrogen bonds between GO nanosheets and ether group of the PEO matrix. These were considered two of the main reasons for better reinforcement and improvement of the mechanical properties, in agreement with the literature [146,238].

The incorporation of 2.0 wt.% narrow-size GO particles provided substantial enhancement by 275%, 92% and 72% in the hardness, whereas the elastic modulus improved by 154%, 21% and 14% of the PGO1-L, PGO1-M and PGO1-S, respectively. These results showed a similar behaviour of the tensile test and observed huge improvement in the hardness and elastic modulus of PGO1-L compared with other nanocomposites.

This study indicated another important parameter, namely, that is the particle size, as the effective length scale of each particle could reach several hundreds of nanometers in more than one direction [293]. This effect plays an important role in transferring the stress between the particles of GO itself and the polymer matrix [146] and The results in a high performance and reinforcement of polymer nanocomposites [238]. However, this can also explain the reduction in the mechanical properties with a decrease in the particle size, where the reduction

of particle size leads to reducing the effective length scale between the nanofiller and the polymer matrix and influences the interfacial interaction and mechanical properties, as the results at the end show. The size of a nanofiller can thus be considered an essential factor in addition to other important factors, such as good dispersion and the compatibility of the nanofiller in the polymer matrix responsible for transferring the efficient load via the strong interfacial interaction and achieving a high-performance and reinforcement of the polymer matrix, as result [223].

Overall, reinforcing the PEO matrix with one range size of GO particles led to substantial improvement of the mechanical properties of nanocomposites than using broad distribution sizes of GO particles, which showed good enhancement in the mechanical properties, whereas, the mechanical properties greatly enhanced at low filler concentrations due to use of a narrow distribution size of GO particles, Meanwhile, the particle size of GO presented a significant increase in the mechanical properties with the contribution of the microsize particle of GO compared with nanosize. Reinforcing the mechanical properties of nanocomposites is influenced by the aspect ratio of the nanofiller [4,138]. A similar phenomenon was reported by Yue et al. [219].

In composites materials, the stress transfers from a low modulus matrix to a high-modulus reinforcing particle. The strain of the matrix is usually the same as that in the particle or of the fibre in case in which the axial deformation of composites with high aspect ratios or long aligned of fillers [213], where the majority of the load is relevant to the high modulus of the fillers that lead to increasing that of the matrix. This situation becomes more complex in the case of small aspect ratios or short fibres, where the stress is a shear between the filler and matrix through the interface so that stress builds up from the ends of the fillers [213]. The shear-lag theory of Cox [294] was first employed to analysis this phenomenon. It is considered an important to understanding and analysing of the composites micromechanics

[289], and reinforcement of a composite by a filler, such as a graphene, where it is considered a two-dimensional version of fibre reinforcement as a starting point [213].

The particles and matrix must be analysed using Young's modulus of nanocomposites as subject to either uniform stress or uniform strain. Young's modulus (Ec) of a particulate composite is given by the rule of mixtures, in case of uniform strain [213,292].

$$E_c = V_p E_p + V_m E_m \quad (6\text{-}1)$$

where E_p, E_m and V_p, V_m are Young's modulus and volume fraction of the particles and matrix, respectively, where $V_p + V_m = 1$ for the composite.

In case of Ep >> Em, this equation of Young's modulus gives very large differences in the calculation of particulate composites. To overcome this problem, the self-consistent micromechanics method of Hill was developed by Halpin and Tsai [292], where they predicted the elastic behaviour for a variety of both particulate and fibre geometries in the composite. Halpin and Thomas [295] employed this approach to calculate the behaviour of ribbon-shaped in the case of an aligned reinforcement. This prediction is relevant to graphene-based composites. The Young's modulus ratio of the composite to the matrix is given by the equation [213,292].

$$E_c/E_m = (1 + \xi \eta V_P)/(1 - \eta \emptyset_P) \quad (6\text{-}2)$$

where ξ is the shape factor that depends on the filler geometry and loading dir ection. This depends on the loading conditions and aspect ratio that is essentially controlled this parameter, for reinforcement. ξ value can be considered by 2l/3t, where l is the length of the ribbon and t is the thickness that is used for reinforcement [146], In case of fully-exfoliated graphene or GO, the ξ parameter is expected to be at least 1000, meaning that these fillers provided strong reinforcement. Therefore, in the case of rigid polymer reinforcement, the value of experimental data should be = 1000 of ξ at very low volume fractions (<0.1%),

whereas in case of volume fractions up to around 0.5%, it must lie in a range between 1000 < n < 100 [213]. In this study this was found to be 1578.3, 905 and 300 of the large, medium and small particle sizes, where, in many cases, the short length of flakes and in complete exfoliation led to the effect of reinforcing the material and turning the value of ξ to less than 1000 [213], whereas η given by:

$$\eta = (\frac{E_p}{E_m} - 1)/(\frac{E_p}{E_m} + \xi) \quad (6\text{-}3)$$

The limiting values of η are 0 to 1 [292]. V_P is the nominal volume fraction, given in the equation (6-4) [296]:

$$V_g = (W/\rho_P)/((W/\rho_P) + (100 - W/\rho_P)) \quad (6\text{-}4)$$

Where W, ρ_P and ρ_m are the weight fraction of GO in the composites, density of GO and density of polymer, respectively, the density of PEO and GO were 1.9 g cm^{-3} and 1.2 g cm^{-3}, the former measured by a pycnometry method and the latter given by the supplier. This model was applied to the nanocomposite samples, where the GO layers were dispersed randomly in two dimensions (2D). The results were calculated using the model that presented lower results than the experimental data Figure 6-8. However, for fully exfoliated GO nanosheets in polymers can be seen to form a layer of adsorbed polymer-chains contributing to the reinforcement, Chen and Evans [297] developed formula of effective volume fraction (V_p') of the reinforcement (6-5):

$$V_P' = V_P(1 + k R_g A_T \rho_P) \quad (6\text{-}5)$$

where k, is a parameter the consistent fraction of the adsorbed layer that is assumed as 0.2 [298] and can be estimated from the mechanical testing or viscosity measurement [297]. The radius of gyration, R_g, was calculated to be 170 nm of PEO (5 × 10^6 Mv) and the specific surface area of the nanofiller/GO powder A_T was 462 m^2 g^{-1}, which was measured by

Brunauer–Emmett–Teller (B.E.T.) surface area analysis as reported [146], respectively. The effect of the effective volume fraction on the reinforcement gives another way of explaining the strong reinforcing of the nanofiller [297].

In comparing V_P and V_P' of the experimental results, the value of the latter was higher for the polymer/GO nanocomposites [146]. Equation (6-5) was substituted in equation (6-2) to consider the effective volume fraction of the reinforcement. Examining the relation between theoretical predictions and experimental data was instructive [213]. Thus, Figure 6-8 shows an elastic modulus of nanocomposite as a function of the hydrodynamic diameter of particle size distributions, h_d compared with the theoretical calculations.

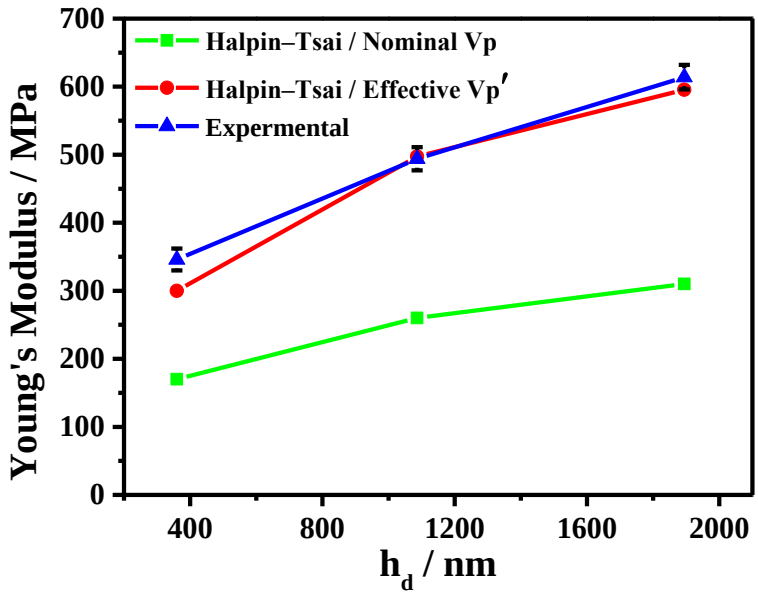

Figure 6-8: Elastic modulus of nanocomposite as a function of the hydrodynamic diameter of particle size distributions, h_d.

In Figure 6-8, the results of theoretical calculation showed the modified Halpin–Tsai model for randomly aligned particles with the effective volume fraction (V_p') matched the experimental results and provided good correlation. This model assumed the fully exfoliation

of graphene oxide in the polymer matrix, whereas using the nominal volume fraction V_p with the same model exhibited underestimated values of the nanocomposites, which did to not considering the contribution of the interface to the Young's modulus [299].

Additionally, for Young's modulus of the nanocomposite increased with the hydrodynamic diameter of graphene oxide filler, as reported by Weerasinghe et al. [152], who illustrated an increase in the modulus of high molecular weight polyethylene composite with an increase of the graphene filler radius. The same group [212]was developed a modified shear-lag model, they used high molecular weight polyethylene as a model and reinforced with nanofillers that were graphene flakes and fullerenes using extensive molecular-dynamics simulations. They induced filler size and more dilute fillers (2.0 wt %), as a significant parameter that play roles of reinforcement [152,212].

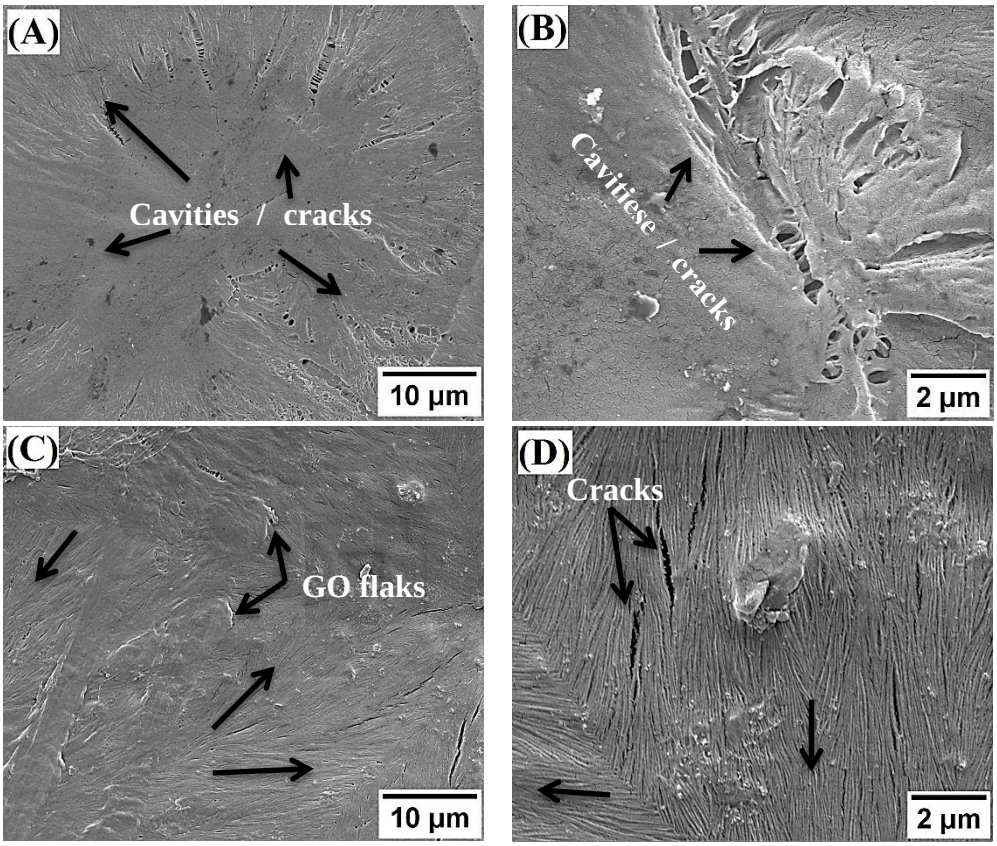

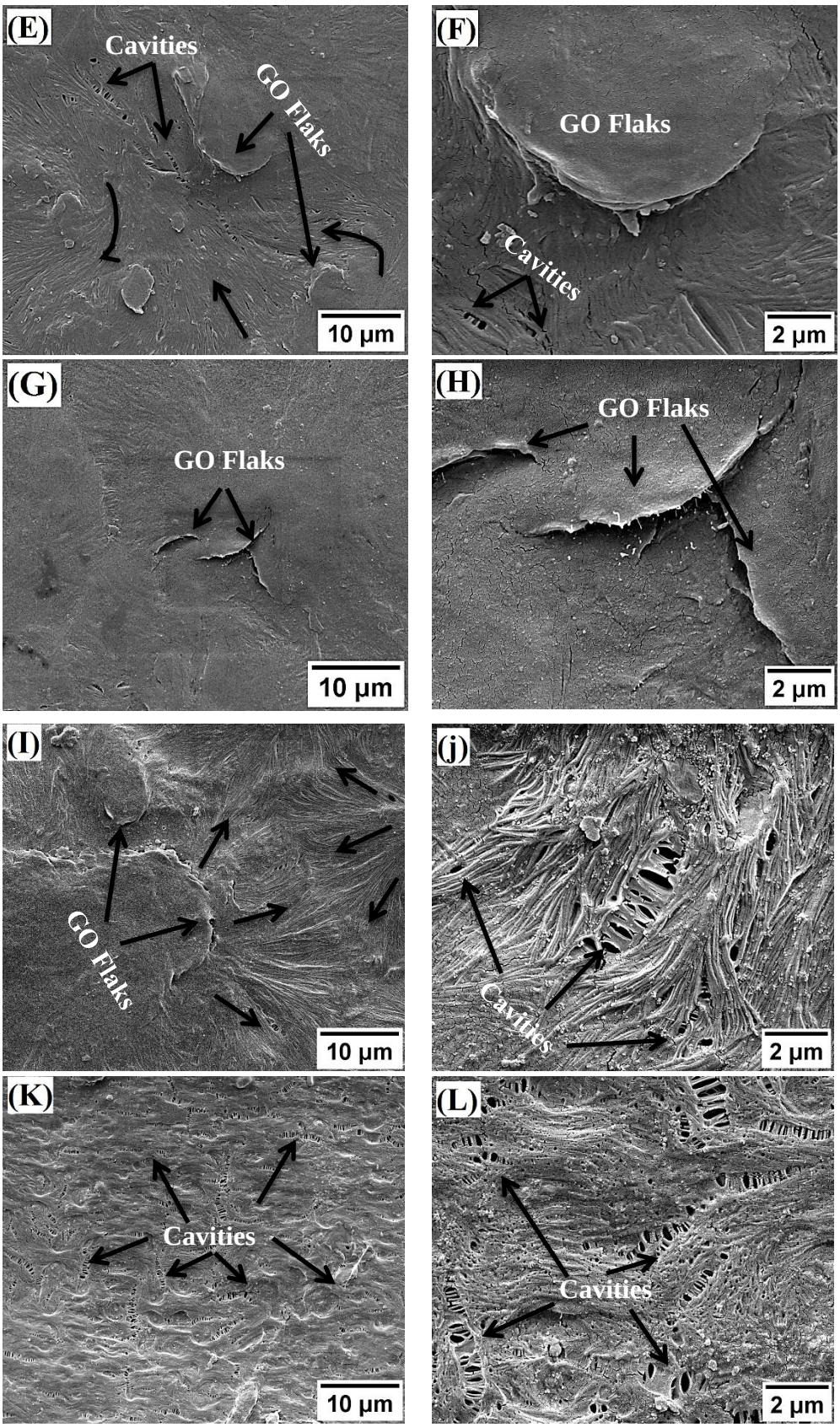

Figure 6-9: SEM images of the fracture surface (A and B) PEO, (C and D) PGO2, (E and F) PGO1, (G and H) PGO1-L, (I and J) PGO1-M and (K and L) PGO1-S.

Figure 6-9 shows the SEM images of the fracture surface of PEO and nanocomposites. In Figure 6-9 (A and B), the PEO fracture surface was clearly smooth surface without defects, such as air bubbles or surface pores but with crazies or chain rupture concentrations, as reported earlier by Stoeckel et al.[300], where, in semicrystalline polymers, cavities and solid inclusions could present or stacks of crystalline lamellae [284]. In Figure 6-9 (C and D), the fracture surface of PGO2 also had a smooth surface with few crazies, in addition to the lines surrounding of GO. This could be the interaction between GO and the PEO matrix or overlap of GO by PEO. PGO1 presented smooth surface textures, whereas some of GO edges with different particle sizes were displayed on the surface as shown in Figure 6-9 (E and F). The incorporation of GO played an important role in the enhancement of the interlocking PEO matrix with a clear reduction of cracks (as indicated by the arrows) on the surface but this did not overcome these cracks, only meaning that some cavities presented.

PGO1-L clearly observed a smooth surface and exhibited fully embedded and overlapped GO particles interlocked with each other and the PEO matrix without cracks and cavities on the surface, whereas few of the GO edges were presented locations pointing out of the fracture surface, as shown in Figure 6-9 (G and H). This observation confirmed that uniform and large particle sizes of GO not only plays an important role in enhancing the fracture surface and overcoming the crazies problem but also help to enable strong interactions with PEO. This gave strongly agreed with the tensile results, where the hydrogen bonding interaction combined the interface of GO with PEO. A similar behaviour was reported between poly(ethene glycol) and GO by others [186,224].

The PGO1-M illustrates a wrinkled surface and other objects like cavities between the GO flakes and polymer matrix, as shown in Figure 6-9 (I and J). These SEM images demonstrated the formulation of many lines emanating from the GO flake in more than one direction [222], or from each end of the graphene flake [211], providing isotropic reinforcement and interactions of GO nanosheets [222] with PEO matrix. Interestingly, these

lines shapes may represent the interaction between GO particle and PEO matrix that showed the shear elastic region to shear stress transfer and could reach about 15 μm, thus much higher than reported in the literature , which is 4 μm [211]. A broad distribution size of GO showed different directions of reinforcement because of the variety of particle size of GO and randomly incorporated of the GO sheets into a polymer matrix. Reducing the particle size of the GO from 1894 to 1082 nm represented a few cavities in the surface of PGO1-M. The number and size of these cavities increased with reducing the particle size of GO to the nanosize of PGO1-S, That led to the reduction of the effective length scale and presented of many crazies like a network in the surface of PGO1-S, where reducing the aspect ratio of the GO particle led to reducing the interfacial interaction and reinforcement of the nanocomposites and observed many cavities in the fracture surface [4,138]. These cavities become larger and propagated through the PEO matrix under strain, then led to new portions of nanocomposites and being plastically deformed [284]. This phenomenon was reported for high-density polyethylene-graphene nanocomposites by Weerasinghe et al. [152], they observed the presence of end stress at the edges of flake and a denser interphase interaction in vicinity of the flake without evidence of de-bonding between the filler and polymer matrix over the range of strains (<0.8%) using the simulation of mechanical testing. This performance could explain the deformation behaviour in the mechanical test and the reduction in the elongation at break value of the samples.

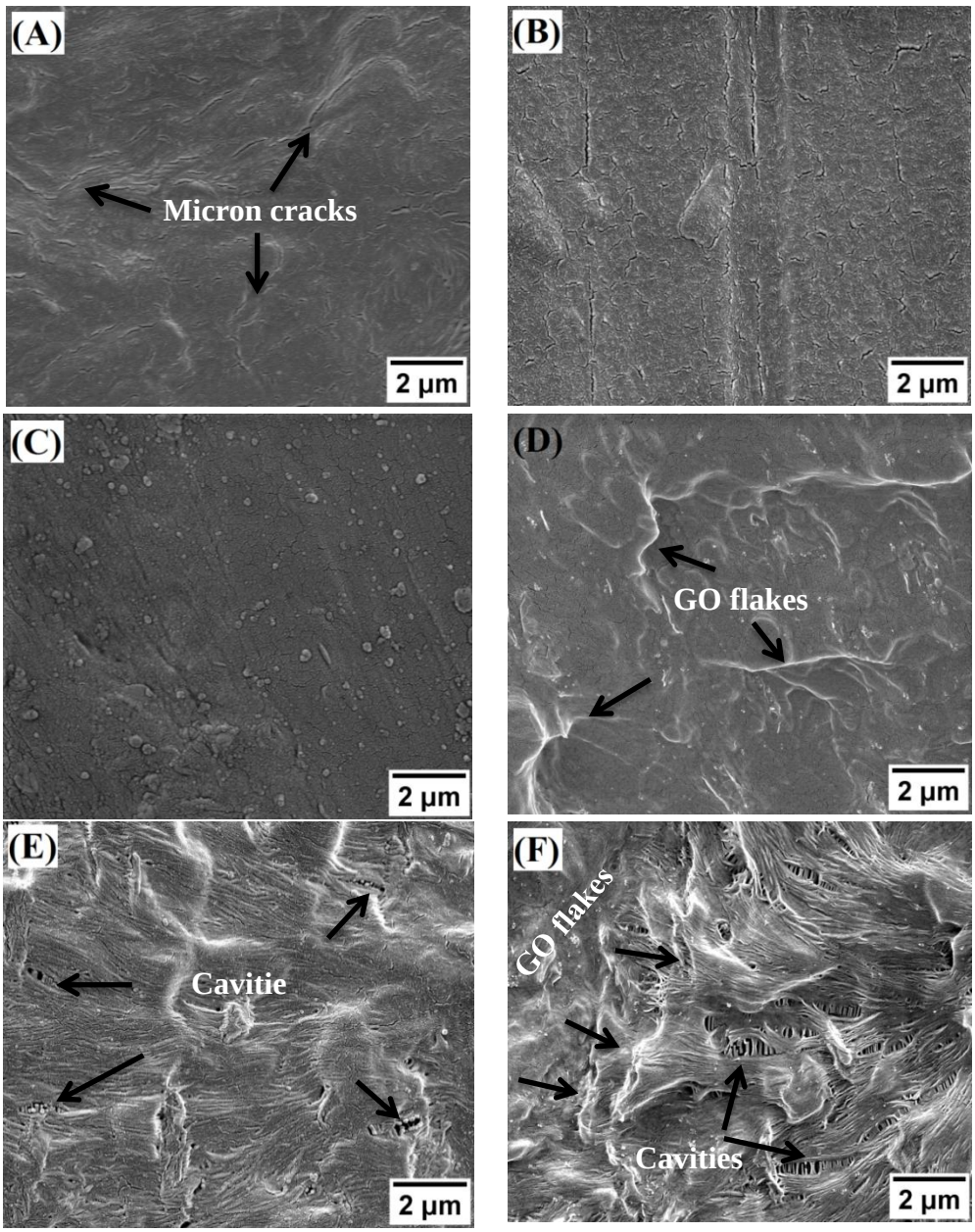

Figure 6-10: SEM images of the cross section of (A) PEO, (B) PGO2, (C) PGO1, (D) PGO1-L, (E) PGO1-M and (F) PGO1-S.

The SEM images of the cross section of PEO/ GO nanocomposites with a loading of 2.0 wt% GO nanosheets showed in Figure 6-10. The PEO image illustrates a smooth surface with many micro-cracks that clearly observed, as shown in Figure 6-10 (A). PGO1 and PGO2 present a clear smooth cross-section, whereas GO reduced the size of the cracks (as indicated by the arrows), as shown in Figure 6-10 (B and C), respectively. Interestingly, the PGO1-L presented a smooth surface and overlapping between GO nanosheets and PEO. The strong

interfacial interaction between graphene oxide with the PEO matrix and the fine homogeneous matrix of the nanocomposites reveal a significant influence and improve the mechanical and thermal properties [149]. The large particle size significantly enhanced the cross-section surface by overcoming the problem of cracks in the structure in addition to some at the GO edges, observed in the white strips (indicated by the arrows) as shown in Figure 6-10 (D). In Figure 6-10 (E), the rough surface with cavities (as indicated by the arrows) presented at the cross-section of PGO1-M, due to a decrease in particle size. The number and size of cavities increased with the reduction of particle size to a nanometer size of GO in the polymer matrix with the random dispersion of nanoparticle size (as indicated by the arrows). This clearly shows an increase in the wrinkled behaviour, with a reduction in the of PGO1-S particle sizes, as shown in Figure 6-10 (F). This behaviour indicated the reduction in the mechanical properties with the reduction of particle size of GO. The short length of flakes and not complete exfoliation affected the reinforcing efficiency in the nanocomposites [163] [213].

In both SEM images of the fracture surface and the cross section, a smooth surface, homogeneous dispersion, strong interfacial interaction and reinforcement in more than one direction were shown. The hydrogen bonding interaction showed a better compatible and more compact combination between the interface of the one uniform particle of GO and PEO [186], in agreement with the tensile results. These lead to reducing the crazies/ cavities by using narrow distribution and large particle size of GO. The samples turned to the more wrinkled surface and involved random dispersion, with the presence of cavities in the polymer matrix, with a reduction of the particle size of GO. Another important finding was related to reducing the particle size of GO. Also, the samples presented interactions like fibres/ lines between the GO and PEO matrix with cavities. SEM images showed clear evidence and explained the reduction of elongation at the break value of PGO1-S. Reducing the aspect ratio

of the nanofiller affect the reinforcement of the properties of the nanocomposites as reported in the literature [4,138].

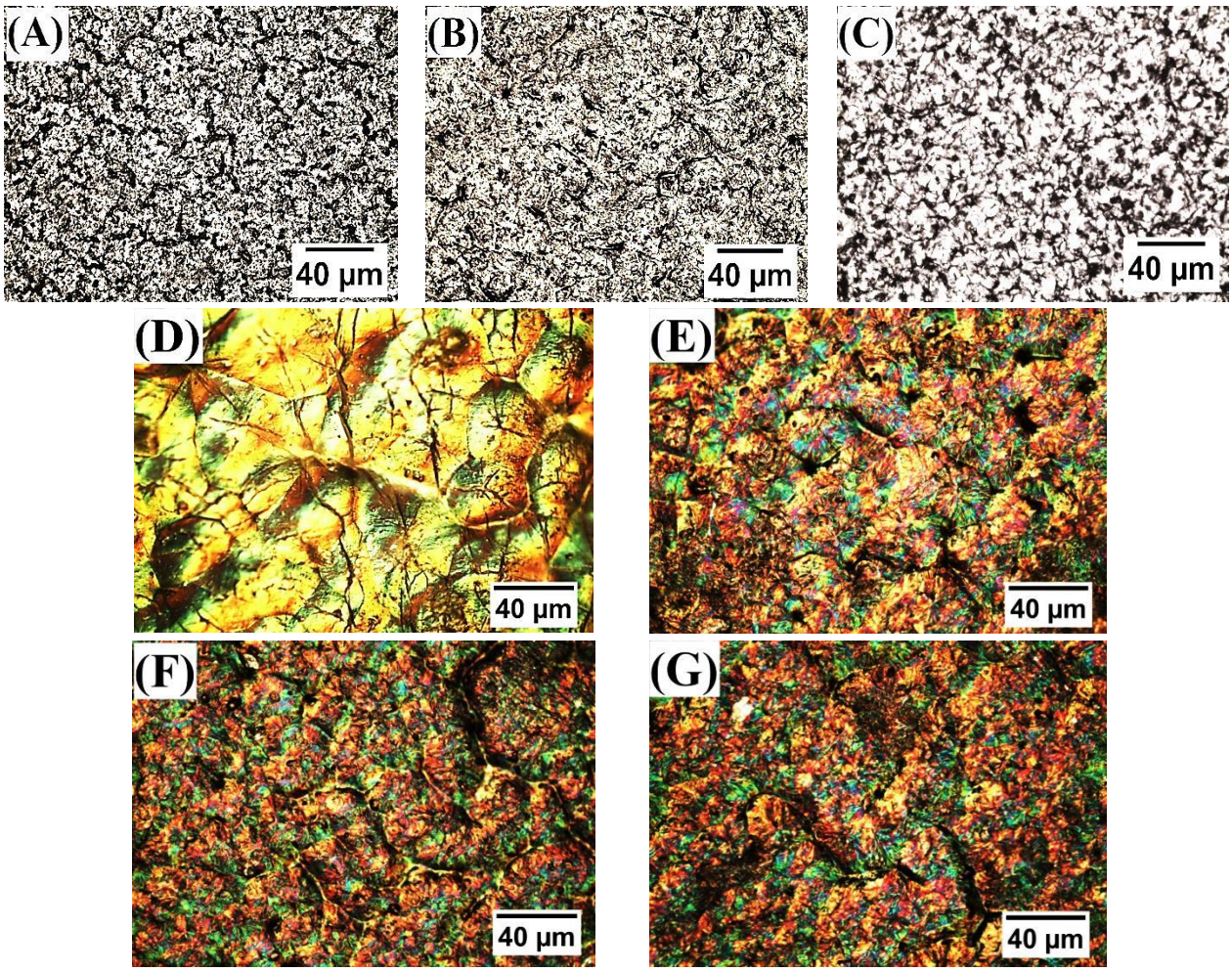

Figure 6-11: Optical images of (A) PGO1-L, (B) PGO1-M and (C) PGO1-S and polarize optical microscopy of (D) PEO, (E) PGO1-L, (F) PGO1-M and (G) PGO1-S.

The dispersion of the GO nanosheets into a polymer matrix was investigated using optical microscopy. Figure 6-11 (A, B and C) shows the optical graphs of the nanocomposites that confirmed a good dispersion of GO nanosheets into the PEO matrix of the PGO1-L, PGO1-M and PGO1-S, respectively. Exfoliating GO before and after mixed with the polar PEO, especially in the presence of high oxygen-contain functional groups on the GO surface, achieved the full dispersion of GO in the PEO matrix. Decreasing the particle size of GO led

to an increase in the transparency of the samples. In addition, to the fact that the nanosized of GO particles may present some aggregating in a few parts of PGO1-S during the strong physical interaction between the nanofiller, which it stacked together by van der Walls force as shown in Figure 6-11 (C).

Figure 6-11 (D) shows the polarized images of PEO films that presented clear semicrystalline behaviour. This was strongly influenced by the contribution of GO; where the GO nanosheets formed strong nucleating that influences the formation of spherulites under identical processing conditions [301]. This achieved a better order of crystallisation of PEO compared to other samples, as shown in Figure 6-11 (E). The growing of crystallising on the nucleation agents depended on the interphase interaction between the filler and matrix properties [242]. This finding strongly agreed with the DSC results, where DSC results also showed a decrease in crystallinity compared to the PEO value, with a reduction in the particle size to nanosize, as shown in Table 6-3. Additionally, similar behaviour was reported in the literature [222], in which a clear effect of GO particle on the nucleating agent was deduced, which led to influence the poly(butylene succinate) crystallinity. The large particle size of GO nanosheets demonstrated a slight reduction of the crystallinity size of PEG, providing more interaction sites, in addition to oxygen functional groups of GO in the volume. PGO1-M and PGO1-S exhibited a clear decrease of crystallite size with a reduction in the particle size of GO particles from 1894 to 1086, and to 360 nm, especially the latter as shown in Figure 6-11 (G).

6.4 Conclusions

The effect of GO size and effective length scale on the mechanical properties of GO nanocomposites is a very important issue for understanding the reinforcement of GO. The effect of a broad and narrow distribution sizes and different size of GO particle on the adsorption behaviour of PEO onto GO nanosheets and their mechanical properties were investigated.

In the adsorption behaviour of PEO, the FTIR results confirmed the preparation of GO nanosheets and adsorption of the PEO onto the GO nanosheets. It showed better interaction, higher vibration peak intensity and more bonds of the hybrids that contained a narrow size distribution of GO particles. The XRD result presented two crystalline peaks in the hybrids related to the GO and the adsorbed PEO. The (002) GO peak shifted due to the intercalated PEO between the GO nanosheets, whereas some peaks were related to adsorbed PEO on the surface. The (120) and (032) reflections of PEO presented sharp peaks with the separated microsize of GO particles, whereas a wide crystalline peak with small features was exhibited by others. This narrow distribution microsize of GO particles provided 54 wt.% as the best adsorption ratio of PEO in PGO1-L. The contribution of GO influenced the melting temperature, whereas SEM images showed the homogeneous and smooth surface of the sample that contained narrow distribution microsize of GO particles, which turned to a rough, fractured surface with the mediam particle size. It became a shrinkage surface with a reduction of the separated nanosize of GO particles. Generally, an increase in GO size leads to an increase in the PEO adsorption amount, which is raised from 47 to 54 wt.%. This means the larger GO exhibits better interaction with PEO than the smaller GO.

In the mechanical properties of PEO, a series of bulk PEO/GO nanocomposites were prepared using solution blending methods to reinforce bulk PEO with 2.0 wt.% GO nanosheets. The incorporation of GO increased the melting temperature of PEO by 2, 1.8 and 1.6 ^{o}C of PGO1-L, PGO1-M and PGO1-S respectively, compared to the neat PEO. The

crystallinity of PEO decreased by 17%. The T_d of PEO was significantly enhanced by 5 ^oC of both PGO1-L and PGO1-M, whereas it was decreased by 7 ^oC of PGO1-S. PGO1-L and PGO1-M, illustrating the best thermal stability are related to the contribution of large GO nanosheets.

The incorporation of a broad size distribution of GO showed an improvement in the mechanical properties, such that Young's modulus increased by 151 and 140% of PGO1 and PGO2, respectively, whereas reinforcing the PEO with separated sizes of GO particles demonstrated a significant increase in mechanical properties, with Young's modulus notably enhancing by 297, 200 and 125% of PGO1-L, PGO1-M and PGO1-S, respectively. This indicates that using GO with separated size enhances Young's modulus by 97%. A nanoindentation test showed similar results in terms of both hardness and elastic modulus. The hardness increased by 18% and 12% in PGO1 and PGO2, whereas it greatly improved by 275, 92 and 72% in PGO1-L, PGO1-M and PGO1-S, respectively. In addition, the elastic modulus was raised by 154, 21 and 14% by GO1-L, GO1-M and GO1-S, respectively. The SEM images of the fracture surface and cross section of PGO1-L showed a smooth surface without any sign of crazes, compared to the other samples.

The effective length scale of GO sheets depends on the GO size. This plays an important role in stress transfer between GO and the polymer matrix, leading to strong interfacial interaction and stronger reinforcement of polymer nanocomposites. The particle size of GO plays an important role in the microstructure of the PEO matrix, where the microsized particle of GO provides a larger effective length scale that led to stronger physical interaction between GO nanosheets and PEO. This, in turn, brought about another increase in tensile strength. The nanosize particle of GO showed good interaction with PEO, whereas under stress, a reduction in the elongation at break due to the limitation of the effective length scale of GO nanosized particles. This influenced the physical interaction between the GO nanoparticle and PEO matrix and led to lower mechanical properties. This result strongly

matched the theoretical calculation of elastic moduli considering the elective volume fraction that developed to take into account the contribution of the adsorbed PEO in the interface.

This study demonstrates that the size distribution and particle size of GO present as strong affecting parameters that not only influence the adsorption behaviour but also the thermal and mechanical properties. This study can be helpful to fill an essential knowledge gap for developing high-performance nanocomposites and facilitating the manufacture of polymer/graphene nanocomposites for a range of applications.

Chapter 7: Conclusions and future work

7.1 Overall conclusions

The adsorption behaviour of the polymer onto GO nanosheets is very important for understanding the interfacial interaction effect of GO nanosheets on the structure and properties of bulk polymer/GO nanocomposites. A series of hybrids were prepared using methods with different parameters, such as mixing time, polymer molecular weight, mixing ratio, washing procedure, the functional group of polymer and particle size of filler.

The characterization results confirmed the successful preparation of GO and the absorption of PEG between GO nanosheets for all samples, shifting the XRD peaks of the GO to lower value with a larger interlayer spacing, where the not-washed samples contained both absorbed and adsorbed polymer. The latter presents on the GO nanosheets surface, which show both XRD and DSC peaks. Manipulating the method and parameters successfully adsorbed the PEO especially for the non-washed samples. The thermal behaviour of the hybrids was improved by the incorporation of GO nanosheets. The absorption amount was enhanced by 46% through reducing the mixing time from 192 h to 72 h, by 13% through increasing the mixing ratio of the PEG, by 1700% when increasing the PEG molecular weight from 1k to 100k, by 44% without a further washing procedure and by 73% for applying these parameters together.

The functional group of polymer is an important factor associated with good interfacial interaction and adsorption of the polymer onto GO nanosheets surface, where the amount of the adsorbed polymer was increased to 22 wt.%, 27 wt.% and 40 wt.% for the PMMA/GO, PMMA-MMA/GO and PMAA/GO respectively. Even with a lower feeding ratio of acid groups (MAA) in the PMMA-co-MAA, it provides a notable enhancement in the adsorption amount up to 23% of PMMA-co-MAA/GO compared to PMMA/GO. PMAA with

a MAA unit showed the best interaction and adsorption rather than PMMA-co-MAA or PMMA, where the adsorption amount improved up to 82% of the PMAA/GO.

The washing procedure provides a direct influence on all the characterization results of the washed samples. It removes most of the adsorbed polymer on the surface of GO nanosheets and a small fraction of the confined polymer, where most of the adsorbed polymer is confined between the GO nanosheets. The incorporation of GO with abundant functional groups of nanosheets strongly restricts the polymers between the 2D layers even with washed samples.

The GO had a broad size distribution of particles with irregular shapes. Each particle size of GO provides different effective length scales, reaching up to several microns. This strongly influences the interfacial interaction and the load transfer between the polymer matrix and the filler. Therefore, a new sonication-centrifugation based green method was developed using different parameters: a low sonication power for a short period of time up to 5 h only, different centrifugal forces and times. A series of the narrow size distribution of GO particles were successfully separated using this developed green method, where it started from ~ 200 nm as the lower particle size to 2000 nm through ~ 600, 800, 500, 1200, 1450, 1600, 1800 and 2000 nm. This method readily separates the GO particle sizes to fill an important technical gap to facilitate graphene oxide (and graphene) nanoparticles with a targeted narrow size distribution for a range of applications.

Using a narrow size distribution of GO particles presented significant enhancement in the adsorption results. It significantly enhanced of the adsorption amount of the samples containing separated large-sized particles up to 54%, compared to the values for a broad size distribution of particles from the study in chapter 3, which reached 38 wt.%. Furthermore increasing the size of the GO particles from nanosize to microsize significantly enhanced the adsorption amount by 42%.

Not only was the adsorption amount significantly influenced by using a narrow size distribution and large particle size of GO particles, but also the interfacial interaction, the melting behaviour and the mechanical properties, where the incorporation of 2.0 wt.% of a narrow size distribution of GO particles showed a notable improvement in T_m and Young's modulus, which was improved by 2 ^oC and 97%, respectively compared to the values for the samples contained a broad size distribution of GO particles.

Samples containing the narrowly distributed microsize of GO particles significantly improved by 77%, in terms of Young's modules, compared to samples containing nanosize GO. All other characterization showed improvements when using one uniform size, even with nanoparticles. The latter showed better results than the samples with a broad size distribution of GO particles, such as Young's modulus of the nanocomposites, enhanced by 57%. Reduction in the particle size to the nanosize of the GO sheets reduced the adsorption amount and mechanical properties. The nanosize particle has a lower effective length scale that influenced the load transfer between the GO nanofiller with the polymer. This led to the reduction of the elongation at break of PGO1-S. Moreover, T_m and X_c were also influenced by the reduction in the particle size of GO by 0.4 ^oC and 9% as well as the crystallite size as presented by OLM.

Generally, this study shows significant factors that can influence the interfacial interaction between the polymer and GO and can improve the nanocomposites' properties. This study is helpful in filling an essential knowledge gap in the quest to develop high-performance nanocomposites whilst also facilitating the processing of graphene-based nanomaterials with targeted particle sizes and size distributions for a range of applications.

7.2 Future work

Future work to be carried out may include the following investigations:

1- The effect of different reduction degrees of GO nanosheets on the polymer adsorption behaviour onto RGO nanosheets.

2- The effect of functional groups of functional polymer with different reduction degree of GO nanosheets on the polymer adsorption behaviour onto RGO nanosheets. This could show how the polymer functional group influences the adsorption amount with RGO sheets with less oxygen contents.

3- The effect of RGO particle size on the adsorption behaviour on the polymer adsorption behaviour onto RGO nanosheets.

4- The effect of RGO particle size on the mechanical properties involved in the polymer adsorption behaviour onto RGO nanosheets,

5- The effect of particle size of RGOs on the electrical properties of polymer/Graphene nanocomposites,

6- The effect of particle size of graphene on the optical properties of polymer/Graphene nanocomposites.

The presence of functional groups on the GO surface provides more compatibles for interaction with a polymer but have the drawback that they reduce the properties of graphene sheets properties. Additionally, a reduction in the functional GO groups leads to the restoration and enhancement of the properties of RGO, such as electrical. These are giving a better performance of nanocomposites and offer a broad line of applications.

References

[1] W. Callister, Fundamentals of Materials Science and Engineering, 5th ed., John Wiley & Sons, Inc., 2001.

[2] S. Anandhan, S. Bandyopadhyay, Polymer Nanocomposites : From Synthesis to Applications, (2003) , PP. 3–28.

[3] R.O. Ebewele, Polymer science and technology, CRC Press LLC, Florida, USA, 2000.

[4] M. Bhattacharya, Polymer nanocomposites-A comparison between carbon nanotubes, graphene, and clay as nanofillers, Materials (Basel). 9, (2016) , PP. 1–35.

[5] I.T. Kim, J.H. Lee, M.L. Shofner, K. Jacob, R. Tannenbaum, Crystallization kinetics and anisotropic properties of polyethylene oxide/magnetic carbon nanotubes composite films, Polymer (Guildf). 53, (2012) , PP. 2402–2411.

[6] R. Krishnamoorti, R.A. Vaia, Polymer Nanocomposites, J. Polym. Sci. Part B Polym. Phys. 45, (2007) , PP. 3252–3256.

[7] D.R. Paul, L.M. Robeson, Polymer nanotechnology: Nanocomposites, Polymer (Guildf). 49, (2008) , PP. 3187–3204.

[8] M. Mohammad, K.I. Winey, Polymer Nanocomposites Containing Carbon Nanotubes, Macromolecules. 39, (2006) , PP. 5194–5205.

[9] J. Pyun, K. Matyjaszewski, Synthesis of Nanocomposite Organic / Inorganic Hybrid Materials Using Controlled /“ Living ” Radical Polymerization, Synthesis (Stuttg). (2001) , PP. 3436–3448.

[10] R.A. Vaia, J.F. Maguire, Polymer nanocomposites with prescribed morphology: Going beyond nanoparticle-filled polymers, Chem. Mater. 19, (2007) , PP. 2736–2751.

[11] I. Kang, Y.Y. Heung, J.H. Kim, J.W. Lee, R. Gollapudi, S. Subramaniam, S. Narasimhadevara, D. Hurd, G.R. Kirikera, V. Shanov, M.J. Schulz, D. Shi, J. Boerio, S. Mall, M. Ruggles-Wren, Introduction to carbon nanotube and nanofiber smart materials, Compos. Part B Eng. 37, (2006) , PP. 382–394.

[12] J.R. Potts, Preparation, Properties and Structure-Property Relationships of Graphene-Polymer Nanocomposites, The University of Texas at Austin, 2012.

[13] C.D. Han, On the mechanisms leading to exfoliated nanocomposites prepared by mixing, Adv. Polym. Sci. 231, (2010) , PP. 1–75.

[14] J. Jancar, J.F. Douglas, F.W. Starr, S.K. Kumar, P. Cassagnau, A.J. Lesser, S.S. Sternstein, M.J. Buehler, Current issues in research on structure-property relationships in polymer nanocomposites, Polymer (Guildf). 51, (2010) , PP. 3321–3343.

[15] K.I. Winey, R. a Vaia, Polymer Nanocomposites, Mrs Bull. 32, (2007) , PP. 314–358.

[16] R.A. Vaia, P. Emmanuel, Polymer Nanocomposites : Status and Opportunities, MRS Bull. (2001) , PP. 394–401.

[17] A.R. Bunsell, B. Harris, Hybrid carbon and glass fibre composites, Composites. 5, (1974) , PP. 157–164.

[18] A. Okada, A. Usuki, Twenty years of polymer-clay nanocomposites, Macromol. Mater. Eng. 291, (2006) , PP. 1449–1476.

[19] D.C. Marcano, D. V Kosynkin, J.M. Berlin, A. Sinitskii, Z. Sun, A. Slesarev, L.B. Alemany, W. Lu, J.M. Tour, Improved synthesis of graphene oxide., ACS Nano. 4, (2010) , PP. 4806–14.

[20] H. Bao, Y. Pan, Y. Ping, N.G. Sahoo, T. Wu, L. Li, J. Li, L.H. Gan, Chitosan-functionalized graphene oxide as a nanocarrier for drug and gene delivery, Small. 7, (2011) , PP. 1569–1578.

[21] S.K. Kumar, R. Krishnamoorti, Nanocomposites: Structure, Phase Behavior, and Properties, Annu. Rev. Chem. Biomol. Eng. 1, (2010) , PP. 37–58.

[22] T.D. Fornes, D.R. Paul, Modeling properties of nylon 6/clay nanocomposites using composite theories, Polymer (Guildf). 44, (2003) , PP. 4993–5013.

[23] S. Park, K.S. Lee, G. Bozoklu, W. Cai, S.B.T. Nguyen, R.S. Ruoff, Graphene oxide papers modified by divalent ions - Enhancing mechanical properties via chemical cross-linking, ACS Nano. 2, (2008) , PP. 572–578.

[24] T.A. Pham, B.C. Choi, K.T. Lim, Y.T. Jeong, A simple approach for immobilization of gold nanoparticles on graphene oxide sheets by covalent bonding, Appl. Surf. Sci. 257, (2011) , PP. 3350–3357.

[25] W. Hummers, R. Offeman, Preparation of Graphitic Oxide, J. Am. Chem. Soc. 80, (1958) , PP. 1339.

[26] S. Thomas, K. Joseph, S.K. Malhotra, K. Goda, Polymer Composites: Volume 1, 1st editio, KGaA, Wiley-VCH Verlag GmbH & Co., 2012.

[27] A. Malkin, A. Askadsky, V. Kovriga, A. Chalykh, Experimental methods of polymer physics, Mir Publishers, Moscow/Prentice-Hall, Englewood Cliffs, NJ, Mir Moscow, 1983.

[28] C. Mayer, X. Wang, M. Neitzel, Macro- and micro-impregnation phenomena in continuous manufacturing of fabric reinforced thermoplastic composites, Compos. Part A Appl. Sci. Manuf. 29, (1998) , PP. 783–793.

[29] S. Komarneni, Nanocornposites, J. Mater. Chem. 2, (1992) , PP. 1219–1230.

[30] S. Hehir, N.R. Cameron, Recent advances in drug delivery systems based on polypeptides prepared from N-carboxyanhydrides, Polym. Int. 63, (2014) , PP. 943–954.

[31] E. Giannelis, Polymer layered silicate nanocomposites, Adv. Mater. (1996) , PP. 29–35.

[32] R.F. Ziolo, E.P. Giannelis, B.A. Weinstein, M.P. O'Horo, B.N. Ganguly, V. Mehrotra, M.W. Russell, D.R. Huffman, Matrix-Mediated Synthesis of Nanocrystalline ggr-Fe2O3: A New Optically Transparent Magnetic Material, Science (80-.). 257, (1992) , PP. 219–223.

[33] S. Divinski, H. Rösner, G. Wilde, Nanostructured Materials, Adv. Mater. 4, (1992) , PP. 474–481.

[34] B.M. Novak, Hybrid Nanocomposite Materials-between inorganic glasses and organic polymers, Adv. Mater. 5, (1993) , PP. 422–433.

[35] S. Cheong, P. Ferguson, K.W. Feindel, I.F. Hermans, P.T. Callaghan, C. Meyer, A. Slocombe, C.H. Su, F.Y. Cheng, C.S. Yeh, B. Ingham, M.F. Toney, R.D. Tilley, Simple synthesis and functionalization of iron nanoparticles for magnetic resonance

imaging, Angew. Chemie - Int. Ed. 50, (2011) , PP. 4206–4209.

[36] V.N. Mochalin, Y. Gogotsi, Nanodiamond-polymer composites, Diam. Relat. Mater. 58, (2015) , PP. 161–171.

[37] A.K.K. Geim, K.S.S. Novoselov, The rise of graphene., Nat. Mater. 6, (2007) , PP. 183–191.

[38] Y.-L. Zhang, Q.-D. Chen, Z. Jin, E. Kim, H.-B. Sun, Biomimetic graphene films and their properties, Nanoscale. 4, (2012) , PP. 4858–4869.

[39] J. Chen, B. Yao, C. Li, G. Shi, An improved Hummers method for eco-friendly synthesis of graphene oxide, Carbon N. Y. 64, (2013) , PP. 225–229.

[40] Y. Zhu, S. Murali, W. Cai, X. Li, J.W. Suk, J.R. Potts, R.S. Ruoff, Graphene and graphene oxide: synthesis, properties, and applications., Adv. Mater. 22, (2010) , PP. 3906–24.

[41] H. Chang, H. Wu, Graphene-based nanocomposites: preparation, functionalization, and energy and environmental applications, Energy Environ. Sci. 6, (2013) , PP. 3483–3507.

[42] X.S. Li, Y.W. Zhu, W.W. Cai, M. Borysiak, B.Y. Han, D. Chen, R.D. Piner, L. Colombo, R.S. Ruoff, Transfer of Large-Area Graphene Films for High-Performance Transparent Conductive Electrodes, Nano Lett. 9, (2009) , PP. 4359–4363.

[43] C. Lee, X. Wei, J.W. Kysar, J. Hone, Measurement of the Elastic Properties and Intrinsic Strength of Monolayer Graphene, Science (80-.). 321, (2008) , PP. 385–388.

[44] C.O. Girit, J.C. Meyer, R. Erni, M.D. Rossell, C. Kisielowski, L. Yang, C.-H. Park, M.F. Crommie, M.L. Cohen, S.G. Louie, A. Zettl, Graphene at the Edge: Stability and Dynamics, Scince. 323, (2009) , PP. 1705–1708.

[45] T. Kavitha, S.I.H. Abdi, S.-Y. Park, pH-sensitive nanocargo based on smart polymer functionalized graphene oxide for site-specific drug delivery., Phys. Chem. Chem. Phys. 15, (2013) , PP. 5176–85.

[46] D. Choi, D. Wang, V. V. Viswanathan, I.T. Bae, W. Wang, Z. Nie, J.G. Zhang, G.L. Graff, J. Liu, Z. Yang, T. Duong, Li-ion batteries from LiFePO4 cathode and anatase/graphene composite anode for stationary energy storage, Electrochem. Commun. 12, (2010) , PP. 378–381.

[47] J.K. Lee, K.B. Smith, C.M. Hayner, H.H. Kung, Silicon nanoparticles–graphene paper composites for Li ion battery anodes, Chem. Commun. 46, (2010) , PP. 2025–2027.

[48] N.O. Weiss, H. Zhou, L. Liao, Y. Liu, S. Jiang, Y. Huang, X. Duan, Graphene: An emerging electronic material, Adv. Mater. 24, (2012) , PP. 5782–5825.

[49] Y. Liu, X. Dong, P. Chen, Biological and chemical sensors based on graphene materials, Chem. Soc. Rev. 41, (2012) , PP. 2283–2307.

[50] W. and et al. Jonathan, Oh, the Places You'll Go with Graphene, Cell. 163, (2013) , PP. 1304–1305.

[51] C. Huang, C. Li, G. Shi, Graphene based catalysts, Energy Environ. Sci. 5, (2012) , PP. 8848–8868.

[52] E. Pop, D. Mann, Q. Wang, K. Goodson, H.J. Dai, Thermal conductance of an individual single-wall carbon nanotube above room temperature, Nano Lett. 6, (2006) ,

PP. 96–100.

[53] S. Park, R.S. Ruoff, Chemical methods for the production of graphenes, Nat. Nanotechnol. 4, (2009) , PP. 217–224.

[54] D.W. Boukhvalov, M.I. Katsnelson, Modeling of Graphite Oxide, 130, (2008) , PP. 10697–10701.

[55] W. Zhang, V. Carravetta, Z. Li, Y. Luo, J. Yang, Oxidation states of graphene: Insights from computational spectroscopy, J. Chem. Phys. 131, (2009) , PP. 1–6.

[56] A. Lerf, H. He, M. Forster, J. Klinowski, Structure of Graphite Oxide Revisited, J. Phys. Chem. B. 102, (1998) , PP. 4477–4482.

[57] H. He, J. Klinowski, M. Forster, A. Lerf, A new structural model for graphite oxide, Chem. Phys. Lett. 287, (1998) , PP. 53–56.

[58] H. Kim, A. Abdala, C. Macosko, Graphene/polymer nanocomposites, Macromolecules. 43, (2010) , PP. 6515–6530.

[59] B.C. Brodie, On the Atomic Weight of Graphite, Philos. Trans. R. Soc. London. 149, (1859) , PP. 249–259.

[60] W. Gao, L.B. Alemany, L. Ci, P.M. Ajayan, New insights into the structure and reduction of graphite oxide, Nat. Chem. 1, (2009) , PP. 403–408.

[61] K.A. Mkhoyan, A.W. Contryman, J. Silcox, A. Derek, G. Eda, C. Mattevi, S. Miller, M. Chhowalla, D.A. Stewart, Atomic and Electronic Structure of Graphene-Oxide, Nano Lett. 9, (2009) , PP. 17–21.

[62] L. Liu, J. Zhang, J. Zhao, F. Liu, Mechanical properties of graphene oxides, Nanoscale. 4, (2012) , PP. 5910–5916.

[63] J.W. Suk, R.D. Piner, J. An, R.S. Ruoff, Mechanical properties of monolayer graphene oxide, ACS Nano. 4, (2010) , PP. 6557–6564.

[64] K. Krishnamoorthy, M. Veerapandian, K. Yun, S.J. Kim, The chemical and structural analysis of graphene oxide with different degrees of oxidation, Carbon N. Y. 53, (2013) , PP. 38–49.

[65] O.C. Compton, D.A. Dikin, K.W. Putz, L.C. Brinson, S.T. Nguyen, Electrically conductive “alkylated” graphene paper via chemical reduction of amine-functionalized graphene oxide paper, Adv. Mater. 22, (2010) , PP. 892–896.

[66] J.P. Zhao, S.F. Pei, W.C. Ren, L.B. Gao, H.M. Cheng, Efficient Preparation of Large-Area Graphene Oxide Sheets for Transparent Conductive Films, ACS Nano. 4, (2010) , PP. 5245–5252.

[67] C. Gómez-Navarro, R.T. Weitz, A.M. Bittner, M. Scolari, A. Mews, M. Burghard, K. Kern, Electronic transport properties of individual chemically reduced graphene oxide sheets, Nano Lett. 7, (2007) , PP. 3499–3503.

[68] H.A. Becerril, J. Mao, Z. Liu, R.M. Stoltenberg, Z. Bao, Y. Chen, Evaluation of solution-processed reduced graphene oxide films as transparent conductors, ACS Nano. 2, (2008) , PP. 463–470.

[69] F. Barroso-Bujans, S. Cerveny, A. Alegría, J. Colmenero, Sorption and desorption behavior of water and organic solvents from graphite oxide, Carbon N. Y. 48, (2010) , PP. 3277–3286.

[70] K. Liul, J.E. Anderson, Solvent Effects on the Proton Magnetic Relaxation of Poly (ethylene oxide), 3, (1969) , PP. 163–164.

[71] Y. Matsuo, T. Miyabe, T. Fukutsuka, Y. Sugie, Preparation and characterization of alkylamine-intercalated graphite oxides, Carbon N. Y. 45, (2007) , PP. 1005–1012.

[72] Y. Matsuo, T. Tabata, T. Fukunaga, T. Fukutsuka, Y. Sugie, Preparation and characterization of silylated graphite oxide, Carbon N. Y. 43, (2005) , PP. 2875–2882.

[73] Y. Matsuo, T. Niwa, Y. Sugie, Preparation and characterization of cationic surfactant-intercalated graphite oxide, Carbon N. Y. 37, (1999) , PP. 897–901.

[74] F. Barroso-Bujans, F. Fernandez-Alonso, J.A. Pomposo, E. Enciso, J.L.G. Fierro, J. Colmenero, Tunable uptake of poly(ethylene oxide) by graphite-oxide-based materials, Carbon N. Y. 50, (2012) , PP. 5232–5241.

[75] F. Barroso-Bujans, A. Alegria, J. Colmenero, Kinetic study of the graphite oxide reduction: Combined structural and gravimetric experiments under isothermal and nonisothermal conditions, J. Phys. Chem. C. 114, (2010) , PP. 21645–21651.

[76] K.S. Novoselov, A.K. Geim, S. V. Morozov, D. Jiang, Y. Zhang, S. V. Dubonos, I. V. Grigorieva, A.A. Firsov, Electric Field Effect in Atomically Thin Carbon Films, Science (80-.). 306, (2004) , PP. 666–669.

[77] N. Behabtu, J.R. Lomeda, M.J. Green, A.L. Higginbotham, A. Sinitskii, D. V Kosynkin, D. Tsentalovich, a N.G. Parra-Vasquez, J. Schmidt, E. Kesselman, Y. Cohen, Y. Talmon, J.M. Tour, M. Pasquali, Spontaneous high-concentration dispersions and liquid crystals of graphene., Nat. Nanotechnol. 5, (2010) , PP. 406–411.

[78] Y. Hernandez, V. Nicolosi, M. Lotya, F.M. Blighe, Z. Sun, S. De, I.T. McGovern, B. Holland, M. Byrne, Y.K. Gun'Ko, J.J. Boland, P. Niraj, G. Duesberg, S. Krishnamurthy, R. Goodhue, J. Hutchison, V. Scardaci, A.C. Ferrari, J.N. Coleman, High-yield production of graphene by liquid-phase exfoliation of graphite., Nat. Nanotechnol. 3, (2008) , PP. 563–568.

[79] A.B. Bourlinos, V. Georgakilas, R. Zboril, T.A. Sterioti, A.K. Stubos, Liquid-Phase Exfoliation of Graphite Towards Solubilized Graphenes, Small. 5, (2009) , PP. 1841–1845.

[80] N. Liu, F. Luo, H. Wu, Y. Liu, C. Zhang, J. Chen, One-step ionic-liquid-assisted electrochemical synthesis of ionic-liquid-functionalized graphene sheets directly from graphite, Adv. Funct. Mater. 18, (2008) , PP. 1518–1525.

[81] S. Stankovich, D. a. Dikin, R.D. Piner, K. a. Kohlhaas, A. Kleinhammes, Y. Jia, Y. Wu, S.T. Nguyen, R.S. Ruoff, Synthesis of graphene-based nanosheets via chemical reduction of exfoliated graphite oxide, Carbon N. Y. 45, (2007) , PP. 1558–1565.

[82] G. Wang, X. Shen, B. Wang, J. Yao, J. Park, Synthesis and characterisation of hydrophilic and organophilic graphene nanosheets, Carbon N. Y. 47, (2009) , PP. 1359–1364.

[83] J.R. Lomeda, C.D. Doyle, D. V. Kosynkin, W.F. Hwang, J.M. Tour, Diazonium functionalization of surfactant-wrapped chemically converted graphene sheets, J. Am. Chem. Soc. 130, (2008) , PP. 16201–16206.

[84] H. Wang, J.T. Robinson, X. Li, H. Dai, Solvothermal reduction of chemically exfoliated graphene sheets, J. Am. Chem. Soc. 131, (2009) , PP. 9910–9911.

[85] H.C. Schniepp, J.L. Li, M.J. McAllister, H. Sai, M. Herrera-Alonson, D.H. Adamson, R.K. Prud'homme, R. Car, D.A. Seville, I.A. Aksay, Functionalized single graphene sheets derived from splitting graphite oxide, J. Phys. Chem. B. 110, (2006) , PP. 8535–8539.

[86] M.J. Mcallister, J. Li, D.H. Adamson, H.C. Schniepp, A. a Abdala, J. Liu, O.M. Herrera-alonso, D.L. Milius, R. Car, R.K. Prud, I. a Aksay, Single Sheet Functionalized Graphene by Oxidation and Thermal Expansion of Graphite, Chem. Mater. 19, (2007) , PP. 4396–4404.

[87] M. Acik, Y.J. Chabal, A Review on Reducing Graphene Oxide for Band Gap Engineering, J. Mater. Sci. Res. 2, (2012) , PP. 101–112.

[88] P. Steurer, R. Wissert, R. Thomann, R. Mülhaupt, Functionalized graphenes and thermoplastic nanocomposites based upon expanded graphite oxide, Macromol. Rapid Commun. 30, (2009) , PP. 316–327.

[89] Y. Zhou, Q. Bao, L.A.L. Tang, Y. Zhong, K.P. Loh, Hydrothermal dehydration for the "green" reduction of exfoliated graphene oxide to graphene and demonstration of tunable optical limiting properties, Chem. Mater. 21, (2009) , PP. 2950–2956.

[90] X. An, T. Simmons, R. Shah, C. Wolfe, K.M. Lewis, M. Washington, S.K. Nayak, S. Talapatra, S. Kar, Stable aqueous dispersions of noncovalently functionalized graphene from graphite and their multifunctional high-performance applications, Nano Lett. 10, (2010) , PP. 4295–4301.

[91] Liu, M.M. Lerner, M. Yan, Derivitization of Pristine Graphene with Well-Defind Chemical Functionalities, Nano Lett. 23, (2008) , PP. 1–7.

[92] X. Qi, K.-Y. Pu, H. Li, X. Zhou, S. Wu, Q.L. Fan, B. Liu, F. Boey, W. Huang, H. Zhang, Amphiphilic graphene composites, Angew. Chemie - Int. Ed. 49, (2010) , PP. 9426–9429.

[93] E.-Y. Choi, T.H. Han, J. Hong, J.E. Kim, S.H. Lee, H.W. Kim, S.O. Kim, Noncovalent functionalization of graphene with end-functional polymers, J. Mater. Chem. 20, (2010) , PP. 1907–1912.

[94] T. Ramanathan, a a Abdala, S. Stankovich, D. a Dikin, M. Herrera-Alonso, R.D. Piner, D.H. Adamson, H.C. Schniepp, X. Chen, R.S. Ruoff, S.T. Nguyen, I. a Aksay, R.K. Prud'Homme, L.C. Brinson, Functionalized graphene sheets for polymer nanocomposites., Nat. Nanotechnol. 3, (2008) , PP. 327–331.

[95] X. Wang, L. Zhi, K. Müllen, Transparent, conductive graphene electrodes for dye-sensitized solar cells, Nano Lett. 8, (2008) , PP. 323–327.

[96] J. Wu, H.A. Becerril, Z. Bao, Z. Liu, Y. Chen, P. Peumans, Organic solar cells with solution-processed graphene transparent electrodes, Appl. Phys. Lett. 92, (2008) , PP. 1–3.

[97] S. Cui, S. Mao, G. Lu, J. Chen, Graphene coupled with nanocrystals: Opportunities and challenges for energy and sensing applications, J. Phys. Chem. Lett. 4, (2013) , PP. 2441–2454.

[98] Y. Li, Y. Hu, Y. Zhao, G. Shi, L. Deng, Y. Hou, L. Qu, An electrochemical avenue to green-luminescent graphene quantum dots as potential electron-acceptors for photovoltaics, Adv. Mater. 23, (2011) , PP. 776–780.

[99] J. Yan, Q. Ye, X. Wang, B. Yu, F. Zhou, CdS/CdSe quantum dot co-sensitized

graphene nanocomposites via polymer brush templated synthesis for potential photovoltaic applications, Nanoscale. 4, (2012) , PP. 2109–2116.

[100] X.-Y. Zhang, H.-P. Li, X.-L. Cui, Y. Lin, Graphene/TiO2 nanocomposites: synthesis, characterization and application in hydrogen evolution from water photocatalytic splitting, J. Mater. Chem. 20, (2010) , PP. 2801–2806.

[101] J.Z. Wang, L. Lu, M. Choucair, J.A. Stride, X. Xu, H.K. Liu, Sulfur-graphene composite for rechargeable lithium batteries, J. Power Sources. 196, (2011) , PP. 7030–7034.

[102] J. Lin, Z. Peng, C. Xiang, G. Ruan, Z. Yan, D. Natelson, J.M. Tour, Graphene nanoribbon and nanostructured SnO2 composite anodes for lithium ion batteries, ACS Nano. 7, (2013) , PP. 6001–6006.

[103] Z.S. Wu, W. Ren, D.W. Wang, F. Li, B. Liu, H.M. Cheng, High-energy MnO2 nanowire/graphene and graphene asymmetric electrochemical capacitors, ACS Nano. 4, (2010) , PP. 5835–5842.

[104] S. Guo, S. Sun, FePt nanoparticles assembled on graphene as enhanced catalyst for oxygen reduction reaction, J. Am. Chem. Soc. 134, (2012) , PP. 2492–2495.

[105] Y. Wen, F. Xing, S. He, S. Song, L. Wang, Y. Long, D. Li, C. Fan, A graphene-based fluorescent nanoprobe for silver(i) ions detection by using graphene oxide and a silver-specific oligonucleotide, Chem. Commun. 46, (2010) , PP. 2596–2598.

[106] H. Zhang, X. Lv, Y. Li, Y. Wang, J. Li, P25-graphene composite as a high performance photocatalyst, ACS Nano. 4, (2010) , PP. 380–386.

[107] F. Schedin, A.K. Geim, S. V. Morozov, E.W. Hill, P. Blake, M.I. Katsnelson, K.S. Novoselov, Detection of individual gas molecules adsorbed on graphene, Nat. Mater. 6, (2007) , PP. 652–655.

[108] T.H. Han, Y.K. Huang, A.T.L. Tan, V.P. Dravid, J. Huang, Steam etched porous graphene oxide network for chemical sensing, J. Am. Chem. Soc. 133, (2011) , PP. 15264–15267.

[109] Q. Ji, I. Honma, S.-M. Paek, M. Akada, J.P. Hill, A. Vinu, K. Ariga, Layer-by-Layer Films of Graphene and Ionic Liquids for Highly Selective Gas Sensing, Angew. Chemie. 122, (2010) , PP. 9931–9933.

[110] W. Li, X. Geng, Y. Guo, J. Rong, Y. Gong, L. Wu, X. Zhang, P. Li, Reduced Graphene Oxide Electrically Contacted Graphene Sensor for Highly Sensitive Nitric Oxide Detection, 5, (2011) , PP. 6955–6961.

[111] G. Singh, A. Choudhary, D. Haranath, A.G. Joshi, N. Singh, S. Singh, R. Pasricha, ZnO decorated luminescent graphene as a potential gas sensor at room temperature, Carbon N. Y. 50, (2012) , PP. 385–394.

[112] N. Mohanty, V. Berry, Graphene-based single-bacterium resolution biodevice and DNA transistor: Interfacing graphene derivatives with nanoscale and microscale biocomponents, Nano Lett. 8, (2008) , PP. 4469–4476.

[113] N. Mohanty, M. Fahrenholtz, A. Nagaraja, D. Boyle, V. Berry, Impermeable graphenic encasement of bacteria, Nano Lett. 11, (2011) , PP. 1270–1275.

[114] M.S. Mannoor, H. Tao, J.D. Clayton, A. Sengupta, D.L. Kaplan, R.R. Naik, N. Verma, F.G. Omenetto, M.C. McAlpine, Graphene-based wireless bacteria detection on tooth

enamel, Nat. Commun. 3, (2012) , PP. 1–8.

[115] K.S. Novoselov, A.K. Geim, S. V. Morozov, D. Jiang, M.I. Katsnelson, I. V. Grigorieva, S. V. Dubonos, A.A. Firsov, Two-dimensional gas of massless Dirac fermions in graphene, Nature. 438, (2005) , PP. 197–200.

[116] H.B. Heersche, P. Jarillo-Herrero, J.B. Oostinga, L.M.K. Vandersypen, A.F. Morpurgo, Bipolar supercurrent in graphene, Nature. 446, (2007) , PP. 56–59.

[117] M.P. Levendorf, C.S. Ruiz-Vargas, S. Garg, J. Park, Transfer-free batch fabrication of single layer graphene transistors, Nano Lett. 9, (2009) , PP. 4479–4483.

[118] Y.-M. Lin, K.A. Jenkins, A. Valdes-Garcia, J.P. Small, D.B. Farmer, P. Avouris, Operation of Graphene Transistors at Gigahertz Frequencies, Nano Lett. 9, (2009) , PP. 422–426.

[119] L.A. Ponomarenko, F. Schedin, M.I. Katsnelson, R. Yang, E.H. Hill, K.S. Novoselov, A. K.Geim, Chaotic Dirac billiard in graphene quantum dots, Science (80-.). 320, (2008) , PP. 356–358.

[120] D. Li, M.B. Müller, S. Gilje, R.B. Kaner, G.G. Wallace, Processable aqueous dispersions of graphene nanosheets., Nat. Nanotechnol. 3, (2008) , PP. 101–105.

[121] K.S. Kim, Y. Zhao, H. Jang, S.Y. Lee, J.M. Kim, K.S. Kim, J. Ahn, P. Kim, J. Choi, B.H. Hong, Large-scale pattern growth of graphene films for stretchable transparent electrodes., Nature. 457, (2009) , PP. 706–710.

[122] H. Tetsuka, R. Asahi, A. Nagoya, K. Okamoto, I. Tajima, R. Ohta, A. Okamoto, Optically tunable amino-functionalized graphene quantum dots, Adv. Mater. 24, (2012) , PP. 5333–5338.

[123] B.J. Hong, O.C. Compton, I.E. Zhi An, S.T. Nguyen, Successful Stabilization of Graphene Oxide in Electrolyte Solutions: Enhancement of Bio-functionalization and Cellular Uptake, ACS Nano. 6, (2012) , PP. 63–73.

[124] O.C. Compton, S.T. Nguyen, Graphene oxide, highly reduced graphene oxide, and graphene: Versatile building blocks for carbon-based materials, Small. 6, (2010) , PP. 711–723.

[125] K. Hu, M.K. Gupta, D.D. Kulkarni, V. V. Tsukruk, Ultra-robust graphene oxide-silk fibroin nanocomposite membranes, Adv. Mater. 25, (2013) , PP. 2301–2307.

[126] J.R. Potts, D.R. Dreyer, C.W. Bielawski, R.S. Ruoff, Graphene-based polymer nanocomposites, Polymer (Guildf). 52, (2011) , PP. 5–25.

[127] F.D.C. Fim, J.M. Guterres, N.R.S. Basso, G.B. Galland, Polyethylene/graphite nanocomposites obtained by in situ polymerization, J. Polym. Sci. Part A Polym. Chem. 48, (2010) , PP. 692–698.

[128] J.Y. Jang, M.S. Kim, H.M. Jeong, C.M. Shin, Graphite oxide/poly(methyl methacrylate) nanocomposites prepared by a novel method utilizing macroazoinitiator, Compos. Sci. Technol. 69, (2009) , PP. 186–191.

[129] Z. Gu, L. Zhang, C. Li, Preparation of Highly Conductive Polypyrrole/Graphite Oxide Composites via in situ Polymerization, J. Macromol. Sci. Part B. 48, (2009) , PP. 1093–1102.

[130] Yang, C. Shan, F. Li, D. Han, Q. Zhang, L. Niu, Covalent functionalization of polydisperse chemically-converted graphene sheets with amine-terminated ionic liquid,

Chem. Commun. (2009) , PP. 3880–3882.

[131] Y. Xu, Z. Liu, X.X. Zhang, Y. Wang, J. Tian, Y. Huang, Y. Ma, X.X. Zhang, Y. Chen, A graphene hybrid material covalently functionalized with porphyrin: Synthesis and optical limiting property, Adv. Mater. 21, (2009) , PP. 1275–1279.

[132] H. Kim, Y. Miura, C. Macosko, Graphene/polyurethane nanocomposites for improved gas barrier and electrical conductivity, Chem. Mater. 22, (2010) , PP. 3441–3450.

[133] N. V. Kozhemyakina, J.M. Englert, G. Yang, E. Spiecker, C.D. Schmidt, F. Hauke, A. Hirsch, Non-covalent chemistry of graphene: Electronic communication with dendronized perylene bisimides, Adv. Mater. 22, (2010) , PP. 5483–5487.

[134] Y. Xu, H. Bai, G. Lu, C. Li, G. Shi, Flexible graphene films via the filtration of water-soluble noncovalent functionalized graphene sheets, J. Am. Chem. Soc. 130, (2008) , PP. 5856–5857.

[135] S. Stankovich, R.D. Piner, S.T. Nguyen, R.S. Ruoff, Synthesis and exfoliation of isocyanate-treated graphene oxide nanoplatelets, Carbon N. Y. 44, (2006) , PP. 3342–3347.

[136] M.B. Smith, J. March, March's advanced organic chemistry, John Wiley & Sons Inc, New York, 2001.

[137] I.S. Blagbrough, N.E. Mackenzie, a I. Scott, The condensation reaction between isocyanates and carboxylic acids.AA practical synthesis of substituted amides and anilides, Pergamon Press Ltd. 27, (1986) , PP. 1251–1254.

[138] L.S. Schadler, S.K. Kumar, B.C. Benicewicz, S.L. Lewis, S.E. Harton, Designed Interfaces in Polymer Nanocomposites: A Fundamental Viewpoint, MRS Bull. 32, (2007) , PP. 335–340.

[139] K. Hu, D.D. Kulkarni, I. Choi, V. V. Tsukruk, Graphene-polymer nanocomposites for structural and functional applications, Prog. Polym. Sci. 39, (2014) , PP. 1934–1972.

[140] E.E. Tkalya, M. Ghislandi, G. de With, C.E. Koning, The use of surfactants for dispersing carbon nanotubes and graphene to make conductive nanocomposites, Curr. Opin. Colloid Interface Sci. 17, (2012) , PP. 225–232.

[141] M. Lotya, P.J. King, U. Khan, S. De, J.N. Coleman, High-concentration, surfactant-stabilized graphene dispersions, ACS Nano. 4, (2010) , PP. 3155–3162.

[142] J.N. Coleman, Liquid-phase exfoliation of nanotubes and graphene, Adv. Funct. Mater. 19, (2009) , PP. 3680–3695.

[143] S.D. Bergin, V. Nicolosi, H. Cathcart, M. Lotya, D. Rickard, Z. Sun, W.J. Blau, J.N. Coleman, Large populations of individual nanotubes in surfactant-based dispersions without the need for ultracentrifugation, J. Phys. Chem. C. 112, (2008) , PP. 972–977.

[144] F. Du, J.E. Fischer, K.I. Winey, Coagulation Method for Preparing Single-Walled Carbon Nanotube / Poly (methyl methacrylate) Composites and Their Modulus , Electrical Conductivity , and Thermal Stability, (2003) , PP. 3333–3338.

[145] G. Mittal, V. Dhand, K.Y. Rhee, S.-J. Park, W.R. Lee, A review on carbon nanotubes and graphene as fillers in reinforced polymer nanocomposites, J. Ind. Eng. Chem. 21, (2015) , PP. 11–25.

[146] C. Wan, B. Chen, Reinforcement and interphase of polymer/graphene oxide nanocomposites, J. Mater. Chem. 22, (2012) , PP. 3637–3646.

[147] G. Zou, H. Luo, B. Sun, M. Jain, H. Peng, Nanocomposites, J. Nanotechnol. 2011, (2011) , PP. 2–4.

[148] P. Rittigstein, R.D. Priestley, L.J. Broadbelt, J.M. Torkelson, Model polymer nanocomposites provide an understanding of confinement effects in real nanocomposites., Nat. Mater. 6, (2007) , PP. 278–282.

[149] X. Zhao, Q. Zhang, D. Chen, P. Lu, Enhanced mechanical properties of graphene-based polyvinyl alcohol composites, Macromolecules. 43, (2010) , PP. 2357–2363.

[150] S. Stankovich, D.A. Dikin, G.H.B. Dommett, K.M. Kohlhaas, E.J. Zimney, E.A. Stach, R.D. Piner, S.T. Nguyen, R.S. Ruoff, Graphene-based composite materials., Nature. 442, (2006) , PP. 282–286.

[151] H. Hu, X. Wang, J. Wang, L. Wan, F. Liu, H. Zheng, R. Chen, C. Xu, Preparation and properties of graphene nanosheets-polystyrene nanocomposites via in situ emulsion polymerization, Chem. Phys. Lett. 484, (2010) , PP. 247–253.

[152] A. Weerasinghe, C. Lu, D. Maroudas, A. Ramasubramaniam, Multiscale Shear-Lag Analysis of Sti ff ness Enhancement in Polymer − Graphene Nanocomposites, (2017) , PP. 1–9.

[153] M.M. Tavakoli, R. Tavakoli, S. Hasanzadeh, M.H. Mirfasih, Interface Engineering of Perovskite Solar Cell Using a Reduced-Graphene Scaffold, J. Phys. Chem. C. 120, (2016) , PP. 19531−19536.

[154] T.G.F. Transistors, U. Jung, Y.J. Kim, Y. Kim, Y.G. Lee, B.H. Lee, S. Member, Extraction of the Interface State Density of Top-Gate Graphene Field-Effect Transistors Ukjin, IEEE Electron. Device Lett. 36, (2015) , PP. 408–410.

[155] K.L. Kim, W. Lee, S.K. Hwang, S.H. Joo, S.M. Cho, G. Song, S.H. Cho, B. Jeong, I. Hwang, J.H. Ahn, Y.J. Yu, T.J. Shin, S.K. Kwak, S.J. Kang, C. Park, Epitaxial Growth of Thin Ferroelectric Polymer Films on Graphene Layer for Fully Transparent and Flexible Nonvolatile Memory, Nano Lett. 16, (2016) , PP. 334–340.

[156] Z. Ma, S. Dou, A. Shen, L. Tao, L. Dai, S. Wang, Angewandte Sulfur-Doped Graphene Derived from Cycled Lithium – Sulfur Batteries as a Metal-Free Electrocatalyst for the Oxygen Reduction Reaction, Angew. Chem. Int. Ed. 54, (2015) , PP. 1888–1892.

[157] S. Dong, Y. Sun, J. Wu, B. Wu, A.E. Creamer, B. Gao, Graphene oxide as filter media to remove levofloxacin and lead from aqueous solution, Chemosphere. 150, (2016) , PP. 759–764.

[158] L. Liu, Z. Niu, J. Chen, Unconventional supercapacitors from nanocarbon-based electrode materials to device configurations, Chem. Soc. Rev. 45, (2016) , PP. 4340–4363.

[159] M. Hu, Z. Yao, K.N. Hui, K.S. Hui, Novel mechanistic view of catalytic ozonation of gaseous toluene by dual-site kinetic modelling, Chem. Eng. J. 308, (2017) , PP. 710–718.

[160] L. Guo, H. Shi, H. Wu, Y. Zhang, X. Wang, D. Wu, L. An, S. Yang, Prostate cancer targeted multifunctionalized graphene oxide for magnetic resonance imaging and drug delivery, Carbon N. Y. 107, (2016) , PP. 87–99.

[161] Y. Ahn, Y. Jeong, D. Lee, Y. Lee, Copper Nanowire-Graphene Core-Shell Nanostructure for Highly Stable Transparent Conducting Electrodes, ACS Nano. 9, (2015) , PP. 3125–3133.

[162] P. a Webb, Introduction to Chemical Adsorption Analytical Techniques and their Applications to Catalysis, MIC Tech. Publ. 13, (2003) , PP. 1–4.

[163] H.N. Patrick, G.G. Warr, S. Manne, I.A. Aksay, Surface Micellization Patterns of Quaternary Ammonium Surfactants on Mica, Langmuir. 15, (1999) , PP. 1685–1692.

[164] S. Manne, J.P. Cleveland, H.E. Gaub, G.D. Stucky, P.K. Hansma, Direct Visualization of Surfactant Hemimicelles by Force Microscopy of the Electrical Double Layer, Langmuir. 10, (1994) , PP. 4409–4413.

[165] F. Tiberg, B. Joesson, B. Lindman, Ellipsometry Studies of the Self-Assembly of Nonionic Surfactants at the Silica-Water Interface: Kinetic Aspects, Langmuir. 10, (1994) , PP. 3714–3722.

[166] I.P. Purcell, J.R. Lu, R.K. Thomas, A.M. Howe, J. Penfold, Adsorption of Sodium Dodecyl Sulfate at the Surface of Aqueous Solutions of Poly(vinylpyrrolidone) Studied by Neutron Reflection, Langmuir. 14, (1998) , PP. 1637–1648.

[167] D. Johannsmann, I. Reviakine, E. Rojas, M. Gallego, Effect of sample heterogeneity on the interpretation of QCM(-D) data: Comparison of combined quartz crystal microbalance/atomic force microscopy measurements with finite element method modeling, Anal. Chem. 80, (2008) , PP. 8891–8899.

[168] H.C. Schniepp, H.C. Shum, D. a. Saville, I. a. Aksay, Orientational Order of Molecular Assemblies on Rough Surfaces, J. Phys. Chem. C. 112, (2008) , PP. 14902–14906.

[169] F. Barroso-Bujans, F. Fernandez-Alonso, J.A. Pomposo, S. Cerveny, A. Alegría, J. Colmenero, Macromolecular Structure and Vibrational Dynamics of Confined Poly(ethylene oxide): From Subnanometer 2D-Intercalation into Graphite Oxide to Surface Adsorption onto Graphene Sheets, ACS Macro Lett. 1, (2012) , PP. 550−554.

[170] H.J. Bae, H.J. Park, S.I. Hong, Y.J. Byun, D.O. Darby, R.M. Kimmel, W.S. Whiteside, Effect of clay content, homogenization RPM, pH, and ultrasonication on mechanical and barrier properties of fish gelatin/montmorillonite nanocomposite films, LWT - Food Sci. Technol. 42, (2009) , PP. 1179–1186.

[171] S. Wu, L. Shi, L.B. Garfield, R.F. Tabor, A. Striolo, B.P. Grady, Influence of surface roughness on cetyltrimethylammonium bromide adsorption from aqueous solution., Langmuir. 27, (2011) , PP. 6091–6098.

[172] B. Chen, J. Evans, S. Holding, Decomposition of poly(ethylene glycol) in nanocomposites, J. Appl. Polym. Sci. 94, (2004) , PP. 548–552.

[173] K. Knop, R. Hoogenboom, D. Fischer, U.S. Schubert, I. Memoriam, V.A. Kabanov, Wirkstoff-Transport Anwendung von Poly(ethylenglycol) beim Wirkstoff- Transport: Vorteile, Nachteile und Alternativen, Angew. Chem. 122, (2010) , PP. 6430–6452.

[174] A. Adhikari, K. Lozano, Effects of carbon nanofibers on the crystallization kinetics of polyethylene oxide, J. Polym. Res. 18, (2010) , PP. 875–880.

[175] G. Pasut, F.M. Veronese, PEG conjugates in clinical development or use as anticancer agents: An overview, Adv. Drug Deliv. Rev. 61, (2009) , PP. 1177–1188.

[176] M.L. Graham, Pegaspargase: A review of clinical studies, Adv. Drug Deliv. Rev. 55, (2003) , PP. 1293–1302.

[177] G. Pasut, Polymers for protein conjugation, Polymers (Basel). 6, (2014) , PP. 160–178.

[178] B. Obermeier, F. Wurm, C. Mangold, H. Frey, Multifunctional poly(ethylene glycol)s,

Angew. Chemie - Int. Ed. 50, (2011) , PP. 7988–7997.

[179] S. Tomita, Y. Nagasaki, K. Shiraki, Different mechanisms of action of poly(ethylene glycol) and arginine on thermal inactivation of lysozyme and ribonuclease A, Biotechnol. Bioeng. 109, (2012) , PP. 2543–2552.

[180] R. Mishra, K.J. Rao, Electrical conductivity studies of poly(ethyleneoxide)-poly(vinylalcohol) blends, Solid State Ionics. 106, (1998) , PP. 113–127.

[181] R. Sengupta, S. Chakraborty, S. Bandyopadhyay, S. Dasgupta, R. Mukhopadhyay, K. Auddy, a S. Deuri, Structure and Properties of Poly(ethylene oxide)-Organo Clay Nanocomposite Prepared via Melt Mixing, Polym. Eng. Sci. 49, (2009) , PP. 379–390.

[182] A.C. French, A.L. Thompson, B.G. Davis, High-purity discrete PEG-oligomer crystals allow structural insight, Angew. Chemie - Int. Ed. 48, (2009) , PP. 1248–1252.

[183] C.B. Roth, K.L. McNerny, W.F. Jager, J.M. Torkelson, Nanocomposites: Model interfaces, Nat. Mater. 6, (2007) , PP. 257–258.

[184] J. Rubio, J.A. Kitchener, The mechanism of adsorption of poly(ethylene oxide) flocculant on silica, J. Colloid Interface Sci. 57, (1976) , PP. 132–142.

[185] S. Mathur, B.M. Moudgil, Adsorption Mechanism (s) of Poly (Ethylene Oxide) on Oxide Surfaces, 98, (1997) , PP. 92–98.

[186] G.Q. Qi, C.L. Liang, R.Y. Bao, Z.Y. Liu, W. Yang, B.H. Xie, M.B. Yang, Polyethylene glycol based shape-stabilized phase change material for thermal energy storage with ultra-low content of graphene oxide, Sol. Energy Mater. Sol. Cells. 123, (2014) , PP. 171–177.

[187] Y. Liu, Y. Zhang, G. Ma, Z. Wang, K. Liu, H. Liu, Ethylene glycol reduced graphene oxide/polypyrrole composite for supercapacitor, Electrochim. Acta. 88, (2013) , PP. 519–525.

[188] F. Barroso-Bujans, F. Fernandez-Alonso, S. Cerveny, S. Parker, A. Alegria, J. Colmenero, Polymers under extreme two-dimensional confinement: Poly(ethylene oxide) in graphite oxide, Soft Matter. 7, (2011) , PP. 7173–7176.

[189] F. Barroso-Bujans, F. Fernandez-Alonso, S. Cerveny, S. Arrese-Igor, A. Alegría, J. Colmenero, Two-Dimensional Subnanometer Confinement of Ethylene Glycol and Poly(ethylene oxide) by Neutron Spectroscopy: Molecular Size Effects, Macromolecules. 45, (2012) , PP. 3137–3144.

[190] R. a. Vaia, B. Sauer, O. Tse, E.P. Giannelis, Relaxations of confined chains in polymer nanocomposites: glass transition properties of poly (ethylene oxide) intercalated in montmorillonite, J. Polym. 35, (1997) , PP. 59–67.

[191] Y. Miwa, A.R. Drews, S. Schlick, Unique structure and dynamics of poly(ethylene oxide) in layered silicate nanocomposites: Accelerated segmental mobility revealed by simulating ESR spectra of spin-labels, XRD, FTIR, and DSC, Macromolecules. 41, (2008) , PP. 4701–4708.

[192] C.C. Su, Y.H. Shen, Adsorption of poly(ethylene oxide) on smectite: Effect of layer charge, J. Colloid Interface Sci. 332, (2009) , PP. 11–15.

[193] P.C. Yuang, Y.H. Shen, Determination of the surface area of smectite in water by ethylene oxide chain adsorption, J. Colloid Interface Sci. 285, (2005) , PP. 443–447.

[194] E. Koksal, R. Ramachandran, P. Somasundaran, C. Maltesh, Flocculation of oxides

using poly(ethylene oxide), Powder Technol. 62, (1990) , PP. 253–259.

[195] N. Rajender, K.I. Suresh, Surface-Initiated Atom Transfer Radical Polymerization (SI-ATRP) from Graphene Oxide: Effect of Functionalized Graphene Sheet (FGS) on the Synthesis and Material Properties of PMMA Nanocomposites, Macromol. Mater. Eng. 301, (2016) , PP. 81–92.

[196] Z. Ma, C. Wu, D.U. Lee, F. Li, T.W. Kim, Carrier transport and memory mechanisms of multilevel resistive memory devices with an intermediate state based on double-stacked organic/inorganic nanocomposites, Org. Electron. Physics, Mater. Appl. 28, (2016) , PP. 20–24.

[197] H. Bin Zhang, W.G. Zheng, Q. Yan, Z.G. Jiang, Z.Z. Yu, The effect of surface chemistry of graphene on rheological and electrical properties of polymethylmethacrylate composites, Carbon N. Y. 50, (2012) , PP. 5117–5125.

[198] Q. Meng, H.C. Kuan, S. Araby, N. Kawashima, N. Saber, C.H. Wang, J. Ma, Effect of interface modification on PMMA/graphene nanocomposites, J. Mater. Sci. 49, (2014) , PP. 5838–5849.

[199] R.K. Layek, A.K. Nandi, A Review on Synthesis and Properties of Polymer Functionalized Graphene, Polymer (Guildf). 54, (2014) , PP. 5087–5103.

[200] T. Sui, B. Song, F. Zhang, Q. Yang, Effects of functional groups on the tribological properties of hairy silica nanoparticles as an additive to polyalphaolefin, R. Soc. Chem. 6, (2016) , PP. 393–402.

[201] L. Casal-Dujat, M. Rodrigues, A. Yagüe, A.C. Calpena, D.B. Amabilino, J. Gonzaílez-Linares, M. Borraís, L. Peírez-Garciía, Gemini imidazolium amphiphiles for the synthesis, stabilization, and drug delivery from gold nanoparticles, Langmuir. 28, (2012) , PP. 2368–2381.

[202] C.A. Grabowski, H. Koerner, S. Meth, A. Dang, C.M. Hui, K. Matyjaszewski, M.R. Bockstaller, M.F. Durstock, R.A. Vaia, Performance of Dielectric Nanocomposites: Matrix-Free, Hairy Nanoparticle Assemblies and Amorphous Polymer − Nanoparticle Blends, ACS Appl. Mater. Interfaces. 6, (2014) , PP. 21500−21509.

[203] X. Lin, W.-L.-J. Hasi, X.-T. Lou, S. Lin, F. Yang, B.-S. Jia, D.-Y. Lin, Z.-W. Lu, Droplet detection: simplification and optimization of detecting conditions towards high sensitivity quantitative determination of melamine in milk without any pretreatment, RSC Adv. 4, (2014) , PP. 51315–51320.

[204] T. Jiang, T. Kuila, N. Hoon, B. Ku, J. Hee, Enhanced mechanical properties of silanized silica nanoparticle attached graphene oxide / epoxy composites, Compos. Sci. Technol. 79, (2013) , PP. 115–125.

[205] V. Mittal, Functional polymer nanocomposites with graphene: A review, Macromol. Mater. Eng. 299, (2014) , PP. 906–931.

[206] A. Badri, M.R. Whittaker, P.B. Zetterlund, Modification of graphene/graphene oxide with polymer brushes using controlled/living radical polymerization, J. Polym. Sci. Part A Polym. Chem. 50, (2012) , PP. 2981–2992.

[207] K.C. Kemp, V. Georgakilas, M. Otyepka, A.B. Bourlinos, V. Chandra, N. Kim, K.C. Kemp, P. Hobza, R. Zboril, K.S. Kim, Functionalization of Graphene : Covalent and Non- Covalent Approaches, Derivatives and Applications, Chem. Rev. 112, (2012) , PP. 6156−6214.

[208] H. Bai, Y. Xu, L. Zhao, C. Li, G. Shi, Non-covalent functionalization of graphene sheets by sulfonated polyaniline., Chem. Commun. (Camb). 4, (2009) , PP. 1667–1669.

[209] R.P. Bagwe, L.R. Hilliard, W. Tan, Surface Modification of Silica Nanoparticles to Reduce Aggregation and Nonspecific Binding Surface Modification of Silica Nanoparticles to Reduce Aggregation and Nonspecific Binding, Langmuir. (2006) , PP. 4357–4362.

[210] S. Ansari, A. Kelarakis, L. Estevez, E.P. Giannelis, Oriented arrays of graphene in a polymer matrix by in situ reduction of graphite oxide nanosheets, Small. 6, (2010) , PP. 205–209.

[211] G. Anagnostopoulos, C. Androulidakis, E.N. Koukaras, G. Tsoukleri, I. Polyzos, J. Parthenios, K. Papagelis, C. Galiotis, Stress Transfer Mechanisms at the Submicron Level for Graphene/ Polymer Systems, ACS Appl. Mater. Interfaces. 7, (2015) , PP. 4216−4223.

[212] C. Lu, A. Weerasinghe, D. Maroudas, A. Ramasubramaniam, A Comparison of the Elastic Properties of Graphene- and Fullerene-Reinforced Polymer Composites : The Role of Filler Morphology and Size, Sci. Rep. 6, (2016) , PP. 1–9.

[213] R.J. Young, I.A. Kinloch, L. Gong, K.S. Novoselov, The mechanics of graphene nanocomposites: A review, Compos. Sci. Technol. 72, (2012) , PP. 1459–1476.

[214] S. Cheng, V. Bocharova, A. Belianinov, S. Xiong, A. Kisliuk, S. Somnath, A.P. Holt, O.S. Ovchinnikova, S. Jesse, H. Martin, T. Etampawala, M. Dadmun, A.P. Sokolov, Unraveling the Mechanism of Nanoscale Mechanical Reinforcement in Glassy Polymer Nanocomposites, Nano Lett. 16, (2016) , PP. 3630−3637.

[215] K.N. Spanos, N.K. Anifantis, Finite element prediction of stress transfer in graphene nanocomposites : The interface effect, Compos. Struct. 154, (2016) , PP. 269–276.

[216] Y. Zhang, X. Zhuang, J. Muthu, T. Mabrouki, M. Fontaine, Load transfer of graphene / carbon nanotube / polyethylene hybrid nanocomposite by molecular dynamics simulation, Compos. Part B. 63, (2014) , PP. 27–33.

[217] P. May, U. Khan, A. O'Neill, J.N. Coleman, Approaching the theoretical limit for reinforcing polymers with graphene, J. Mater. Chem. 22, (2012) , PP. 1278–1282.

[218] U. Khan, A. O'Neill, M. Lotya, S. De, J.N. Coleman, High-concentration solvent exfoliation of graphene, Small. 6, (2010) , PP. 864–871.

[219] H. Yue, W. Wei, Z. Yue, B. Wang, N. Luo, Y. Gao, D. Ma, G. Ma, Z. Su, The role of the lateral dimension of graphene oxide in the regulation of cellular responses, Biomaterials. 33, (2012) , PP. 4013–4021.

[220] Y.C. Cao, C. Xu, X. Wu, X. Wang, L. Xing, K. Scott, A poly (ethylene oxide)/graphene oxide electrolyte membrane for low temperature polymer fuel cells, J. Power Sources. 196, (2011) , PP. 8377–8382.

[221] W.E. Mahmoud, Morphology and physical properties of poly(ethylene oxide) loaded graphene nanocomposites prepared by two different techniques, Eur. Polym. J. 47, (2011) , PP. 1534–1540.

[222] C. Wan, B. Chen, Reinforcement of biodegradable poly(butylene succinate) with low loadings of graphene oxide, J. Appl. Polym. Sci. 127, (2013) , PP. 5094–5099.

[223] D. Cai, K. Yusoh, M. Song, The mechanical properties and morphology of a graphite

oxide nanoplatelet/polyurethane composite, Nanotechnology. 20, (2009) , PP. 1–5.

[224] S.B. Jagtap, R.K. Kushwaha, D. Ratna, Novel green method of preparation of a poly (ethylene oxide)/graphene nanocomposite using organic salt assisted dispersion, RSC Adv. 5, (2015) , PP. 30555–30563.

[225] G. Wang, Z. Wei, L. Sang, G. Chen, W. Zhang, X. Dong, M. Qi, Morphology, Crystallization And Mechanical Properties Of Poly(E -Caprolactone)/Graphene Oxide Nanocomposites, Chinese J. Polym. Sci. 31, (2013) , PP. 1148–1160.

[226] W.M. Doyle, Principles and applications of Fourier transform infrared (FTIR) process analysis *, Tech. Note AN–906 Rev. C. 2, (1992) , PP. 1–24. http://www.hellma-axiom.com/pdf/technical_notes/AN-906.pdf.

[227] PerkinElmer, FT-IR Spectroscopy: Attenuated Total Reflectance (ATR), (2005) , PP. 5. http://www.utsc.utoronto.ca/~traceslab/ATR_FTIR.pdf.

[228] Perkin Elmer, Thermogravimetric Analysis (TGA), 2004. doi:10.1198/tech.2005.s328.

[229] B.M. Ganesh, A.M. Isloor, A.F. Ismail, Enhanced hydrophilicity and salt rejection study of graphene oxide-polysulfone mixed matrix membrane, Desalination. 313, (2013) , PP. 199–207.

[230] C. Wang, L. Feng, H. Yang, G. Xin, W. Li, J. Zheng, W. Tian, X. Li, Graphene oxide stabilized polyethylene glycol for heat storage, Phys. Chem. Chem. Phys. 14, (2012) , PP. 13233–13238.

[231] S. Gao, J. Zhong, G. Xue, B. Wang, Ion conductivity improved polyethylene oxide/lithium perchlorate electrolyte membranes modified by graphene oxide, J. Memb. Sci. 470, (2014) , PP. 316–322.

[232] Y. Yang, C.-H. Zhou, S. Xu, J. Zhang, S.-J. Wu, H. Hu, B.-L. Chen, Q.-D. Tai, Z.-H. Sun, W. Liu, X.-Z. Zhao, Optimization of a quasi-solid-state dye-sensitized solar cell employing a nanocrystal-polymer composite electrolyte modified with water and ethanol., Nanotechnology. 20, (2009) , PP. 1–9.

[233] M. Pulst, M.H. Samiullah, U. Baumeister, M. Prehm, J. Balko, T. Thurn-Albrecht, K. Busse, Y. Golitsyn, D. Reichert, J. Kressler, Crystallization of Poly(ethylene oxide) with a Well-Defined Point Defect in the middle of the Polymer Chain, Macromolecules. 49, (2016) , PP. 6609–6620.

[234] Y. Li, G. Louarn, P.H. Aubert, V. Alain-Rizzo, L. Galmiche, P. Audebert, F. Miomandre, Polypyrrole-modified graphene sheet nanocomposites as new efficient materials for supercapacitors, Carbon N. Y. 105, (2016) , PP. 510–520.

[235] R.A. Vaia, W. Liu, X-ray powder diffraction of polymer/layered silicate nanocomposites: Model and practice, J. Polym. Sci. Part B Polym. Phys. 40, (2002) , PP. 1590–1600.

[236] Y.K. Godovsky, G.L. Slonimsky, N.M. Garbar, Effect of molecular weight on the crystallization and morphology of poly (ethylene oxide) fractions, J. Polym. Sci. Part C Polym. Symp. 38, (1972) , PP. 1–21.

[237] A. Nelson, T. Cosgrove, Dynamic light scattering studies of poly(ethylene oxide) adsorbed on laponite: Layer conformation and its effect on particle stability, Langmuir. 20, (2004) , PP. 10382–10388.

[238] C. Wan, B. Chen, Poly(ε-caprolactone)/graphene oxide biocomposites: mechanical

properties and bioactivity, Biomed. Mater. 6, (2011) , PP. 1–8.

[239] S. Pavlidou, C.D. Papaspyrides, A review on polymer–layered silicate nanocomposites, Prog. Polym. Sci. 33, (2008) , PP. 1119–1198.

[240] Y. Tong, Y. Lin, S. Wang, M. Song, A study of crystallisation of poly (ethylene oxide) and polypropylene on graphene surface, Polymer (Guildf). 73, (2015) , PP. 52–61.

[241] J. Jin, M. Song, F. Pan, A DSC study of effect of carbon nanotubes on crystallisation behaviour of poly(ethylene oxide), Thermochim. Acta. 456, (2007) , PP. 25–31.

[242] Z. Luo, C. Cong, J. Zhang, Q. Xiong, T. Yu, The origin of sub-bands in the Raman D-band of graphene, Carbon N. Y. 50, (2012) , PP. 4252–4258.

[243] F. Thomsen, Practical Contact Angle Measurement (2) Measurement with nicely deposited drops, 2007.

[244] A.R. Kumarasinghe, L. Samaranayake, F. Bondino, E. Magnano, N. Kottegoda, E. Carlino, U.N. Ratnayake, A.A.P. De Alwis, V. Karunaratne, G.A.J. Amaratunga, Self-assembled multilayer graphene oxide membrane and carbon nanotubes synthesized using a rare form of natural graphite, J. Phys. Chem. C. 117, (2013) , PP. 9507–9519.

[245] G. Sun, X. Li, Y. Qu, X. Wang, H. Yan, Y. Zhang, Preparation and characterization of graphite nanosheets from detonation technique, Mater. Lett. 62, (2008) , PP. 703–706.

[246] A.W. Hull, A New Method Of X-Ray Crystal Analysis, Phys. Rev. Journals. 10, (1917) , PP. 661–697.

[247] Y.-H. Chou, Y.-C. Chiu, W.-C. Chen, High-k polymer-graphene oxide dielectrics for low-voltage flexible nonvolatile transistor memory devices., Chem. Commun. 50, (2014) , PP. 3217–3219.

[248] P. Slobodian, P. Svoboda, P. Riha, R. Boruta, P. Saha, Synthesis of PMMA-co-PMAA Copolymer Brush on Multi-Wall Carbon Nanotubes, 2012, (2012) , PP. 221–226.

[249] K.-H. Liao, S. Aoyama, A.A. Abdala, C. Macosko, Does Graphene Change Tg of Nanocomposites, Macromolecules. 47, (2014) , PP. 8311–8319.

[250] H.P. Fu, R.Y. Hong, Y.J. Zhang, H.Z. Li, B. Xu, Y. Zheng, D.G. Wei, Preparation and properties investigation of PMMA/silica composites derived from silicic acid, Polym. Adv. Technol. 20, (2009) , PP. 84–91.

[251] N. Gatica, N. Alvarado, D. Sepulveda, Blends of Poly(Methyl Methacrylate-Co-Methacrylic Acid) and Two Dihydric Phenols: Thermal and Infrared Spectroscopic Studies, J. Chil. Chem. Soc. 51, (2006) , PP. 945–949.

[252] S. Zinadini, A.A. Zinatizadeh, M. Rahimi, V. Vatanpour, H. Zangeneh, Preparation of a novel antifouling mixed matrix PES membrane by embedding graphene oxide nanoplates, J. Memb. Sci. 453, (2014) , PP. 292–301.

[253] L. Brown, T. Koerner, J.H. Horton, R.D. Oleschuk, Fabrication and characterization of poly(methylmethacrylate) microfluidic devices bonded using surface modifications and solvents., Lab Chip. 6, (2006) , PP. 66–73.

[254] G. Asman, Use of Poly(methyl methacrylate-co-methacrylic acid) Membranes in the Ultrafiltration of Aqueous Fe3+ Solutions by Complexing with Poly(vinyl pyrrolidone) and Dextran, Sep. Sci. Technol. 44, (2009) , PP. 1164–1180.

[255] S. Hosseini, F. Ibrahim, L.H. Koole, I. Djordjevic, Polyacrylate spin-coated surfaces

with controllable functionality: Potential biochips for diagnostic devices, IECBES 2014, Conf. Proc. - 2014 IEEE Conf. Biomed. Eng. Sci. “Miri, Where Eng. Med. Biol. Humanit. Meet.” (2014) , PP. 582–585.

[256] V. Vatanpour, S.S. Madaeni, R. Moradian, S. Zinadini, B. Astinchap, Fabrication and characterization of novel antifouling nanofiltration membrane prepared from oxidized multiwalled carbon nanotube/polyethersulfone nanocomposite, J. Memb. Sci. 375, (2011) , PP. 284–294.

[257] K.N. Kudin, B. Ozbas, H.C. Schniepp, R.K. Prud’homme, I.A. Aksay, R. Car, Raman spectra of graphite oxide and functionalized graphene sheets, Nano Lett. 8, (2008) , PP. 36–41.

[258] G. Gonçalves, P. a. a. P. Marques, A. Barros-Timmons, I. Bdkin, M.K. Singh, N. Emami, J. Grácio, Graphene oxide modified with PMMA via ATRP as a reinforcement filler, J. Mater. Chem. 20, (2010) , PP. 9927–9934.

[259] X. Sun, Z. Liu, K. Welsher, J.T. Robinson, A. Goodwin, S. Zaric, H. Dai, Nano-Graphene Oxide for Cellular Imaging and Drug Delivery, Nano Res. 1, (2008) , PP. 203–212.

[260] M. Lundqvist, J. Stigler, G. Elia, I. Lynch, T. Cedervall, K.A. Dawson, Nanoparticle size and surface properties determine the protein corona with possible implications for biological impacts., Proc. Natl. Acad. Sci. U. S. A. 105, (2008) , PP. 14265–70.

[261] W. Jiang, B.Y.S. Kim, J.T. Rutka, W.C.W. Chan, Nanoparticle-mediated cellular response is size-dependent., Nat. Nanotechnol. 3, (2008) , PP. 145–50.

[262] D. Rickwood, J. Graham, Biological Centrifugation, Cell Biochem. Funct. 20, (2002) , PP. 357–358.

[263] S.O. Majekodunmi, A Review on Centrifugation in the Pharmaceutical Industry, Am. J. Biomed. Eng. 5, (2015) , PP. 67–78.

[264] Thermo Fisher Scientific Inc, Pierce Biotechnology, Convert between times gravity (× g) and centrifuge rotor speed (RPM), Thermo Fish. Sci. (2009). http://www.sportsmed.theclinics.com/issues#.

[265] D. Rickwood, T. Ford, J. Steensgaard, Centrifugation: Essential Data, John Wiley & Son Ltd., 1994.

[266] D. Rickwood, Preparative Centrifugation: A Practical Approach, RL Press at Oxford University Press, 1992.

[267] C. Ford, J.M. Graham., An Introduction to Centrifugation, Bios Scientific Publishers, Oxford., 1991.

[268] R. Shaw, Dynamic Light Scattering Training Achieving reliable nano particle sizing, Dyn. Light Scatt. Train. Achiev. Reliab. Nano Part. Sizing. Accessed 2, (2014). https://www.chem.uci.edu/~dmitryf/manuals/Fundamen.

[269] Y. Li, A.R. Barron, Dynamic light scattering, Openstax-Cnx Modul. m50236. 796, (2014) , PP. 1–13.

[270] R. Xu, Particle Characterization: Light Scattering Methods, Kluwer Academic Publishers, Miami, U.S.A, 2002.

[271] B.B. Weiner, What Is Particle Size Distribution Weighting : How to Get Fooled about What Was Measured and What it Means ?, Brookhaven Instruments Corp. White Pap.

What. (2011) , PP. 1–4.

[272] A. V Talyzin, T. Hausmaninger, S. You, T. Szabó, The structure of graphene oxide membranes in liquid water, ethanol and water-ethanol mixtures., Nanoscale. 6, (2014) , PP. 272–81.

[273] M. Khenfouch, Morphological, Vibrational and Thermal Properties of Confined Graphene Nanosheets in an Individual Polymeric Nanochannel by Electrospinning, Graphene. 1, (2012) , PP. 15–20.

[274] S. Zhang, Q. Tao, Z. Wang, Z. Zhang, Controlled heat release of new thermal storage materials: the case of polyethylene glycol intercalated into graphene oxide paper, J. Mater. Chem. 22, (2012) , PP. 20166–20169.

[275] M.A. Aldosari, A.A. Othman, E.H. Alsharaeh, Synthesis and characterization of the in situ bulk polymerization of PMMA containing graphene sheets using microwave irradiation, Molecules. 18, (2013) , PP. 3152–3167.

[276] M. Yoonessi, J.R. Gaier, Highly Conductive Multifunctional Graphene Polycarbonate Nanocomposites, ACS Nano. 4, (2010) , PP. 7211–7220.

[277] M. Wang, H.-G. Braun, E. Meyer, Crystalline structures in ultrathin poly(ethylene oxide)/poly(methyl methacrylate) blend films, Polymer (Guildf). 44, (2003) , PP. 5015–5021.

[278] J. Baschnagel, K. Binder, On the influence of hard walls on structural properties in polymer glass simulation, Macromolecules. 28, (1995) , PP. 6808–6818.

[279] Y. Han, T. Wang, X. Gao, T. Li, Q. Zhang, Preparation of thermally reduced graphene oxide and the influence of its reduction temperature on the thermal, mechanical, flame retardant performances of PS nanocomposites, Compos. Part A Appl. Sci. Manuf. 84, (2016) , PP. 336–343.

[280] R. Qiao, L. Catherine Brinson, Simulation of interphase percolation and gradients in polymer nanocomposites, Compos. Sci. Technol. 69, (2009) , PP. 491–499.

[281] M.A.S.A. Samir, F. Alloin, J.Y. Sanchez, A. Dufresne, Cross-linked nanocomposite polymer electrolytes reinforced with cellulose whiskers, Macromolecules. 37, (2004) , PP. 4839–4844.

[282] Y.W. Chang, K.S. Lee, Y.W. Lee, J.H. Bang, Poly(ethylene oxide)/graphene oxide nanocomposites: structure, properties and shape memory behavior, Polym. Bull. 72, (2015) , PP. 1937–1948.

[283] Y.R. Lee, A. V Raghu, H.M. Jeong, B.K. Kim, Properties of Waterborne Polyurethane / Functionalized Graphene Sheet Nanocomposites Prepared by an in situ Method, Macromol. Chem. Phys. 210, (2009) , PP. 1247–1254.

[284] A. Pawlak, A. Galeski, A. Rozanski, Cavitation during deformation of semicrystalline polymers, Prog. Polym. Sci. 39, (2014) , PP. 921–958.

[285] M.F. Butler, A.M. Donald, A.J. Ryan, Time resolved simultaneous small- and wide-angle X-ray scattering during polyethylene deformation-I. Cold drawing of copolymer, Polymer (Guildf). 39, (1998) , PP. 39–52.

[286] R. Liu, S. Liang, X.-Z. Tang, D. Yan, X. Li, Z.-Z. Yu, Tough and highly stretchable graphene oxide/polyacrylamide nanocomposite hydrogels, J. Mater. Chem. 22, (2012) , PP. 14160–14167.

[287] D. Ratna, S. Divekar, A.B. Samui, B.C. Chakraborty, A.K. Banthia, Poly(ethylene oxide)/clay nanocomposite: Thermomechanical properties and morphology, Polymer (Guildf). 47, (2006) , PP. 4068–4074.

[288] D. Shah, P. Maiti, D.D. Jiang, C.A. Batt, E.P. Giannelis, Effect of nanoparticle mobility on toughness of polymer nanocomposites, Adv. Mater. 17, (2005) , PP. 525–528.

[289] R.J. Young, P.A. Lovell, Introduction To Polymers, 3rd ed., London: CRC Press, 2011.

[290] U. Khan, P. May, A. O'Neill, J.N. Coleman, Development of stiff, strong, yet tough composites by the addition of solvent exfoliated graphene to polyurethane, Carbon N. Y. 48, (2010) , PP. 4035–4041.

[291] H. Kim, C.W. Macosko, Morphology and Properties of Polyester / Exfoliated Graphite Nanocomposites, Direct. (2008) , PP. 3317–3327.

[292] J.C.H. Affdl, J.L. Kardos, The Halpin-Tsai equations: A review, Polym. Eng. Sci. 16, (1976) , PP. 344–352.

[293] B. Chen, J.R.G. Evans, H.C. Greenwell, P. Boulet, P. V Coveney, A. a Bowden, A. Whiting, A critical appraisal of polymer-clay nanocomposites., Chem. Soc. Rev. 37, (2008) , PP. 568–94.

[294] Y. Itin, F.W. Hehl, The elasticity and strength of paper and other fibrous materials, Br. J. Appl. Phys. 3, (1951) , PP. 72–79.

[295] J.C. Halpin, R.L. Thomas, Ribbon Reinforcement of Composites, J. Compos. Mater. 2, (1968) , PP. 488–497.

[296] R. Justin, B. Chen, Strong and conductive chitosan–reduced graphene oxide nanocomposites for transdermal drug delivery, J. Mater. Chem. B. 2, (2014) , PP. 3759–3770.

[297] B. Chen, J. Evans, Nominal and Effective Volume Fractions in Polymer - Clay Nanocomposites, Macromolecules. 39, (2006) , PP. 1790–1796.

[298] C. Wan, M. Frydrych, B. Chen, Strong and bioactive gelatin – graphene oxide nanocomposites, Soft Matter. 7, (2011) , PP. 6159–6166.

[299] B. Chen, J. Evans, Poly(ε-caprolactone)−Clay Nanocomposites: Structure and Mechanical Properties, Macromolecules. 39, (2006) , PP. 747–754.

[300] T.M. Stoeckel, J. Blasius, B. Crist, Chain rupture and tensile deformation of polymers, J. Polym. Sci. Polym. Phys. Ed. 16, (1978) , PP. 485–500.

[301] R. Adhikari, G.H. Michler, Polymer Nanocomposites Characterization by Microscopy, Polym. Rev. 49, (2009) , PP. 141–180.

Appendix of Chapter 3

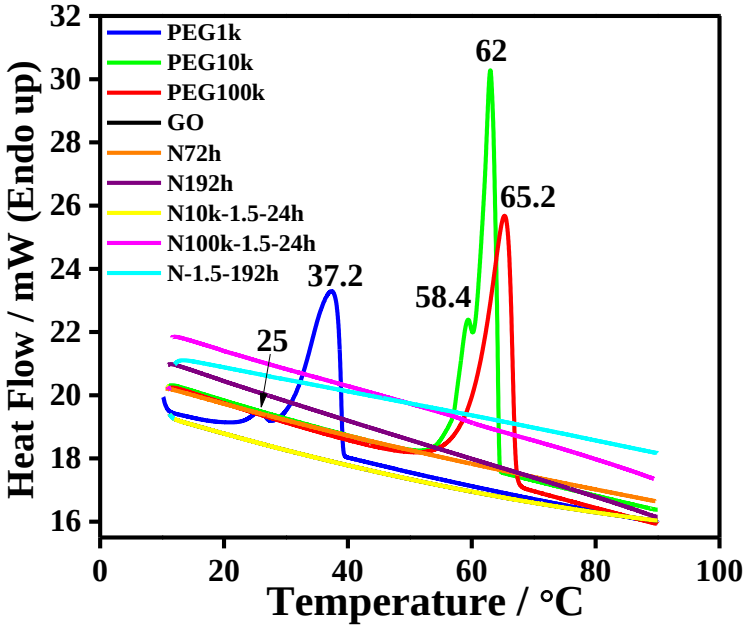

Figure A3-1. The second DSC heating cycle of PEGs and hybrids.

The polymer presented without melting peaks in these washed hybrids, which were from N1h to N1.5-192-0w. Therefore, all these washed samples had a confined polymer between the GO sheets only.

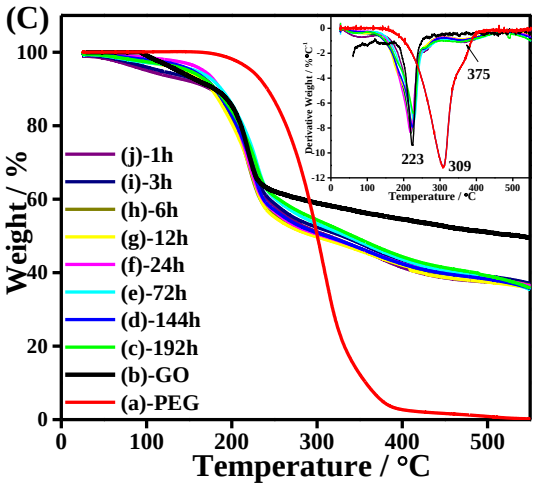

Figure A3-2. The TGA curves presented the calibrated GO and hybrids.

Appendix of Chapter 5

New Methods to Separate Graphene Oxide Particle Sizes Using Centrifuge And Sonication Methods: The Effect of graphene Particle Sizes on Adsorb High Molecular Weight Poly(ethylene oxide) Behaviour.

AFM Images

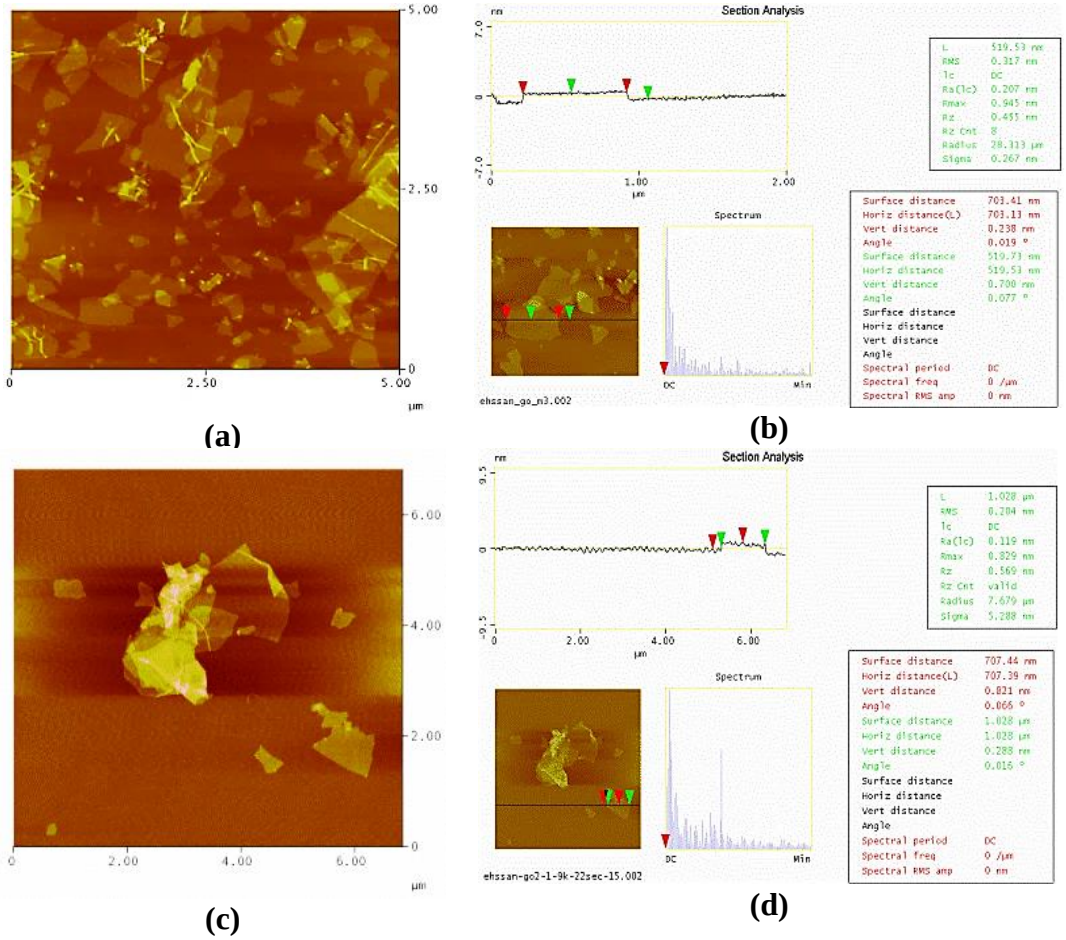

Figure A5-1: AFM images of (a, b and c) GO1 and (d, e, f and g) GO2.

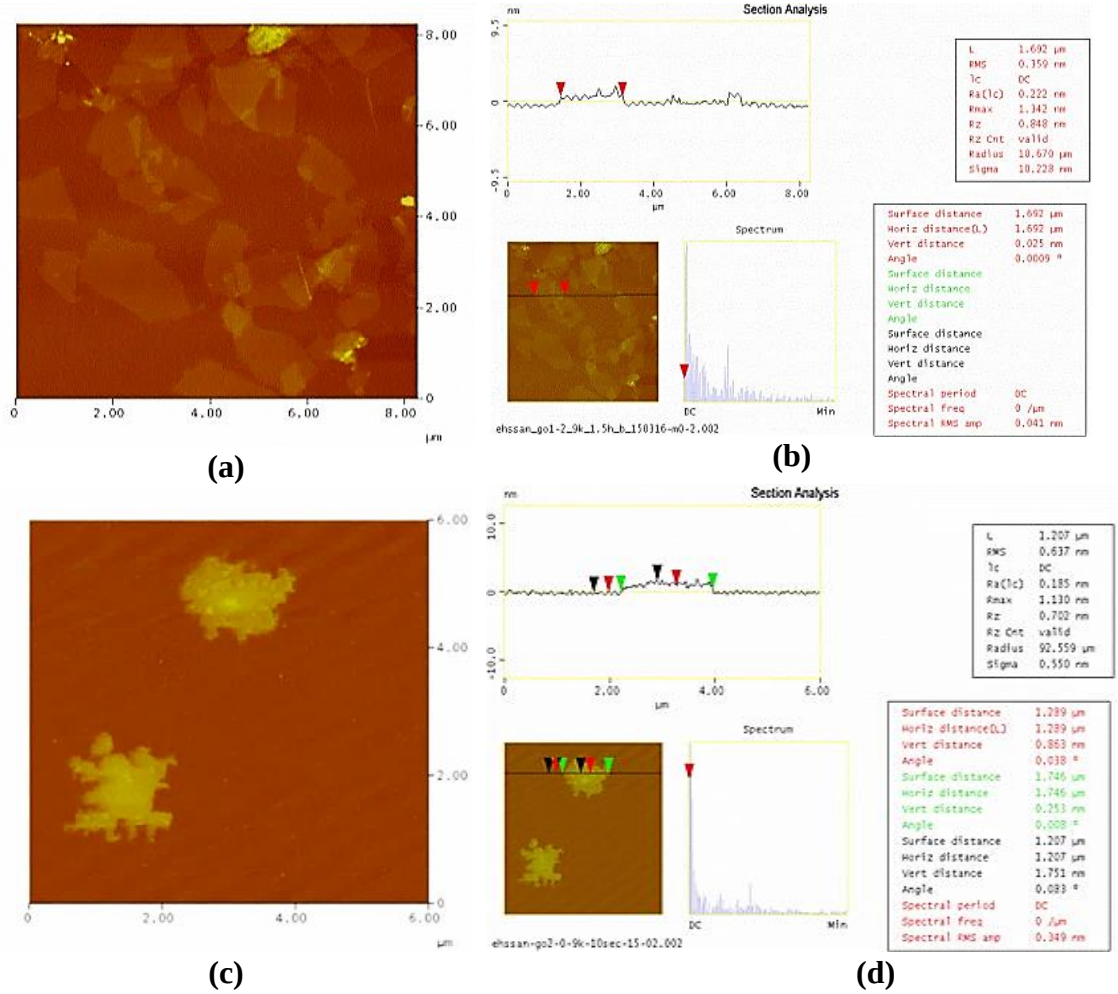

Figure A5-2: AFM images of the GO samples sonicated for 30 minutes then centrifuged at 11138 g for 5 seconds of (a) GO1 and (b) GO2.

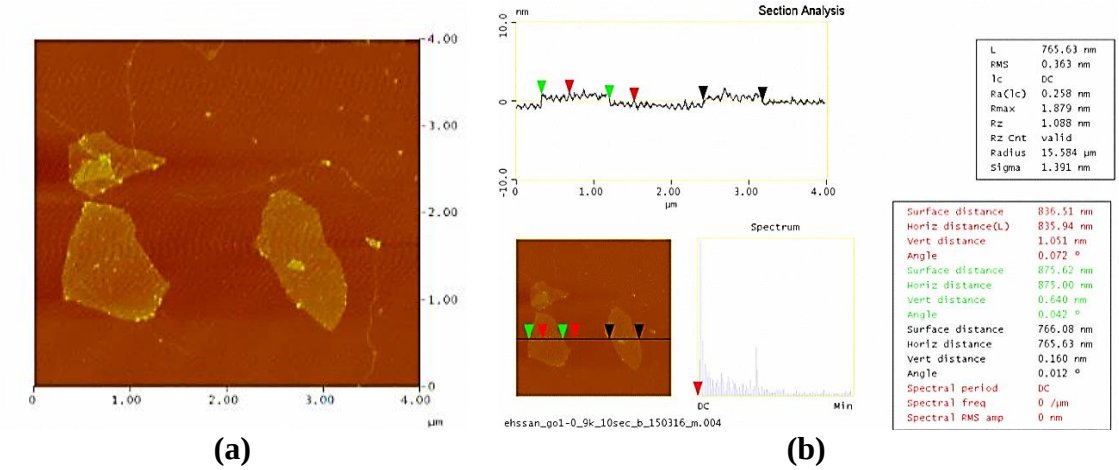

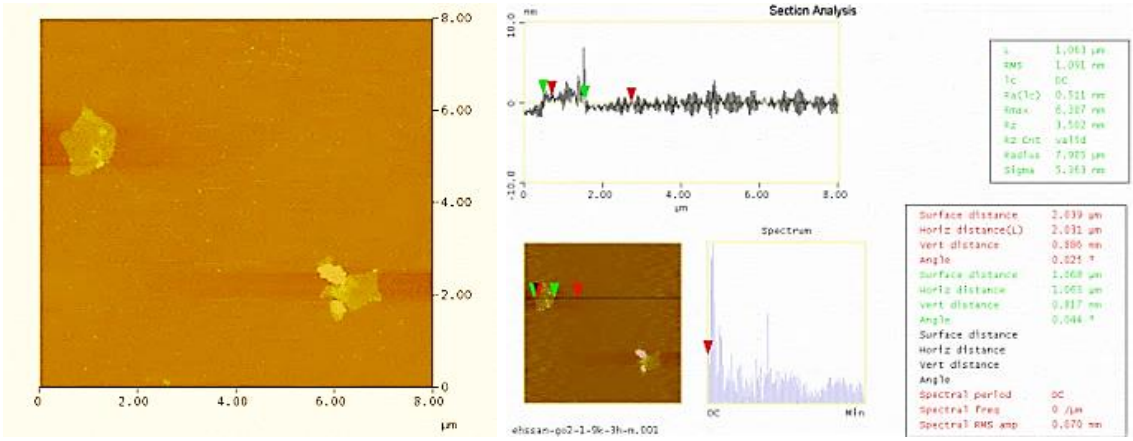

(c) **(d)**

Figure A5-3: AFM images of the bottom sample were sonicated for 1 h and centrifuged for 1.5 h at 11138 g of (a) GO1, (b) GO1.

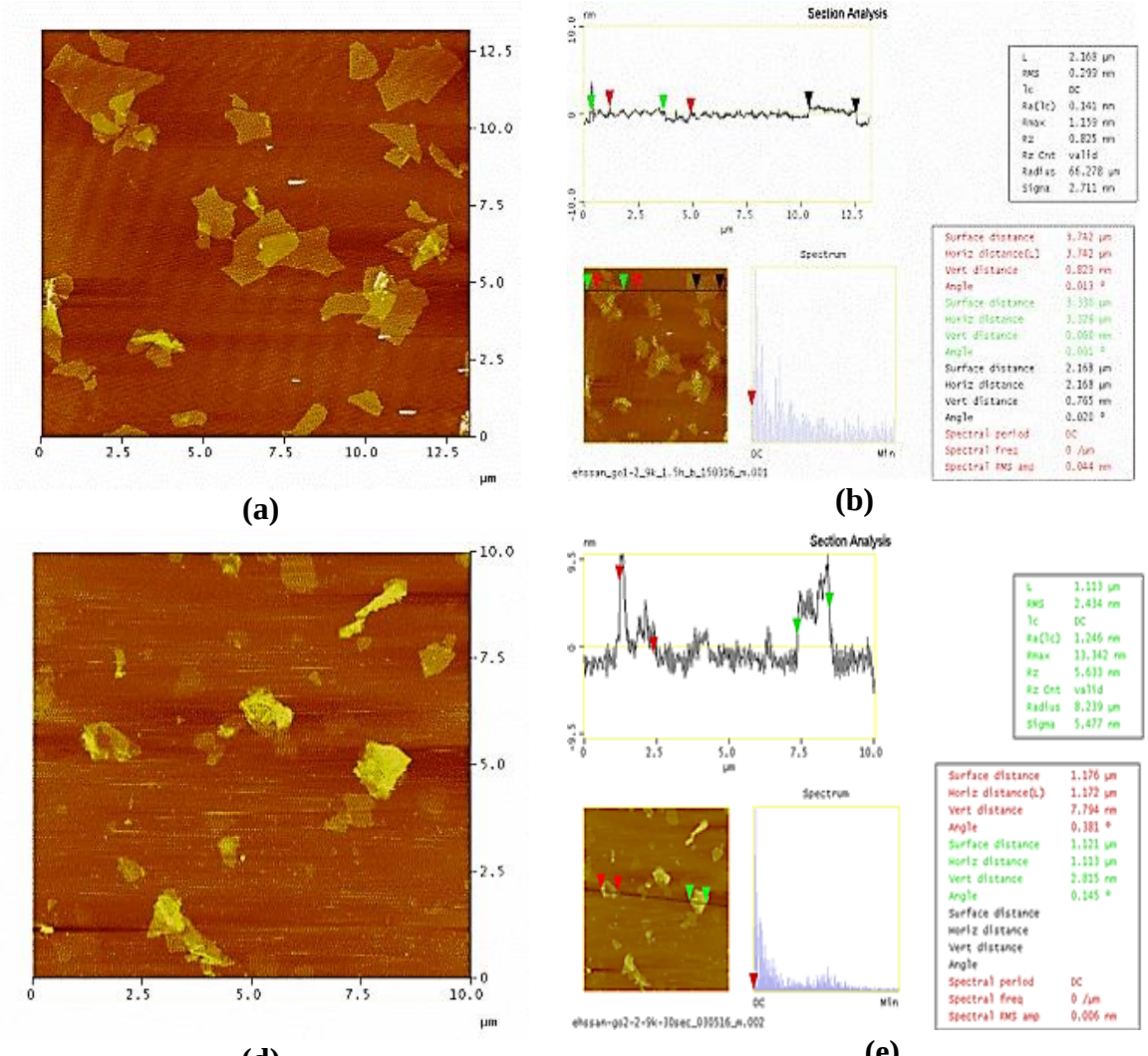

(a) **(b)**

(d) **(e)**

Figure A5-4: AFM images of the bottom samples were sonicated for 3 h and centrifuged for 3 h at 11138 g of (a) GO1, (b) GO2.

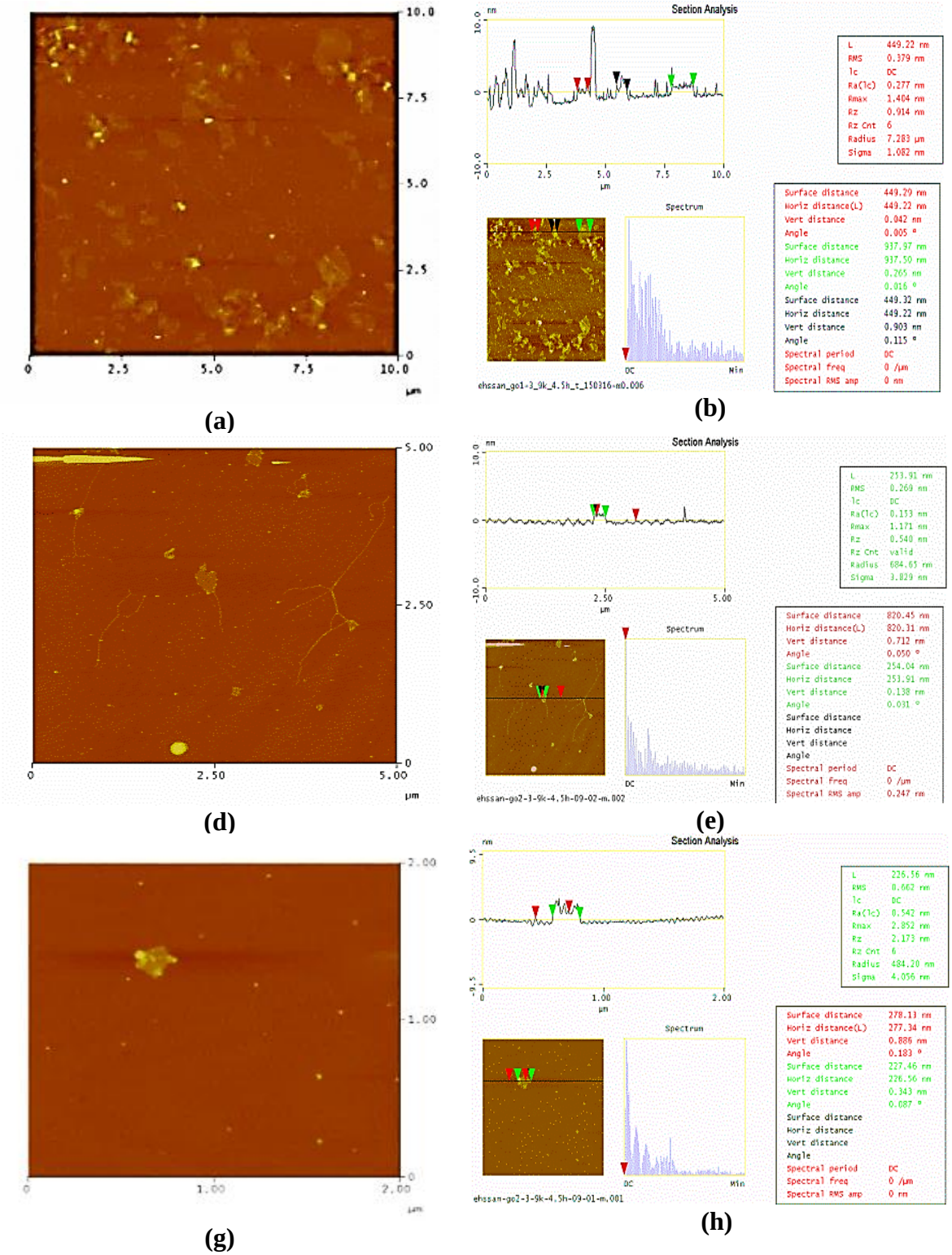

Figure A5-5: AFM images of the top samples were sonicated for 3 h and centrifuged for 4.5 h at 11138 g of (a, b and c) GO1 and (d, e, g and h) GO1.

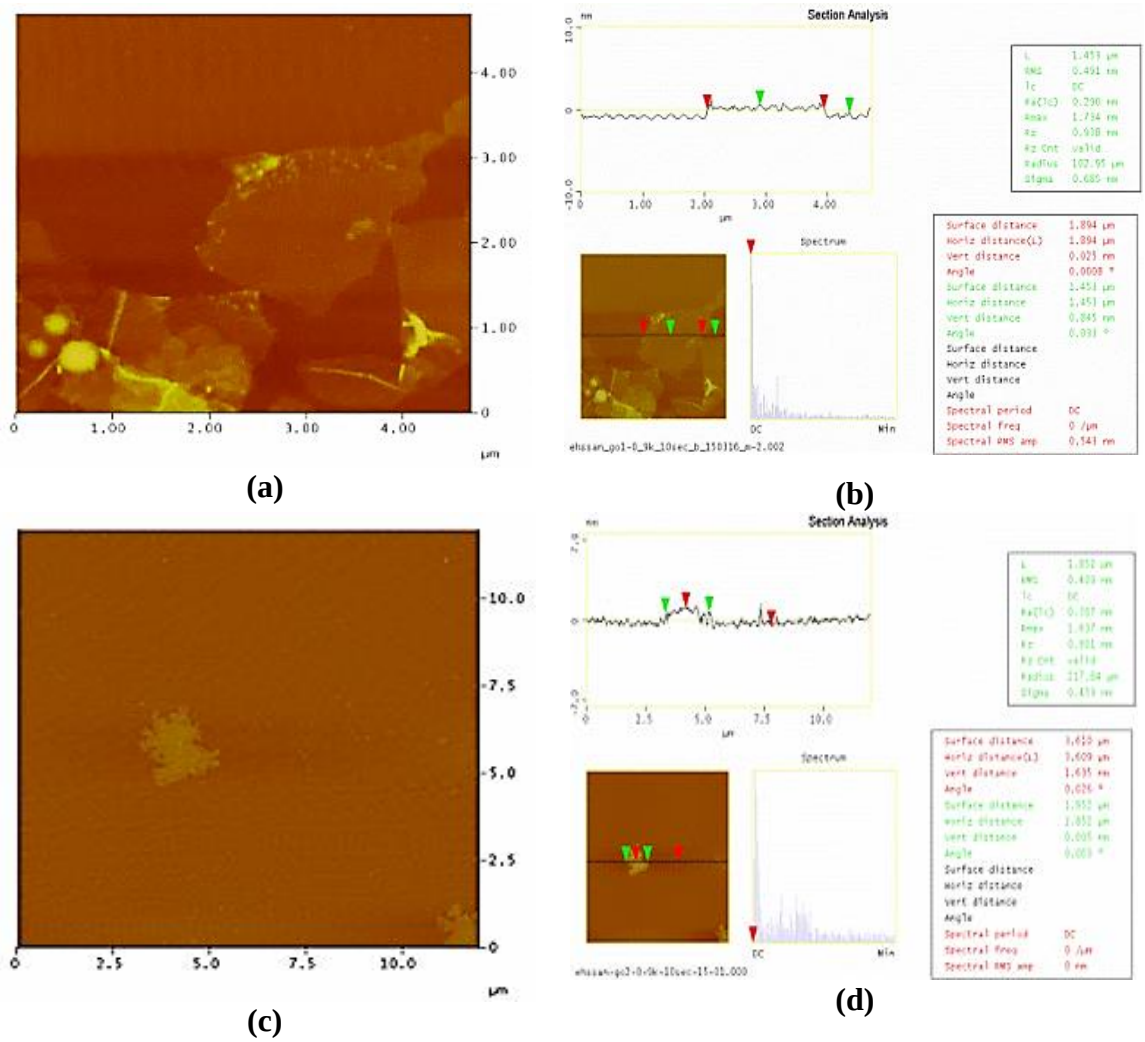

Figure A5-6: The effective diameter of sediment samples sonicated for 60 minutes and centrifuge speeds for 60 seconds at 4950 g (a, b, c and d) GO1 and (e and f) GO2.

Appendix of Chapter 6

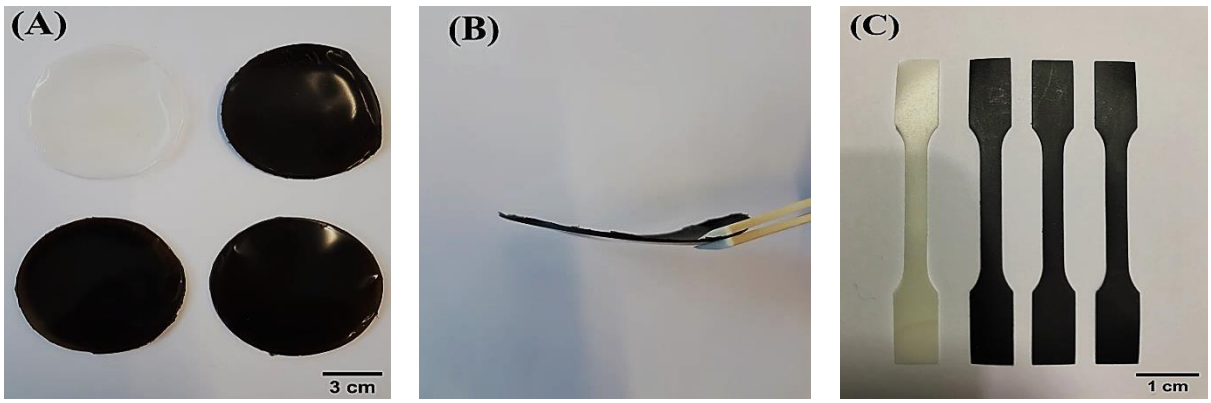

Figure A6-1: Optical microscopy images of PEO, PGO1-L, PGO1-M and PGO1-S.

Optical microscopy images show the optical images of PEO and nanocomposites. Optical images showed that the membrane without defects such as air bubbles or pores of both PEO and nanocomposites as shown in Figure 6-11 (A, B and C). These optical images observed the good dispersion without any aggregation of GO into PEO that led to the fairly smooth surface of the nanocomposites.